Quantum Effects Inside Rotating, Accreting Black Holes

by

Tyler Christian McMaken

B.A., Case Western Reserve University, 2018

M.S., University of Colorado Boulder, 2020

A thesis submitted to the

Faculty of the Graduate School of the

University of Colorado in partial fulfillment

of the requirements for the degree of

Doctor of Philosophy

Department of Physics

2024

Committee Members:

Andrew J.S. Hamilton, *Chair*

Oliver DeWolfe

Paul Romatschke

Andrew Lucas

Jason Dexter

McMaken, Tyler Christian (Ph.D., Physics)

Quantum Effects Inside Rotating, Accreting Black Holes

Thesis directed by Professor Andrew J.S. Hamilton

Models of black holes in general relativity have a problem. Rotating spacetimes like the Kerr metric do incredibly well at predicting observed phenomena outside of the event horizon, despite the fact that these models assume that the spacetime is completely empty and stationary, or at the least that any added matter or radiation will not contribute any gravity of its own. However, if this matter or radiation falls below the event horizon into a black hole's interior, counter-propagating streams will grow in energy and eventually diverge before they even reach the central singularity, at a special surface called the inner horizon. This divergence will trigger an inflationary instability that calls into question the self-consistency of the Kerr metric and the very stability of black holes as astrophysical (and especially as quantum mechanical) objects.

In this thesis, the astrophysically relevant effects of rotation and accretion are examined in detail to understand how they contribute self-consistently to the spacetime geometry of a black hole near its inner horizon. First, a model is developed (which I call the inflationary Kasner metric) that reproduces and generalizes the aforementioned inflationary instability within the framework of general relativity. Then, the effects of a quantum field near an inner horizon are explored. In particular, Hawking radiation emanating from the past horizon will accumulate and eventually diverge in temperature as the inner horizon is approached, and more numerically intensive calculations of the renormalized stress-energy tensor reveal that this diverging radiation plays a substantial role in modifying the black hole's interior geometry and replacing the inner horizon with a strong, chaotic, spacelike singularity. By analyzing the effects of both classical and quantum fields within black holes, one can thus come to a closer understanding of how astrophysically realistic black holes should appear in the context of semiclassical gravity.

Dedication

To Bill Brockmueller, whose love for physics and for God had such a great impact on all those around him during his short time on this Earth.

Acknowledgements

I would like to thank my advisor, Andrew Hamilton, for his encouraging support, vast knowledge, and continual advocacy throughout my educational journey. I am also grateful for the amazing network of friends, family, and coworkers that have helped me to thrive throughout my time in Boulder.

Soli Deo gloria

Publications

Publications included in this dissertation

[125] **T. McMaken** and A. J. S. Hamilton (2021),

"Geometry near the inner horizon of a rotating, accreting black hole",

Phys. Rev. D **103**, 084104.

[126] **T. McMaken** and A. J. S. Hamilton (2022),

"Renormalization of $\langle \varphi^2 \rangle$ at the inner horizon of rotating, accreting black holes",

Phys. Rev. D **105**, 125020.

[127] **T. McMaken** and A. J. S. Hamilton (2023),

"Hawking radiation inside a charged black hole",

Phys. Rev. D **107**, 085010.

[123] **T. McMaken** (2023),

"Semiclassical instability of inner-extremal regular black holes",

Phys. Rev. D **107**, 125023.

[128] **T. McMaken** and A. J. S. Hamilton (2024),

"Hawking radiation inside a rotating black hole",

Phys. Rev. D **109**, 065023.

[124] **T. McMaken** (2024),

"Backreaction from quantum fluxes at the Kerr inner horizon",

Phys. Rev. D (submitted).

Other publications

[121] **T. McMaken** (2022),

"Notes on primordial black hole origin for thermal gamma-ray bursts",

MNRAS **511**, 1218.

[89] A. J. S. Hamilton and **T. McMaken** (2022),

"Wave equations in conformally separable, accreting, rotating black holes",

Phys. Rev. D **106**, 124031.

[83] A. J. S. Hamilton and **T. McMaken** (2023),

"Unification of the four forces in the Spin(11,1) geometric algebra",

Phys. Scr. **98**, 085306.

[98] K. Jhurani and **T. McMaken** (2023),

"Existence of time-like geodesics in asymptotically flat spacetimes: A generalized topological criterion",

Adv. Stud. Theor. Phys. **17**, 109.

[122] **T. McMaken** (2023),

"Pancakification and negative Hawking temperatures",

Int. J. Mod. Phys. D **32**, 2342017.

Contents

Chapter

Figures

Figure

"I apologize if this letter is longer than usual, because I have not had time to write a shorter one."

–Blaise Pascal, *Lettres Provinciales Seize*, 1657

Chapter 1

Introduction: The Inner Horizon

1.1   Motivation

In 2017, the year before I began my Ph.D., the Nobel Prize in Physics was awarded to Rainer Weiss, Barry Barish, and Kip Thorne for the first detection of gravitational waves, with a remarkably short wait time between the award and the announcement of the discovery from the Laser Interferometer Gravitational-Wave Observatory (LIGO) a year prior [1]. The discovery provided novel evidence for the existence of two black holes merging together, the first of many such observations that helped usher in an unprecedented era of multimessenger astronomy.

Just a few years later, in 2020 the Nobel Prize in Physics was awarded to Roger Penrose, Reinhard Genzel and Andrea Ghez for their work on the theory of black hole formation and the observation of a supermassive compact object at the center of the Milky Way galaxy [74, 76, 151]. This object, now named Sagittarius A*, was later imaged directly (or rather, its ring of accreted plasma was imaged) by the Event Horizon Telescope (EHT) Collaboration [60], who had earned the Breakthrough Prize in Fundamental Physics in 2020 for taking the first direct image of a black hole shadow, for the supermassive black hole within the elliptical galaxy M87 [59].

Countless other recent discoveries have transformed our understanding of black holes, both on the observational side with detections from the James Webb Space Telescope, the Gaia telescope, and the GRAVITY Collaboration [78], and on the theoretical side with a resurgence of interest in the information paradox in 2019-20 [3, 150] and in renormalization techniques that laid the groundwork for the final two chapters of this thesis (see Chapter 3 for an overview).

What have we learned from this "golden decade" of black hole research? We now are certain that the Universe is filled with objects so massive yet so small that Newtonian physics fails to describe them and instead, Einstein's theory of general relativity reigns supreme (up to the classical limit). These objects are generically rotating, accreting matter and radiation, and, according to the traditional picture in semiclassical gravity, originally arose from the gravitational collapse of a star down to a radius so small that an event horizon (beyond which no matter or radiation can escape) forms. In fact, there are no known laws of classical physics that would prevent this collapse from continuing until its density reaches infinity [151]. In light of these unphysically infinite singularities, black holes offer themselves as one of the few places in the Universe where even general relativity fails and one can be sure to find new physics within. This new physics will broadly be referred to by the term *quantum gravity*.

It is worth distinguishing two separate but related concepts: the first is *astrophysical black holes*, which here are taken to represent those compact, rotating, accreting objects that really exist in nature. The second are *mathematical black holes*, which represent the mathematical models of spacetime geometries that feature an event horizon (or at the least an apparent horizon). Mathematical black holes predicted by general relativity often possess rich causal structures within their interiors, such as bifurcate inner horizons and time-traveling geodesics of the Kerr metric for rotating vacuum black holes that will be described in more detail in Sec. 1.2, but these structures may not form in astrophysically realistic systems. One of the goals of the present thesis is to understand whether the inner horizon structure of mathematical black holes also exists in astrophysical black holes.

Throughout my years of study of black hole interiors and discussions from researchers around the globe, I have found that though there are few who dare to study inner horizons, those who do are generally driven by one of two motivations (or three, when my advisor is included in the mix).[1] The first motivation, sought after largely by mathematicians and mathematical physicists, is

---

[1]Though there are many additional research groups interested in black hole interiors from a holographic perspective to understand, e.g., the black hole information problem, they generally ignore the inner horizon, assume a spacelike singularity (as supported by the conclusions of this thesis), or in a small number of cases [11] fit under the category of

to understand the strong cosmic censorship conjecture, which states that spacetime can never be extended past an inner (specifically, Cauchy) horizon and therefore that general relativity is purely deterministic (see Sec. 1.2 for details). Such a conjecture implies that travelers falling into a black hole (whether astrophysical in origin or artificially constructed in the far future) will never be able to continue through a wormhole to a new universe, even though such a wormhole is predicted for rotating or charged mathematical black holes. The potential for black holes to provide a mechanism to travel through time and/or space drives much of the perception of black holes in popular culture, aside from its utility as a mathematical problem in its own right.

The second main motivation many researchers have to study black hole inner horizons is to answer the long-standing open question, "what is the generic final state of a gravitational collapse?" For stellar objects below a given mass threshold, their collapse will eventually be stalled indefinitely by quantum degeneracy pressure to form either a white dwarf or a neutron star. But above this threshold, the collapse should continue until a black hole is formed. Beyond this point, the collapsing material may form a spacelike singularity without an inner horizon, a timelike singularity hidden by an inner horizon, or a lightlike (null) singularity along the inner horizon.[2] But one can probe even more deeply than to ask about the nature of the classical singularity produced from gravitational collapse. For example, Kerr himself espouses the idea that the collapse will eventually stall to form a star-like object within the inner horizon [102] (the viability of these so-called "regular" or "singularity-free" models will be examined in detail throughout Chapters 4 and 6, with the general conclusion that they are not semiclassically stable). Alternatively, various theories of quantum gravity make largely unconstrained predictions about how collapse toward a singularity might lead to a bounce toward a white hole or might destabilize the black hole to form a compact horizonless object (like a fuzzball or gravastar) or might cause the black hole to evaporate completely. The inner horizon and the instabilities it induces can thus serve as a theoretical testbed to differentiate various

_____

the first motivation mentioned in this paragraph.

[2]See Sec. 2.1 for details on the history of this problem of understanding the genericity of spacelike BKL singularities versus null singularities as the final endpoint of collapse-driven perturbations.

models in quantum gravity and understand what black holes really look like once they form.

A third potential motivation to study the inner horizon arises from the acknowledgment that the inflationary instability described in detail in Chapter 2 has the potential to produce a natural particle accelerator with energies orders of magnitude above anything we might ever hope to produce on Earth. Not only are black hole interiors ripe with new physics beyond the standard model that has yet to be explored, but they also have the potential to host collisions so large that baby universes may form [82]. While such an idea will not be explored further in this thesis, it would have profound implications for many of the outstanding problems of quantum information and of fine-tuning in cosmology.

As a primer for the reader, in the context of the first motivation described above, the conclusions of this thesis support the claim that both classical and quantum perturbations act to block off the inner horizon completely and prevent any possibility of traveling through a wormhole. In the context of the second motivation, the conclusions of this thesis support the claim that spacelike singularities are the generic result of any gravitational collapse with angular momentum and quantum matter, and these singularities persist up to at least Planckian energies over astrophysical time scales. In the context of the third motivation, the conclusions of this thesis are that not only will classical matter inflate to an exponentially diverging energy-momentum near the inner horizon, but even in a perfect vacuum, the mere presence of an inner horizon will cause the local, spontaneous production of Hawking radiation that will quickly exceed Big-Bang energies.

Whatever the reason for studying inner horizons within black holes, it is hopefully clear that something both complex and fascinating is happening within the heart of astrophysical black holes. Near-inner-horizon effects stand at the cutting edge of our pursuit of knowledge not only in the world of mathematics but also in our physical understanding of the ability of theories like general relativity and quantum gravity to model the real world. In the next section, a deeper focus will be placed on the nature of the inner horizon and other structures predicted by general relativity within mathematical black holes.

1.2   Anatomy of a black hole

In general relativity, space and time combine to form a single 4-dimensional manifold. One consequence of this fact is that black holes usually cannot be visualized comprehensively with cartoon diagrams that keep track of only spatial features. Instead, each observer within a spacetime will experience the black hole differently as they move in time along their own worldline.

As an example, the experience of a freely falling radial observer for the simplest possible model for black holes (the Schwarzschild metric) is shown in Fig. 1.1. Each frame in this figure was computed with the help of the Black Hole Flight Simulator [81], a ray-tracing code written by Andrew Hamilton that solves the geodesic equations so that various black hole spacetimes can be visualized in real time for any choice of observer. In the first frame of this figure, the observer begins in free-fall outside of the black hole. The most prominent feature in the image is the *black hole shadow*, the voided portion of the field of view caused by the bending of light rays near the central source of gravity. This shadow will also be referred to throughout this thesis as the *past horizon*, since its image lies at the same radius as the event horizon, though the event and past horizons are separate hypersurfaces—the observer passes directly through the event horizon in the third frame of Fig. 1.1, while the past horizon continues to appear ahead of the observer as they continue their descent all the way to $r = 0$.

Once the observer crosses the event horizon and enters into the interior of the black hole, they will never be able to return to the exterior portion of the Universe unless they travel faster than the speed of light (which is strictly forbidden for any object with mass). Instead, they are always doomed to reach the central spacelike singularity at $r = 0$. One might assume that this singularity would appear as a single point with infinite density, but rather, the final frames of Fig. 1.1 reveal that at the spacelike singularity, the past horizon appears as a planar surface extending infinitely far in every direction.

The black hole of Fig. 1.1 can also be visualized more comprehensively with the help of a conformal spacetime diagram, also called a Penrose diagram, as in Fig. 1.2. Such a diagram plots
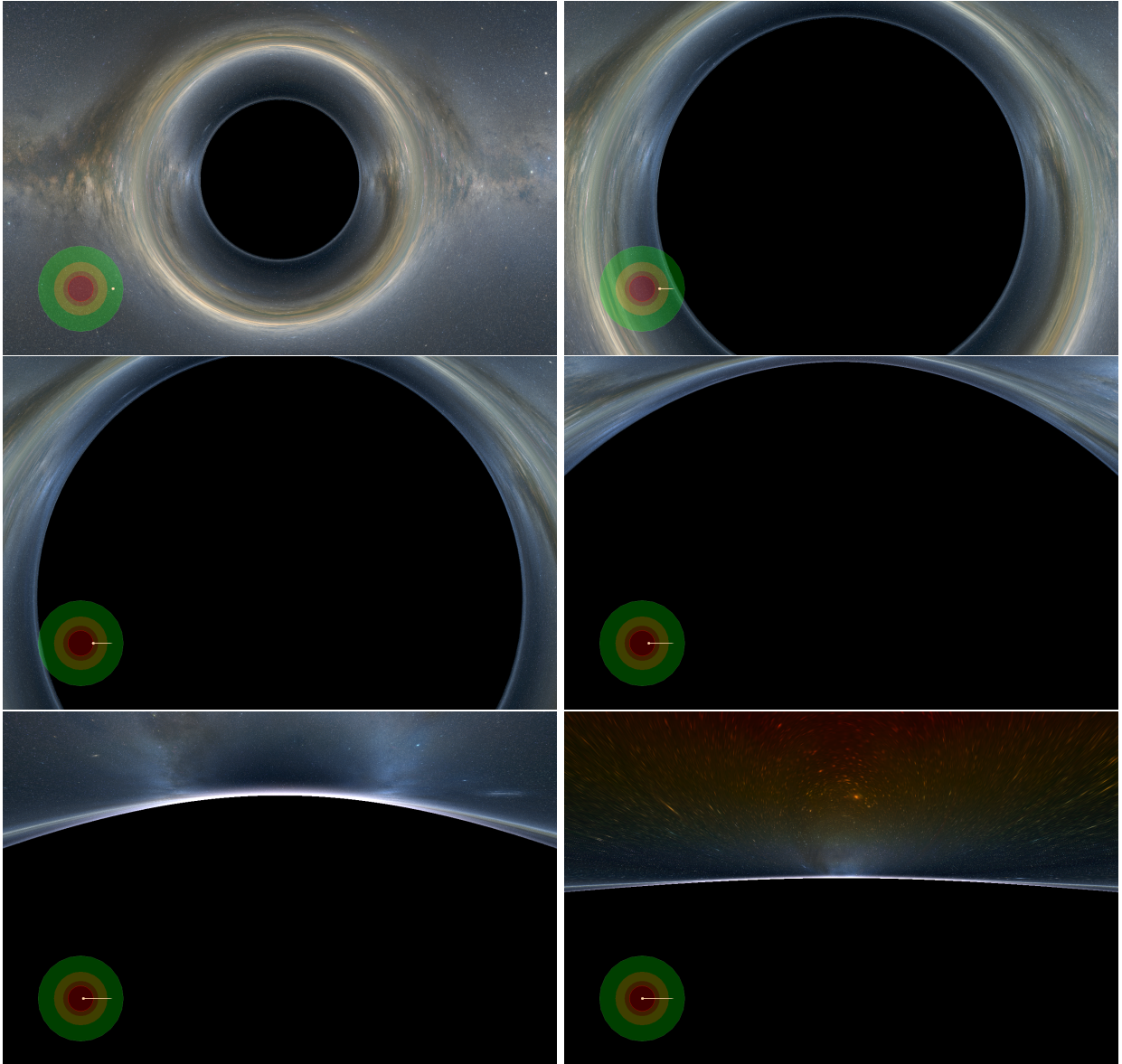
Figure 1.1: Six frames from a visualization of the view seen by an observer who free-falls radially through the horizon of a Schwarzschild black hole. From left to right then top to bottom, the observer is at radii $r = 10$, 3, 2, 1, 0.2, and 0.02 (in units of the gravitational radius GM/c^2). The inset at the bottom left shows the location of the observer in an equatorial spatial slice of the black hole spacetime, with the innermost red circle corresponding to the event horizon at $r = 2$. The background is an image of the Milky Way from Gaia Data Release 3 [72].
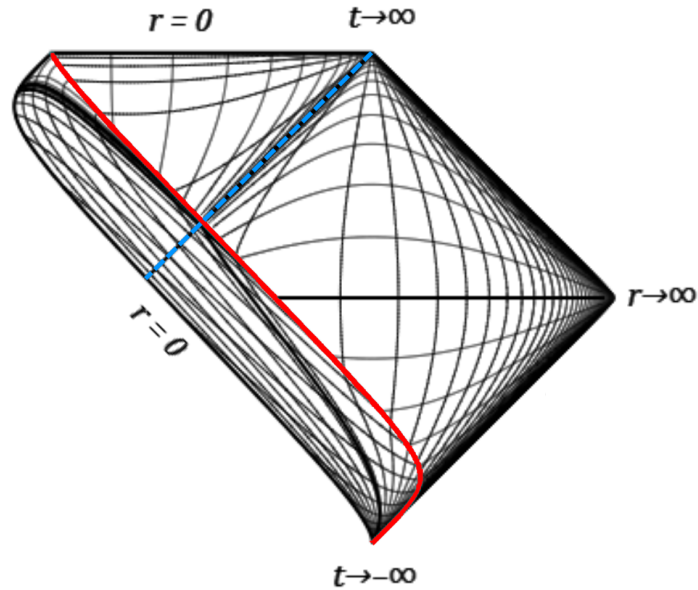
Figure 1.2: Penrose diagram for the gravitational collapse of a shell of matter (red curve) in a spherically symmetric, electrically neutral black hole. The event horizon is shown by the dashed blue line.

both radial and temporal coordinates, while suppressing the angular coordinates (every point on this diagram has the topology of a 2-sphere). Penrose diagrams are specially constructed so that radial light rays always appear with a slope of ±1 (in units where the speed of light $c = 1$) and all regions at infinity are conformally scaled to a finite position on the plot.

The Penrose diagram of Fig. 1.2 specifically depicts the Oppenheimer-Snyder spacetime, which models the gravitational collapse of a shell of matter into a black hole. Everywhere outside the shell (to the right of the red curve), the spacetime is identical to the Schwarzschild spacetime. Therefore, it is common to take the collapse to have occurred sufficiently far into the past that the full spacetime can be taken to be the Schwarzschild metric, equipped with the appropriate boundary conditions. For example, the visualizations of Fig. 1.1 were produced solely in the context of an eternal Schwarzschild black hole, where the past horizon is painted black. In the maximal analytic extension, that surface would correspond to the horizon of a white hole, but for a realistic black hole, the past horizon should coincide with the dimming, redshifting surface of the star that collapsed long ago to form the black hole, which will become too dark to see after just a few light-crossing times.

As previously mentioned, the black hole spacetimes depicted in Figs. 1.1 and 1.2 include the simplest class of black holes, the Schwarzschild metric. Schwarzschild black holes contain an event horizon at $r = 2GM/c^2$, a spacelike singularity at $r = 0$, and not much else. If one wishes to model a black hole that also contains an inner horizon, one can either add to the spacetime a non-zero electric charge (the Reissner-Nordström metric), non-zero angular momentum (the Kerr metric), or both (the Kerr-Newman metric). Consider, for example, the experience of an infalling observer in a charged black hole, as depicted in Fig. 1.3.

The first three panels of Fig. 1.3 appear almost identical to that of Fig. 1.1, since both follow an observer along a radial free-fall trajectory within a spherically symmetric spacetime. The main difference in the initial frames is in the positions and apparent sizes of the horizons—for a charged black hole, the event horizon will be at a smaller radius the greater the charge.

After the third frame of Fig. 1.3, the experience of the observer will change drastically depending on their trajectory. If the observer continues in free-fall (not shown), the black hole shadow will eventually stop growing in their field of view and instead will begin to shrink until it disappears entirely once the observer reaches the inner horizon. In contrast, Fig. 1.3 shows what happens if the interior observer accelerates outwards until they have negative specific energy with respect to an asymptotically distant observer (this energy E is the constant of motion corresponding to the covariant t-component of their 4-momentum; see, e.g., Eq. (2.42)). In that case, the black hole shadow will not shrink and vanish but instead will grow until it takes up the observer's entire field of view at the inner horizon, as shown in Fig. 1.3. A third intermediate case, where the interior observer's specific energy is precisely zero, may result in the black hole shadow only taking up half of the sky at the inner horizon; for Kerr black holes this special case is known as the Carter frame and is the frame of choice for the inflationary Kasner metric derived in Chapter 2.

Why does the sky shrink to a point in the final frames of Fig. 1.3 as the observer approaches the inner horizon, and how is the inner horizon even defined? The spacetime line element for an empty, charged black hole (or any static, spherically symmetric vacuum spacetime) can be written with free-fall coordinate time $t_{\rm ff}$ in the mostly pluses signature $(- + + +)$ (the metric signature of
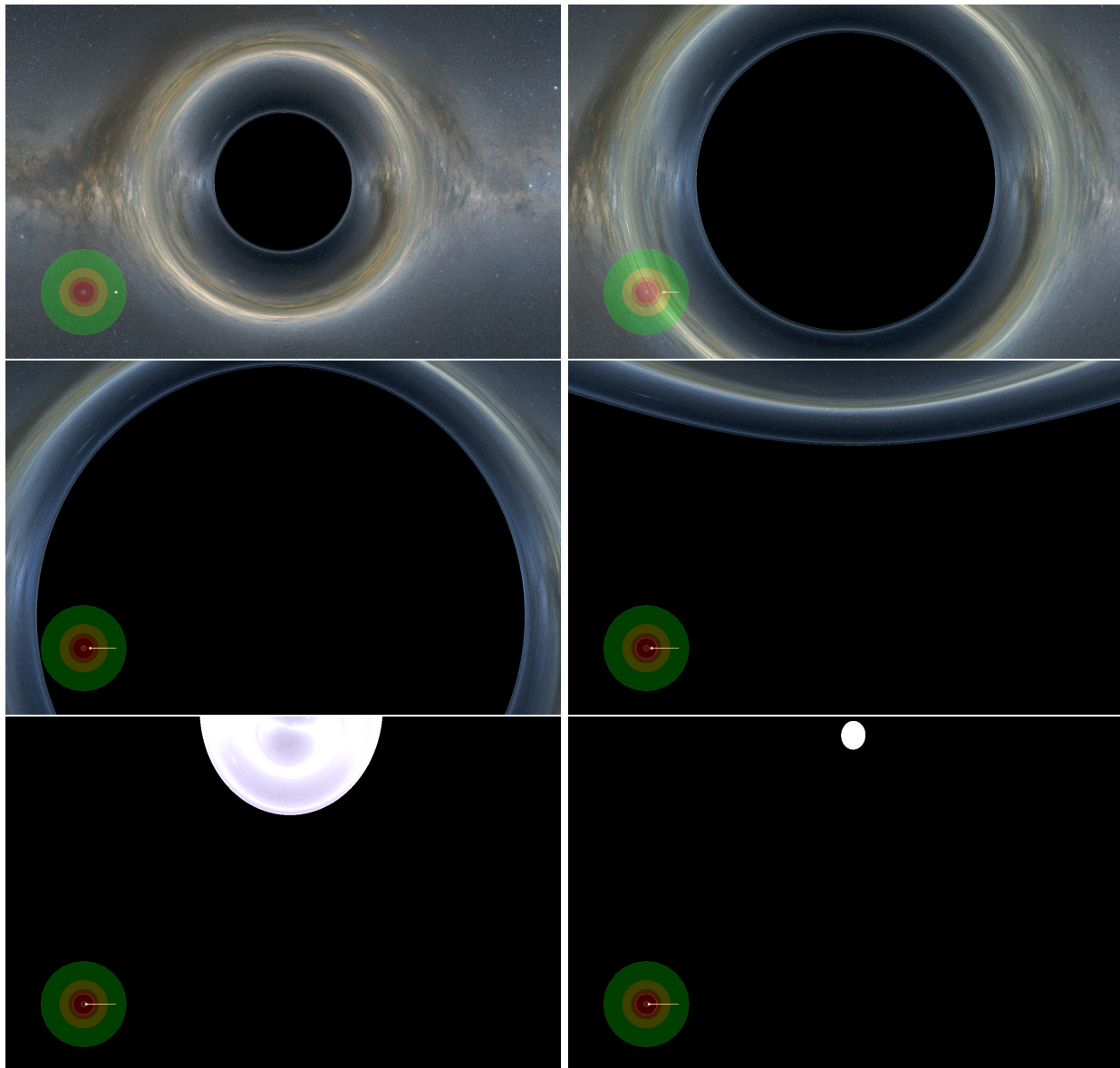
Figure 1.3: Six frames from a visualization of the view seen by an observer who free-falls radially into a Reissner-Nordström black hole with electric charge $Q = 0.8$ (in units of the gravitational electric charge $M\sqrt{4\pi\epsilon_0 G}$). From left to right then top to bottom, the observer is at radii $r = 10$, 3, 1, 0.8, 0.401, and 0.4001 (in units of the gravitational radius GM/c^2). Between the third and fourth frames, the observer briefly accelerates outward to return home, but since they have already crossed the event horizon at $r = 1.6$, their efforts are in vein—the sky above shrinks to an exponentially blueshifted point as they approach the inner horizon at $r = 0.4$.

choice throughout this thesis) as

$$ds^2 = -c^2 dt_{\rm ff}^2 + (dr + \beta c\ dt_{\rm ff})^2 + r^2(d\theta^2 + \sin^2\theta d\varphi^2), \tag{1.1}$$

where β is the Newtonian escape velocity, which for a Reissner-Nordström black hole with Misner-Sharp mass $M(r) = M - Q^2/(8\pi\epsilon_0 rc^2)$ is given by[3]

$$\beta c = \sqrt{\frac{2GM(r)}{r}} \tag{1.2}$$

(for comparison, the line element in the standard static coordinate chart is given in Eq. (4.1)). The key takeaway from this line element is that for constant free-fall time, $dt_{\rm ff} = 0$, the metric appears spatially flat (Minkowski), and therefore, the geometry can be understood as space itself flowing inward like a river at a speed βc, while any observers in free-fall are simply carried along by the river as they obey the rules of special relativity [88]. The place where the inflow of space reaches the speed of light, $\beta = 1$, corresponds to the event horizon, since beyond this point, the inflow speed β is greater than 1 and the observer will never be able to back-paddle fast enough to escape the black hole.

With this picture in mind, the inner horizon can be defined as the second spot in the infaller's trajectory (after the event horizon) where the inflow of space reaches the speed of light, this time with β approaching 1 from above. Conceptually, one can imagine a "force" (electric in the case of Reissner-Nordström or centrifugal in the case of Kerr) that couples to gravity to slow the inflow of space back down to subluminal speeds close enough to the central singularity. An infaller is then prevented from going too close to the gravitationally repulsive singularity at the core but is otherwise free to travel forward or backward in radius in the region beyond the inner horizon.

When an infaller has negative specific energy within a black hole, as in the last three frames

---

[3]It can often be a bit of a hassle to keep track of every fundamental constant throughout every calculation. For the remaining chapters of this thesis, geometrized units will be used so that the constants c, G, $4\pi\epsilon_0$, k_B, and $\hbar$ can be safely set to unity, with the only remaining degree of freedom for any quantity's units given by a mass dimension.
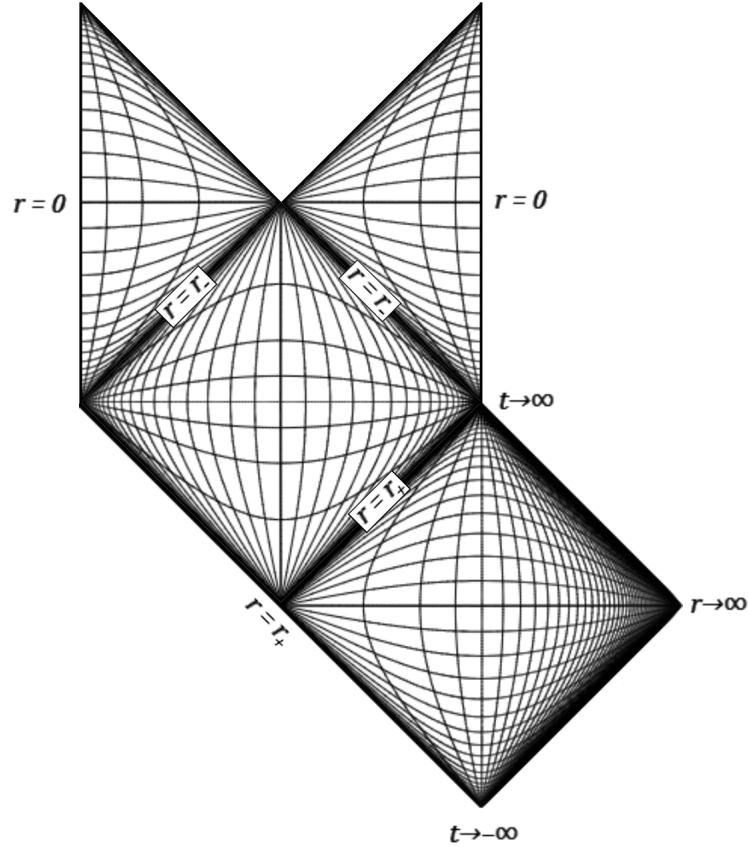
Figure 1.4: Penrose diagram for a static, charged (Reissner-Nordström) black hole.

of Fig. 1.3, it can thus be pictured as a futile back-paddling against the superluminal inflow of space, and they are doing so strongly enough that by the time they reach the inner horizon (where β slows to 1), an infinite amount of time has passed from the perspective of the outside Universe. Thus, the bright point in the last frame of Fig. 1.3 actually corresponds to light that is becoming infinitely blueshifted from a Universe approaching the end of time.

The causal structure of the inner horizon can be explained more comprehensively with the help of the Penrose diagram of Fig. 1.4, which equivalently models the spacetimes of Reissner-Nordström black holes and equatorial cuts of Kerr black holes. In this diagram, the collapsing shell of matter that first formed the black hole is assumed to have occurred far enough into the past that it coincides with the past horizon (the bottom-left diagonal at radius $r = r_+$). But more importantly, the inner horizon in this figure (at $r = r_-$) is split into two separate hypersurfaces—one that is only traversable

by ingoing (i.e., left-moving, positive-energy) observers, and one that is only traversable by outgoing (i.e., right-moving, negative-energy) observers. The observer of Fig. 1.3 is reaching this latter, rightmost portion of the inner horizon. At this hypersurface, note that the observer will see ingoing light signals from the entire future of the Universe (note where $t \to \infty$) all at once. The observer's evolution could in principle be continued past this point into the wormhole region at $0 < r < r_-$, but as Penrose was the first to point out [152], the light from the infinite future of the external Universe will be infinitely blueshifted at the inner horizon and would likely trigger an instability that substantially modifies the local geometry. This classical instability, known as *mass inflation*, is the subject of Chapter 2.

As a final comment on terminology, it is worth distinguishing the general notion of an *inner horizon*, as defined above in terms of the space inflow speed β, from the term *Cauchy horizon*, which refers to the boundary of predictability, beyond which one cannot deterministically extend the development of a Cauchy surface due to the presence of a timelike singularity. In all of the black hole spacetimes mentioned thus far (in particular, the Reissner-Nordström and Kerr metrics), the inner horizon is also a Cauchy horizon, but in general, it is possible to construct dynamically evolving black hole models where the two notions do not coincide (e.g., if the black hole evaporates). One may worry that the results of this thesis only apply to Cauchy horizons, and that in more realistic dynamical cases, inner horizons do not suffer any instabilities. However, recent work [39] has shown that this is not the case—an exponential buildup in energy is a generic feature of any slowly evolving inner horizon subject to perturbations. Thus, mass inflation is not simply an artificial byproduct of the fact that the Cauchy horizon receives infinitely blueshifted light from timelike infinity, but rather, this thesis is justified in its use of such stationary spacetimes as a minimal model for the generic divergent behavior near any inner horizon where ingoing and outgoing perturbations intersect and rapidly inflate to energies above the Planck scale.

1.3   Overview of remaining chapters

The central goal of this thesis is to show that although many mathematical black hole models feature inner horizons hiding timelike singularities, such structures break down and collapse into spacelike singularities when the astrophysically relevant effects of rotation and accretion are included. The progression of the thesis begins with arguments from classical physics (i.e., general relativity and classical field theory) in Chapters 1–2 before shifting focus to semiclassical physics (i.e., quantum field theory in curved spacetime) in Chapters 3–6. The fascinating conclusion is that even if a black hole is completely isolated and free of accretion that would trigger the classical mass inflation instability, the very presence of an empty quantum field is enough to create new particles from the vacuum once the black hole is formed that will diverge in energy near the would-be inner horizon.

On the side of classical physics, Chapter 2 presents a novel model I developed during the course of my Ph.D. that describes the geometry of spacetime near the inner horizon when a rotating black hole is subject to a small but continuous bath of accretion. The model, dubbed the *inflationary Kasner* metric, derives from a much more complex model of rotating, accreting black holes analyzed by Hamilton a decade prior [84, 85, 90], the *conformally separable Kerr* metric. While this latter model provides a complete global picture of how a rotating black hole responds to accretion, its behavior near the inner horizon becomes quite intractable when performing calculations from the full metric, especially if one wishes to analyze the effects of quantum fields. Consequently, the inflationary Kasner metric serves as a local proxy that captures the main perturbative effects near the inner horizon in a simple yet comprehensive manner.

The inflationary Kasner model presented in Chapter 2 is derived from the assumptions that near the inner horizon, the backreacting geometry evolves quickly enough in time that any spatial effects can be ignored (and therefore the metric is locally homogeneous), and the dynamics are sourced primarily by collisionless, hyperrelativistic fluid streams along the principal null directions. Under these simple assumptions (which agree with the full behavior in the conformally separable Kerr solution), the spacetime will evolve through two epochs. The first, associated with mass

inflation, predicts the traditional exponential increase in energy-momentum from generic perturbing accretion. But then, the evolution will transition into a collapse epoch, where the geometry will stop compressing along the direction of the accreted streams and instead will begin to stretch along the same direction as the transverse directions collapse until a spacelike singularity is reached.

After analyzing the classical effects of accretion inside a rotating black hole in Chapter 2, the question may then be asked of whether one can probe further beyond the straightforward conclusion that the inner horizon should be replaced with a spacelike singularity. The notion of a singularity in physics is a general one used to describe any appearance of infinite quantities that signal the breakdown of the theory; for example, in electromagnetism, the Coulomb potential features a singularity at $r = 0$ that can be truncated or screened with the help of quantum field theory, or in hydrodynamics, the edge of a shock wave or the pinch point of an emerging drop contain infinite velocity gradients or curvatures, respectively, which signal the need for a microscopic description of the physical behavior. In the case of gravitational curvature singularities like the one formed from perturbation instabilities near the inner horizon, the increase in energy beyond the Planck scale signals the need for a quantum description of gravity.

Chapter 3 describes precisely this quantum description of gravity. The framework of choice, semiclassical gravity, is an effective field theory able to probe the singularity more deeply than classical general relativity, or potentially to remove it entirely. Chapter 3 provides an overview of the formalism of quantum field theory in curved spacetime, describing the theoretical underpinnings, open problems, and quantities of interest to be calculated. Then, Chapters 4–6 examine the three most important quantities for various black hole models: Chapter 4 focuses on the particle number operator $\hat{N}$, which is used in calculations of Hawking radiation, Chapter 5 focuses on the squared field operator $\hat{\phi}^2$, which, when renormalized, gives information about vacuum polarization, and Chapter 6 focuses on the stress-energy tensor operator $\hat{T}_{\mu\nu}$, which, when renormalized, gives information about backreaction effects via a semiclassical modification to Einstein's field equations.

The central conclusion of these semiclassically-focused chapters is that both charged and rotating black hole spacetimes feature semiclassical divergences at the inner horizon even when they

are in a vacuum and devoid of accretion. In Chapter 4, the most extensive chapter (it combines two and half published works, one on Reissner-Nordström, one on Kerr, and part of one on singularity-free black holes), it is shown by several independent means that an infalling observer will experience a diverging amount of Hawking radiation as they approach the inner horizon. Similarly for Chapters 5 and 6, it is shown that even if one regards these Hawking particles as locally unphysical, other semiclassical quantities also act to backreact on the spacetime and produce the same dynamic evolution predicted in the classical case in Chapter 2.

The conclusion is simple—inner horizons are not stable. If someone (or something) were to fall into an astronomically realistic black hole, they could not enter into a wormhole or orbit a stable, regular core, but instead, the effects of both general relativity and 1-loop quantum field theory always conspire to block off their descent. The generic outcome appears to be the formation of a strong, chaotic, spacelike singularity in place of the inner horizon, thus restoring the notion of determinism within semiclassical gravity.

Chapter 2

Classical Mass Inflation

The contents of this chapter have been published as [125].

2.1   Introduction

Physicists have long wondered what happens inside astrophysically realistic black holes. The exterior geometry of a back hole has been well-established to be described completely by the Kerr-Newman metric, since any perturbations during a generic collapse will be radiated away and leave the black hole with only three uniquely-identifying parameters: a charge Q, angular momentum J, and mass M. But when the Kerr-Newman solution is extended to the interior of a black hole's event horizon, some puzzling, nonphysical structures emerge.

Within the simplest model of black holes (the Schwarzschild solution), no major peculiarities or nonphysical structures arise except the divergence of the spacetime curvature at $r=0$ at a spacelike singularity. Prior to the 1960s, many opposed the idea that a realistic gravitational collapse would lead to a singularity, since most known models of collapse were highly idealized and unstable to perturbations [115]. However, in 1965, Penrose published a theorem demonstrating the inevitability of singularities within event horizons of black holes [151], and soon after, Belinskii, Khalatnikov, and Lifschitz found a realistic model for such a collapse to a spacelike singularity (the so-called BKL collapse), which is highly complex and oscillatory [24].

In spite of these efforts, the fact remains that most, if not all, black holes are not spherically symmetric and instead carry at least some angular momentum. The structure of the Kerr-Newman

interior differs drastically from that of a Schwarzschild black hole—instead of a spacelike singularity at the center, the Kerr-Newman solution has a timelike singularity along with a second horizon within the event horizon. This inner horizon coincides with the singularity when $J = 0$ and $Q = 0$, but for nonzero spin or charge, the spacetime between the inner horizon and the singularity forms a region in which predictability breaks down—general relativity is powerless to predict unambiguously what would happen if an observer passes through the inner horizon, because such an observer would be able to view the singularity.

Aside from the breakdown of predictability, the added interior structure of a rotating or charged black hole is problematic for another reason. As first pointed out by Penrose in the context of a Reissner-Nordström (charged) black hole, the inner horizon is a surface of infinite blueshift, so that an infalling observer at an inner horizon would see the entire history or future of the Universe flash before their eyes as the energy of any incoming radiation becomes classically unbounded [152]. Penrose conjectured that the added effects of this diverging radiation would change the underlying spacetime curvature of the vacuum solution [165]. This conjecture was finally confirmed a few decades later, when Poisson and Israel performed a nonlinear perturbation analysis in a seminal 1990 paper [23, 154]. Poisson and Israel concluded that the crossing of ingoing and outgoing shells of null dust at the inner horizon would lead to a divergence of the spacetime curvature. Poisson and Israel dubbed this divergence "mass inflation," because an observer near the inner horizon would measure an exponentially large quasi-local internal mass parameter (though the global mass as measured at infinity would remain finite).

Classically, the Poisson-Israel toy model of mass inflation leads to the formation of a null weak curvature singularity, in which the curvature locally diverges but the tidal distortion of extended objects traveling along timelike geodesics remains finite, allowing for the continuation of spacetime beyond the Cauchy surface [138, 139]. Dafermos extended this result for the less-simplified Einstein-Maxwell-real scalar field equations [49], and Ori and others found that null curvature singularities provide a generic class of solutions to the Einstein equations, adding it to the list of known possible singularities that had previously only included the BKL singularity [32, 140, 142]. The BKL and

null curvature singularities are quite different in nature—though they both may be oscillatory in nature, the BKL singularity is strong and spacelike, whereas the null curvature singularity is weak and lightlike [141].

Despite the enticement of the null weak curvature singularity, both in its mathematical accessibility and in its potential to allow for a gateway to another Universe, it suffers one fatal flaw. One of the key assumptions for all the models that predict a null weak singularity is that the collapsed black hole is in complete isolation. Under this assumption, which still dominates much of the research program for mass inflationary phenomena to this day [37], the only source of ingoing perturbations is the Price tail, a stream of gravitational waves emitted and backscattered during the collapse. The Price tail decays with an inverse power law in advanced time, and calculations for the formation of a null weak singularity assume that no additional radiation perturbs the metric above that power law [156]. However, astrophysical black holes continue to accrete material long after the initial gravitational collapse, and even the cosmic microwave background radiation would dominate over the longest-lived Price tail modes of a stellar-mass black hole after only 1 second [86].

Motivated by this shortcoming, Burko found numerically that a null weak singularity only forms for a sufficiently steep radiation power law drop-off, and that if it does not drop off quickly enough, a spacelike singularity will form at the intersection of the ingoing and outgoing inner horizons and grow until it has completely sealed off the Kerr tunnel [34, 35].

Hamilton subsequently developed a self-similar model for the inner horizon spacetime that generalizes the mass inflation phenomenon to include arbitrary ingoing and outgoing collisionless streams of radiation at arbitrary times, first for spherical-symmetric spacetimes [91] and soon after for the more realistic case of rotating black holes [84, 85, 90]. The rotating case, which assumes conformal separability, is reviewed in more detail in Section 2.3.1. The key conclusion from this model is that the continued streams eventually slow the inflation of the curvature, causing the spacetime to collapse radially. The resulting global geometry, used throughout this chapter, is shown in the Penrose diagram of Fig. 2.1.

Though the conformally separable model of Hamilton is valid through the inflation and the
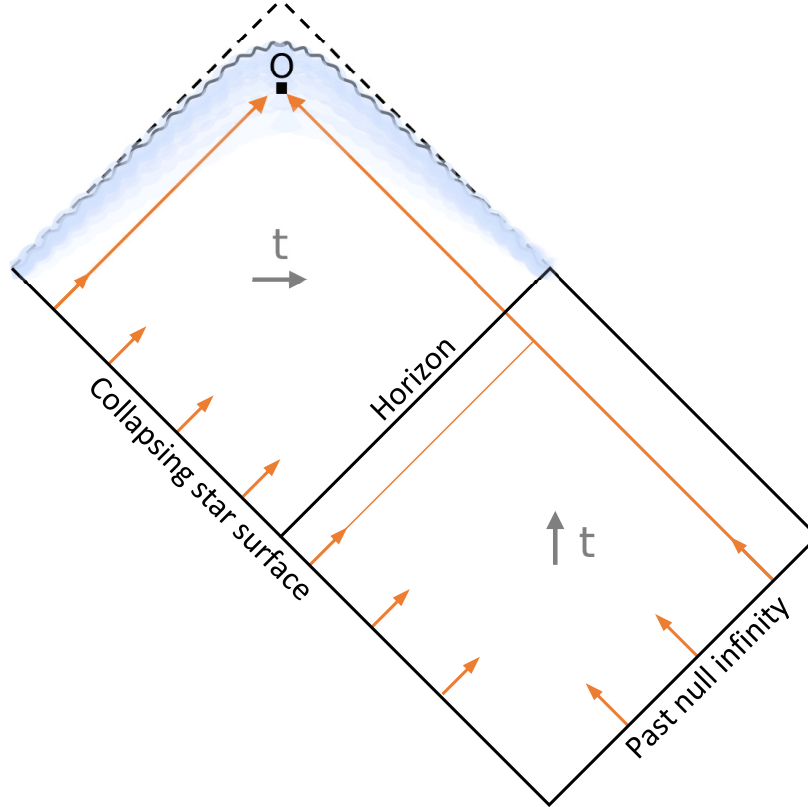
Figure 2.1: Penrose diagram for the late-time evolution of a collapsed star with a Kerr exterior (white) matched to an inflationary Kasner regime (shaded blue). The inner horizons (dashed lines) of the Kerr metric are superseded by the BKL singularity of the inflationary Kasner model (squiggled line). The gray arrows labeled t indicate the direction of increasing Boyer-Lindquist time.

beginning of the subsequent collapse of the spacetime, it eventually fails once the rotational motion of the streams becomes comparable to their radial motion. After this point, numerical calculations indicate that the collapse follows a BKL-like behavior [86]. However, recent semiclassical calculations suggest that quantum backreaction effects may alter or even invert the collapse [18]. Thus, one may wish to calculate the renormalized stress-energy tensor in the conformally separable Kerr spacetime. Such a calculation has not yet been attempted because of the complexity of Hamilton's model; however, here we derive a new model that considerably simplifies the conformally separable Kerr model while still retaining its essential features of inflation and collapse. This model, dubbed the inflationary Kasner model, will be shown to provide a reasonable continuation of the Kerr metric

near the inner horizon through the first two Kasner epochs of its BKL collapse, and it will hopefully allow for future quantum calculations in this region (see Chapter 5).

In Section 2.2, the inflationary Kasner metric is derived as a general solution to Einstein's equations for a homogeneous spacetime sourced by a null, perfect fluid. In particular, it is found that for a line element of the form

$$ds^2 = -\alpha(T)^2 dT^2 + a_1(T)^2 dx^2 + a_2(T)^2 dy^2 + a_3(T)^2 dz^2, \tag{2.1}$$

the general solution for an energy-momentum tensor whose only non-negligible components are $T_{00} = T_{11}$ takes the form

$$a_1 \propto T^{-p/2} \exp\left(T^{2p}\right), \qquad a_2 \propto a_3 \propto T^p, \tag{2.2}$$

for some arbitrary constant p, the arbitrariness of which reflects the gauge freedom in the choice of the time coordinate T. This metric is dubbed the inflationary Kasner metric because it is a natural non-vacuum extension of the Kasner metric, a vacuum solution used to model collapse to a BKL singularity. During a BKL collapse, the spacetime undergoes a series of "BKL bounces," between which the evolution is described by the Kasner metric's power law behavior. The BKL model is described in more detail in Sec. 2.2.3, in which it is shown how the two epochs of the inflationary Kasner solution can be reduced in certain limits to previously obtained results.

Then, in Sec. 2.3, it is shown how the inflationary Kasner model can be applied to the inner geometry of astrophysical black holes. To do so, the model is connected to the Kerr metric in a regime where both are valid, employing Hamilton's conformally separable Kerr model to facilitate the matching and to determine the degree to which the assumptions of the inflationary Kasner model are valid near the inner horizon. Sec. 2.3.1 is devoted to reviewing the conformally separable Kerr model and comparing it to the inflationary Kasner model, where it is found that the inflationary exponent ξ of the conformally separable model is related to the inflationary Kasner time T via the relation $T^p \propto e^{-\xi}$. Then, in Sec. 2.3.2, the behavior of null geodesics in the model is analyzed, via ray-tracing from an observer in the inflationary Kasner spacetime backwards until they connect to

null geodesics in the Kerr spacetime. Such a matching allows one in Sec. 2.4 to answer the practical question of what an observer falling toward the inner horizon of an astrophysical, classical black hole might see.

2.2 Inflationary Kasner metric

2.2.1 Preliminaries

The present analysis uses an orthonormal tetrad formalism, in which quantities are defined in the tetrad basis $\{e_{\hat{m}}\}$ to yield physically measured components in the local, Cartesian frame of an observer. In such a formalism, coordinate-frame quantities can be converted into tetrad-frame quantities through the vierbein $e^{\hat{m}}{}_{\mu}$, which can be read off directly from a line element via

$$ds^2 = g_{\mu\nu}dx^\mu dx^\nu = \eta_{\hat{m}\hat{n}}e^{\hat{m}}{}_{\mu}e^{\hat{n}}{}_{\nu}dx^\mu dx^\nu. \tag{2.3}$$

Indices for abstract, Einstein-summed tetrad-frame quantities are denoted by lowercase Latin letters with hats, while indices for abstract, Einstein-summed coordinate-frame quantities are denoted by lowercase Greek letters. Indices for specific components of tetrad-frame quantities are denoted by Arabic numerals, while those of coordinate-frame quantities are given by their standard Latin or Greek letters. Thus a tetrad-frame four-vector can be expressed as $k^{\hat{m}} = \{k^0, k^1, k^2, k^3\}$, a coordinate-frame one as $k^\mu = \{k^t, k^r, k^\theta, k^\phi\}$, and the conversion between the two is given by

$$k^{\hat{m}} = e^{\hat{m}}{}_{\mu}k^\mu. \tag{2.4}$$

For a more complete review of the tetrad formalism, see Müller's "Catalogue of Spacetimes" [134] or Chandrasekhar's *The Mathematical Theory of Black Holes* [42].

2.2.2   Derivation of the line element

The purpose of this subsection is to derive the line element for the inflationary Kasner metric, which in its final form reads

$$ds^2 = a_1^2 \left(-dT^2 + dx^2 \right) + a_2^2 \left(dy^2 + dz^2 \right),$$
(2.5)

with

$$a_1 = \frac{\mathrm{e}^{(T-T_0)/2}}{\sqrt{16\pi\Phi_0 T_0}} \left(\frac{T}{T_0} \right)^{-1/4}, \qquad a_2 = \frac{1}{\sqrt{16\pi\Phi_0 T_0}} \left(\frac{T}{T_0} \right)^{1/2},$$
(2.6)

where the time coordinate T progresses backward from the positive constant T_0 to 0, and the positive constant Φ_0 represents the mass-energy density of the streams of fluid seen by an observer at $T = T_0$. In general, the mass-energy density will be found to depend on T through the relation

$$\Phi(T) = \frac{\Phi_0}{\sqrt{T/T_0} \; \mathrm{e}^{T-T_0}}.$$
(2.7)

The form of the inflationary Kasner line element of Eq. (2.5) relies on two main assumptions. First, assume the metric is spatially homogeneous, so that the metric coefficients are functions only of the time coordinate T. Such a requirement exists in a more stringent form for the Kasner metric described in the next section, in which the metric coefficients are power laws in T during a BKL collapse. Second, assume the solution to Einstein's equations is sourced by a collisionless, null, perfect fluid in the radial direction. In a tetrad frame, such a source corresponds to the energy-momentum tensor

$$T_{\hat{m}\hat{n}} = \begin{pmatrix} \Phi & 0 & 0 & 0 \\ 0 & \Phi & 0 & 0 \\ 0 & 0 & 0 & 0 \\ 0 & 0 & 0 & 0 \end{pmatrix},$$
(2.8)

where Φ is the mass-energy density of the null streams. For a realistic accreting black hole, even if the accreted material is not null and purely radial, near the inner horizon, all streams of matter and radiation are expected to focus along the principal null directions ultrarelativistically, so that the

energy-momentum tensor to a good approximation takes the form above.

Assume the line element (and therefore the vierbein) can be written in a diagonal basis. Thus, the tetrad 1-forms may be written as

$$e^0_{\ \mu}dx^\mu = \frac{a_1 a_2 a_3}{T}dT, \tag{2.9a}$$

$$e^1_{\ \mu}dx^\mu = a_1 dx, \tag{2.9b}$$

$$e^2_{\ \mu}dx^\mu = a_2 dy, \tag{2.9c}$$

$$e^3_{\ \mu}dx^\mu = a_3 dz, \tag{2.9d}$$

where the scale factors a_i are functions only of the time coordinate T but are otherwise left arbitrary. The choice of the present form of $e^0_{\ T}$ will help to simplify later calculations; in general, $e^0_{\ T}$ may be any function of T after a suitable transformation of the T coordinate.

Instead of working in a coordinate basis and using the metric components to find the Christoffel connection coefficients $\Gamma^\mu_{\ \nu\rho}$, here we work entirely in a tetrad basis without reference to the coordinate frame, so we must first find the analogous tetrad connection coefficients. In the tetrad basis, the connection 1-forms $\omega^{\hat{m}}_{\ \hat{n}}$ (which are antisymmetric in their tetrad-frame indices) can be defined by the torsion-free condition

$$de^{\hat{m}} + \omega^{\hat{m}}_{\ \hat{n}} \wedge e^{\hat{n}} = 0, \tag{2.10}$$

or in component form,

$$\omega^{\hat{m}}_{\ \hat{n}\rho} = e^{\hat{m}}_{\ \mu}\nabla_\rho\, e_{\hat{n}}^{\ \mu}. \tag{2.11}$$

Converting all indices of the connection 1-form components to a tetrad basis then yields the Ricci rotation coefficients $\omega_{\hat{m}\hat{n}\hat{r}}$, antisymmetric in their first two indices:

$$\omega_{\hat{m}\hat{n}\hat{r}} = \eta_{\hat{\ell}\hat{m}}e_{\hat{r}}^{\ \rho}\omega^{\hat{\ell}}_{\ \hat{n}\rho} = e_{\hat{m}}^{\ \mu}e_{\hat{r}}^{\ \rho}\nabla_\rho\, e_{\hat{n}\mu}. \tag{2.12}$$

For the tetrad 1-forms of Eqs. (2.9), the six nonvanishing Ricci rotation coefficients are as follows,

where $i \in \{1, 2, 3\}$ and a dot above a variable indicates differentiation with respect to the time coordinate T:

$$\omega_{0ii} = -\omega_{i0i} = \frac{T}{a_1 a_2 a_3} \frac{\dot{a}_i}{a_i}. \tag{2.13}$$

The tetrad-frame Riemann curvature tensor components $R_{\hat{k}\hat{\ell}\hat{m}\hat{n}} = e_{\hat{k}}{}^{\kappa} e_{\hat{\ell}}{}^{\lambda} e_{\hat{m}}{}^{\mu} (\nabla_{\kappa}\nabla_{\lambda} - \nabla_{\lambda}\nabla_{\kappa}) e_{\hat{n}\mu}$ can then be calculated, yielding 18 nonzero components: for $i, j \in \{1, 2, 3\}$ and $i \neq j$,

$$R_{0i0i} = R_{i0i0} = -R_{0ii0} = -R_{i00i} = \frac{T^2}{a_1^2 a_2^2 a_3^2} \left(\frac{\dot{a}_i}{a_i} \frac{d \ln (a_1 a_2 a_3 / T)}{dT} - \frac{\ddot{a}_i}{a_i} \right), \tag{2.14a}$$

$$R_{ijij} = -R_{ijji} = \frac{T^2}{a_1^2 a_2^2 a_3^2} \frac{\dot{a}_i \dot{a}_j}{a_i a_j}. \tag{2.14b}$$

Then, the tetrad-frame Ricci tensor $R_{\hat{k}\hat{m}} = \eta^{\hat{\ell}\hat{n}} R_{\hat{k}\hat{\ell}\hat{m}\hat{n}}$, Ricci scalar $R = \eta^{\hat{k}\hat{m}} R_{\hat{k}\hat{m}}$, and tetrad-frame Einstein tensor $G_{\hat{k}\hat{m}} = R_{\hat{k}\hat{m}} - \frac{1}{2}\eta_{\hat{k}\hat{m}} R$ follow naturally. The resulting four nonzero Einstein components, where $i \in \{1, 2, 3\}$ with cyclic addition, are

$$G_{00} = \frac{T^2}{a_1^2 a_2^2 a_3^2} \left(\frac{\dot{a}_1 \dot{a}_2}{a_1 a_3} + \frac{\dot{a}_1 \dot{a}_3}{a_1 a_3} + \frac{\dot{a}_2 \dot{a}_3}{a_2 a_3} \right), \tag{2.15a}$$

$$G_{ii} = G_{00} - \frac{T}{a_1^2 a_2^2 a_3^2} \frac{d}{dT} \left(\left(\frac{\dot{a}_{i+1}}{a_{i+1}} + \frac{\dot{a}_{i+2}}{a_{i+2}} \right) T \right). \tag{2.15b}$$

Under the assumption that the tetrad-frame energy-momentum tensor has the form of Eq. (2.8), Einstein's equations give a system of four nontrivial equations:

$$G_{00} = 8\pi\Phi, \tag{2.16a}$$

$$G_{11} = 8\pi\Phi, \tag{2.16b}$$

$$G_{22} = 0, \tag{2.16c}$$

$$G_{33} = 0. \tag{2.16d}$$

The most natural solution to Eqs. (2.15) and (2.16) can be obtained by setting $a_2 = a_3$, which reduces Eqs. (2.16c) and (2.16d) to the same equation. Physically, this corresponds to the assumption

that the y-z plane, orthogonal to the streams of matter, remains isotropic, a reasonable assumption close to the horizon, given that any streams will focus ultrarelativistically in the x-direction. The remaining three equations simplify to

$$8\pi\Phi = \frac{T^2 H_2}{a_1^2 a_2^4}(2H_1 + H_2), \tag{2.17a}$$

$$8\pi\Phi = \frac{T^2 H_2}{a_1^2 a_2^4}\left(2H_1 + H_2 - \frac{2\dot{H}_2}{H_2} - \frac{2}{T}\right), \tag{2.17b}$$

$$0 = 2H_1 H_2 + H_2^2 - \frac{H_1 + H_2}{T} - \dot{H}_1 - \dot{H}_2, \tag{2.17c}$$

where we have introduced the quantities

$$H_i \equiv \frac{\dot{a}_i}{a_i} \qquad \Longrightarrow \qquad \dot{H}_i = \frac{\ddot{a}_i}{a_i} - H_i^2 \tag{2.18}$$

for $i \in \{1, 2\}$. Combining Eqs. (2.17a) and (2.17b) to eliminate Φ yields

$$\frac{\dot{H}_2}{H_2} = -\frac{1}{T}$$

$$\Longrightarrow H_2 = \frac{p}{T}$$

$$\Longrightarrow a_2 = C_2 T^p, \tag{2.19}$$

where p and C_2 are arbitrary integration constants. Substituting this solution into Eq. (2.17c) yields

$$\dot{H}_1 - \frac{(2p-1)}{T}H_1 - \frac{p^2}{T^2} = 0$$

$$\Longrightarrow H_1 = -\frac{p}{2T} + qT^{2p-1}$$

$$\Longrightarrow a_1 = C_1 T^{-p/2} \exp\left(\frac{q}{2p}T^{2p}\right), \tag{2.20}$$

where q and C_1 are arbitrary integration constants and the first-order differential equation in H_1 is most easily solved with the help of the integration factor $\exp\left(-\int \frac{2p-1}{T} dT\right) = T^{1-2p}$.

Thus, the tetrad 1-forms for the inflationary Kasner metric are

$$e^0{}_\mu dx^\mu = C_1 C_2^2 T^{3p/2-1} \exp\left(\frac{q}{2p} T^{2p}\right) dT, \tag{2.21a}$$

$$e^1{}_\mu dx^\mu = C_1 T^{-p/2} \exp\left(\frac{q}{2p} T^{2p}\right) dx, \tag{2.21b}$$

$$e^2{}_\mu dx^\mu = C_2 T^p dy, \tag{2.21c}$$

$$e^3{}_\mu dx^\mu = C_2 T^p dz. \tag{2.21d}$$

Without loss of generality, replace the constants C_1, C_2, and p through a set of redefinitions and coordinate transformations with the constants T_0 and Φ_0, so that the vierbein becomes

$$e^0{}_\mu dx^\mu = \frac{\mathrm{e}^{(T-T_0)/2}}{\sqrt{16\pi\Phi_0 T_0}} \left(\frac{T}{T_0}\right)^{-1/4} dT, \tag{2.22a}$$

$$e^1{}_\mu dx^\mu = \frac{\mathrm{e}^{(T-T_0)/2}}{\sqrt{16\pi\Phi_0 T_0}} \left(\frac{T}{T_0}\right)^{-1/4} dx, \tag{2.22b}$$

$$e^2{}_\mu dx^\mu = \frac{1}{\sqrt{16\pi\Phi_0 T_0}} \left(\frac{T}{T_0}\right)^{1/2} dy, \tag{2.22c}$$

$$e^3{}_\mu dx^\mu = \frac{1}{\sqrt{16\pi\Phi_0 T_0}} \left(\frac{T}{T_0}\right)^{1/2} dz. \tag{2.22d}$$

These tetrad 1-forms lead directly to the line element of Eqs. (2.5) and (2.6) through the relation in Eq. (2.3). This form is chosen to illuminate the physical meaning of the constants (as described in the next section) and to keep the exponential dependence in T as simple as possible. The radial component of the tetrad-frame energy-momentum tensor, $T_{00} = T_{11} = \Phi$, then reduces to Eq. (2.7).

2.2.3   Interpretation

The evolution of the inflationary Kasner geometry is visualized in Fig. 2.2. The evolution begins at $T = T_0$, when the mass-energy density Φ is at its small initial value of Φ_0. At this point, an observer might see such a geometry if, for example, they fall inside a rotating, accreting black hole and approach its inner horizon. Once the observer has come close enough to the inner horizon, the inflation epoch will begin, characterized by the rapid exponentiation of the observed stream energy
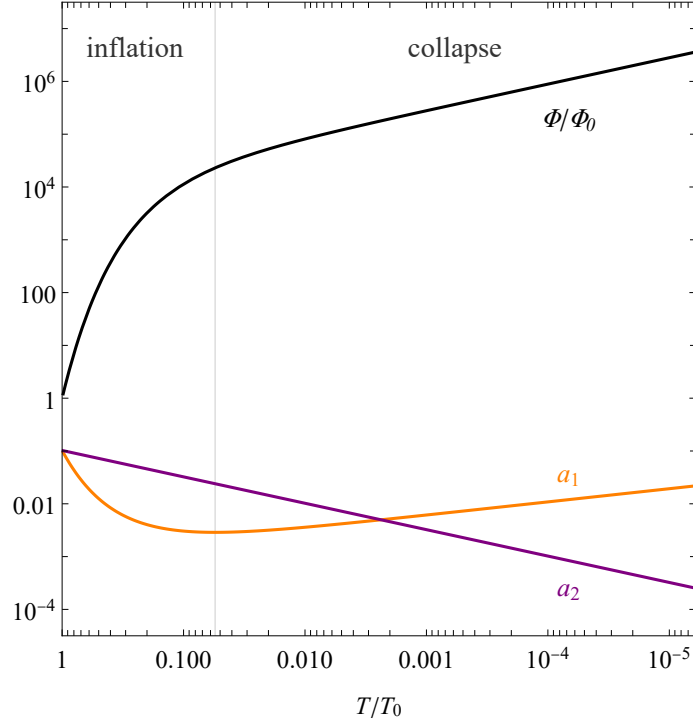
Figure 2.2: Evolution of the inflationary Kasner geometry and radial energy-momentum from the initial Kerr vacuum at time $T = T_0$ through inflation and collapse. The plotted quantities are the normalized tetrad-frame mass-energy density Φ/Φ_0 (black) from Eq. (2.7) and the scale factors a_1 (orange) and a_2 (purple) from Eq. (2.6). The parameters chosen here are $T_0 = 9.09$ and $\Phi_0 = 0.209$, so as to match the parameters used in the remaining plots via Eq. (2.38).

density. As the observer's proper time progresses forward and T progresses backward from T_0, the inflation will slow until a_1 turns around (at the vertical gray line in Fig. 2.2), signaling the start of the collapse epoch. The inflation-collapse transition occurs when T is of order unity, or more precisely, when H_1 changes sign from positive to negative at $T = 1/2$ (independent of the value of T_0). During the collapse epoch, Φ continues to increase as the spacetime collapses in the y- and z-directions and the observer approaches the inflationary Kasner singularity at $T = 0$ where the inner horizon would have been.

We have chosen to call the metric of Eq. (2.5) the inflationary Kasner metric because of its similarity to a homogeneous vacuum solution first found by the mathematician Edward Kasner in

1921 [99]. For three spatial dimensions, the Kasner metric has the line element

$$ds^2 = -dT^2 + a_1^2 dx^2 + a_2^2 dy^2 + a_3^2 dz^2, \tag{2.23}$$

where the scale factors a_i evolve purely as power laws in time, $a_i = T^{p_i}$, for exponents p_i that were found in the vacuum solution to satisfy the following conditions:

$$\sum_i p_i = \sum_i p_i^2 = 1. \tag{2.24}$$

From these Kasner conditions it can be shown that one of the exponents must always be negative or zero while the other two are nonnegative. More specifically, if the Kasner exponents are labeled in increasing order, they will satisfy the condition

$$-\frac{1}{3} \le p_1 \le 0 \le p_2 \le \frac{2}{3} \le p_3 \le 1. \tag{2.25}$$

This mathematical picture can be physically interpreted as an evolution in which one spacetime axis expands while the other two collapse (assuming the time coordinate T is positive and decreases with increasing proper time; otherwise the Kasner solution would describe a globally expanding spacetime).

The significance and applicability of the Kasner metric for black hole interiors was explored in the 1970s by Belinskii, Khalatnikov, and Lifschitz, who described a collapse consisting of a series of "Kasner epochs" during which the geometry is approximated by a Kasner metric with constant Kasner exponents p_i [24]. According to the BKL model, the three spatial components of the metric evolve in such a way so that the metric determinant decreases monotonically to zero in a finite time, but one spatial component always increases while the other two decrease (cf. Eq. (2.25)). Once one of the decreasing components has collapsed to a small enough value, the geometry then undergoes a "BKL bounce," in which one of the two collapsing components begins to grow, the previously expanding component begins to collapse, and the angles of orientation for the collapsing

and expanding axes change.

In 2017, the evolution of the inner horizon of a rotating, accreting black hole was explored numerically by Hamilton, who found that the spacetime approximately undergoes a BKL collapse as predicted a half a century earlier [86]. Here, we find that the inflationary Kasner solution is an analytic model of such a collapse, with two Kasner epochs as described below.

The first epoch in the inflationary Kasner solution, labeled "inflation" on Fig. 2.2, begins at $T = T_0$. During inflation, the exponential terms in the line element of Eq. (2.5) dominate the evolution of the geometry, so that the scale factor for the x-axis collapses while those of the y- and z-axes remain approximately static. The behavior can thus be approximated as that of Minkowski space with accelerated radar-like coordinates in the x-direction [130]. The inflation epoch resembles a Kasner epoch with exponents

$$(p_1, p_2, p_3) = (1, 0, 0), \tag{2.26}$$

corresponding to a spacetime collapsing only in the radial direction (indeed, the growing streams focus along the principal null directions during inflation). The inflation continues as the locally-measured energy-momentum Φ grows at an absurdly fast rate with a scale factor of order $\sim e^{1/\Phi_0}$ (as confirmed in the next section, in which it is found that the Kasner time T_0 scales as $1/u \sim 1/\Phi_0$). For an astronomically realistic black hole, in which the initial mass-energy density of accreted matter or radiation is generally quite small after the initial collapse, Φ could reach 10^{100} and beyond. It is perhaps fitting that Kasner himself (with his nine-year-old nephew) was the coiner of the term "googol" [100].

Once the Kasner time T has grown small enough, the exponential terms in the Eq. (2.5) freeze out, leaving the power laws in T to dominate the geometry's evolution. The result is the collapse epoch, beginning at around $T = 1/2$, in which the scale factor for the x-axis turns around and begins to grow, the scale factors in the y- and z-directions continue to collapse, and the streams' energy-momenta continues to grow, albeit at a slower rate in $\log(T)$. This corresponds to a Kasner

epoch with exponents

$$(p_1, p_2, p_3) = \left(-\frac{1}{3}, \frac{2}{3}, \frac{2}{3}\right), \tag{2.27}$$

which can be found by a coordinate transformation of T from the $\left(-\frac{1}{4}, \frac{1}{2}, \frac{1}{2}\right)$ form of Eq. (2.5) in order to satisfy the Kasner conditions of Eq. (2.24). This epoch approximates a Schwarzschild geometry asymptotically close to the Schwarzschild singularity. To see why this is the case, note that in the limit as $r \to 0$, the Schwarzschild line element takes the form

$$ds^2 \approx \frac{2M}{r} dt^2 - \frac{r}{2M} dr^2 + r^2 d\Omega^2, \tag{2.28}$$

where $d\Omega^2 = d\theta^2 + \sin^2\theta \; d\phi^2$ is the 2-sphere line element.

With the coordinate transformations $r \to T^{2/3}$ and $t \to x$ (note that r is timelike and t spacelike in this regime), the line element becomes

$$ds^2 \approx -dT^2 + T^{-2/3} dx^2 + T^{4/3} d\Omega^2, \tag{2.29}$$

where the constants have been absorbed into the coordinates for simplicity. This is precisely the $\left(-\frac{1}{3}, \frac{2}{3}, \frac{2}{3}\right)$ Kasner epoch when the θ-ϕ plane is transformed into the y-z plane.

Thus, the inflationary Kasner metric provides a simple model that encompasses all the relevant features of the evolution of the geometry near the inner horizon of a rotating, accreting black hole as it undergoes a BKL-like collapse. That collapse consists of two Kasner epochs, an inflationary epoch characterized by Kasner exponents $(1, 0, 0)$ that matches the behavior of the traditional Poisson-Israel mass-inflation regime, and a subsequent collapse epoch characterized by Kasner exponents $\left(-\frac{1}{3}, \frac{2}{3}, \frac{2}{3}\right)$ as the geometry approaches a spacelike singularity at $T = 0$.

In the next section, we confirm the applicability of this model to astrophysical inner horizons by comparing it to a more complex model, the conformally separable Kerr model, with the eventual goal of finding the necessary boundary conditions to attach the inflationary Kasner metric to the Kerr metric far enough above the inner horizon.

2.3   Matching near the inner horizon

We have yet to verify explicitly that the assumptions of the inflationary Kasner metric hold true near the inner horizon of an astrophysical black hole. In order to do so, we employ Hamilton's conformally separable Kerr metric, which has already been shown to provide a reasonable classical model of the inner workings of an accreting black hole [84, 85, 90].

In Sec. 2.3.1, we review the conformally separable model, finding that it exactly matches the behavior of the inflationary Kasner model for asymptotically small accretion rates. Specifically, we find in Eqs. (2.38) a set of transformations between the parameters and coordinates of the inflationary Kasner and conformally separable Kerr models. These relations confirm the validity and applicability of the inflationary Kasner model to an astrophysical inner horizon.

Then, in Sec. 2.3.2, we use the transformations of Eqs. (2.38) to match the inflationary Kasner solution to the Kerr metric. Such a matching allows us to ray-trace null geodesics across both regimes, from the Kerr background to an inflationary Kasner observer.

2.3.1   Conformally separable Kerr solution

Just as the inflationary Kasner metric provides a non-vacuum generalization of the vacuum solution of the Kasner metric to include the effects of accretion, so too does the conformally separable Kerr metric provide a generalization of the vacuum Kerr solution to include the effects of accretion. Here we present the main results of the conformally separable model; a more complete review can be found in Refs. [84, 85, 90] (or, in the Boyer-Lindquist form used here, in Ref. [86]).

Consider a rotating, accreting black hole with external mass M. For an ideal, rotating Kerr black hole, three assumptions hold true: the black hole is axisymmetric, the spacetime is stationary, and its Hamilton-Jacobi equations are separable [40]. The conformally separable model presented below was developed in an attempt to find the most general metric that still satisfies these conditions. To allow for the inclusion of accreting matter or radiation, however, the conditions required slight modification. In particular, instead of strict stationarity, the assumption of conformal

stationarity adopted here implies that the spacetime expands in a self-similar fashion with time at an asymptotically small rate (this rate is the accretion rate v that is taken to be asymptotically close to zero in Eq. (2.37)) [84]. Such a condition may not apply at the onset of a gravitational collapse when the accretion is supplied by the bulk of the collapsing matter, but that collapse occurs within a small proper time, and at late times, a black hole will only grow at a rate on the order of its light crossing time divided by the age of the Universe, a very small number. However, it will still accrete, so the assumptions of isolation and Price tail decay from models with a null weak singularity at the inner horizon will not apply.

It should be noted that strictly speaking, there is no inner horizon in the conformally separable model (nor in the inflationary Kasner model), since mass inflation near that region of spacetime will give way to collapse. When we refer to the inner horizon, we thus mean the region of spacetime within the black hole asymptotically close to the dimensionless Boyer-Lindquist radius $r_- \equiv 1 - \sqrt{1 - a^2}$, in which crossing streams focus along the principal null directions and cause inflation and collapse. Also, strictly speaking, the conformally separable model does not hold for extremal black holes, for which Δ_0' defined in Eq. (2.34) is zero. However, this should not be too worrisome, since astronomically realistic black holes are expected to have spins no higher than the Thorne limit [171].

Under the assumptions of conformal stationarity, axial symmetry, and conformal separability, the conformally separable line element takes the form [86]

$$ds^2 = \rho_s^2 \, \mathrm{e}^{2(vt-\xi)} \left(\frac{dr^2}{(r^2+a^2)^2 \, \mathrm{e}^{3\xi}\Delta_r} + \frac{\sin^2\theta}{\Delta_\theta}d\theta^2 + \frac{-\mathrm{e}^{3\xi}\Delta_r(dt - \omega_\theta d\phi)^2 + \Delta_\theta(d\phi - \omega_r dt)^2}{(1 - \omega_r\omega_\theta)^2} \right), \quad (2.30)$$

where $x^\mu = \{r, t, \theta, \phi\}$ are dimensionless Boyer-Lindquist coordinates (the radial coordinate is written first to emphasize that r is timelike within the outer horizon). The function Δ_r is the horizon function, whose zeros define the location of the geometry's horizons, and Δ_θ is the polar function, whose zeros define the location of the north and south poles. Additionally, ω_r is the angular velocity of the principal frame through the coordinates, and ω_θ is the specific angular momentum of principal null congruence photons. The r and θ subscripts denote functions of only r and θ, respectively, and

ρ_s is the separable part of the conformal factor. Eq. (2.30) reduces to the familiar Kerr line element when the following definitions are made:

$$\Delta_r = \frac{r^2 - 2r + a^2}{(r^2 + a^2)^2}, \qquad \Delta_\theta = \sin^2\theta,, \qquad \omega_r = \frac{a}{r^2 + a^2}, \qquad \omega_\theta = a\sin^2\theta, \tag{2.31a}$$

$$\rho_s = M\sqrt{r^2 + a^2\cos^2\theta}, \qquad \xi = v = 0, \tag{2.31b}$$

$$\{r, t, \theta, \phi\} = \left\{\frac{r_{\mathrm{BL}}}{M}, \frac{t_{\mathrm{BL}}}{M}, \theta_{\mathrm{BL}}, \phi_{\mathrm{BL}}\right\}, \tag{2.31c}$$

where M is the black hole's external mass, $a \equiv J/M^2$ is the black hole's dimensionless spin parameter, and $\{r_{\mathrm{BL}}, t_{\mathrm{BL}}, \theta_{\mathrm{BL}}, \phi_{\mathrm{BL}}\}$ are the standard (dimensionful) Boyer-Lindquist coordinates.

If the vacuum Kerr form of Eq. (2.30) is generalized to include the effects of accretion, the solution to Einstein's equations sourced by ingoing and outgoing collisionless null streams implies that three of the above definitions in Eqs. (2.31) are amended:

(1) The dimensionless factor v becomes an arbitrary free parameter, which can be interpreted (with the proper gauge choice) as the black hole's net accretion rate $\dot{M}$, or equivalently, the difference in the flux of outgoing and ingoing streams near the inner horizon. This factor can be treated as very small and reduces to zero for equal streams of ingoing and outgoing radiation.

(2) The inflationary exponent ξ, which measures the degree to which the geometry has undergone self-similar compression, changes with the radius and accretion parameters, behaving like a step function near the inner horizon as inflation is ignited.

(3) The horizon function Δ_r strays from its Kerr value near the inner horizon, "freezing out" at a small, negative value during collapse instead of reaching zero at $r = r_-$.

In the conformally separable solution, ξ and Δ_r are governed by the highly nonlinear pair of relations in Eq. 88 of Ref. [84] (where $x = \frac{1}{a}\cot^{-1}\left(\frac{r}{a}\right)$, $y = -\cos\theta$, and $\Delta_x = e^{3\xi}\Delta_r$). To simplify their behavior, it suffices to assume their Kerr values (Eqs. (2.31a) and (2.31b)) for all portions

of spacetime except just above the inner horizon. In the regime near the inner horizon, ξ rapidly increases from zero as r remains frozen at its inner horizon value of r_-, and the equations governing the evolution of ξ and Δ_r simplify to

$$\mathrm{e}^\xi = \left(\frac{(U_r + v)(U_r - v)}{(u + v)(u - v)}\right)^{1/4}, \qquad \Delta_r = \Delta_0 \left(\frac{(U_r + v)(u - v)}{(U_r - v)(u + v)}\right)^{\Delta'/(4v)}, \tag{2.32}$$

where Δ_0 is a constant of integration equal to the linear extrapolation of Δ_r evaluated away from the inner horizon when $\xi = 0$, $U_r = u$, and Δ_r still equals its Kerr value. The dimensionless parameter u, the counter-streaming velocity, represents the average of the initial accretion rates from the two streams. The accretion parameters satisfy $0 < v < u \ll 1$, and the outgoing and ingoing accretion rates are proportional to $u \pm v$. The function U_r is defined by

$$U_r \equiv \frac{d\xi}{dr}(r^2 + a^2)\,\mathrm{e}^{3\xi}\Delta_r. \tag{2.33}$$

In addition, the constant Δ' in Eq. (2.32) is proportional to the radial derivative of the Kerr horizon function evaluated at the inner horizon:

$$\Delta' \equiv -\frac{d\Delta_r}{dr}\bigg|_{r_-}(r_-^2 + a^2) = \frac{2\left(r_-^3 - 3r_-^2 + a^2 r_- + a^2\right)}{(r_-^2 + a^2)^2}. \tag{2.34}$$

The conformally separable Kerr model predicts that the geometry of the inner horizon will be divided into three distinct epochs, as shown in Fig. 2.3. The parameter ξ represents the timelike coordinate separating these epochs, just as T does for the inflationary Kasner model (in fact, it will be shown later, Eqs. (2.38), that the identification $T \propto \mathrm{e}^{-2\xi}$ generally holds).

Initially, the geometry resembles the Kerr vacuum when ξ is negligibly small and r is just above its inner horizon value. Then, as r approaches r_-, the mass inflation epoch begins as the locally-measured radial energy-momentum T_{11} of the streams rapidly inflates (along with the internal mass parameter and the Weyl curvature). The horizon function dominates the geometry's evolution during this epoch as Δ_r deflates toward 0^-. Throughout the inflation and collapse epochs, r remains
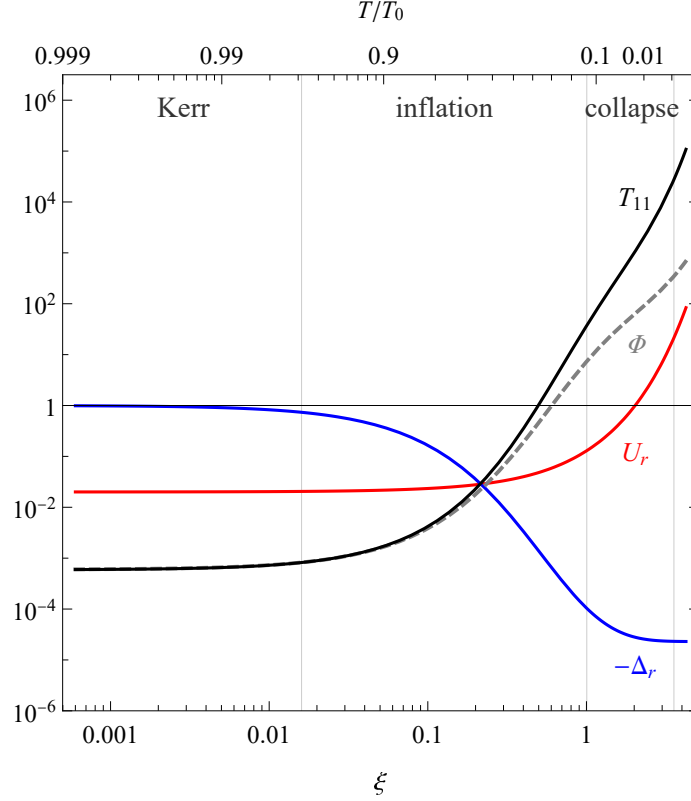
Figure 2.3: Evolution of quantities in the conformally separable Kerr model. Plotted are the tetrad-frame energy-momentum component T_{11} from Eq. (2.36) (black), the corresponding inflationary Kasner energy-momentum Φ (the $v \to 0$ limit of the conformally separable T_{11}) (gray dashed), and the parameter U_r (red) and horizon function Δ_r (blue) from Eq. (2.32). The parameters of this model have been chosen to avoid numerical overflow while still allowing the solution to capture the full behavior; in particular, $u = 0.02$, $v = 0.01$, and $a = 0.96$. The difference in the appearance of Φ here vis-à-vis Fig. 2.2 is solely due to a difference in the scaling of the axes.

approximately frozen at its inner horizon value of r_-.

Finally, inflation is slowed once ξ grows large enough and begins to dominate, causing a self-similar collapse of the geometry. During the collapse epoch, the curvature and T_{11} once again begin to diverge, while the horizon function freezes out at an exponentially small value. The collapse epoch then continues until Eq. (2.32) is no longer valid because of the increasing angular motion of the streams. However, it is possible that the conformally separable solution will break down regardless after this point, once the curvature exceeds the Planck scale.

The connections between the conformally separable Kerr model and the inflationary Kasner

model become evident when considering the energy-momentum tensor seen in a tetrad frame. A natural tetrad frame to choose is the one encoded by the line element in Eq. (2.30), with 1-forms

$$e^0{}_\mu dx^\mu = \frac{\rho_s\, e^{vt-5\xi/2}}{(r^2+a^2)\sqrt{-\Delta_r}}dr, \tag{2.35a}$$

$$e^1{}_\mu dx^\mu = \frac{\rho_s\, e^{vt+\xi/2}\sqrt{-\Delta_r}}{1-\omega_r\omega_\theta}\left(dt - \omega_\theta d\phi\right), \tag{2.35b}$$

$$e^2{}_\mu dx^\mu = \frac{\rho_s\, e^{vt-\xi}\sin\theta}{\sqrt{\Delta_\theta}}d\theta, \tag{2.35c}$$

$$e^3{}_\mu dx^\mu = \frac{\rho_s\, e^{vt-\xi}\sqrt{\Delta_\theta}}{1-\omega_r\omega_\theta}\left(d\phi - \omega_r dt\right). \tag{2.35d}$$

In the Kerr limit, the tetrad frame in Eqs. (2.35) reduces to the interior Carter frame, in which observers at rest see the principal null directions as purely radial (in the x^1-direction) as the frame follows them freely falling and rotating inward. The interior Carter frame differs from the standard (exterior) Carter frame only in the swapping of $e^0{}_\mu \leftrightarrow e^1{}_\mu$ and $\sqrt{-\Delta_r} \leftrightarrow \sqrt{+\Delta_r}$, since below the outer horizon, r becomes timelike and Δ_r becomes negative.

In this tetrad frame, Einstein's equations yield the following non-negligible components of the energy-momentum tensor seen by a Carter observer:

$$T_{00} = T_{11} = \frac{U_r\Delta' - v^2}{8\pi\rho_s^2\, e^{2vt+\xi}(-\Delta_r)} \tag{2.36}$$

(cf. Eqs. 125-128 in Ref. [84]). These components, which rapidly diverge during inflation and collapse (see Fig. 2.3), represent the net combination of the energy-momenta of ingoing and outgoing collisionless streams observed in the radial direction. Their behavior is dominated by the vanishing of Δ_r during inflation and by the conformal piece $e^{-\xi}$ once the horizon function freezes out during collapse. In terms of the counter-streaming velocity u, a Taylor expansion for small v yields

$$T_{00} = T_{11} \approx \frac{e^\xi u\Delta'}{8\pi\rho_s^2(-\Delta_0)}\, e^{\frac{\Delta'}{2u}\left(1-e^{-2\xi}\right)} + \mathcal{O}\left(v\right). \tag{2.37}$$

The radial energy-momentum thus grows as $\sim e^{1/u}$, so that, perhaps counterintuitively, the

smaller the value of u, the more rapid the inflation. For astronomically realistic black holes, the above expansion is generally valid, since v scales as the black hole light crossing time t_{BH} divided by the accretion (mass-doubling) time t_{acc}, and for most of the lifetime of the black hole, $t_{\mathrm{acc}} \gg t_{\mathrm{BH}}$ [91].

When comparing the energy-momentum tensor of the conformally separable Kerr metric in Eq. (2.37) with the energy-momentum tensor of the inflationary Kasner metric in Eq. (2.7), the two are equivalent in the limit $v \to 0$, when the following definitions are made:

$$T = T_0 \ \mathrm{e}^{-2\xi}, \tag{2.38a}$$

$$T_0 = \frac{\Delta'}{2u}, \tag{2.38b}$$

$$\Phi_0 = \frac{u\Delta'}{8\pi\rho_-^2(-\Delta_0)}, \tag{2.38c}$$

where ρ_- is the value of the separable conformal factor ρ_s at the inner horizon.

Thus, the inflationary Kasner solution provides a simple yet precise approximation of the conformally separable Kerr spacetime seen in the tetrad rest frame of a Carter observer, through the matching of Eqs. (2.38). The conformally separable solution, in turn, provides an approximation of the geometry of a rotating, accreting black hole, which reduces to the inflationary Kasner solution near the inner horizon in the limit of an asymptotically small accretion rate v.

T_{00} and T_{11} remain the only non-negligible components of $T_{\hat{m}\hat{n}}$ through inflation and collapse, and the collapse epoch of the conformally separable solution is defined to end when other components of $T_{\hat{m}\hat{n}}$ (namely, T_{12} and T_{22}), which initially diverge at a much slower rate, become comparable in magnitude to the radial components. This occurs at $\xi = \Delta'/(6u) - \ln\sqrt{-\Delta_0}$ (or equivalently, at $T/T_0 = -\Delta_0 \ \mathrm{e}^{-\Delta'/(3u)} \approx 10^{-5}$ in Fig. 2.2), and beyond this point, the approximations of Eqs. (2.32) and (2.36) are no longer valid. The classical solution can be continued numerically for higher ξ, yielding a series of even more complex Kasner epochs and BKL bounces, although an extension of the classical solution may fail if quantum effects become important once the curvature passes the Planck scale [86].

2.3.2   Null geodesic behavior

What will an observer in the inflationary Kasner spacetime see? To answer this question, consider a Carter observer (at rest in the tetrad of Eqs. (2.35)) falling into a rotating black hole from rest at infinity and approaching the inner horizon.

The Kerr metric provides an excellent approximation of a rotating black hole's geometry far above the inner horizon, so the Kerr null geodesic equations will provide the trajectory of a photon in this regime. However, once the observer approaches the inner horizon, streams of ingoing and outgoing matter will focus along the radial directions in the Carter tetrad and will begin to inflate, causing the geometry to be better approximated by the inflationary Kasner metric. Thus, here we find the equations for null geodesics in the inflationary Kasner spacetime and then connect them to null geodesics in the Kerr spacetime in a regime near the inner horizon where both are valid.

To find null geodesic trajectories in the inflationary Kasner spacetime, note that because the metric is homogeneous, there are three conserved quantities corresponding to each of the spatial coordinates x, y, and z. These momenta are simply the covariant forms of the spatial components of a photon's coordinate-frame four-momentum,

$$k_i = g_{i\mu} \frac{dx^\mu}{d\lambda}, \qquad \text{where } i \in \{x, y, z\}. \tag{2.39}$$

When Eqs. (2.39) are combined with the condition $k^\mu k_\mu = 0$, the four components of the four-momentum can be expressed in terms of the coordinate time T and conserved quantities k_x, k_y, and k_z. In the tetrad frame of Eq. (2.5), these components take the form

$$(k_{\text{IK}})^0 = -\sqrt{\frac{k_x^2}{a_1^2} + \frac{k_y^2 + k_z^2}{a_2^2}}, \tag{2.40a}$$

$$(k_{\text{IK}})^1 = \frac{k_x}{a_1}, \tag{2.40b}$$

$$(k_{\text{IK}})^2 = \frac{k_y}{a_2}, \tag{2.40c}$$

$$(k_{\text{IK}})^3 = \frac{k_z}{a_2}, \tag{2.40d}$$

where the subscript IK denotes quantities valid in the inflationary Kasner regime. The negative sign for $(k_{\text{IK}})^0$ is chosen so that the affine parameter increases as T decreases from T_0 just above the inner horizon to 0 at the inflationary Kasner singularity.

In the coordinate frame, Eqs. (2.40) lead to the following equations of motion that can be integrated:

$$\frac{dT}{d\lambda} = -\frac{\mathcal{E}}{a_1}\sqrt{\left(\frac{a_1^{\text{obs}}}{a_1}\right)^2 \cos^2\chi + \left(\frac{a_2^{\text{obs}}}{a_2}\right)^2 \sin^2\chi}, \tag{2.41a}$$

$$\frac{dx}{d\lambda} = -\frac{\mathcal{E}}{a_1}\frac{a_1^{\text{obs}}}{a_1}\cos\chi, \tag{2.41b}$$

$$\frac{dy}{d\lambda} = -\frac{\mathcal{E}}{a_2}\frac{a_2^{\text{obs}}}{a_2}\sin\chi\cos\psi, \tag{2.41c}$$

$$\frac{dz}{d\lambda} = -\frac{\mathcal{E}}{a_2}\frac{a_2^{\text{obs}}}{a_2}\sin\chi\sin\psi, \tag{2.41d}$$

where a_i^{obs} is the value of a_i at the observer's position, and the constants of motion k_i have been replaced by the observer's viewing angles $\chi \in [0, \pi]$ and $\psi \in [0, 2\pi)$ (and the normalization factor $\mathcal{E}$), which indicate the position of the photon in the observer's field of view. More details about the definitions of these angles and their relations to other quantities used throughout this chapter are given in Appendix A. The important point to note here is that $\chi = 0°$ corresponds to an ingoing photon reaching an observer looking in the principal null direction away from the black hole, and $\chi = 180°$ corresponds to an observer looking directly toward the black hole in the principal null direction.

The evolution of null geodesics seen by an observer at T_{obs} looking in different directions is shown in Fig. 2.4 during both the inflation and collapse epochs. In these plots, the positive x-direction is aligned with the principal null direction away from the black hole. Since the inflationary Kasner metric is isotropic in the y-z plane, the dependence on the viewing angle ψ is trivial—the geodesics of Fig. 2.4 can be revolved around the x-axis in 3D space to obtain solutions with different values of ψ.

The inflation epoch is characterized by the focusing of null geodesics along the principal null
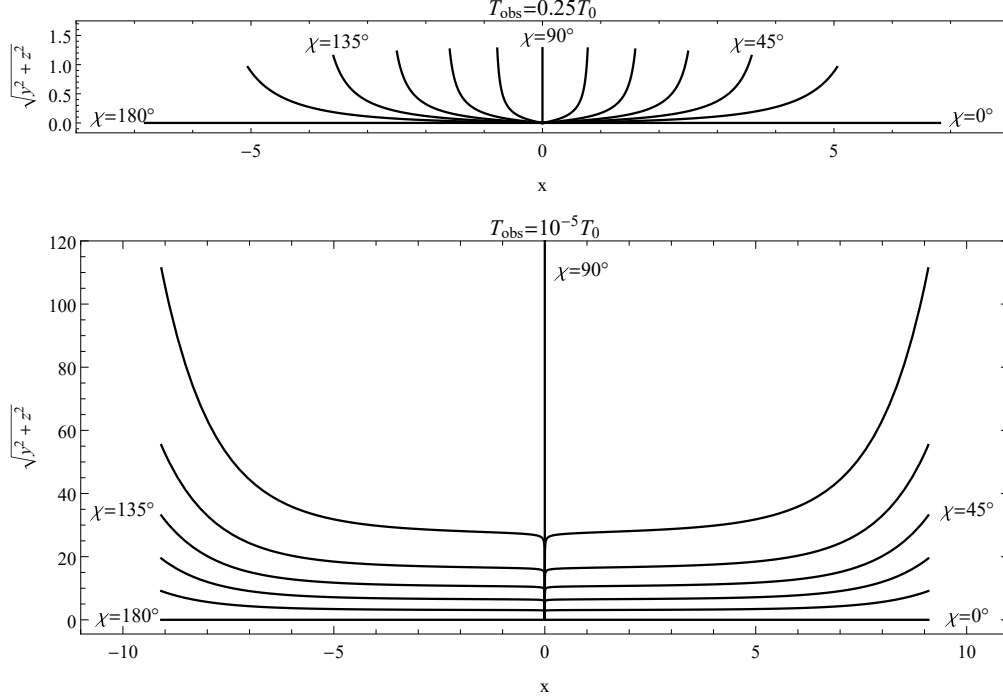
Figure 2.4: Null geodesics seen by an observer at the origin in the inflationary Kasner spacetime. Geodesics are parametrized by the observer's viewing angle χ at an equal spacing of $15°$, from an observer looking directly outward ($\chi = 0°$) to one looking directly inward toward the black hole's center ($\chi = 180°$). All geodesics end at the origin at $T = T_{\mathrm{obs}}$ and are ray-traced backwards via Eqs. (2.41) to $T = T_0$. The upper plot shows an observer at $T_{\mathrm{obs}} = 0.25T_0$ near the end of the inflation epoch, and the lower plot shows an observer at $T_{\mathrm{obs}} = 10^{-5}T_0$ near the end of the collapse epoch. The parameters chosen here are $T_0 = 9.09$ and $\Phi_0 = 0.209$.

directions. An observer in the inflation epoch (upper panel of Fig. 2.4) will thus see both ingoing and outgoing null geodesics that have begun to align along the x-axis, so that an increasingly large portion of the observer's sky is taken up by a narrowing band of the inflationary Kasner background orthogonal to the principal null axis. The same inflation power law behavior from the upper panel of Fig. 2.4 is also seen in the lower panel, in which the photons undergo both inflation and collapse. These photons all start at $T = T_0$, corresponding to $x = \pm T_0$ for all but the $\chi = 90°$ geodesic (which begins at approximately $\sqrt{y^2 + z^2} \propto (T_0/T_{\mathrm{obs}})^{3/4}$, far outside the range of this plot). The photons in this plot begin by proceeding inward toward the origin, curving toward the x-axis as they undergo inflation. Then, once the photons reach the collapse epoch, they turn sharply, orthogonal to the x-axis, until they reach the observer at the origin. As the observer continues farther into the collapse

epoch, the turns sharpen even more, and the locations of the turns spread out farther in the $y - z$ plane as most of the background radiation from T_0 reaching the observer becomes squeezed into a band around $\chi = 90°$. Once the observer has reached the singularity at $T = 0$ in the Carter tetrad frame, the entire inflationary Kasner background in the observer's field of view will be squashed into the ring at $\chi = 90°$, and photons arriving at any other position in the sky must have originated from a vanishingly small patch of the background along one of the principal null directions.

From the behavior of the null geodesics in Fig. 2.4, one must be careful not to jump too quickly to any conclusions about what an observer near the inner horizon would see, especially since, as we shall see, most of the photons arriving at an observer deep in the collapse epoch tend to align almost exactly with part of the boundary of the black hole's shadow. To be certain about each photon's complete path, we must continue the ray-tracing backwards beyond T_0 to $r \gg r_-$, where only the Kerr solution is valid.

In the Kerr spacetime, any geodesic is characterized by three conserved quantities: the energy E, angular momentum L, and Carter constant K, defined by

$$E \equiv -k_t, \quad L \equiv k_\phi, \quad K \equiv k_\theta^2 + \frac{(k_\phi + \omega_\theta k_t)^2}{\Delta_\theta}, \tag{2.42}$$

where k_t, k_ϕ, and k_θ are the covariant components of a photon's Kerr coordinate-frame four-momentum. Just as with the inflationary Kasner metric, these conserved quantities lead in a straightforward way to the following four-momentum components in the Carter tetrad frame, defined by $(k_K)^{\hat{m}} \equiv e^{\hat{m}}{}_\mu (dx^\mu/d\lambda)$:

$$(k_K)^0 = \pm \frac{1}{\rho_s} \sqrt{K - \frac{(\omega_r L - E)^2}{\Delta_r}}, \tag{2.43a}$$

$$(k_K)^1 = \frac{\omega_r L - E}{\rho_s \sqrt{-\Delta_r}}, \tag{2.43b}$$

$$(k_K)^2 = \pm \frac{1}{\rho_s} \sqrt{K - \frac{(L - \omega_\theta E)^2}{\Delta_\theta}}, \tag{2.43c}$$

$$(k_K)^3 = \frac{L - \omega_\theta E}{\rho_s \sqrt{\Delta_\theta}}, \tag{2.43d}$$

where the subscript K indicates quantities valid in the Kerr regime.

In the coordinate frame, Eqs. (2.43) lead to the following equations of motion:

$$\frac{dr}{d\lambda'} = \pm\sqrt{R(r)}, \tag{2.44a}$$

$$\frac{dt}{d\lambda'} = \frac{E - \omega_r L}{\Delta_r} + \frac{L - \omega_\theta E}{\Delta_\theta}\omega_\theta, \tag{2.44b}$$

$$\frac{d\theta}{d\lambda'} = \pm\sqrt{\Theta(\theta)}, \tag{2.44c}$$

$$\frac{d\phi}{d\lambda'} = \frac{E - \omega_r L}{\Delta_r}\omega_r + \frac{L - \omega_\theta E}{\Delta_\theta}, \tag{2.44d}$$

written in terms of the Mino time $d\lambda' \equiv d\lambda/\rho_s^2$ and the effective potentials

$$R(r) \equiv \left((\omega_r L - E)^2 - K\Delta_r\right)(r^2 + a^2)^2, \tag{2.45a}$$

$$\Theta(\theta) \equiv \left(K\Delta_\theta - (L - \omega_\theta E)^2\right)\csc^2\theta. \tag{2.45b}$$

Below the outer horizon, $(k_{\mathrm{K}})^0$ must be negative, since the radial coordinate is timelike and decreases as the affine parameter increases, so that all geodesics are necessarily infalling. Thus, only the lower sign for Eq. (2.43a) and Eq. (2.44a) is valid below the outer horizon. However, $(k_{\mathrm{K}})^1$ may be positive or negative in this regime depending on the relative magnitudes of L and E, and a geodesic with positive (negative) $(k_{\mathrm{K}})^1$ is said to be outgoing (ingoing). Additionally, a positive (negative) sign for Eq. (2.43c) and Eq. (2.44c) corresponds to a geodesic whose polar angle θ increases (decreases) as the affine parameter increases.

The Kerr and inflationary Kasner metrics are both valid in a small domain just above the inner horizon, and we choose to match their null geodesics at the Boyer-Lindquist radius r_1 and corresponding Kasner time T_1. The exact value of these parameters is not too important; the results of matching the null geodesics are robust for a range of values as long as T is close enough to T_0 that Δ_r is well-approximated by the Kerr horizon function but far enough into the inflation epoch that r has frozen out and the streams have begun to focus along the principal null directions, so that the inflationary Kasner solution is valid. Practically, for the parameters used in the plots

throughout this chapter, we choose to match geodesics at $r_1 = 0.73$ (with the inner horizon at $r_- = 0.72$), corresponding to $T_1 \approx 0.388 T_0$.

The assumption $(k_{\mathrm{IK}})^{\hat{m}}|_{T=T_1} = (k_{\mathrm{K}})^{\hat{m}}|_{r=r_1}$, matching Eqs. (2.40) and (2.43), leads to a direct mapping between the orbital parameters (k_x, k_y, k_z) and (E, L, K):

$$E = \frac{\rho_s}{1 - \omega_r \omega_\theta} \left(\frac{k_z \omega_r \sqrt{\Delta_\theta}}{a_2} - \frac{k_x \sqrt{-\Delta_r}}{a_1} \right), \tag{2.46a}$$

$$L = \frac{\rho_s}{1 - \omega_r \omega_\theta} \left(\frac{k_z \sqrt{\Delta_\theta}}{a_2} - \frac{k_x \omega_\theta \sqrt{-\Delta_r}}{a_1} \right), \tag{2.46b}$$

$$K = \frac{\rho_s^2}{a_2^2} \left(k_y^2 + k_z^2 \right), \tag{2.46c}$$

where the functions Δ_r, Δ_θ, ω_r, ω_θ, ρ_s, a_1, and a_2 are all evaluated at the point of matching just above the inner horizon, where $T = T_1$, $r = r_1$, and $\theta = \theta_1$. Additionally, in order to obtain the complete Kerr solution, the proper signs must be specified. With reference to Eqs. (2.44), one must require:

$$\mathrm{sgn}\left(\pm \sqrt{R(r)} \right) = -1, \tag{2.47a}$$

$$\mathrm{sgn}\left(\pm \sqrt{\Theta(\theta)} \right) = \mathrm{sgn}\left(k_y \right). \tag{2.47b}$$

With this matching, it is then possible to continue the inflationary Kasner geodesics of Fig. 2.4 to their points of origin in the Kerr spacetime. Here we consider two domains for the points of origin of Kerr photons: the first source is the fixed background of stars, galaxies, and radiation traveling inward from infinity, and the second source is the collapsing surface of the star that formed the black hole, emitting radiation outward. By the time photons from the latter source reach the observer, they will be so redshifted and dimmed that the star's surface will be practically imperceptible, so any part of the observer's sky consisting solely of photons from this source will form the black hole's shadow. As an example, the schematic Penrose diagram of Fig. 2.1 shows the paths of ingoing and outgoing photons from both of these sources reaching an observer near the inner horizon at point O.

It may seem counterintuitive that outward-directed photons from the collapsing star's surface

near $r \approx r_+$ could reach an observer near r_-. The paths of these photons fall under two general cases: if the photons were emitted during the collapse just before the formation of the event horizon (at $r > r_+$), they may reach a turning point below the photon sphere and travel inward until reaching the observer. Alternatively, if they were emitted below the event horizon (at $r < r_+$), they can remain outgoing as their Boyer-Lindquist radius decreases, until they are detected by an observer looking inward.

Some examples of photon paths reaching observers near the inner horizon are shown in Fig. 2.5. To avoid the effects of any coordinate singularities at the horizons, the paths are plotted using Doran coordinates, which are related to the Boyer-Lindquist coordinates by the transformations

$$r_{\mathrm{D}} = r_{\mathrm{BL}}, \tag{2.48a}$$

$$dt_{\mathrm{D}} = dt_{\mathrm{BL}} + \frac{\sqrt{2Mr(r^2 + a^2)}}{r^2 + a^2 - 2Mr} dr_{\mathrm{BL}}, \tag{2.48b}$$

$$\theta_{\mathrm{D}} = \theta_{\mathrm{BL}}, \tag{2.48c}$$

$$d\phi_{\mathrm{D}} = d\phi_{\mathrm{BL}} + \frac{a\sqrt{2Mr/(r^2 + a^2)}}{r^2 + a^2 - 2Mr} dr_{\mathrm{BL}} \tag{2.48d}$$

[55]. We limit our analysis to two equatorial observers, one in the inflation epoch ($T_{\mathrm{obs}} = 0.25T_0$) and one deep into the collapse epoch ($T_{\mathrm{obs}} = 10^{-5}T_0$); a more complete analysis of which photons arrive from which sources for different observer latitudes and radii is given in Sec. 2.4.

The two left panels of Fig. 2.5 show null geodesics in the equatorial plane, reaching an observer at $(x, y) \approx (1.2, 0)$ just above the inner horizon. These geodesics are the continuation of the geodesics of Fig. 2.4 when $\psi = 270°$—once the inflationary Kasner geodesics have been traced back from the observer to the point of matching at $T = T_1$, here they are continued backward in the Kerr metric to their point of origin at infinity (blue) or the outer horizon (red). As χ increases, the geodesics become more and more skewed until they asymptotically wrap around the photon sphere given by the dashed curve. The $\chi = 180°$ geodesic is omitted from the top left panel for simplicity; its form is identical to the $\chi = 180°$ geodesic in the lower left panel.
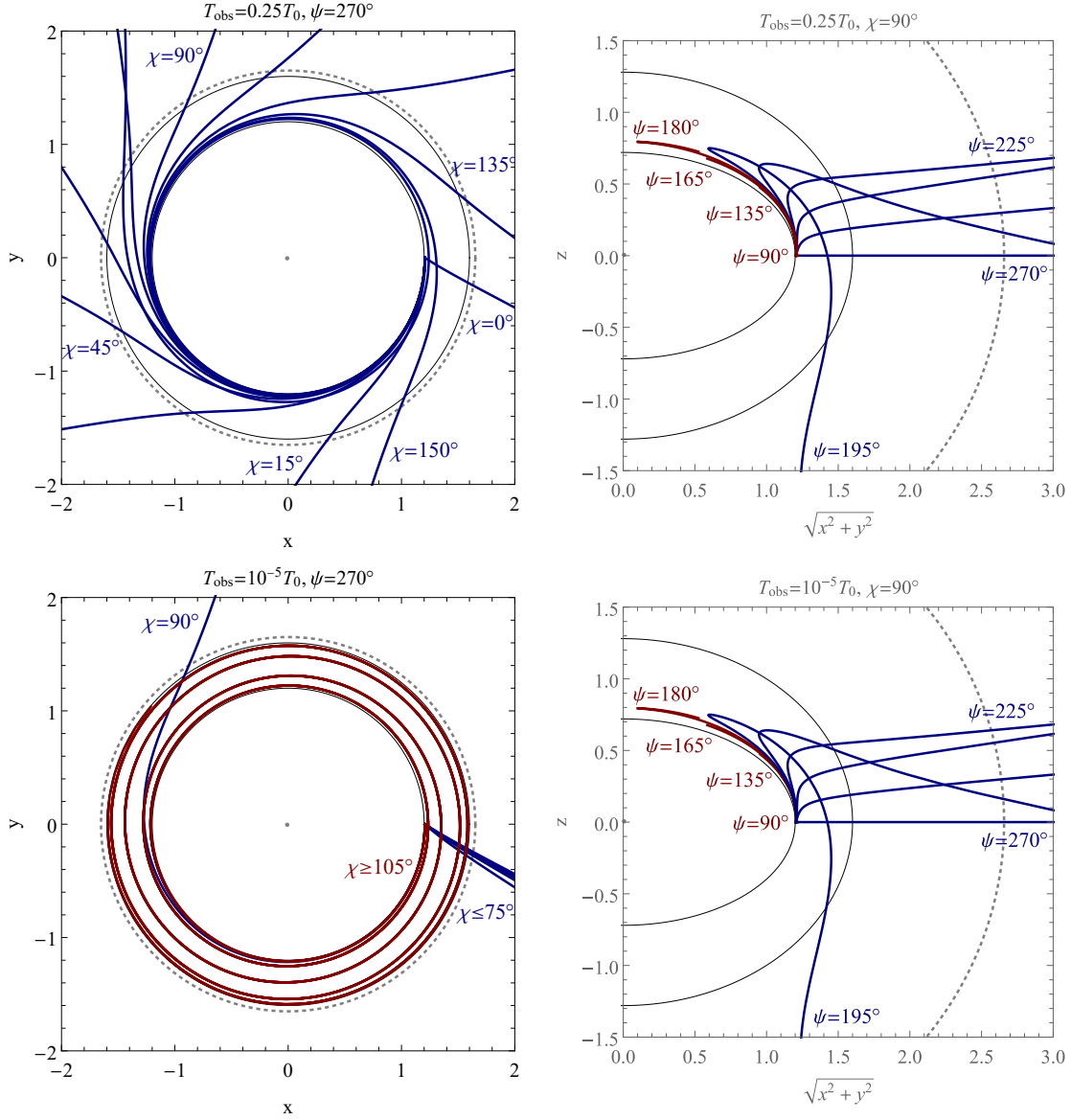
Figure 2.5: Null geodesics ray-traced backwards from an equatorial inflationary Kasner observer at $T_{\rm obs} = 0.25T_0$ (top two panels) and $T_{\rm obs} = 10^{-5}T_0$ (bottom two panels) to their Kerr origins. The left panels show a slice of the equatorial plane with Doran azimuthal coordinates, viewed from over the pole, and the right panels show a polar slice in co-rotating coordinates. In all panels, the two thin solid black curves shows the locations of the inner and outer horizons, and the dashed curves show the location of the null circular prograde equatorial (left) and polar (right) orbits. All geodesics are labeled by the viewing angle of the inflationary Kasner observer, equally spaced at intervals of 15°, and they originate either from the background at infinity (dark blue) or from the surface of the collapsing star (dark red). The parameters chosen here are $u = 0.02$, $r_1 = 0.73$, $\theta_1 = 90°$, and $a = 0.96$.

The behavior of the geodesics in the left two panels of Fig. 2.5 matches that of Fig. 2.4. In particular, when the observer has progressed deep into the collapse epoch (when $T_{\mathrm{obs}} \ll T_0$), most light tends to focus along the principal null directions, so that most of the observer's field of view contains light originating from a small patch of the background (when $\chi \leq 75°$) or illusory horizon (when $\chi \geq 105°$). In the collapse epoch, therefore, the observer sees most of the background sky squashed into a thin band close to $\chi = 90°$.

The right panels of Fig. 2.5 show geodesics for a fixed value of χ instead of ψ. Here, the observer is looking up and down instead of only looking within the equatorial plane. With this polar view, some geodesics ($\psi = 195°$ to $\psi = 270°$) originate from infinity, but the others ($\psi = 90°$ to $\psi = 180°$) originate at some arbitrary location below the outer horizon, where the collapsing star's surface existed at some point in the past. Though it may not be apparent from this view, these geodesics become increasingly skewed in the direction of the black hole's rotation as ψ decreases, with the equatorial geodesic with $\psi = 90°$ occupying a single point in the polar view. Additionally, note that the geodesics in this right panel can be reflected across the $z = 0$ line to obtain the geodesics for $\psi < 90°$ and $\psi > 270°$.

The polar null geodesics in the right two panels of Fig. 2.5 remain unchanged for an observer traveling from inflation to collapse, a consequence of the fact that the inflationary Kasner metric is isotropic in the y-z plane, so that the dependence on ψ in this case is trivial. Thus, an infalling equatorial Carter observer will see more and more of the sky flattening out and piling up toward the edges of the black hole's shadow, though the view at different altitudes will remain relatively unaffected by the inflationary Kasner metric.

2.4   The Carter observer's experience

As a brief caveat, it should be noted that the observer's field of view and the angles (χ, ψ) defined in this chapter are completely dependent on the choice of tetrad frame. The interior Carter tetrad is adopted in this chapter because of its simplicity and natural alignment with the principal null directions, but it is only a valid inertial rest frame for a free-falling observer below the outer

horizon. In particular, an observer of mass m at rest in the Carter frame must have orbital parameters $E = 0$, $L = 0$, and $K = (ma\cos^2\theta)^2$ (where E, L, and K are defined analogously to Eq. (2.42) but for a timelike geodesic). Nevertheless, a free-falling observer can decelerate to $E = 0$ once they have passed through the outer horizon in order to stay at rest in the Carter frame and reproduce the results found here.

With that caveat out of the way, consider the complete field of view of a Carter observer during their descent into a black hole. The relevant object of analysis here is the black hole's shadow, the portion of the observer's sky void of any background photons. The perceived boundary between the black hole's shadow and the sky is determined by the location of the photon sphere, where photons circulate on a null, circular orbit for an indefinitely long amount of time before peeling off and reaching the observer. The orbital parameters of these photons (and the corresponding viewing angles) are given by the solutions to the equations

$$R(r) = 0, \qquad \frac{dR(r)}{dr} = 0, \tag{2.49}$$

parametrized by the allowed prograde $(-)$ and retrograde $(+)$ photon orbital radii, whose extremes are given by

$$r_c = 2M\left(1 + \cos\left(\frac{2}{3}\cos^{-1}(\pm a)\right)\right) \tag{2.50}$$

[22]. Though we have been working with dimensionless Boyer-Lindquist coordinates, in this section we restore factors of M to connect our equations to physical quantities.

The black hole's shadow is shown in Fig. 2.6 for an equatorial observer at rest in the Carter frame at various radii and inflationary Kasner times. The observer's sky is displayed with a Mollweide projection, where the center corresponds to the observer's view directly ahead toward the black hole at $\chi = 180°$, the leftmost and rightmost points correspond to the view directly behind the observer at $\chi = 0°$, and the top and bottom points correspond to the view directly above ($\chi = 90°$, $\psi = 270°$) and below ($\chi = 90°$, $\psi = 90°$) the observer, respectively. More details about the projection are given in Appendix A. The black hole's spin axis is pointed to the right, so that the flow of spacetime is

towards the observer above the shadow and away from the observer below the shadow.

The progression of images in Fig. 2.6 from top left to bottom right shows the view of the black hole as a Carter observer gets progressively closer to the inner horizon. Far from the black hole, the characteristic asymmetrical silhouette is seen in the top left image, with the background sky slightly blueshifted and the collapsing star's surface extremely redshifted (the color in these images is calculated from the energy component k^0 of the photon's four-momentum, normalized to k^0 at its point of origin). Then, as the observer approaches the outer horizon at $r_+ = 1.28M$ in the (non-inertial) exterior Carter frame, the shadow takes up more and more of the observer's view until the entire background sky is reduced to a single point behind the observer at the outer horizon. Then, as the Carter frame continues inward, the background sky behind the observer begins to grow again, until it takes up a little less than half the field of view once the observer reaches near the inner horizon (here $r_- = 0.72M$).

As detailed in Appendix A, the field of view in Fig. 2.6 changes orientation between the exterior to the interior of the black hole. For $r > 1.28M$, the black hole is in front of the observer and the sky is behind the observer, but for $r < 1.28M$, we choose the black hole to be below the observer and the sky to be above, just as it is for the familiar case of an observer on the surface of Earth.

How does the inflationary Kasner solution modify the observer's view as they approach the inner horizon? The bottom two rows of Fig. 2.6 show a Carter observer's view in the inflation and collapse epochs. As inflation progresses, the black hole's shadow takes up approximately half of the equatorial observer's field of view, and the sky becomes more and more blueshifted. Then, as the observer continues into the collapse epoch, the black hole's shadow changes orientation until it appears as an infinite plane below the observer, taking up half of the field of view (in comparison, at a Schwarzschild singularity, an observer in free-fall also sees the shadow take up exactly half the field of view). Most of the sky above becomes squashed into a narrow band around $\chi = 90°$ (the horizontal midline in these images) as the observer approaches the inflationary Kasner singularity, as shown in the previous section. The validity of these images can be at least partially verified by comparing the points of origin of the geodesics of Fig. 2.5 in conjunction with their location in the
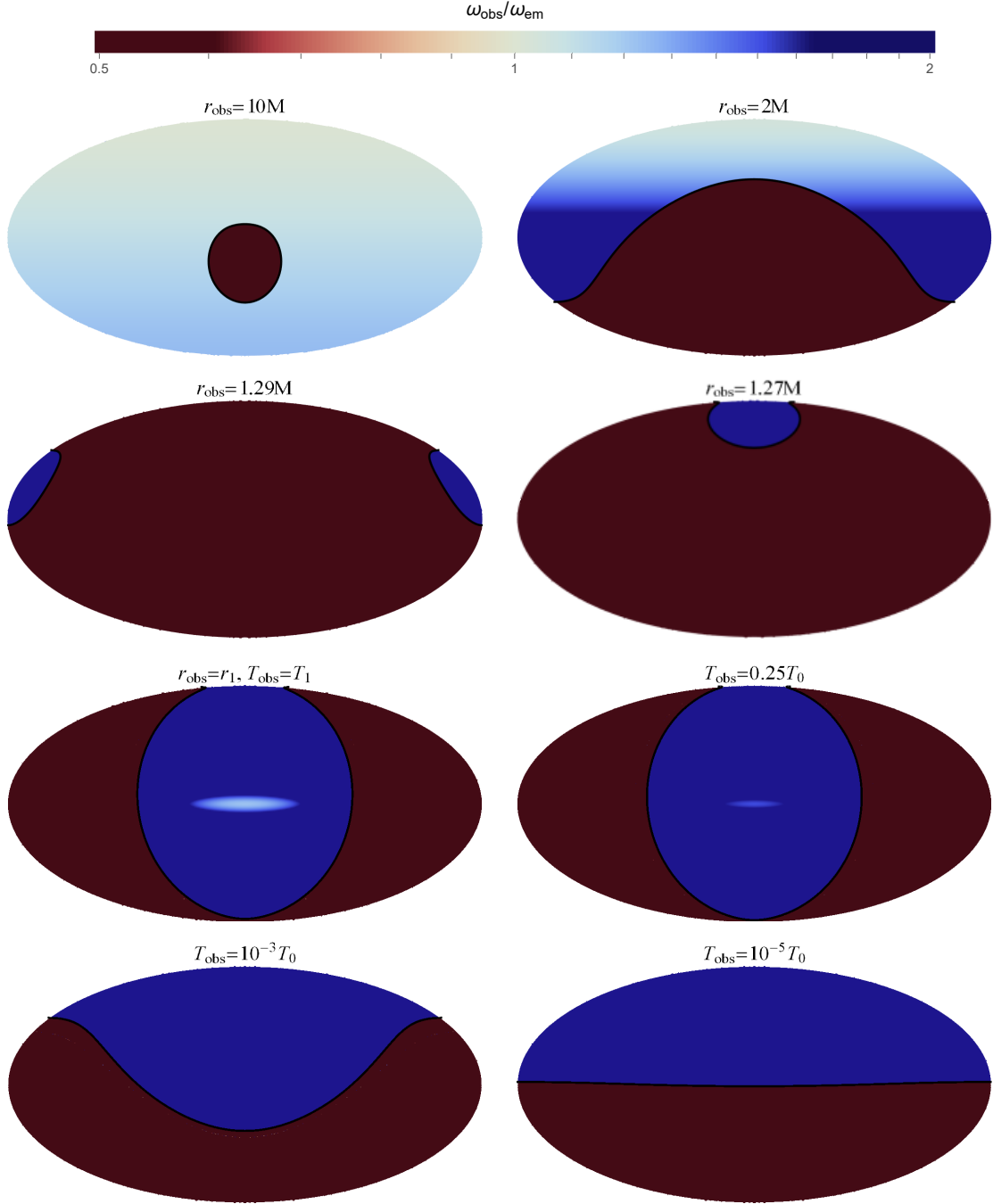
Figure 2.6: Mollweide projection of the full field of view of an infalling Carter observer in the equatorial plane at various radii and inflationary Kasner times recorded above each image. The black hole silhouette (black curve) separates the (generally) blueshifted photons sourced from $r \to \infty$ from the extremely redshifted photons sourced from $r \approx r_+$. The color represents the degree of redshift/blueshift. Note the change in the observer's orientation between the exterior $(r > 1.28M)$ and interior $(r < 1.28M)$ regions. The parameters used here are $u = 0.02$, $r_1 = 0.73$, $\theta_1 = 90°$, $T_1 \approx 0.388T_0$ and $a = 0.96$.

images of Fig. 2.6 for $T_{\rm obs} = 0.25 T_0$ and $T_{\rm obs} = 10^{-5} T_0$. To find the location of each (χ, ψ) point on the images of Fig. 2.6, refer to Fig. A.2 in Appendix A.

What about observers outside of the equatorial plane? The final shape of the black hole's shadow depends on the Boyer-Lindquist latitude of the observer, as shown in Fig. 2.7. Near the end of the inflation epoch (top image), in the black hole's equatorial plane ($\theta_{\rm obs} = 90°$), the black hole takes up a little more than half of the observer's field of view. But at higher latitudes ($\theta_{\rm obs} < 90°$), the shadow takes up more and more of the field of view, so that the sky in front of the observer appears as a thinner and thinner band connecting the principal null directions. Then, above some critical latitude, all photons must be ingoing, so that the shadow takes up the entire field of view at the end of the inflation epoch. An observer approaching the inner horizon at these latitudes close to the pole will see the sky constrict to a single point directly behind them. However, deep into the collapse epoch (bottom image), regardless of whether the observer is above or below the critical latitude, the black hole's shadow will always take up half the field of view below the observer, shifted $90°$ from its location during the inflation epoch.

How much time passes for an observer experiencing the inflation and collapse of a black hole's inner horizon geometry? In the simplest case, for an equatorial observer of mass m at rest in the interior Carter tetrad frame, the proper time that passes from the point of matching at $T = T_1$ to
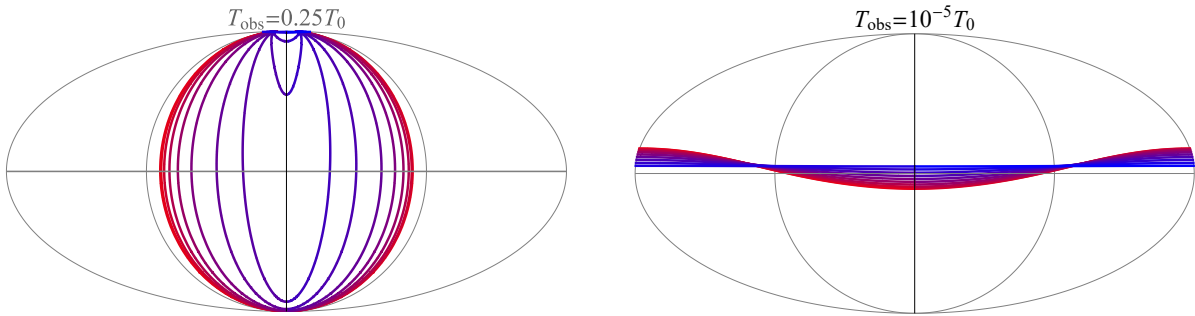
Figure 2.7: Black hole silhouettes for an inflationary Kasner observer near the end of the inflation (upper panel) and collapse (lower panel) epochs, at a Boyer-Lindquist latitude ranging from the equator at $\theta_{\rm obs} = 90°$ (blue) to the pole at $\theta_{\rm obs} = 0°$ (red). The projection is the same as that of Figs. 2.6 and A.2b, and the parameters chosen here are $u = 0.02$, $r_1 = 0.73$, and $a = 0.96$.

the singularity at $T = 0$ is given by

$$\tau = -M \int_{T_1}^{0} \frac{e^{(T-T_0)/2}}{\sqrt{16\pi\Phi_0 T_0}} \left(\frac{T}{T_0}\right)^{-1/4} dT. \tag{2.51}$$

For the parameters used in Fig. 2.2, the proper time experienced by the observer is approximately

$$\tau \approx \left(\frac{M}{M_\odot}\right) \times 10^{-7} \text{ seconds}, \tag{2.52}$$

where $M/M_\odot$ is the mass of the black hole in units of solar masses. This proper time only changes by an order of magnitude or two at most across the physically valid domains of a, θ_0, r_0, and u. In particular, the integral in Eq. (2.51) approaches a constant value in the limit of an asymptotically small initial counter-streaming velocity u. However, in the same limit, the total time spent just in the collapse epoch ($T < 1/2$) becomes exponentially tiny (for the parameters used in Fig. 2.2 the time spent in the collapse epoch is already less than 1% of the time spent in the inflation epoch).

As a final note, the inflationary Kasner proper time calculated above is about an order of magnitude smaller than the proper time experienced by an equivalent observer in the Kerr spacetime traveling from the point of matching ($r = r_1$) to the inner horizon ($r = r_-$).

2.5   Conclusions

The general classical outcome of the effect of accreted matter and radiation on a rotating black hole is the inflation and subsequent collapse of the spacetime near the inner horizon into a spacelike, BKL-like singularity. Here we have developed a simplified model that connects this collapsing geometry near the inner horizon to the Kerr exterior. The model, which we have called the inflationary Kasner model, is derived under the assumption that streams of matter near the inner horizon focus along the principal null directions at ultrarelativistic speeds, so that the Einstein tensor in the Carter frame approximately corresponds to that of a null, perfect fluid streaming at equal rates along the x-direction. Such an assumption leads to a Kasner-like form with two epochs,

one corresponding to a purely radial collapse with Kasner exponents $(1, 0, 0)$, and a subsequent epoch with exponents $(-\frac{1}{3}, \frac{2}{3}, \frac{2}{3})$. The end result of the model is the termination of geodesics at a spacelike singularity at $T = 0$; notably, the inner horizon and all the additional structure beyond it never get the chance to form.

We have verified the applicability of the inflationary Kasner metric to the near-inner-horizon geometry of rotating, accreting black holes through comparison to a previously-derived solution, the conformally separable Kerr metric. This solution comes equipped with a natural connection to the Kerr metric, along with a continuous evolution through the inflation and collapse epochs (and beyond, as has been shown computationally, through several BKL bounces [86]). In the limit of asymptotically small accretion rates ($v \to 0$), the conformally separable solution is equivalent to the inflationary Kasner solution during inflation and collapse, which lends credence to the validity of the latter model and allows for a more thorough interpretation of its parameters.

During the collapse epoch, the black hole's shadow spreads out to take up half of a Carter observer's field of view, exactly as in the Schwarzschild case, but the shadow is shifted 90° from its position at the end of the classical Poisson-Israel mass inflation epoch, and unlike that latter case, the view is independent of the observer's latitude. Once the collapse epoch has proceeded long enough, the curvature will have diverged to such a large extent that the classical solution will surely break down. A calculation of the quantum back reaction will thus be necessary if one wishes to explore the spacetime evolution past this point in order to determine the final outcome of the collapse. The inflationary Kasner metric will hopefully provide a simpler basis for quantum calculations than more complicated models like the conformally separable solution.

Chapter 3

Formalism of Semiclassical Gravity

This chapter reviews the formalism used in the remainder of the thesis to understand how quantum fields respond to the presence of curved spacetimes. Though it is often stated that a theory of quantum gravity is still at large among the physics community (or at least that there is no consensus what the "right" theory is), there is consensus that quantum gravity can already be modeled in a perfectly well-posed, robust way in the context of effective field theories, as long as the observables being studied lie below a specified cutoff energy scale.

The effective field theory of choice throughout this thesis, that of a quantized massless bosonic field minimally coupled to a classical background gravitational field, is described in Sec. 3.1. The theory should remain valid to one-loop order for energies up to the Planck scale at $\sim 10^{19}$ GeV.[1] Then, the foundations for the semiclassical calculations involving Hawking radiation (the subject of Chapter 4) and renormalization (the subject of Chapters 5 and 6) are covered in Secs. 3.2 and 3.3, respectively.

3.1   Approach to quantization

Just as Maxwell's theory of electromagnetism is the unique local, Lorentz-invariant field theory of massless, spin-1 particles with two degrees of freedom (called *photons*), so too is Einstein's theory

---

[1] For reference, the energy scale at the core of the hottest neutron stars is $\sim 10^{-1}$ GeV, the highest human-made energies achieved by the Large Hadron Collider are $\sim 10^4$ GeV, the highest energies detected from cosmic rays are $\sim 10^{11}$ GeV, and the energy scale where the three gauge interactions of the Standard Model are expected to unify into a single force is $\sim 10^{16}$ GeV.

of general relativity the unique low-energy field theory of massless, spin-2 particles (called *gravitons*) that satisfies locality and Lorentz invariance [176]. In order to represent gravity as a geometric theory, the Lagrangian density for the theory (and therefore the action) should consist solely of local scalar functions built out of a rank-2 tensor (the metric $g_{\mu\nu}$) and its derivatives. As an effective field theory, the terms with the fewest derivatives will be most important at low energies. Thus, one can proceed by expanding in the number of derivatives. The most general terms that satisfy locality and Lorentz invariance yield the following action:

$$S = \int dx^4 \sqrt{-g} \left(-\frac{\Lambda}{8\pi G} + \frac{1}{16\pi G} R + c_1 R^2 + c_2 R_{\mu\nu} R^{\mu\nu} + c_3 R_{\mu\nu\rho\sigma} R^{\mu\nu\rho\sigma} + \ldots \right), \qquad (3.1)$$

where $g = \det(g_{\mu\nu})$, the quantities involving R are specific functions of the metric and its first and second derivatives (the Ricci scalar $R = R^\mu_\mu$, Ricci tensor $R_{\mu\nu} = R^\rho_{\mu\rho\nu}$, and Riemann tensor $R_{\mu\nu\rho\sigma}$), and the coupling constants for each term are written in terms of physically relevant quantities when possible (in particular, Λ is the cosmological constant and G is Newton's universal gravitational constant).

The only term in Eq. (3.1) that is zeroth order in derivatives of the metric is the term with the cosmological constant, which will be ignored for the remainder of this analysis, since it can be absorbed into the as-of-yet unspecified stress-energy content from the matter sector, and further, the cosmological constant has been measured with high precision to have an altogether negligible value of $\Lambda = 2.4 \times 10^{-46}\ c^4/(GM_\odot)^2$ [153]. The action contains no terms that are first order in derivatives, since doing so would leave an unpaired index ∇_μ and break Lorentz invariance. At second order in derivatives, the only term in Eq. (3.1) is the one involving the Ricci scalar curvature R, and it is this term that defines the Einstein-Hilbert action, which leads to the theory of general relativity. The final three terms in Eq. (3.1) are fourth order in derivatives and consist of combinations of the Ricci scalar R, Ricci tensor $R_{\mu\nu}$, and Riemann tensor $R_{\mu\nu\rho\sigma}$, but their contributions to observable effects are so small that the constants c_1, c_2, and c_3 have only been constrained to values less than about 10^{74} [167]. These higher-order terms beyond the Einstein-Hilbert action encompass the theory

of Lovelock gravity and specifically form the so-called Gauss-Bonnet term when $c_1 = -c_2/4 = c_3$.

In the background field method, field fluctuations are treated as perturbations about a smooth background metric $\tilde{g}_{\mu\nu}$:

$$g_{\mu\nu} = \tilde{g}_{\mu\nu} + \epsilon\, h_{\mu\nu}. \tag{3.2}$$

The fluctuations $h_{\mu\nu}$ represent high-frequency ripples over a background that is slowly varying. They could describe, for example, gravitational waves; in the context of quantum field theory, the tensor $h_{\mu\nu}$ will model the spin-2 graviton.

Considering just the Einstein-Hilbert term in Eq. (3.1), the decomposition of Eq. (3.2) leads to a perturbative expansion of the action in the order-counting parameter ϵ:

$$S_{\text{EH}} = \frac{1}{16\pi G} \int dx^4 \sqrt{-g} \left[\mathscr{L}_{\text{EH}}^{(0)} + \epsilon \mathscr{L}_{\text{EH}}^{(1)} + \epsilon^2 \mathscr{L}_{\text{EH}}^{(2)} + \mathscr{O}(\epsilon^3) \right], \tag{3.3}$$

where

$$\mathscr{L}_{\text{EH}}^{(0)} = \tilde{R}, \qquad \mathscr{L}_{\text{EH}}^{(2)} = \frac{1}{8} \tilde{\nabla}_\mu \bar{h} \tilde{\nabla}^\mu \bar{h} + \frac{1}{2} \tilde{\nabla}_\rho \bar{h}_{\mu\nu} \tilde{\nabla}^\nu \bar{h}^{\mu\rho} - \frac{1}{4} \tilde{\nabla}_\rho \bar{h}_{\mu\nu} \tilde{\nabla}^\rho \bar{h}^{\mu\nu}, \tag{3.4}$$

with the trace-reversed metric perturbation defined as

$$\bar{h}^{\mu\nu} = h^{\mu\nu} - \frac{1}{2} \tilde{g}^{\mu\nu} h. \tag{3.5}$$

The term that is first order in ϵ will generally be non-zero, but after short-wavelength averaging and integrating by parts to remove boundary terms, the odd-order terms will vanish and fail to contribute to observables at spatial infinity [159].

The variation of the action of Eq. (3.3) with respect to the background inverse metric $\tilde{g}^{\mu\nu}$ leads directly to the well-known Einstein field equations; if the expansion parameter ϵ is taken to match the Newtonian gravitational coupling parameter, the variation yields:

$$\tilde{R}_{\mu\nu} - \frac{1}{2} \tilde{R}\tilde{g}_{\mu\nu} = -\frac{16\pi G}{\sqrt{-\tilde{g}}} \frac{\delta S_{\text{EH}}^{(2)}}{\delta \tilde{g}^{\mu\nu}}. \tag{3.6}$$

The quantity on the left hand side of Eq. (3.6) is the standard Einstein tensor for the background field, and the quantity on right hand side of Eq. (3.6) represents the stress-energy content of the spacetime. In the case of classical perturbations, one can define a stress-energy pseudotensor $t_{\mu\nu} \equiv \sqrt{-\tilde{g}}^{-1} \delta S_{\text{EH}}^{(2)}/\delta \tilde{g}^{\mu\nu}$, such that the total stress-energy tensor sourced by the perturbations is proportional to the short-wavelength-averaged pseudotensor, $T_{\mu\nu} = -2\langle t_{\mu\nu}\rangle$ [159]. One could also do without the perturbative analysis of Eqs. (3.2)–(3.5) and instead add to the original Einstein-Hilbert action a separate matter field of any spin, in which case the stress-energy would be defined in terms of the variation of that matter field's Lagrangian. But even in the absence of such a field, metric perturbations themselves can be treated as a source of stress-energy.

Up until now, the discussion has been entirely classical. Now, consider how the above analysis might be adapted to allow for quantized metric perturbations $\hat{h}_{\mu\nu}$. The quantization of an effective field theory in the path-integral framework is an entirely straightforward albeit involved process. To quantize $h_{\mu\nu}$, one first needs to fix the gauge, which necessitates adding a term to the action that is invariant under background gauge transformations but breaks gauge transformations of the quantum fluctuations [171]. Then, a second term must be added to the action to accommodate the complex Faddeev-Popov ghost field. These terms will not be written explicitly here; see [54] for details of their construction.

The resulting action to zeroth order is the same Einstein-Hilbert action as in the classical case, once again yielding the Einstein tensor of the background field on the left hand side of the field equation. However, the right hand side is a bit more troublesome. In considering the action to quadratic order with the additional gauge-fixing and ghost terms, the integration to average over the gravitational degrees of freedom yields a functional that in general is nonlocal and divergent. One would like to find an effective action W associated with this quadratic term, such that

$$-\frac{2}{\sqrt{-\tilde{g}}} \frac{\delta W}{\delta \tilde{g}^{\mu\nu}} \equiv \langle T_{\mu\nu}\rangle, \tag{3.7}$$

where the angle brackets $\langle\rangle$ here and in what follows denote a sense of "quantum averaging," defined

explicitly as the renormalized vacuum expectation value of an operator-valued quantity.

The definition of the effective action W will depend on the Feynman diagram loop cutoff, as expected for any effective field theory. Consider diagrams with up to one loop. Though the bare action is nonlocal and divergent, the one-loop effective action can be constructed by subtracting out the one-loop divergences, which are local and readily calculated using dimensional regularization:

$$\mathcal{L}_{\text{div}}^{\{1\}} = \frac{1}{8\pi^2(4-d)}\left(\frac{1}{120}\tilde{R}^2 + \frac{7}{20}\tilde{R}_{\mu\nu}\tilde{R}^{\mu\nu}\right), \tag{3.8}$$

where d is the number of dimensions [171]. Herein lies the problem with quantum gravity as a complete quantized field theory: in other field theories, the divergent term in the quantized action has the same order as the original terms in the action, so that the divergence can simply be absorbed into the coupling constant. But for gravity, the divergences that arose from the Einstein-Hilbert action are not proportional to R (second order in derivatives of the metric) but instead are fourth order in derivatives of the metric, so that the divergences cannot simply be absorbed by renormalizing the coupling constant G. Instead, one must add to the Einstein-Hilbert action the fourth order terms of Eq. (3.1) and absorb the one-loop divergent term into the coupling constants c_1, c_2, and c_3. However, quantization of the extended action of Eq. (3.1) would then introduce new divergent terms that are sixth order in derivatives of the metric, which would need to be absorbed into renormalized coupling constants from an even further extended action, and the process would keep repeating *ad nauseam*. As a result, gravity is said to be *non-renormalizable*.

Nonetheless, each iteration in the process described above will increase the accuracy of the one-loop effective action, controlled by the order of the graviton's coupling parameter (the Planck mass), so that even to the lowest order in the metric derivatives, observables will remain valid up to $\sim 10^{19}$ GeV. The precise details of how the one-loop effective action is derived and leads to a finite stress-energy $\langle T_{\mu\nu} \rangle$ will not be covered here; for a review, see, e.g., Chapter 6 of [29]. The result is the following field equations:

$$\tilde{R}_{\mu\nu} - \frac{1}{2}\tilde{R}\tilde{g}_{\mu\nu} = 8\pi G\langle T_{\mu\nu} \rangle. \tag{3.9}$$

Eq. (3.9) is often named for its pioneers, Møller [132] and Rosenfeld [158]; here it will usually be referred to by a more descriptive title, the semiclassical field equations. The left hand side dictates that the spacetime geometry of a background field should be treated classically as in general relativity, while the right hand side indicates that quantum fluctuations on top of that background will produce gravity of their own through the graviton's renormalized stress-energy tensor. Though here it is only stated how the field's stress-energy content can be formally renormalized at the level of the effective action, details of how renormalization calculations can be done in practice will be given in Sec. 3.3.

Now that it can be seen how gravity itself can be quantized and graviton perturbations can source stress-energy in the same way that an independent matter field would source stress-energy, the remainder of this thesis will assume an action with a classical background coupled to a separate field, so that focus can be shifted away from any complications with path-integral quantization and ghost fields. Many such separate fields are expected to exist in nature; massless spin-2 fields represent the effects of gravitons, massless spin-1 fields represent the electromagnetic effects of photons, spin-$1/2$ fields describe fermionic fields (historically, neutrinos for the massless fields and electrons for the massive fields), and massive spin-0 fields represent the effects of the Higgs boson. The contributions from all these fields are in principle important, but practically, it suffices to consider the effects of the simplest choice, a massless spin-0 (scalar) field, since fields with other spins generally lead to similar behavior. A brief comparison and analysis of higher-spin fields to that of scalar fields will be given in Sec. 4.5.2.2.

The semiclassical action will thus be written as

$$S = \int dx^4 \sqrt{-g}\left[\frac{1}{16\pi G}R - \frac{1}{2}\partial_\mu\phi\partial^\mu\phi - \frac{1}{2}\left(m^2 + \xi R\right)\phi^2\right], \tag{3.10}$$

where ϕ is a quantized scalar field with mass m (taken to be zero in the remaining chapters) coupled to gravity with a coupling strength ξ. The case of a minimally coupled field corresponds to the choice $\xi = 0$, and the case of a conformally coupled field (where the field equations become invariant under conformal transformations in the massless case) corresponds to the choice $\xi = (d-2)/(4d-4)$,

which reduces to $\xi = 1/6$ for 4-dimensional spacetimes.

Variation of this action with respect to the inverse metric $g^{\mu\nu}$ leads directly to the semiclassical field Eqs. (3.9). Conversely, variation of the action with respect to the field ϕ leads to a different equation, which is often confusingly called a field equation but here will be referred to as a wave equation (or, in the case of a scalar field, the Klein-Gordon equation):

$$\left(\Box - m^2 - \xi R \right) \phi = 0, \tag{3.11}$$

where $\Box \equiv \nabla^\mu \nabla_\mu$ is the d'Alembert operator, which for a scalar field takes the form

$$\Box \phi = \frac{1}{\sqrt{-g}} \partial_\mu \left(\sqrt{-g} \, \partial^\mu \phi \right). \tag{3.12}$$

Eq. (3.11) encodes all the dynamics of the field and is a crucial starting point for the calculations of both Hawking radiation and the renormalized stress-energy tensor, as detailed in the following two sections, respectively.

3.2   Bogoliubov coefficients

The black hole spacetimes considered in this thesis possess a high degree of symmetry, including azimuthal and time-translation invariance. As such, the wave Eq. (3.11) can be most easily solved by performing a mode decomposition of the field. Since the field is quantized, it can be expressed as a mode sum of ladder operators $\hat{a}_{\omega\ell m}$ and their Hermitian conjugates:

$$\hat{\phi}(x) = \int_0^\infty d\omega \sum_{\ell=0}^\infty \sum_{m=-\ell}^\ell \left(\phi_{\omega\ell m}(x) \hat{a}_{\omega\ell m} + \phi^*_{\omega\ell m}(x) \hat{a}^\dagger_{\omega\ell m} \right), \tag{3.13}$$

where the modes $\phi_{\omega\ell m}(x)$ as a function of the spacetime coordinate x can then be further decomposed by separation of variables and can be treated classically as solutions to the wave Eq. (3.11) [29].

Quantization necessitates that the ladder operators satisfy the commutation relations

$$\left[\hat{a}_{\omega\ell m}, \hat{a}^{\dagger}_{\bar{\omega}\bar{\ell}\bar{m}}\right] = \delta^{\bar{\omega}\bar{\ell}\bar{m}}_{\omega\ell m}, \qquad [\hat{a}_{\omega\ell m}, \hat{a}_{\bar{\omega}\bar{\ell}\bar{m}}] = \left[\hat{a}^{\dagger}_{\omega\ell m}, \hat{a}^{\dagger}_{\bar{\omega}\bar{\ell}\bar{m}}\right] = 0. \qquad (3.14)$$

In the Heisenberg picture, the quantum states of the theory span a Hilbert space, which in the Fock representation can be expressed as a basis built out of a no-particle (vacuum) state $|0\rangle$ that is annihilated by all the operators $\hat{a}_{\omega\ell m}$:

$$\hat{a}_{\omega\ell m}|0\rangle = 0 \qquad \forall \ \omega, \ell, m. \qquad (3.15)$$

A fundamental problem with the above treatment is that for a general curved spacetime, in the absence of Poincaré invariance, there is no privileged set of coordinates, no natural mode decomposition, and no universal vacuum state shared by all inertial observers. Thus, one can just as easily use a different complete set of orthonormal mode functions $\bar{\phi}_{\bar{\omega}\bar{\ell}\bar{m}}$, defined by

$$\hat{\phi}(x) = \int_0^{\infty} d\bar{\omega} \sum_{\bar{\ell}=0}^{\infty} \sum_{\bar{m}=-\bar{\ell}}^{\bar{\ell}} \left(\bar{\phi}_{\bar{\omega}\bar{\ell}\bar{m}}(x)\hat{\bar{a}}_{\bar{\omega}\bar{\ell}\bar{m}} + \bar{\phi}^{*}_{\bar{\omega}\bar{\ell}\bar{m}}(x)\hat{\bar{a}}^{\dagger}_{\bar{\omega}\bar{\ell}\bar{m}} \right), \qquad (3.16)$$

with a new vacuum state $|\bar{0}\rangle$ defined by

$$\hat{\bar{a}}_{\bar{\omega}\bar{\ell}\bar{m}}|\bar{0}\rangle = 0 \qquad \forall \ \bar{\omega}, \bar{\ell}, \bar{m}. \qquad (3.17)$$

The goal of this section is to see how these two vacuum states compare. Physically, one can imagine an asymptotically flat spacetime with a well-defined initial vacuum state $|\bar{0}\rangle$, which subsequently undergoes a gravitational collapse to form a black hole. Long after the black hole has formed, an inertial observer will have their own definition of the vacuum $|0\rangle$ in their own rest frame, but in terms of the original vacuum $|\bar{0}\rangle$, the observer will see particles. These particles are known as Hawking radiation.

To relate the two vacua in a general curved spacetime, the new barred modes can be expanded

in terms of the original ones:

$$\bar{\phi}_{\bar{\omega}\bar{\ell}\bar{m}} = \int_0^\infty d\omega \sum_{\ell=0}^\infty \sum_{m=-\ell}^\ell \left(\alpha_{\bar{\omega}\bar{\ell}\bar{m}}^{\omega\ell m} \phi_{\omega\ell m} + \beta_{\bar{\omega}\bar{\ell}\bar{m}}^{\omega\ell m} \phi_{\omega\ell m}^* \right), \tag{3.18}$$

or equivalently, the ladder operators can be related:

$$\hat{a}_{\omega\ell m} = \int_0^\infty d\bar{\omega} \sum_{\bar{\ell}=0}^\infty \sum_{\bar{m}=-\bar{\ell}}^{\bar{\ell}} \left(\alpha_{\bar{\omega}\bar{\ell}\bar{m}}^{\omega\ell m} \hat{\bar{a}}_{\bar{\omega}\bar{\ell}\bar{m}} + \beta_{\bar{\omega}\bar{\ell}\bar{m}}^{\omega\ell m *} \hat{\bar{a}}_{\bar{\omega}\bar{\ell}\bar{m}}^\dagger \right). \tag{3.19}$$

The coefficients α and β are known as Bogoliubov[2] coefficients.

Observable quantities in quantum field theory arise as the expectation value of operators. One particularly useful operator in the Fock representation is the number operator $\hat{N}_{\omega\ell m} = \hat{a}_{\omega\ell m}^\dagger \hat{a}_{\omega\ell m}$, which encodes the number of $\phi_{\omega\ell m}$-mode particles in a given quantum state. One can show that this operator is related directly to the Bogoliubov coefficient β via the relation [29]

$$\langle \bar{0} | \hat{N}_{\omega\ell m} | \bar{0} \rangle = \int_0^\infty d\bar{\omega} \sum_{\bar{\ell}=0}^\infty \sum_{\bar{m}=-\bar{\ell}}^{\bar{\ell}} \left| \beta_{\bar{\omega}\bar{\ell}\bar{m}}^{\omega\ell m} \right|^2. \tag{3.20}$$

Thus, if one wishes to calculate the number of particles seen in an inertial observer's rest frame state with respect to an initial vacuum state $|\bar{0}\rangle$, one must calculate the Bogoliubov coefficients between the two states.

In order to proceed any further, the field modes $\phi_{\omega\ell m}$ must be normalized with respect to some inner product. The natural choice for such an inner product is the one whose kernel is the Wronskian operator for the field's wave equation, in analogy to the scalar product required of the inverse transform for the Fourier coefficients $a_{\omega\ell m} = \langle \phi | \phi_{\omega\ell m} \rangle$:

$$\langle \phi_1 | \phi_2 \rangle \equiv -i \int_\Sigma d\Sigma \; n^\mu \sqrt{-g_\Sigma} \; \phi_1 \overleftrightarrow{\partial}_\mu \phi_2^*, \tag{3.21}$$

---

[2]Nikolay Bogoliubov and John Valentin both independently developed these transformations in 1958 in the context of BCS theory. Bogoliubov, the son of a priest and faithful Christian throughout his life, has a last name that is the Russian equivalent of the Latin "Amadeus" and the Hebrew "Jedediah," meaning "lover of God."

where Σ is an arbitrary spacelike Cauchy hypersurface that terminates at spacelike infinity and is orthogonal to a future-directed unit vector n^μ, and where the bidirectional derivative $\overset{\leftrightarrow}{\partial}_\mu$ is defined below Eq. (C.6). With this Klein-Gordon inner product, the Bogoliubov coefficients can be calculated via

$$\alpha^{\omega\ell m}_{\bar{\omega}\bar{\ell}\bar{m}} = \langle \bar{\phi}_{\bar{\omega}\bar{\ell}\bar{m}} | \phi_{\omega\ell m} \rangle, \qquad \beta^{\omega\ell m}_{\bar{\omega}\bar{\ell}\bar{m}} = -\langle \bar{\phi}_{\bar{\omega}\bar{\ell}\bar{m}} | \phi^*_{\omega\ell m} \rangle. \tag{3.22}$$

Therefore, the number of particles seen by any observer in a spacetime can in principle be calculated using Eqs. (3.20) and (3.22), once the mode solutions $\phi_{\omega\ell m}$ to the wave Eq. (3.11) are found. Unfortunately, even for the simplest black hole spacetime (Schwarzschild), the Klein-Gordon equation's radial mode solutions belong to a class of special functions known as confluent Heun functions, a generalization of hypergeometric functions, whose analytic properties are still being explored in the mathematical literature (see Appendix B for details).

Nonetheless, radial eigenmode solutions to Eq. (3.11) exist in simple form in the limit as $r \to \infty$, and Hawking was able to compute the Bogoliubov coefficients for an arbitrary collapsing black hole spacetime by considering a late-time observer asymptotically far from the black hole, with a vacuum state initialized by modes asymptotically far in the past [93, 94]. In that case, since the observer's modes correspond precisely to radial plane waves with frequencies uniquely determined by the spacetime's Killing vector, the inner product between the observer's modes and the modes of the vacuum state reduce to a Fourier transform over the vacuum state's exponentially redshifted modes. The result (see Appendix C for the full derivation) is a number operator spectrum governed by Planck's law (i.e., a blackbody spectrum).

The goal of the present work is to extend Hawking's results so that the particle content of the pre-collapse vacuum can be found for any freely falling observer, whether they are asymptotically far from the black hole, approaching the event horizon, or even inside the black hole. The above approach using the vacuum expectation value of the particle number operator $\hat{N}_{\omega\ell m}$ should continue to represent the notion of physical particle detection for any inertial observer's rest frame state, with a few caveats. First, the usual definition of a physical, no-particle state only matches that of $\langle \hat{N} \rangle$

in an asymptotically flat, static region, where all inertial observers can agree on the definition of positive frequency. But for general dynamical, non-Minkowski regions of spacetime, each inertial observer will see a different vacuum state, so that the very concept of a particle is ill-defined in semiclassical gravity. Additionally, the number operator measures values for definite frequencies, and therefore the uncertainty principle dictates that the result can only be treated in an averaged sense over an infinite amount of time—the entirety of future null infinity, in the case of Hawking, though one can then take the time $u \to \infty$ due to asymptotic flatness. A discussion of how wave packets can ameliorate this issue in non-Minkowski regions is given in Appendix C. Finally, $\langle \hat{N} \rangle$ is a globally defined quantity, relying on information about the behavior of modes long before before the observer ever existed. One may wish to work with a local notion of particle detection via, e.g., renormalized Unruh-deWitt detectors [135, 162], but alternatively, the path taken in this thesis after calculating $\langle \hat{N} \rangle$ is to move on to the renormalization of $\langle \hat{T}_{\mu\nu} \rangle$, a locally-defined quantity that is Lorentz covariant by construction (if $\langle \hat{T}_{\mu\nu} \rangle = 0$ for one observer, it will remain zero for any inertial observer at that point in spacetime).

With these caveats out of the way, consider how the Bogoliubov coefficients might be calculated for inertial observers that are not asymptotically far from a black hole. As it turns out, the limit $r \to \infty$ is not the only instance where the mode solutions to the wave Eq. (3.11) reduce to simple plane-wave eigenmodes; the Klein-Gordon potential also vanishes at the inner and outer horizons of the black hole. Using this fact, one can then set up a quantum scattering problem, determine the reflection and transmission coefficients between an initial vacuum state and the state of an observer at one of these horizons, and use this information to find the full Hawking spectrum. The details of this calculation for the Kerr spacetime are given in Appendix C, and the numerical results are presented in Sec. 4.5.

However, one may further wish to analyze the production of Hawking radiation for observers who are at an arbitrary radial coordinate r_{ob} in the spacetime, not precisely at one of the horizons. To do so, consider the details of Hawking's calculation for asymptotically distant observers. These

observers have eigenmodes of the form

$$\phi_{\omega\ell m} \propto \mathrm{e}^{-i\omega u}, \tag{3.23}$$

where $u = t - r^{\star}$ is the outgoing Eddington-Finkelstein coordinate and $r^{\star}$ is the radial tortoise coordinate. The vacuum state, however, has different modes. Though they begin in the above form asymptotically far into the past, once the black hole has formed from a gravitational collapse, these modes are scattered by the gravitational Klein-Gordon potential. By the time the vacuum state's modes reach the asymptotic future where the observer is located,[3] Hawking showed that they generically take the form

$$\bar{\phi}_{\bar{\omega}\bar{\ell}\bar{m}} \propto \mathrm{e}^{-i\bar{\omega}U}, \tag{3.24}$$

where $U \propto \exp(-\kappa_{+}u)$ is the outgoing Kruskal-Szekeres coordinate and κ_{+} is the surface gravity of the event horizon,[4] which in the limit $u \to \infty$ measures the rate of redshift (or the "peeling" of null geodesics). The number operator's vacuum expectation value is then calculated as the squared modulus of the Bogoliubov coefficient β via Eqs. (3.20) and (3.22):

$$\langle \bar{0} | \hat{N}_{\omega\ell m} | \bar{0} \rangle \propto \int_{0}^{\infty} d\bar{\omega} \left| \langle \mathrm{e}^{-i\bar{\omega}U} | \mathrm{e}^{i\omega u} \rangle \right|^{2}, \tag{3.25}$$

which, after some calculus, yields a Planckian spectrum in ω with temperature $\kappa_{+}/(2\pi)$.

If one wishes to generalize this calculation so that the observer is no longer at $r_{\mathrm{ob}} \to \infty$, the

---

[3] Recall that the inner product of Eq. (3.21) must be performed along a spacelike hypersurface where both the observer's modes and the vacuum state's modes are known, so one must propagate one set of modes through the spacetime to reach the surface along which the other set of modes was initialized.

[4] The surface gravity $\kappa_{+}c^2$ has units of acceleration and is the black-hole generalization of the Earth's surface gravity $g \approx 9.8 \text{ m/s}^2$, with the additional complication that a stationary observer at the event horizon would technically measure an infinite acceleration, so $\kappa_{+}c^2$ is actually defined as the acceleration redshifted to infinity; i.e., the gravitational acceleration measured by dangling an ideal string from $r \to \infty$ down to $r = r_{+}$.

only change will be to replace the observer's modes $\exp(-i\omega u)$ with modes of the form

$$\phi_{\omega\ell m} \propto \mathrm{e}^{-i\omega p^{-1}(U)}, \tag{3.26}$$

where $p(u) = U$ is a function connecting the observer's state and the vacuum state with a null geodesic. Why use null geodesics instead of waves moving through the scattering potential? The answer is that Hawking's original calculation makes use of the *geometric optics approximation.*

In the geometric optics (or eikonal, or high-frequency) approximation, the field's wave Eq. (3.11) is solved with the Ansatz

$$\phi_{\omega\ell m}(x) = \mathcal{A}(x) \, \mathrm{e}^{i\omega\Theta(x)}, \tag{3.27}$$

which leads to an equation for the eikonal phase function $\Theta(x)$ when the result is expanded to leading order in inverse powers of the frequency ω:

$$\partial^\mu\Theta\partial_\mu\Theta = 0. \tag{3.28}$$

It can be shown by covariant differentiation of Eq. (3.28) that it is a geodesic equation for a null vector field $k^\mu \equiv \partial^\mu\Theta$ normal to the family of constant-Θ hypersurfaces. Thus, any wave scattering problem can be reduced in the geometric optics limit to a ray-tracing problem along the eikonal hypersurface-orthogonal null congruence.

Thus, imagine that the observer (at an arbitrary spacetime event x_{ob}) is watching a null ray originating from some emitter located at x_{em} in the asymptotic past, where the vacuum state was initialized. The emitter itself is not the source that is creating Hawking radiation; rather, it is a proxy to help determine how the modes from an initially empty, no-particle state will be mixed and redshifted by the time they reach an observer. Sec. 4.2 will go into further details of how the vacuum state can be constructed in terms of such emitters for both spherical and rotating black holes.

Progress toward the calculation of Hawking radiation for an arbitrary observer was made in Refs. [20, 21] with the realization that one can define an "effective temperature" function κ_{eff} that

reduces to the surface gravity κ_+ when it is sufficiently adiabatic over an interval. This effective temperature is simply a measure of the rate of exponential redshifting seen by an observer from modes climbing out of collapsing matter's gravitational potential. Mathematically, it is defined as

$$\kappa_{\text{eff}}(u) \equiv -\frac{d}{du} \ln\left(\frac{dU}{du}\right) = -\frac{\ddot{p}(u)}{\dot{p}(u)}. \tag{3.29}$$

where the outgoing null coordinate u gives the observer's position and the null coordinate $U = p(u)$ gives the position of an emitter that defines the vacuum state. By a slight abuse of notation, the two worldlines labeled by coordinates U and u are connected by a null ray encoded by the function $U(u)$. The key insight is that as long as $\kappa_{\text{eff}}(u)$ remains approximately constant over a small interval around some point u_*, Eq. (3.29) can be integrated to yield

$$U = U_* + C_* \int_{u_*}^{u} d\bar{u} \, \exp\left[-\int_{u_*}^{\bar{u}} d\tilde{u} \, \kappa_{\text{eff}}(\tilde{u})\right] = U_* + C_* \, e^{\kappa_{\text{eff}}(u_*)(\bar{u}-u_*)} + \mathcal{O}(\epsilon^2), \tag{3.30}$$

where the parameter ϵ is known as the adiabatic control function and is defined by

$$\epsilon(u) \equiv \frac{1}{\kappa_{\text{eff}}^2} \left|\frac{d\kappa_{\text{eff}}}{du}\right|. \tag{3.31}$$

If $\epsilon(u_*) \ll 1$, then Eq. (3.30) reduces to the same mode definition used by Hawking to calculate the Bogoliubov coefficient of Eq. (3.25), and a thermal Hawking flux will be detected at u_* with temperature [16]

$$T_H(u_*) = \frac{\kappa_{\text{eff}}(u_*)}{2\pi}. \tag{3.32}$$

However, even if the adiabatic condition is not satisfied, a nonzero κ_{eff} still implies the detection of particles corresponding to a nonzero Bogoliubov coefficient β; the only difference is that the spectral content will generally be non-Planckian.

Instead of working in null coordinates u and U, the analysis in Chapter 4 will work in a slightly more tangible coordinate frame. Since both the observer and emitter can naturally use their proper

times τ_{ob} and τ_{em} to label the different null rays they encounter throughout their journey, Eq. (3.29) can be recast in a more intuitive form:

$$\kappa_{\text{eff}} = -\frac{d}{d\tau_{\text{ob}}} \ln\left(\frac{\omega_{\text{ob}}}{\omega_{\text{em}}}\right), \tag{3.33}$$

where the frequency ω_i ($i = $ "ob" or "em"), defined by

$$\omega_i \equiv -k^\mu \dot{x}_\mu, \tag{3.34}$$

is the temporal component of a null particle's coordinate 4-velocity $k^\mu \equiv dx^\mu/d\lambda$, measured in the frame of an observer or emitter with coordinate 4-velocity $\dot{x}^\mu \equiv dx^\mu/d\tau$. The mathematical details of how this formula is derived and how it can be extended for non-radial viewing directions is given in Appendix D.

Eq. (3.33) makes it apparent that the effective temperature κ_{eff} is nothing more than a measure of the rate of frequency redshifting seen by an observer, an indicator of the exponential peeling of null rays first noted by Hawking as the crucial feature of black hole horizons responsible for particle creation [93, 94]. For black hole spacetimes with a Killing horizon, in the limit as an observer approaches future timelike infinity, the notion of the effective temperature $\kappa_{\text{eff}}(\tau)$ defined above coincides precisely with the notion of the surface gravity κ_+ used to define a black hole's Hawking temperature [20]. But even in the absence of a true event horizon, an adiabatic rate of redshifting governed by $\kappa_{\text{eff}}(\tau)$ implies the existence of Hawking radiation for any observers around or inside of a black hole.

The perception of Hawking radiation for an arbitrary observer was first calculated more than a decade ago for observers in the Schwarschild spacetime, outside of the event horizon [16, 79]. Then, the perception of Hawking radiation inside of the Schwarzschild radius was analyzed [87, 160], with the general conclusion that the effective temperature steadily rises for a free-faller until diverging at the black hole's central singularity. This thesis then takes the next natural step into

non-Schwarzschild spacetimes—Chapter 4 will tackle the problem of how Hawking radiation is perceived for black holes with an inner horizon.

One additional contribution made by Hamilton in Ref. [87] was to extend the analysis of the effective temperature to an observer looking in an arbitrary direction. Hawking and most others after him focused solely on scattering from radial modes, though in general, vacuum-state modes will be reaching the observer from all directions with angular momentum mode numbers $\ell \geq 0$. Additional subtleties arise when considering non-radial modes (see Appendix D) that will be addressed throughout Chapter 4.

3.3   Renormalization techniques

The vacuum expectation value of the number operator $\langle 0|\hat{N}_{\omega\ell m}|0\rangle$ considered in the previous section is not the only quantity that can be calculated for black hole spacetimes in the context of quantum field theory in curved spacetimes. Here, two more quantities will be considered: the vacuum expectation value of the squared field operator, $\langle 0|\hat{\phi}^2|0\rangle$ (the subject of Chapter 5), and the vacuum expectation value of the field's stress-energy tensor, $\langle 0|\hat{T}_{\mu\nu}|0\rangle$ (the subject of Chapter 6). These two quantities have the additional complication that they are formally divergent, as a result of singular behavior within their Hadamard parametrices, so that they must be renormalized to yield finite observables. In Sec. 3.1 it was shown how renormalization is formally accomplished at the level of the one-loop effective action; now focus will be placed on how renormalization may be practically carried out when calculating these quantities.

Just as in Sec. 3.2, the vacuum expectation values for $\langle 0|\hat{\phi}^2|0\rangle$ and $\langle 0|\hat{T}_{\mu\nu}|0\rangle$ will be calculated by first breaking down the field operator into an expansion in $\omega\ell m$-modes. Then, the contributions from the creation and annihilation operators conspire to convert the quantum field theoretic problem into a completely analogous classical problem, with mode solutions $\phi_{\omega\ell m}$ to the wave Eq. (3.11)

equipped with Cauchy boundary conditions defined by the choice of vacuum:

$$\langle\bar{0}|\hat{\phi}^2(x)|\bar{0}\rangle = \int_0^\infty d\bar{\omega} \sum_{\bar{\ell}=0}^\infty \sum_{\bar{m}=-\bar{\ell}}^{\bar{\ell}} \left[\phi_{\bar{\omega}\bar{\ell}\bar{m}}(x)\phi^*_{\bar{\omega}\bar{\ell}\bar{m}}(x)\right], \tag{3.35}$$

$$\langle\bar{0}|\hat{T}_{\mu\nu}(x)|\bar{0}\rangle = \langle\bar{0}|\mathscr{D}_{\mu\nu}\hat{\phi}(x)|\bar{0}\rangle = \int_0^\infty d\bar{\omega} \sum_{\bar{\ell}=0}^\infty \sum_{\bar{m}=-\bar{\ell}}^{\bar{\ell}} \left[\mathscr{D}_{\mu\nu}\phi_{\bar{\omega}\bar{\ell}\bar{m}}(x)\right], \tag{3.36}$$

where $\mathscr{D}_{\mu\nu}$ is a second-order, bilinear differential operator, which for the scalar field in the action of

Eq. (3.10) can be obtained by the functional differentiation of the action, $T_{\mu\nu} \equiv 2\frac{\delta S_\phi}{\delta g^{\mu\nu}}$, yielding

$$\mathscr{D}_{\mu\nu}\phi = \left(\frac{1}{2}-\xi\right)\{\nabla_\mu\phi,\nabla_\nu\phi\} - \left(\frac{1}{4}-\xi\right)g_{\mu\nu}\{\nabla_\sigma\phi,\nabla^\sigma\phi\}$$
$$+ \xi\left(-\{\nabla_\mu\nabla_\nu\phi,\phi\} + g_{\mu\nu}\{\nabla_\sigma\nabla^\sigma\phi,\phi\} + \frac{1}{2}G_{\mu\nu}\{\phi,\phi\}\right) - \frac{1}{4}m^2 g_{\mu\nu}\{\phi,\phi\}, \tag{3.37}$$

where ∇_μ denotes covariant differentiation, $G_{\mu\nu}$ is the Einstein tensor, and the symbol $\{,\}$ represents

anticommutation. In the massless, minimally coupled limit, $m = \xi = 0$, the second line in Eq. (3.37)

vanishes, simplifying calculations greatly.

When performing the mode integral and mode sums in the above equations, the resulting

quantities diverge, quadratically for $\langle\hat{\phi}^2\rangle$ and quartically for $\langle\hat{T}_{\mu\nu}\rangle$. Students of quantum field theory

learn a variety of regularization and renormalization[5] techniques to "subtract away" these infinities

and leave a finite, physical result, but unfortunately, many of these techniques are only applicable in

Minkowski (or in some cases, Euclidean) spacetimes and will not work for black hole geometries.

One could imagine regularizing the integrals with a finite UV cutoff parameter Λ, but such a cutoff

would violate Lorentz invariance. Other techniques like dimensional regularization and zeta function

regularization rely on analytic continuations that only apply for specific Feynman propagators with

the wave equation for a flat spacetime, but for black hole metrics equipped with a pre-collapse

---

[5]*Regularization* refers to the introduction of new parameters so that a formally divergent theory can be evaluated in an explicit form (e.g., solving a divergent integral in terms of a cutoff parameter instead of simply writing "∞") and the divergent pieces can be identified. *Renormalization* refers to the process of combining those regularization parameters with the theory's original bare quantities so that any physical observables will only depend on finite, physical parameters.

vacuum state, the mode solutions to the wave Eq. 3.11 are not simply plane-wave eigenmodes and must either be computed numerically or written in terms of special functions that possess no known analytic continuations. Even more fundamentally, renormalization in flat spacetime utilizes normal-ordering, by which the energy of the vacuum state is set to zero, but for a general curved spacetime, there is no invariant vacuum.

Instead of searching for another method to isolate and remove divergences specific to the case at hand and see whether it matches other renormalization techniques for validation (which is how the renormalization program initially progressed in an *ad hoc* fashion), in the late 1970s Wald attempted to remove ambiguities by taking an axiomatic approach to the problem of renormalization [175]. The goal was to understand what constraints must be placed on the method of renormalization (specifically in the context of the stress-energy tensor operator) when a set of five general axioms are imposed, including causality, covariant conservation, and consistency with normal ordering in the Minkowski limit. The general conclusion of the study pointed toward a specific unique approach based around *covariant point-splitting renormalization.*

The point-splitting approach, pioneered by DeWitt [52], is motivated by the fact that while the field operator $\hat{\phi}(x)$ on its own evaluated at a single spacetime point makes complete mathematical sense as an operator-valued distribution smeared over the entire spacetime (along with any operations that are linear in the field), nonlinear combinations of field operators like $\hat{\phi}(x)\hat{\phi}(x)$ and $\hat{T}_{\mu\nu}(x)$ have no natural mathematical meaning (since products of distributions generally do not result in distributions) [175]. However, a quantity that makes perfect sense mathematically is the 2-point distribution $\hat{\phi}(x)\hat{\phi}(x')$, where the smearing occurs separately in two independent spacetime events x and x'. If one begins with such bilinear operators and then subsequently takes the coincidence limit as $x' \to x$, then it immediately becomes apparent where renormalization must come into play. Hadamard [80] showed that a solution $\mathscr{H}$ to a bilinear wave equation of the form of Eq. (3.11) must always possess the following singularity structure near the point x' in a 4-dimensional, analytic spacetime:

$$\mathscr{H}(x,x') = \frac{U}{\sigma} + V \log \sigma + W, \qquad (3.38)$$

where 2σ is the square of the geodesic distance between x and x' (which goes to zero in the coincidence limit), and U, V, and W are well-behaved functions of x. In other words, every curved spacetime appears locally flat if one zooms in enough, and so the two-point function will always locally diverge in the same way as it does for the Minkowski spacetime, via Eq. (3.38). Thus, the divergence can be isolated and renormalized in the coincidence limit to yield a finite result, and this procedure ends up providing the unique method of renormalization that satisfies Wald's axioms.[6]

Exact values for the functions U and V in Eq. (3.38) were soon found as a function of the metric tensor and its derivatives in a set of works by DeWitt and Christensen [43, 44, 53] so that the divergent pieces of the stress-energy tensor for an arbitrary spacetime metric could be isolated and renormalized (the additional function W is not purely geometric and instead is fixed by the choice of vacuum state). Thus, whenever the wave equation's mode solutions $\phi_{\omega\ell m}$ can be summed over all modes and expressed in terms of the spacetime's square geodesic distance 2σ, then a counterterm in the form of Eq. (3.38) can be constructed and subtracted from the stress-energy tensor to field a finite, renormalized result.

Two different renormalization techniques will be used in this thesis, both with connections to the Hadamard point-splitting approach. The first, used in Chapter 5 to calculate $\langle \hat{\phi}^2 \rangle$ in the inflationary Kasner spacetime, is adiabatic regularization. This technique is motivated by the fact that while a divergent counterterm can in theory always be constructed and subtracted from the two-point function to yield a finite, renormalized result, in practice, the two-point function often cannot be cast in a form where the singularity structure of Eq. (3.38) is analytically manipulable. Instead, the two-point function (refer to Eq. (3.35)) is usually expressed as a mode sum where the mode solutions to the wave Eq. (3.11) are only known numerically or as intractable special functions. Thus, one would be forced to perform a divergent integral numerically and subtract the infinite

---

[6]As a mild technical note, Wald [175] was only able to show that the renormalized stress-energy tensor satisfying all five of his axioms would be unique if it existed, but he could only prove existence in the form of the Hadamard point-splitting prescription for four of the five axioms. The sticking point, the fifth axiom concerning point-wise convergence in the classical limit, requires knowledge of metric variations that is generally not easily derived.

result from another divergent counterterm (a computational impossibility).

The way adiabatic regularization gets around this issue is by performing an adiabatic (Wentzel-Kramers-Brillouin, or WKB) expansion of the field modes in powers of the inverse frequency ω^{-1}. This expansion will match the exact mode sum in the limit of large ω (where the integral diverges), but with the advantage that it is built out of analytic functions that can be matched to the Hadamard counterterm explicitly. The renormalized vacuum expectation value of the squared field operator then takes the form

$$
\begin{aligned}
\langle \hat{\phi}^2 \rangle_{\text{ren}} = &\lim_{x' \to x} \left[\langle \hat{\phi}(x)\hat{\phi}(x') \rangle - \langle \hat{\phi}_{\text{WKB}}(x)\hat{\phi}_{\text{WKB}}(x') \rangle \right] \\
&+ \lim_{x' \to x} \left[\langle \hat{\phi}_{\text{WKB}}(x)\hat{\phi}_{\text{WKB}}(x') \rangle - \mathscr{H}(x, x') \right]
\end{aligned}
\tag{3.39}
$$

The first line in Eq. (3.39) can be calculated numerically by bringing both the bare mode solutions $\phi_{\omega\ell m}$ and the approximate WKB-type solutions $\phi_{\omega\ell m}^{\text{WKB}}$ under the same integral, so that the coincidence limit can be taken at the beginning of the calculation and the integral up to $\omega \to \infty$ will be guaranteed not to diverge. The second line in Eq. (3.39) can then be derived analytically for any particular spacetime. This second line is treated as negligible in Chapter 5, so that focus can be placed on the part of $\langle \hat{\phi}^2 \rangle$ directly connected to the low-energy modes instead of on the minutiae of point-splitting, but in principle, both lines in Eq. (3.39) can be computed with effort.

The second technique, used in Chapter 6, is state subtraction. It can be viewed as a generalized form of adiabatic regularization, in the following sense: instead of performing an adiabatic expansion of the modes, the terms labeled "WKB" in Eq. (3.39) can be treated as another mode-summed two-point function, only for a different vacuum state. The original two-point function of interest is the expectation value in the Unruh vacuum state (the late-time limit of the pre-collapse Minkowski vacuum introduced in Sec. 3.2), but one can also define other vacuum states in black hole spacetimes (like the Boulware state corresponding to the experience of a stationary observer, or the Hartle-Hawking state corresponding to a black hole in thermal equilibrium with a bath of radiation). These other vacuum states may not necessarily be physically relevant, but when subtracted from

the Unruh state, they should make the integral in first line of Eq. (5.34) finite and calculable. A further simplification throughout Chapter 6 is to choose a state such that the second line of Eq. (3.39) vanishes, or equivalently, to choose a difference state where the renormalized vacuum expectation value $\langle \hat{\phi}^2_{\text{diff}} \rangle_{\text{ren}}$ is already known (and therefore the renormalized value of interest, $\langle \hat{\phi}^2 \rangle_{\text{ren}} = \langle \hat{\phi}^2 - \hat{\phi}^2_{\text{diff}} \rangle_{\text{ren}} + \langle \hat{\phi}^2_{\text{diff}} \rangle_{\text{ren}}$, can be known exactly).

In this way, the vacuum expectation values of $\langle \hat{\phi}^2 \rangle$ and $\langle \hat{T}_{\mu\nu} \rangle$ can be computed as finite numerical integrals over sets of modes. All other details related to the computation of scattering coefficients for the mode solutions, the numerical integration schemes, and the interpretation of the results are presented in Chapters 5 and 6.

Chapter 4

Hawking Radiation: $\langle \hat{N} \rangle$

The contents of this chapter have been published as Ref. [127] (Secs. 4.2.1, 4.3.1, 4.4.1, 4.5.1, and 4.6), part of Ref. [123] (Secs. 4.3.1.5 and 4.3.2.3), and Ref. [128] (Secs. 4.1, 4.2.2, 4.3.2, 4.4.2, and 4.5.2).

4.1   Introduction

If a classical black hole that formed from a gravitational collapse is immersed within a quantum field initially in a vacuum state, someone far away from that black hole will eventually detect excitations of that quantum field in an effect known as Hawking radiation [93]. This radiation was found to follow a thermal distribution in the geometric optics (high-frequency) limit, with a temperature proportional to the surface gravity κ_+ of the black hole at the event horizon. The key feature required for such radiation to exist is a characteristic exponential redshifting of modes near a (quasi-)trapping horizon. As a result, the Hawking effect can also be related to the radiation seen by, e.g., an accelerating observer or a moving mirror model, where such a redshifting also occurs [20, 21].

The Hawking radiation detected asymptotically far from a black hole is negligibly small for all known astrophysical black holes, orders of magnitude below current observational capabilities. However, the radiation can take on a substantially different form when an observer approaches and/or falls into a black hole. For such an observer, instead of seeing a Hawking temperature proportional to the surface gravity κ_+, one can define an effective temperature function κ_{eff} that tracks the rate of redshifting they perceive, and this κ_{eff} reproduces the thermal Hawking result

when a suitable adiabatic condition is met (see Sec. 3.2 for more details) [20, 21]. One may wonder whether the Hawking temperature closer to a black hole's event horizon may be high enough to observe secondary astrophysical effects, but more importantly, the Hawking flux detected *inside* a black hole can be enormous and has profound implications for the self-consistency of black hole models in semiclassical gravity (i.e., quantum field theory placed over a classical background).

The perception of Hawking radiation has been analyzed for various classes of observers during and after gravitational collapse in the Schwarzschild exterior [16, 79] and the Schwarzschild interior [87, 160]. The goal of the present chapter is to extend this analysis to the late-time behavior of black holes with inner horizons, described by the Reissner-Nordström and Kerr metrics.

What should one hope to see when analyzing the Hawking content in black hole spacetimes with inner horizons? Here are some key takeaways:

(1) For an inertial observer in the vicinity of the *event horizon*, the effective temperature has roughly the same order of magnitude as the standard tiny Hawking temperature at infinity (i.e., the event horizon is semiclassically well behaved) [16, 79, 87, 160].

(2) For an observer in the vicinity of the *inner horizon*, the effective temperature is negative and diverges in the same manner as the Penrose blueshift perturbation singularity [127, 128, 152, 165].

(3) Hawking radiation is not confined to the radial direction—an observer looking in an arbitrary direction in their field of view will still see the characteristic exponential redshifting of modes, with higher Hawking temperatures toward the edge of the black hole's shadow and an increasingly isotropic distribution as they approach the inner horizon [87, 127, 128].

(4) The Hawking temperature can become negative even *outside* of the event horizon for a black hole close enough to extremality (e.g. for a Reissner-Nordström charge $Q/M > \sqrt{8/9}$, although adiabaticity may not necessarily be satisfied there) [127, 128].

(5) Though the spectral distribution of Hawking radiation appears as a blackbody from asymp-

totically far away (in the eikonal limit), graybody corrections to the spectrum become more important as one falls into the black hole [127, 128].

The results of this chapter confirm through entirely analytical means the same semiclassical divergence recently seen numerically for the renormalized stress-energy tensor at the Kerr Cauchy horizon [178] (see Chapter 6). This divergence points towards a semiclassical form of the cosmic censorship conjecture, that quantum effects will always act to close off Cauchy horizons that would otherwise serve as entryways to wormholes and timelike singularities. Though the true quantum gravitational nature of a black hole interior remains elusive, these first-order results from quantum field theory over curved spacetime imply either that the Cauchy horizon is the source of a roiling quantum atmosphere that marks the boundary endpoint of spacetime itself, or that the Cauchy horizon is so unstable that it will evaporate outward to meet the event horizon within a matter of seconds to form an extremal black hole or a compact horizonless object [18].

The perception of Hawking radiation for various infalling observers looking in the radial direction is explored in Sec. 4.3 using the geometric optics effective temperature formalism, first for spherically symmetric black holes and then for rotating black holes. Then, the effective temperature for observers looking in an arbitrary direction in their field of view is explored in Sec. 4.4. However, these results not only are unreliable at low frequencies, but they also depend crucially on the adiabaticity of the observer at each point of interest. To address both of these concerns, in Sec. 4.5 a full numerical analysis of the wave scattering problem is performed in order to calculate the Bogoliubov spectrum of Hawking radiation in the limits where such a calculation can be feasibly done; in particular, for an observer at infinity, at the event horizon, and at the ingoing and outgoing portions of the Cauchy horizon. For a Reissner-Nordström black hole, the calculations show that the Hawking spectrum appears as a graybody at the event horizon but becomes ultraviolet-divergent at the Cauchy horizon, in accord with the geometric optics effective temperature results that predict an infinite negative κ_{eff} there. The Kerr spectra follow the same trends as in the spherically symmetric case, except that the calculations are able to be extended to high enough frequencies to show that

the Cauchy horizon radiation does not actually diverge in the ultraviolet regime in most cases (nor should it be expected to—see Sec. 4.5.2.1 for more details). However, as an observer approaches the Cauchy horizon, they should in general see Hawking radiation glowing brightly in every direction they look, as if they are diving into a thick quantum atmosphere with ever-increasing energy.

Despite the success and relative robustness of Hawking's calculation, much debate has continued to this day concerning the nature, origin, and implications of Hawking radiation. From the perspective of quantum information theory, a driving question has been to understand how black holes evolve unitarily in spite of their seemingly thermal, information-free radiation. Though the calculations given in this chapter give no quantitative measure of entropy and thus cannot address this problem directly, it may be that the increasing (and eventually diverging) presence of Hawking radiation found here as one ventures farther into a black hole's interior is closely tied to the mediation of unitary evolution, or at the least helps explain the vast number of degrees of freedom a black hole is expected to host in its interior.

Before diving into the bulk of the chapter, it is worth pausing to comment on the implications (and especially the nonimplications) of a negative Hawking temperature. Hawking radiation is often pictured as a positive flux of particles escaping a black hole's horizon, coinciding with a negative flux of partner particles traveling inward to the black hole's singularity [94]. However, the negative-temperature Hawking flux analyzed here is not simply an observation of the inward-traveling negative-energy Hawking partners. In contrast, these negative temperature will be found in both the ingoing and outgoing radiation sectors, and further, these calculations do not involve any tunneling across horizons. It may still be possible to formulate a local picture for the global calculations done here, but instead of the simple pair splitting at the outer horizon, one should imagine that virtual particle pairs created anywhere near and inside the black hole will be perturbed by radial gravitational tidal forces, and a negative temperature is realized because these forces will begin compressing instead of stretching once an observer comes close enough to the inner horizon [45, 136]. For more details, see my short study of these "pancakifying" forces in the essays for the Gravity Research Foundation [122].

How then should one interpret a negative Hawking temperature under the present formalism? The most straightforward answer is that the modes reaching an observer are blueshifting instead of redshifting, and this blueshift will result in a change in sign of the effective temperature of Eq. (3.33) below. However, the thermodynamic implications of such a change in sign are less apparent. Ref. [47] was the first to comment on the implications of the fact that the surface gravity κ_- defined at the inner horizon is negative, and many authors since have attempted to provide a consistent thermodynamic picture of a black hole with a negative-temperature inner horizon [48, 146, 149, 172]. However, here no claims will be made based on the Bekenstein-Hawking entropy nor any thermodynamic laws, and there will also be no assumptions made about what happens beyond the inner horizon. It may well be that the negative surface gravity has some implication for the temperature of a purely mathematical, analytically extended white hole emerging from an inner horizon. Nonetheless, the inner horizon effective temperature κ_{eff} describing the experience of an infalling observer is distinct from the global surface gravity κ_-, and in fact κ_{eff} will be found either to diverge at the inner horizon or to equal some constant multiple of κ_- (see Sec. 4.3.1.2), depending on whether the observer looks up or down.

4.2   Construction of the Unruh vacuum state

Instead of performing calculations in a fully dynamical collapse spacetime, it is common to formulate an equivalent problem in an empty, eternal black hole spacetime like the Schwarzschild metric [173]. As a result, the collapsing body must be replaced by appropriate boundary conditions on the past horizon, and these boundary conditions define the quantum field's vacuum state in that spacetime. Three options are generally discussed in the literature: the Boulware state, in which the quantum field's modes are defined to be positive frequency with respect to the Killing vector $\partial/\partial t$ on both the past horizon and past null infinity; the Hartle-Hawking state, in which modes are defined

to be positive frequency with respect to the past boundaries' canonical affine coordinates[1] $\partial/\partial U$ and $\partial/\partial V$; and the (past) Unruh state [173], in which modes are defined to be positive frequency with respect to $\partial/\partial U$ on the past horizon and $\partial/\partial t$ at past null infinity. The last of these states is the one that is most physically relevant to the production of a Hawking flux to the future of a collapsing black hole and is the state that will be employed here.

In the effective temperature framework, the vacuum state is specified by the spacetime position and state of motion (the orbital parameters) of the emitter. For example, the Boulware state corresponds to a static emitter maintaining a constant radius r_0. This state is thus only defined for the exterior portion of the black hole, since an emitter cannot remain static below the event horizon. A freely falling observer measuring in the Boulware state will see diverging stress-energy at the horizon, as a result of the diverging acceleration required for the Boulware emitter to remain static there.

In contrast, the Unruh state is associated with a freely falling emitter, positioned either at the black hole's horizon or at infinity. The outgoing Unruh modes correspond to the limit $r_{\text{em}} \to r_+$, so that the observer sees the emitter frozen on the past horizon (one may equivalently take the Unruh emitter's descent into the black hole to have occurred sufficiently far into the past), and the ingoing Unruh modes correspond to the limit $r_{\text{em}} \to \infty$, so that the observer sees the emitter safely resting in the sky above. Since the observer and the Unruh emitter are generally not located at the same spacetime coordinate (as in the Boulware state), their modes must be connected via a null geodesic, null because the quantum field under study here is massless.

In Sec. 4.2.1, it will be shown that in spherically symmetric spacetimes, the freely falling emitters described above see modes in their own proper time that tick at the same rate as the modes used to define the Unruh state, and therefore that they are the right choice of emitters in the effective temperature formalism to describe the Hawking content of dynamically formed black holes. Then in

---

[1] For example, for a Schwarzschild black hole, $U = -4Me^{-u/(4M)}$ is the outgoing Kruskal-Szekeres coordinate, whose vector field $\partial/\partial U$ is of Killing type on the past horizon. Positive frequency modes are then defined to be the eigenfunctions of the Lie derivative of the field in the $\partial/\partial U$ direction.

Sec. 4.2.2, the equivalent analysis will be carried out for black holes with only azimuthal symmetry (i.e., the rotating Kerr spacetime). Once these foundations for constructing the vacuum state are laid out, the analysis will proceed with the radial effective Hawking temperature κ_{eff} in Sec. 4.3.

4.2.1 Spherical black holes

To see how the choice of vacuum corresponds to the specification of the emitter's worldline, consider an emitter radially free-falling from rest at infinity[2] into a static, asymptotically flat, spherically symmetric black hole, which is given by the line element

$$ds^2 = -\Delta(r)\ dt^2 + \frac{dr^2}{\Delta(r)} + r^2\left(d\theta^2 + \sin^2\theta d\phi^2\right). \tag{4.1}$$

The horizon function $\Delta(r)$ has the property that it vanishes linearly as r approaches a horizon, and it asymptotes to unity as $r \to \infty$. For the Reissner-Nordström metric, the horizon function is $\Delta = 1 - 2M/r + Q^2/r^2$, but for now it will be left arbitrary.

Such an emitter will have coordinate 4-velocity with nonzero components

$$\dot{t} \equiv \frac{dt}{d\tau} = \frac{1}{\Delta}, \tag{4.2a}$$

$$\dot{r} \equiv \frac{dr}{d\tau} = -\sqrt{1 - \Delta}. \tag{4.2b}$$

When the emitter is at infinity ($\Delta \to 1$) sending modes inward, Eq. (4.2a) implies that the emitter's proper time τ will tick at the same proportionate rate as the global timelike Killing coordinate t. Thus, t will be the coordinate the emitter uses to define positive frequency, just as expected for ingoing Hawking modes originating from past null infinity.

However, when the emitter reaches a horizon ($\Delta \to 0$), Eq. (4.2a) implies that the static Schwarzschild time t will tick at an infinitely faster rate than the emitter's proper time τ. So

---

[2]The same arguments should hold for any inertial free-faller; here, the radial, $E = 1$ case is presented for simplicity.

heuristically, instead of seeing wave modes of the form $\exp(-i\omega t)$, the emitter should end up seeing modes of the form $\exp[-i\omega \exp(-kt)]$ (for some constant k), so that even when t diverges, the emitter's proper time will still remain finite. The new time coordinate defined by these modes will be found to coincide with the oft-studied Kruskal-Szekeres coordinate U.

To make the above arguments more precise, and to extend the discussion to distinguish ingoing and outgoing modes (which depend on both the emitter's proper time and the proper distance between wavefronts), consider a set of eikonal waves in the emitter's locally orthonormal tetrad frame $\{\gamma_0, \gamma_1, \gamma_2, \gamma_3\}$, whose tangent-space coordinates will be labeled ξ^0, ξ^1, ξ^2, and ξ^3. This tetrad frame is constructed so that it is continuous across the event horizon and so that the time axis γ_0 is always timelike and future-directed, while the radial axis γ_1 is always spacelike and outward-directed. In the limit of large frequency ω, to leading order in $1/\omega$, the ingoing (+) or outgoing (−) components of the eikonal wavefront will follow a null geodesic congruence with tetrad-frame 4-momentum (neglecting any normalization factors)

$$k^{\hat{m}} \equiv \frac{d\xi^{\hat{m}}}{d\lambda} = \left(1,\ \pm 1,\ 0,\ 0\right). \tag{4.3}$$

The transformation from the emitter's local tetrad frame to a coordinate frame can be accomplished through the use of the appropriate vierbein. For an external[3] radial free-faller with specific energy E (where $E = 1$ corresponds to rest at infinity), in the static polar spherical chart this vierbein reads

$$e^{\hat{m}}{}_{\mu} = \begin{pmatrix} E & \sqrt{E^2 - \Delta} & 0 & 0 \\ \sqrt{E^2 - \Delta} & E & 0 & 0 \\ 0 & 0 & r & 0 \\ 0 & 0 & 0 & r\sin\theta \end{pmatrix} \tag{4.4}$$

(where rows label the coordinates ξ^0, ξ^1, ξ^2, ξ^3 of the emitter's locally inertial frame, and columns

---

[3]The case of a free-faller in the black hole interior follows the same line of reasoning as the exterior case presented here, *mutatis mutandis*.

label the global coordinates t, r^*, θ, φ). Here we define the tortoise coordinate r^* by

$$\frac{dr}{dr^*} = \Delta. \tag{4.5}$$

The coordinate-frame 4-momentum $k^\mu = k^{\hat{m}} e_{\hat{m}}{}^\mu$ then follows immediately:

$$k^\mu = \left(\frac{E \mp \sqrt{E^2 - \Delta}}{\Delta}, \ \pm \frac{E \mp \sqrt{E^2 - \Delta}}{\Delta}, \ 0, \ 0 \right). \tag{4.6}$$

If the emitter defines some positive frequency ω (along with the corresponding wave number ω/c), then their natural choice of ingoing (upper sign) or outgoing (lower sign) modes will take the form $\exp[-i\omega(\xi^0 \pm \xi^1)]$, which can be written in coordinate form by matching the affine distances of Eqs. (4.3) and (4.6):

$$d\xi^0 \pm d\xi^1 = \frac{\Delta}{E \mp \sqrt{E^2 - \Delta}} \left(dt \pm dr^* \right). \tag{4.7}$$

Asymptotically, as a unit-energy emitter approaches infinity ($\Delta \to 1$), the fraction in Eq. (4.7) reduces to unity, so that the proper choice of coordinates to define Unruh modes at infinity is the Eddington-Finkelstein double null coordinate system, defined in both the exterior and interior as

$$u \equiv t - r^*, \quad v \equiv t + r^*, \tag{4.8}$$

where u here is the same outgoing null coordinate as in Eq. (3.29).

When the emitter is at a horizon ($\Delta \to 0$), the mode behavior depends on whether the waves are ingoing or outgoing. For the ingoing modes of a positive-energy free-faller or the outgoing modes of a negative-energy free-faller (neither of which are needed to define an Unruh emitter but will prove useful later to define the natural modes seen by horizon observers), the fraction in Eq. (4.7) reduces to $2E$, so that the proper modes (after ω is properly scaled) are once again the Eddington-Finkelstein modes $\exp[-i\omega(t \pm r^*)]$.

But for the outgoing modes of a positive-energy free-faller or the ingoing modes of a negative-

energy free-faller at the horizon, the fraction in Eq. (4.7) vanishes, so a more appropriate coordinate choice must be found. Define a new coordinate $\bar{U}$ such that the outgoing Unruh modes at the horizon will be written as $\exp[-i\omega\bar{U}]$. Then Eq. (4.7) implies that $\bar{U}$ must satisfy

$$\frac{d\bar{U}}{du} \underset{\Delta\to 0}{=} \frac{\Delta}{2E} \approx \frac{r - r_\pm}{2E} \frac{d\Delta}{dr}\bigg|_{r_\pm} \tag{4.9}$$

in the near-horizon limit. From this expression one can identify the quantity

$$\kappa_\pm \equiv \frac{1}{2}\frac{d\Delta}{dr}\bigg|_{r_\pm} \tag{4.10}$$

as the outer (+) or inner (−) horizon's surface gravity. For an emitter with $E = 1$, since from Eqs. (4.3), (4.5), and (4.6), the radius r is related to the horizon-limit outgoing proper null coordinate $\bar{U}$ by

$$\frac{dr}{d\bar{U}} = -\frac{1 + \sqrt{1 - \Delta}}{2} \underset{\Delta\to 0}{=} -1, \tag{4.11}$$

then Eq. (4.9) solves as

$$\bar{U} \propto \exp\left(-\kappa_\pm u\right). \tag{4.12}$$

Eq. (4.12) assumes that $\bar{U}$ is chosen to begin at 0 at the event horizon, when $u \to \infty$. This form of the emitter's proper time (up to an irrelevant normalization factor) is precisely the form of the outgoing Kruskal-Szekeres coordinate U used by Unruh to define positive frequency on the past horizon [173]. Thus, the outgoing modes of the Unruh state correspond to those seen as positive frequency by an emitter in free fall asymptotically close to the past horizon.

In some sense, nothing more has been done than to "rederive the obvious" in showing how one may obtain past Unruh null boundary conditions. However, in addition to providing yet another way of understanding the validity of this choice of vacuum state, the generalized derivation above also provides a natural specification of ingoing and outgoing modes for freely falling observers at either horizon, without any reliance on global Killing vector fields or asymptotically Minkowski regimes.

This idea will return when considering solutions to the wave equation in Sec. 4.5.

As a final comment concerning the choice of vacuum state, an additional family of vacuum states was used by Ref. [16] to mimic the switching on of Hawking radiation as a black hole first forms during a collapse. These "collapse vacua" correspond to emitters in free fall from rest at infinity, each separated from the observer by a time delay $\delta\tau$ (as in the Unruh state), but not necessarily in the limit as they approach the horizon or infinity. However, this chapter is not concerned with the initial transient collapse dynamics of a black hole; rather, focus is placed on the late-time steady-state behavior once the black hole has settled down into the Unruh state, which should occur only a few light-crossing times after the black hole's formation.

4.2.2 Rotating black holes

Rotating, empty black holes are modeled with the Kerr spacetime, which is given by the line element (in Boyer-Lindquist coordinates) [40]

$$ds^2 = \frac{\rho^2}{\Delta}dr^2 - \frac{\Delta}{\rho^2}\left(a\sin^2\theta \; d\varphi - dt\right)^2 + \rho^2 d\theta^2 + \frac{\sin^2\theta}{\rho^2}\left(R^2 d\varphi - a \; dt\right)^2, \tag{4.13}$$

where $R^2 \equiv r^2 + a^2$, where $a \equiv J/M$ is the black hole's spin parameter (in terms of the black hole's angular momentum J and mass M), the conformal factor $\rho^2 \equiv r^2 + a^2\cos^2\theta$ contains zeros at the black hole's ring singularity, and the horizon function $\Delta \equiv r^2 + a^2 - 2Mr$ contains zeros at the black hole's event $(r = r_+)$ and Cauchy $(r = r_-)$ horizons.

The geodesic equations of motion in this spacetime are separable [40]:

$$\dot{t} = \frac{1}{\rho^2}\left(\frac{R^2 P_r}{\Delta} + aP_\theta\right), \tag{4.14a}$$

$$\dot{r}^2 = \frac{1}{\rho^4}\left(P_r^2 - \left(K + r^2\delta\right)\Delta\right), \tag{4.14b}$$

$$\dot{\theta}^2 = \frac{1}{\rho^4}\left(K - a^2\cos^2\theta \; \delta - \frac{P_\theta^2}{\sin^2\theta}\right), \tag{4.14c}$$

$$\dot{\varphi} = \frac{1}{\rho^2}\left(\frac{aP_r}{\Delta} + \frac{P_\theta}{\sin^2\theta}\right), \tag{4.14d}$$

where

$$P_r(r) \equiv R^2 E - aL, \tag{4.15a}$$

$$P_\theta(\theta) \equiv L - aE \sin^2\theta, \tag{4.15b}$$

with an overdot representing differentiation with respect to affine time (τ for massive geodesics and λ for massless geodesics), with constants of motion written in terms of the Killing energy per unit mass E, Killing angular momentum along the axis of rotation per unit mass L, and Carter constant $K = Q + (aE - L)^2$, and where $\delta = 1$ for massive particles while $\delta = 0$ for massless particles (which will be denoted with scripted constants of motion $\mathcal{E}$, $\mathcal{L}$, $\mathcal{K}$ in contrast to the massive particle's constants E, L, K).

As a reminder, in the effective temperature formalism, the appropriate choice of vacuum state for gravitational collapse leading to the formation of a black hole is that of an inertial emitter in the asymptotic past, when the spacetime is still flat and the black hole has not yet formed. However, the Kerr metric models an eternal black hole (or, by analytic extension, a white hole-black hole system), not a dynamical collapse. Thus, instead of starting with a Minkowski vacuum in the asymptotic past, one must specify boundary conditions on the Kerr past horizon that match the exponential redshifting one would expect near a collapsing shell of matter, and these boundary conditions are precisely the ones used to define the (past) Unruh vacuum state used here. This state exactly mimics the physical state coming from gravitational collapse in all portions of the spacetime except along the (now singular) past horizon and along the left leg of the inner horizon (which in the dynamical case may not be a Cauchy horizon as it is in Kerr; see Ref. [107] for a proposed construction in the analogous charged case).

The Unruh state is formally defined by taking modes to be positive frequency with respect to the Killing vector field ∂_t along past null infinity and with respect to the Kruskalized canonical affine field ∂_U along the past horizon [173]. The latter coordinate is defined in the physical regions

of interest by

$$U \equiv \frac{\text{sgn}(r_+ - r)}{\kappa_+} \, \mathrm{e}^{-\kappa_+ u}, \tag{4.16}$$

where

$$\kappa_\pm \equiv \frac{1}{2R_\pm^2} \frac{d\Delta}{dr}\bigg|_{r_\pm} = \pm \frac{r_+ - r_-}{2R_\pm^2} \tag{4.17}$$

is the surface gravity at the Kerr black hole's event horizon (κ_+) or Cauchy horizon (κ_-) with the definition $R_\pm^2 \equiv r_\pm^2 + a^2$, and once again,

$$u \equiv t - r^*, \qquad v \equiv t + r^* \tag{4.18}$$

are the outgoing and ingoing Eddington-Finkelstein coordinates, defined in the same way for both the interior and exterior portions of the spacetime.

Since the definition of a vacuum state primarily concerns the choice of positive frequency with respect to a timelike coordinate, the choice of angular modes will not substantially influence the final results of the calculations done here [179]. For the Unruh modes along past null infinity, azimuthal modes of the form $\exp(i\bar{m}\varphi)$ are used, while the Unruh modes along the past horizon are taken to be $\exp(i\bar{m}\varphi_+)$, where

$$\varphi_\pm \equiv \varphi - \Omega_\pm t, \tag{4.19}$$

with the angular velocity $\Omega_\pm$ of the horizon at $r = r_\pm$ defined in Eqs. (4.61) and (4.137). The azimuthal coordinate φ_+ is regular at the horizon, and additionally, it defines the Killing vector $\partial_t + \Omega_+ \partial_\varphi$ that generates the Killing horizon at $r = r_+$.

In what follows, it will be shown that the Unruh state can be encoded in the geometric optics framework by a family of phase-aligned, freely falling emitters placed at $r \to \infty$ for ingoing modes and $r \to r_+$ for outgoing modes. Consider first the ingoing Unruh sector, which is defined with no mode contributions from the past horizon and with modes of the form $\exp(-i\bar{\omega}v)$ along past null infinity [173]. In the geometric optics limit, these ingoing modes should follow a null congruence hypersurface-orthogonal to the eikonal phase front defined by taking $\Theta = v$ along past null infinity;

recall Eq. (3.28). However, these null geodesics could just as easily be labeled by the proper time of an infaller asymptotically far from the black hole: from Eqs. (4.14), (4.18), and (4.134), as an infaller's radius r is taken to infinity, the ingoing time behaves as

$$\lim_{r\to\infty} \frac{dv}{d\tau} = \lim_{r\to\infty} \left(\dot{t} + \frac{R^2}{\Delta}\dot{r} \right) = E - \sqrt{E^2 - 1}. \tag{4.20}$$

If the infaller is taken to be at rest asymptotically far from the black hole ($E = 1$), then Eq. (4.20) implies that $d\tau = dv$; i.e., the infaller's proper time will tick at the same rate as the null coordinate used to define the Unruh state at past null infinity.

Now consider the outgoing Unruh sector, which is defined with no mode contributions from past null infinity and with modes of the form $\exp(-i\bar{\omega}U)$ along the past horizon [173]. At the past horizon, when $r \to r_+$ (and $\Delta \to 0$), the rate of change of an infaller's outgoing Eddington-Finkelstein coordinate u with respect to their proper time will diverge:

$$\lim_{r\to r_+} \frac{du}{d\tau} = \frac{2R^2 P_r}{\rho^2 \Delta} + \mathcal{O}(1). \tag{4.21}$$

In order to show that the appropriate choice of coordinate is actually U instead of u, consider how u explicitly depends on an infaller's proper time. First, define the Mino time $\tilde{\tau}$ [131] by the relation

$$\frac{d\tau}{d\tilde{\tau}} = \rho^2 \tag{4.22}$$

so that as $r \to r_+$, Eq. (4.14b) can be integrated to yield the asymptotic timelike geodesic solution

$$\lim_{r\to r_+} \tilde{\tau} = \tilde{\tau}_0 - \frac{r - r_+}{|P_r|} + \mathcal{O}\left[(r - r_+)^2 \right], \tag{4.23}$$

with an integration constant $\tilde{\tau}_0$. Similarly, Eq. (4.14a) can be integrated in the same asymptotic

limit to yield the timelike geodesic solution

$$
\begin{aligned}
\lim_{r \to r_+} t &= \lim_{r \to r_+} \left(\int dr \frac{R^2 P_r}{(dr/d\tilde{\tau})\Delta} + \int d\theta \frac{a P_\theta}{d\theta/d\tilde{\tau}} \right) \\
&= \int dr \frac{R^2}{\Delta} + \mathcal{O}(1) \\
&= r^* + \mathcal{O}(1),
\end{aligned} \tag{4.24}
$$

where the final $\mathcal{O}(1)$ term encompasses terms at least constant in r, including terms dependent on the latitude θ. The outgoing Eddington-Finkelstein coordinate u can therefore be written from Eqs. (4.18) and (4.24) as

$$
\lim_{r \to r_+} u = -2r^* + \mathcal{O}(1) = -\frac{1}{\kappa_+} \ln |r - r_+| + \mathcal{O}(1), \tag{4.25}
$$

with the surface gravity κ_+ from Eq. (4.17). Inverting Eq. (4.25) and substituting in the inverse of Eq. (4.23) gives the well-known exponential relation

$$
\lim_{r \to r_+} \tilde{\tau} \propto \mathrm{e}^{-\kappa_+ u} + \mathcal{O}(1), \tag{4.26}
$$

which is precisely the relation used to define the Kruskalized coordinate U in Eq. (4.16). Thus, the proper time of an ingoing infaller asymptotically close to the event horizon labels outgoing null geodesics in the same fashion as the Kruskalized coordinate U used to define the Unruh state.

As can be seen from the analysis above, the choice of the infaller emitting null rays to define the Unruh state is independent of that infaller's orbital parameters and angular position, as long as they begin at rest asymptotically far from the black hole, follow along an ingoing timelike geodesic, and reside either at $r \to \infty$ (for ingoing modes) or $r \to r_+$ (for outgoing modes).

When considering the geometric optics Unruh state in the Kerr geometry, an additional subtlety arises that is not present in the Schwarzschild or Reissner-Nordström geometries. For those simpler, spherically symmetric cases, an observer in radial free-fall looking down at an Unruh emitter
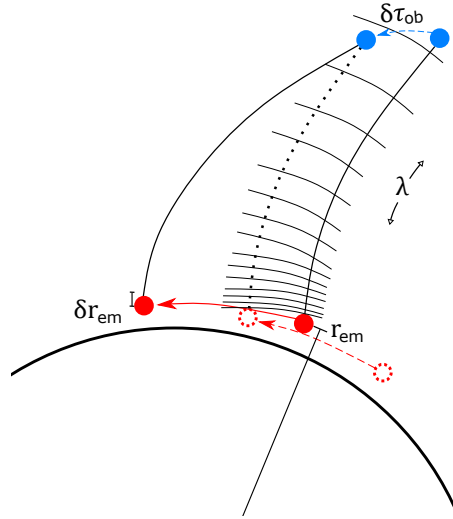
Figure 4.1: An inertial observer (blue) cannot follow outgoing null geodesics from one emitter (solid red) without rotating their frame of reference. But if they stare in a fixed direction, the new emitter they see (dashed red) after an infinitesimal proper time $\delta\tau_{\rm ob}$ must be shifted by a radial distance $\delta r_{\rm em}$ so that all emitters remain in phase. Then, the total affine distance λ will change, but the affine distance weighted by the emitter's frequency $\omega_{\rm em}$, Eq. (4.28), will stay constant.

asymptotically close to the event horizon is able to watch the same emitter for their entire journey into the black hole. However, for a Kerr black hole, an observer in free-fall generally (except for a few privileged frames analyzed in Sec. 4.3.2) cannot watch the same emitter at the horizon without rotating their field of view or otherwise accelerating. The reason for the complication is that the emitter for the outgoing Unruh state is within the ergosphere and must orbit the black hole with the geometry. An observer would therefore not see the redshifting emitter freeze in place as they approach the horizon, but instead at late times they would see the emitter steadily moving across the surface of the past horizon until reaching the edge of the black hole's shadow, becoming heavily distorted, and reappearing on the opposite side.

As has been argued in previous studies [87], an observer who rotates their frame of reference to follow a single emitter will induce undesired non-inertial particle creation effects, which are fundamentally distinct from the particle creation due to the Hawking effect. For the Kerr geometry, one must therefore consider a *family* of Unruh emitters at the event horizon, all chosen to lie along the same eikonal wave front, so that as the observer falls toward the black hole, their non-rotating

(Fermi-Walker transported) view will sweep across different emitters all remaining in phase with each other (see Fig. 4.1).

The implementation of a family of phase-aligned Unruh emitters is carried out in Sec. 4.4.2. The key constraint imposed on the calculation of the effective temperature of Eq. (3.33) is that the affine distance of the null geodesic measured in the frame of the emitter must be held constant for fixed observer position as the emitter's position is varied along the horizon. The affine distance λ along a Kerr null geodesic, analogous to the proper time τ for timelike geodesics, can be obtained by quadrature of Eqs. (4.14b) and (4.14c):

$$\lambda = \int_{r_{\rm em}}^{r_{\rm ob}} \frac{r^2\ dr}{\pm\sqrt{P_r^2 - \mathcal{K}\Delta}} + \int_{\theta_{\rm em}}^{\theta_{\rm ob}} \frac{a^2\cos^2\theta\ d\theta}{\pm\sqrt{\mathcal{K} - P_\theta^2\csc^2\theta}}. \tag{4.27}$$

This affine distance can be scaled by the null particle's frequency ω_i to yield proper distances in the frames of the emitter ($\lambda_{\rm em}$) or the observer ($\lambda_{\rm ob}$):

$$\lambda = \frac{\lambda_{\rm em}}{\omega_{\rm em}} = \frac{\lambda_{\rm ob}}{\omega_{\rm ob}}. \tag{4.28}$$

Eq. (4.28) can then be substituted into Eq. (3.33) to give a new expression for the effective temperature $\kappa_{\rm eff}$, with the constraint that $\lambda_{\rm em}$ be kept constant:

$$\kappa_{\rm eff}(\tau_{\rm ob}) = -\frac{d}{d\tau_{\rm ob}}\ln\left(\frac{\omega_{\rm ob}\lambda}{\lambda_{\rm em}}\right) = -\frac{d\ln\omega_{\rm ob}}{d\tau_{\rm ob}} - \frac{d\ln\lambda}{d\tau_{\rm ob}}. \tag{4.29}$$

Now that it has been shown how the Unruh vacuum state in the effective temperature formalism can be encoded by a family of freely falling emitters skimming the appropriate past null boundaries, the calculation of the effective temperature can commence in the following sections.

4.3   Effective Hawking temperature κ_{eff} (radial modes)

4.3.1   Spherical black holes

Here, the effective temperature seen by a freely falling inertial observer in a charged black hole spacetime with a quantized scalar field is examined. First, the effective temperature κ_{eff} is calculated for an observer looking in the radial direction via Eq. (3.33), then in Sec. 4.3.1.4 the adiabaticity condition on κ_{eff} is analyzed.

Consider the line element of Eq. (4.1), which describes the geometry of a charged, spherically symmetric black hole when the horizon function Δ takes the form

$$\Delta = \left(1 - \frac{r_+}{r}\right)\left(1 - \frac{r_-}{r}\right), \qquad r_\pm \equiv M \pm \sqrt{M^2 - Q^2}. \tag{4.30}$$

The black hole modeled by this geometry is known as the Reissner-Nordström black hole, which possesses a mass M and a charge Q. The length scales r_+ and r_- are referred to respectively as the outer (event) horizon and the inner (Cauchy) horizon.

The rate of redshift seen by a radially infalling observer has already been calculated for the spacetime of Eq. (4.1) for arbitrary Δ (see Appendix B of Ref. [87]), though that analysis was only carried out explicitly for Schwarzschild ($Q/M = 0$). Here the main results are quoted, and special attention is then drawn to Reissner-Nordström with a focus on the inner horizon.

The frequency ω measured in the frame of an observer ($\equiv \omega_{\mathrm{ob}}$) or emitter ($\equiv \omega_{\mathrm{em}}$) with specific energy E, normalized to the frequency ω_∞ seen at rest at infinity, is

$$\frac{\omega}{\omega_\infty} = \frac{E \pm \sqrt{E^2 - \Delta}}{\Delta}, \tag{4.31}$$

where the upper (lower) sign applies to outgoing (ingoing) null rays. The effective temperature κ_{eff}

can then be calculated with the help of the chain rule:

$$
\begin{aligned}
\kappa_{\text{eff}} &= -\frac{d}{d\tau_{\text{ob}}} \ln\left(\frac{\omega_{\text{ob}}}{\omega_{\text{em}}}\right) \\
&= -\omega_{\text{ob}}\left(\frac{\dot{r}_{\text{ob}}}{\omega_{\text{ob}}}\frac{\partial \ln\omega_{\text{ob}}}{\partial r_{\text{ob}}} - \frac{\dot{r}_{\text{em}}}{\omega_{\text{em}}}\frac{\partial \ln\omega_{\text{em}}}{\partial r_{\text{em}}}\right) \\
&= \mp\frac{1}{2}\frac{\omega_{\text{ob}}}{\omega_{\infty}}\left(\frac{d\Delta_{\text{ob}}}{dr_{\text{ob}}} - \frac{d\Delta_{\text{em}}}{dr_{\text{em}}}\right),
\end{aligned}
\tag{4.32}
$$

where an overdot signifies differentiation with respect to the observer's or emitter's proper time τ.

For outgoing modes (upper sign), the Unruh emitter must be placed at the event horizon $(r_{\text{em}} \to r_+)$, and for ingoing modes (lower sign), the Unruh emitter resides at infinity $(r_{\text{em}} \to \infty)$. The result, for an observer in free fall from rest at infinity $(E_{\text{ob}} = 1)$, is the sensation of two independent effective temperatures corresponding to the outgoing (κ_{eff}^+) and ingoing (κ_{eff}^-) Hawking modes (throughout the rest of this paper, $\pm$ superscripts will always refer to outgoing/ingoing quantities, while $\pm$ subscripts will always refer to outer/inner horizon quantities):

$$
\kappa_{\text{eff}}^+ = \frac{Mr_{\text{ob}}\left(1 - r_{\text{ob}}^2/r_+^2\right) - Q^2\left(1 - r_{\text{ob}}^3/r_+^3\right)}{r_{\text{ob}}^2\left(-r_{\text{ob}} + \sqrt{2Mr_{\text{ob}} - Q^2}\right)},
\tag{4.33a}
$$

$$
\kappa_{\text{eff}}^- = \frac{Mr_{\text{ob}} - Q^2}{r_{\text{ob}}^2\left(r_{\text{ob}} + \sqrt{2Mr_{\text{ob}} - Q^2}\right)}.
\tag{4.33b}
$$

The rest of this Sec. 4.3.1 will be devoted to exploring the implications of Eqs. (4.33). As a first comment, because of the square root in the denominator, both temperatures become imaginary when the observer is located close enough to the origin, specifically when $r_{\text{ob}} < Q^2/(2M)$. However, such values of r_{ob} are strictly less than the inner horizon radius r_- for all choices of Q, and the failure of Eqs. (4.33) in this region coincides with the failure of Gullstrand-Painlevé coordinates in the same region, indicative of the presence of an unphysical negative interior mass $M(r)$ (i.e., this is where an infaller would bounce back due to the effects of the repulsive charged singularity on the spacetime) [88]. Since the region below the inner horizon should be physically disregarded due to the semiclassical singular behavior examined below, that region will not be explored any further here.

Second, it should be noted that for an observer asymptotically far from the black hole, the above formulas reproduce familiar results: the outgoing sector's temperature asymptotically approaches the black hole's surface gravity κ_+ defined by Eq. (4.10), and the ingoing Hawking sector vanishes:

$$\lim_{r_{\mathrm{ob}}\to\infty} \{\kappa_{\mathrm{eff}}^+,\ \kappa_{\mathrm{eff}}^-\} = \left\{ \frac{r_+ - r_-}{2r_+^2},\ 0 \right\}. \tag{4.34}$$

As expected, κ_{eff}^+ approaches $1/(4M)$ in the Schwarzschild $Q/M = 0$ limit and vanishes in the extremal $Q/M = 1$ limit. These limits can be seen in the respective panels of Fig. 4.2, which shows the full behavior of $\kappa_{\mathrm{eff}}^+(r_{\mathrm{ob}})$ and $\kappa_{\mathrm{eff}}^-(r_{\mathrm{ob}})$ for different choices of the black hole's charge-to-mass ratio.

4.3.1.1   Negative $\kappa_{\mathbf{eff}}$ at the event horizon and beyond

As an observer freely falling from infinity approaches the Reissner-Nordström event horizon and enters the black hole, the effective Hawking temperatures κ_{eff}^+ and κ_{eff}^- grow from their initial values at infinity until reaching a maximum value, after which they quickly drop to zero and become negative (excepting the special cases $Q/M = 0, 1$). When the observer crosses the event horizon, the effective temperatures in the outgoing and ingoing sectors are

$$\lim_{r_{\mathrm{ob}}\to r_+} \{\kappa_{\mathrm{eff}}^+,\ \kappa_{\mathrm{eff}}^-\} = \left\{ \frac{2\left(r_+ - 2r_-\right)}{r_+(r_+ - r_-)},\ \frac{r_+ - r_-}{4r_+^2} \right\}. \tag{4.35}$$

The most notable feature of Fig. 4.2 is the fact that κ_{eff}^+ and κ_{eff}^- become negative (indicated by the dashed lines) if the observer is close enough to the inner horizon, corresponding to a blueshifting of the observed modes instead of the usual exponential redshifting. The exact regions with negative temperature depend heavily on the charge Q, generally extending farther outward with increasing charge. The ingoing radiation (the blue curve) has negative temperature only below the event horizon, coinciding exactly with the change in sign of the Weyl scalar at $r = Q^2/M$, but curiously enough, the outgoing radiation (red) can have negative temperature even above the event horizon, and in the extremal case, the effective temperature in the entire exterior is negative. How large a charge is
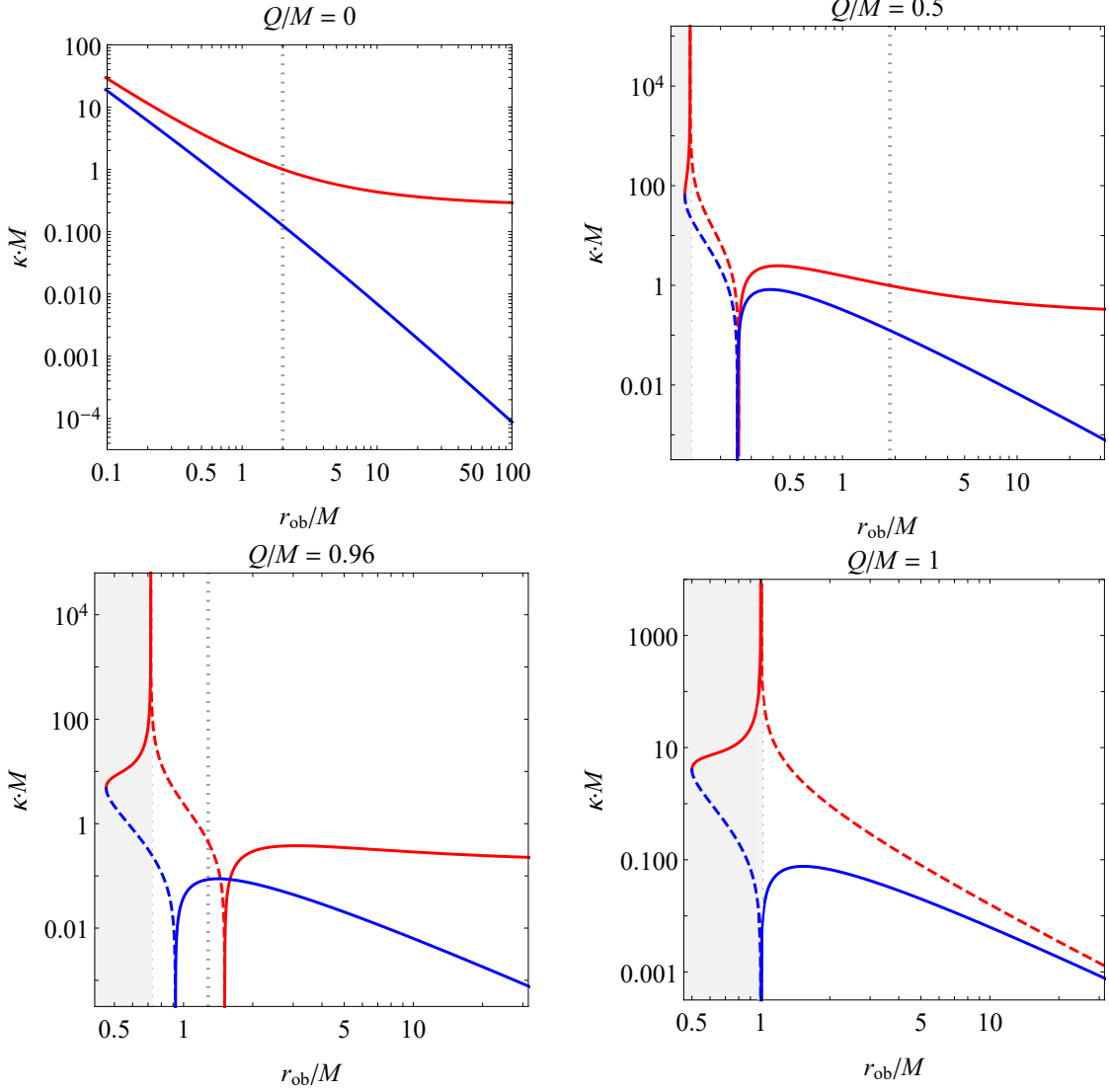
Figure 4.2: Outgoing effective temperature $\kappa_{\mathrm{eff}}^{+}$ (red curve) and ingoing effective temperature $\kappa_{\mathrm{eff}}^{-}$ (blue curve) as a function of observer radius r_{ob} for various choices of the Reissner-Nordström black hole charge Q, all in units of the black hole mass M. Solid curves indicate positive values on the log plot, and dashed curves indicate negative values. The inner and outer horizons are shown with gray, dotted vertical lines, and the unphysical region below the inner horizon is grayed out.

necessary for a negative temperature to be detected outside the black hole? From Eq. (4.35), $\kappa_{\mathrm{eff}}^{+}$ will be negative above the event horizon if the event horizon is less than double the inner horizon's radius, which occurs when $(Q/M)^2 > 8/9$. This special value of Q is shown in Fig. 4.3 with a red dot marking the intersection of the solid red and dotted black curves.

The value $(Q/M)^2 = 8/9$, where the event horizon coincides with the radial inflection point in
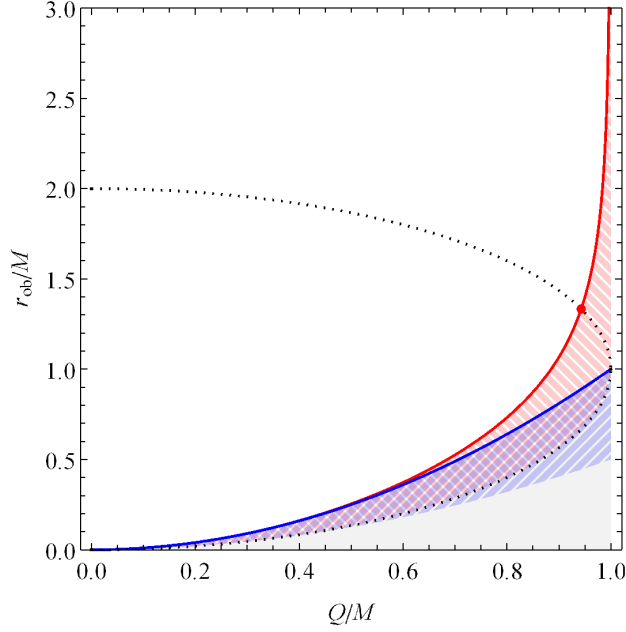
Figure 4.3: Regions of negative effective temperature in the Reissner-Nordström charge-radius parameter space. The black dotted curve shows the inner and outer horizons, which converge in the extremal limit $Q/M = 1$. The red (blue) curve shows regions where the effective temperature in the outgoing sector κ_{eff}^+ (ingoing sector κ_{eff}^-) equals zero, and the red (blue) hatched shading shows regions where the effective temperature κ_{eff}^+ (κ_{eff}^-) is negative. The red dot marks the charge $Q/M = \sqrt{8/9}$ above which the effective temperature κ_{eff}^+ becomes negative outside the event horizon. As in Fig. 4.2, the unphysical region below the inner horizon is shaded out gray.

the black hole's horizon function Δ, has shown up previously in the literature for Reissner-Nordström black holes in varying contexts. Ong and Good [136] used a heuristic gravitational analog of the Schwinger effect to show that the energy of two Hawking quanta split apart from tidal forces will be negative near the horizon when $(Q/M)^2 > 8/9$. This change in sign can be traced to the change in the radial tidal force, as measured by the proper acceleration of the free-fall-frame geodesic deviation vector, from the usual stretching force into a compressing force as Q is increased [45]. Similarly, the square of the free-fall temperature obtained by embedding the black hole in a six-dimensional flat spacetime and finding the Unruh temperature of the analogous observer was found to be negative for $(Q/M)^2 > 8/9$ [33], which those authors interpreted as a failure to detect any radiation. Finally, in the 1+1D case, the renormalized expectation values of the temporal and radial components of a scalar field's stress-energy tensor $\langle T_\mu{}^\nu \rangle$ become negative at the event horizon in the exact same

range [117]. These studies apply to a variety of different semiclassical effects that all point toward similar semiclassical behavior, but in the present case, the physical interpretation of a negative effective temperature κ_{eff} is not so clear-cut, especially given the lack of adiabaticity in some regions of interest (described in Sec. 4.3.1.4). A more robust physical interpretation is therefore deferred until the spectral analysis of Sec. 4.5.

4.3.1.2   Diverging κ_{eff} at the inner horizon

Now, consider the effective temperature seen when the observer reaches the inner horizon. As can be seen from Figs. 4.2 and 4.3, both the outgoing and ingoing effective temperatures κ_{eff}^+ and κ_{eff}^- are always nonpositive at the inner horizon.[4] The effective temperature κ_{eff}^- for the ingoing sector remains finite for all nonzero values of Q, but the outgoing temperature κ_{eff}^+ always diverges at the inner horizon. Defining a new coordinate $z_{\text{ob}} \equiv (r_{\text{ob}} - r_-)/(r_+ - r_-)$ representing the observer's dimensionless distance above the inner horizon, in the limit of small $z_{\text{ob}} \ll 1$, one has (to leading order in z_{ob}):

$$\lim_{\substack{z_{\text{ob}} \to 0, \\ E_{\text{ob}} \to 1}} \{\kappa_{\text{eff}}^+, \ \kappa_{\text{eff}}^-\} = \left\{ -\frac{r_+^2 + r_-^2}{r_+^2(r_+ - r_-)z_{\text{ob}}}, \ -\frac{r_+ - r_-}{4r_-^2} \right\}. \tag{4.36}$$

From Eq. (4.36), one can see that the perceived temperature from outgoing radiation at the inner horizon (when the observer looks straight down at the past horizon) quickly approaches negative infinity, while the practically irrelevant perceived temperature from ingoing radiation (when the observer looks up at the sky above) equals half the inner horizon's surface gravity κ_- of Eq. (4.10).

Note that the above analysis applies only to an ingoing observer, who must pass through the left leg of the inner horizon (labeled $\mathcal{H}_{r_-}^-$ in Fig. 4.13). In order to reach the right leg of the inner horizon, an infalling observer must accelerate outward until they acquire negative energy as measured by another observer at infinity. For an observer with specific energy $E_{\text{ob}} = -1$ (who can exist only inside the event horizon, where the Killing time coordinate t is spacelike), the only change

---

[4]Here values of $\kappa_{\text{eff}} \to \pm\infty$ are treated as equivalent to maintain consistency with the standard entropic definition of temperature, where both coincide with zero inverse thermodynamic temperature β.

to Eqs. (4.33) that is needed is to swap their denominators. With this change, the resulting effective temperatures for an outgoing observer at the inner horizon are

$$\lim_{\substack{z_{\text{ob}} \to 0, \\ E_{\text{ob}} \to -1}} \{\kappa_{\text{eff}}^+, \ \kappa_{\text{eff}}^-\} = \left\{ -\frac{r_+ - r_-}{4r_-^2}\left(1 - \frac{r_+ - r_-}{r_+^2}\right), \ -\frac{1}{(r_+ - r_-)z_{\text{ob}}} \right\}. \tag{4.37}$$

Both effective temperatures are still negative. The main change to be noticed when traveling through the right portion of the inner horizon instead of the left portion is that the ingoing effective temperature κ_{eff}^- seen from the sky above diverges instead of the outgoing temperature seen from the past horizon below. This divergence of κ_{eff}^- is consistent with the inner horizon blueshift divergence first noted by Penrose [152]. In contrast, the outgoing effective temperature κ_{eff}^+ remains finite for large Q, vanishing as $Q/M \to 1$, though as $Q/M \to 0$, κ_{eff}^+ diverges (just as κ_{eff}^- does in the case of an ingoing observer at the inner horizon).

One final special case is an observer with zero energy, who passes through the intersection of the left and right legs of the inner horizon (the uppermost point in Fig. 4.13). At this special location, the ingoing and outgoing effective temperatures both diverge:

$$\lim_{\substack{z_{\text{ob}} \to 0, \\ E_{\text{ob}} \to 0}} \{\kappa_{\text{eff}}^+, \ \kappa_{\text{eff}}^-\} = \left\{ -\frac{r_+^2 + r_-^2}{2r_+^2 r_- \sqrt{z_{\text{ob}}}}, \ -\frac{1}{2r_- \sqrt{z_{\text{ob}}}} \right\}. \tag{4.38}$$

Thus, no matter what portion of the inner horizon the observer reaches, at least one of the Hawking sectors will always feature a divergent, negative temperature.

Divergent semiclassical behavior at the Reissner-Nordström inner horizon is already well anticipated in the literature. As early as 1980, it was argued that the renormalized expectation value of the stress-energy tensor in regular coordinates must diverge on at least one of the two legs of the inner horizon [95]. More recently, the renormalized stress-energy tensor in the Unruh state was computed explicitly at the inner horizon, and it was found generically to diverge [180]. There are a few differences between that study's results and the results found here; namely, the sign of $\langle T_{uu} \rangle_{\text{ren}}^U$ and $\langle T_{vv} \rangle_{\text{ren}}^U$ at the inner horizon can be either positive or negative depending on the charge Q (as

opposed to the purely negative $\kappa_{\mathrm{eff}}^{\pm}$ found here), and those stress-energy tensor fluxes both vanish in the extremal limit (while only $\kappa_{\mathrm{eff}}^{+}$ vanishes as $Q/M \to 1$ for outgoing observers) [181]. However, the effective temperature and the renormalized stress-energy tensor should not be expected to agree, since the former describes the perception by an infaller of a spectral distribution while the latter describes the tensorial flux and energy density of that radiation—a perceptual formulation of $\langle T_{\mu\nu} \rangle$ would depend not only on κ_{eff} but also on $\dot{\kappa}_{\mathrm{eff}}$ [17].

4.3.1.3   Dependence of κ_{eff} on the observer's energy

Finally, consider how the effective temperatures $\kappa_{\mathrm{eff}}^{\pm}$ given by Eq. (4.32) change for arbitrary observer energies. Can an observer eliminate the detection of Hawking radiation, or perhaps even change its sign, simply by Lorentz-boosting to a different frame?

The only contribution to the effective temperatures of Eq. (4.32) that depends on the observer's specific energy E_{ob} is the factor ω_{ob}, the observer-frame frequency. Thus, any Lorentz-boosting effects on the effective temperature seen by a radial observer are solely confined to those caused by a Doppler factor shift. This shift will never change the sign of $\kappa_{\mathrm{eff}}^{\pm}$ for an observer at a given radius; it will only change the overall magnitude. In particular, as the observer speeds up, in the limit $E_{\mathrm{ob}} \gg 1$ (or $E_{\mathrm{ob}} \ll -1$), the magnitude of $\kappa_{\mathrm{eff}}^{+}$ (or $\kappa_{\mathrm{eff}}^{-}$, respectively) will increase linearly with E_{ob}. Similarly, in the limit $E_{\mathrm{ob}} \ll -1$ (or $E_{\mathrm{ob}} \gg 1$), the magnitude of $\kappa_{\mathrm{eff}}^{+}$ (or $\kappa_{\mathrm{eff}}^{-}$, respectively) will drop reciprocally to zero. Between these two limits, $\kappa_{\mathrm{eff}}^{\pm}$ varies monotonically with E_{ob}, so even if an interior observer's energy passes through zero, $\kappa_{\mathrm{eff}}^{\pm}$ will always remain the same sign.

The change in sign in the radial effective temperature for an inertial observer is thus purely geometrical in origin. As an observer changes their energy (or even their viewing direction in a given patch of sky, as shall be seen in Sec. 4.4), they can never fully eliminate the presence of Hawking radiation, and the effective temperature will always change sign once they have entered into a region of the spacetime geometry where their local surface gravity (governed by radial gradient of the black hole's horizon function Δ, Eq. (4.10)) exceeds that of the Unruh emitter (or vice versa). This radiation in the radial direction can thus be regarded as "real" in the sense that it behaves in the

same Lorentz-covariant way as any classical radiation detected by a free-faller would.

4.3.1.4 Adiabaticity

As mentioned in Sec. 3.2, the identification of the effective temperature κ_{eff} with a thermal Hawking flux is strictly only valid in conjunction with the adiabatic condition, that κ_{eff} must remain approximately constant over enough e-folds of the arriving modes [20, 21]. This condition is quantified by the adiabatic control function ϵ, which for radial modes in a static, spherically symmetric black hole can be written as

$$\epsilon(r_{\mathrm{ob}}) \equiv \left| \frac{\dot{\kappa}_{\mathrm{eff}}}{\kappa_{\mathrm{eff}}^2} \right| = \left| \frac{\dot{r}_{\mathrm{ob}}}{\kappa_{\mathrm{eff}}^2} \frac{d\kappa_{\mathrm{eff}}}{dr_{\mathrm{ob}}} \right|. \tag{4.39}$$

Whenever $\epsilon \ll 1$, the adiabatic condition is satisfied and a thermal Hawking spectrum is perceived by the observer.

The exact analytic form of $\epsilon(r_{\mathrm{ob}})$ for the Reissner-Nordström free-faller in the Unruh state is not too illuminating; nonetheless, several key features can be identified. As $r_{\mathrm{ob}} \to \infty$, the adiabatic control function for the outgoing modes drops to zero (as anticipated to recover Hawking's original thermal calculation), except in the extremal case where κ_{eff} itself is already zero and ϵ therefore diverges. Similar diverging behavior in ϵ is observed whenever the effective temperature κ_{eff} vanishes, as a result of the κ_{eff}^2 term in the denominator of Eq. (4.39), since it is meaningless to define a thermal flux at zero temperature.

Based on the above observations, one might expect that ϵ would drop to zero whenever κ_{eff} diverges (e.g. when one observes outgoing modes at the inner horizon). However, the adiabatic control function at the inner horizon instead passes through a finite, nonzero value, which nonetheless is still usually smaller than unity for outgoing modes. Specifically, for an ingoing observer,

$$\lim_{r_{\mathrm{ob}} \to r_-} \{\epsilon^+,\ \epsilon^-\} = \left\{ \frac{r_+^2}{2(2M^2 - Q^2)},\ \frac{5Q^2 + 4M\sqrt{M^2 - Q^2} - 3M^2}{M^2 - Q^2} \right\}. \tag{4.40}$$

This equality technically only holds when $Q \neq 0$; in the Schwarzschild case, instead of approaching unity, both ϵ^+ and ϵ^- will asymptotically approach 3 (see the left panel of Fig. 4.4). But for $Q > 0$,
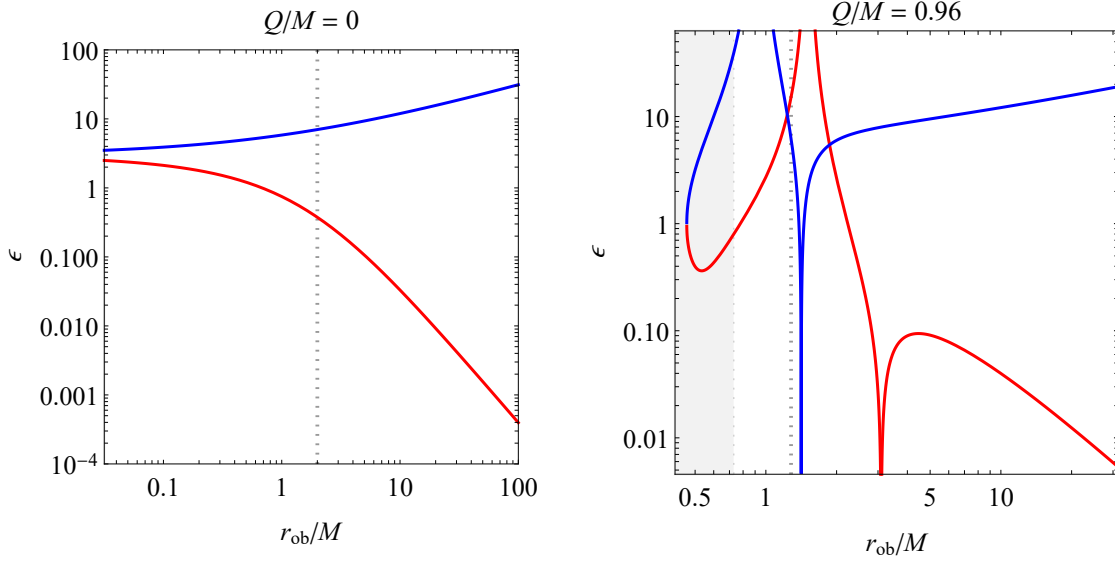
Figure 4.4: Outgoing and ingoing adiabatic control functions ϵ^+ (red curve) and ϵ^- (blue curve), respectively, as a function of an ingoing observer's position r_{ob} for two choices of the Reissner-Nordström black hole charge Q, in units of the black hole mass M. As in Fig. 4.2, the inner and outer horizons are shown with gray, dotted vertical lines, and the unphysical region below the inner horizon is grayed out.

the value of ϵ^+ at the inner horizon is always less than 1, and ϵ^- is always greater than 1. For large enough charge Q, Eq. (4.40) thus implies that the outgoing temperature should be approximately thermal for an ingoing observer close enough to the inner horizon. This behavior holds even (and especially) for $Q/M = 1$, where the inflating negative temperature just above the merged horizons occurs in the black hole's exterior.

For reference, the behavior of $\epsilon^+(r_{\mathrm{ob}})$ and $\epsilon^-(r_{\mathrm{ob}})$ are plotted in Fig. 4.4 for two of the same values of Q used in Fig. 4.2. One may observe that for many choices of r_{ob}, κ_{eff} behaves adiabatically and the thermal results fall into place. However, for much of the observer's trajectory, ϵ far exceeds unity, and deeper analysis is required, as examined in Sec. 4.5.

One final technical point related to the discussion of adiabaticity is the comment made by the authors of Ref. [20] that the effective temperature adiabaticity formalism described above is valid "under mild technical assumptions." These assumptions are related to the more generalized, precise

form of the adiabaticity condition, which assumes the existence of a finite quantity

$$D \equiv \sup_{n>0} \left[\frac{1}{(n+1)!} \frac{|\kappa_{\text{eff}}^{(n)}|}{\kappa_{\text{eff}}^{n+1}} \right]^{1/(n+1)} \tag{4.41}$$

such that adiabaticity is implied by the condition $2D^2 \ll 1$ (instead of $\epsilon \ll 1$). Usually, the $n = 1$ term in the definition of Eq. (4.41) dominates so that the quantity $2D^2$ is equivalent to the adiabatic control function ϵ of Eq. (4.39). But in certain special cases, such as the dip observed in the blue curve in the right panel of Fig. 4.4 as ϵ^- goes to zero just above the outer horizon, higher-n terms in Eq. (4.41) dominate. As a result, adiabaticity is not satisfied there, even though $\dot{\kappa}_{\text{eff}}^-$ (and therefore ϵ^-) vanishes.

4.3.1.5 Inner-extremal regular black holes

To close this Sec. 4.3.1 on κ_{eff} in spherically symmetric black holes, consider how the above results might be generalized beyond the Reissner-Nordström spacetime. In order to circumvent the mass inflation problem, a number of regular black hole solutions have been recently developed that possess an inner horizon with zero surface gravity, first in the spherical case [38] and subsequently in the rotating case [67]. For a static, spherically symmetric black hole with line element of Eq. (4.1), the horizon function $\Delta(r)$ contains zeros at the locations of the horizons (at $r = r_+$ for the outer horizon and $r = r_-$ for the inner horizon) and asymptotes to unity as $r \to \infty$ (assuming the spacetime is asymptotically flat). The (generalized) surface gravity κ at any radius r in this spacetime is defined by

$$\kappa(r) \equiv \frac{1}{2} \frac{d\Delta}{dr}, \tag{4.42}$$

so in order for κ to vanish at the inner horizon, the horizon function must contain a degenerate root at that horizon. Such a condition is satisfied for extremal black holes, where the inner horizon coincides with the outer horizon ($r_+ = r_-$), but if one wishes to keep the outer horizon sufficiently separated from any exotic quantum gravitational physics modifying the inner horizon (and indeed, neither have extremal black holes been observed in nature nor should be they theoretically possible

by the third law of black hole thermodynamics), the next-simplest choice for the horizon function is a triple root at r_-:

$$\Delta(r) = \frac{(r - r_+)(r - r_-)^3}{F(r)}, \tag{4.43}$$

where

$$F(r) \equiv (r - r_+)(r - r_-)^3 + 2Mr^3 + (a_2 - 3r_-(r_+ + r_-)) r^2$$

[38]. Here M is the mass of the black hole and a_2 is a real parameter that must satisfy

$$a_2 \gtrsim \frac{9}{4} r_+ r_- \tag{4.44}$$

in order for the horizon function to contain no poles along the real axis. The authors of Ref. [38] additionally assume that r_+ lies in the vicinity of $2M$, while r_- lies in the vicinity of 0. With these choices, one thus has an "inner-extremal" regular black hole that behaves approximately like Schwarzschild outside the outer horizon but contains a regular de Sitter core within, fine-tuned so that $\kappa(r_-) = 0$. In particular, near $r = 0$, the spacetime possesses a cosmological constant

$$\Lambda = 3 \; \frac{a_2 - 3r_-(r_+ + r_-)}{r_+ r_-^3}, \tag{4.45}$$

while all remaining stress-energy contributions to the spacetime curvature vanish.

As mentioned in Sec. 4.2, for outgoing modes (upper sign), the Unruh emitter must be placed at the outer horizon ($r_{\text{em}} \to r_+$), and for ingoing modes (lower sign), the Unruh emitter resides at infinity ($r_{\text{em}} \to \infty$). The result is the sensation of two independent effective temperatures corresponding to the outgoing (κ_{eff}^+) and ingoing (κ_{eff}^-) Hawking modes originating from the past horizon below and the sky above the observer, respectively. These effective temperatures for an inertial observer at radius r looking in a radial direction take on the following forms, consisting of a Doppler factor

multiplied by an observer-dependent surface gravity and a state-dependent surface gravity:

$$\kappa_{\text{eff}}^+(r) = \frac{-E - \sqrt{E^2 - \Delta(r)}}{\Delta(r)} \left(\kappa(r) - \kappa(r_+)\right), \tag{4.46a}$$

$$\kappa_{\text{eff}}^-(r) = \frac{E - \sqrt{E^2 - \Delta(r)}}{\Delta(r)} \kappa(r), \tag{4.46b}$$

where $\kappa(r)$ is the generalized surface gravity defined by Eq. (4.42).

For an observer at rest far away from the black hole, if the spacetime is asymptotically flat, the outgoing effective temperature κ_{eff}^+ of Eq. (4.46a) approaches $\kappa(r_+)$, while the ingoing effective temperature κ_{eff}^- of Eq. (4.46b) vanishes, as predicted by Hawking. But for an observer near one of the black hole's horizons, Eqs. (4.46) warrant closer examination.

First, consider the effective temperatures seen at the outer horizon r_+. An observer crossing the event horizon must have $E > 0$, so that in the limit $\Delta \to 0$, the outgoing and ingoing effective temperatures simplify to

$$\lim_{r \to r_+} \kappa_{\text{eff}}^+(r) = -\frac{E \kappa'(r_+)}{\kappa(r_+)}, \tag{4.47a}$$

$$\lim_{r \to r_+} \kappa_{\text{eff}}^-(r) = \frac{\kappa(r_+)}{2E}, \tag{4.47b}$$

where a prime denotes differentiation with respect to r. Eq. (4.47a) makes the same assumption as Ref. [38] that the surface gravity $\kappa(r_+)$ of the spherical inner-extremal regular black hole's outer horizon is non-zero; if on the contrary the outer horizon is degenerate, the outgoing effective temperature κ_{eff}^+ will depend heavily on the choice of how limits are taken: if the collapse occurred far enough into the past that the Unruh emitter's position can be treated as fixed at r_+, the outgoing effective temperature κ_{eff}^+ will diverge as a power law when the outer horizon is degenerate, but once the observer reaches and passes below r_+, the effective temperature will instantaneously drop to zero.

While the outer horizon's ingoing effective temperature seen from the sky above is always positive, the sign of the outer horizon's outgoing effective temperature originating from the past horizon below depends on the radial gradient of the outer horizon's surface gravity. Assuming $\kappa(r_+)$

takes on a positive, non-zero value, if the horizon function is concave down at the outer horizon, $\Delta''(r_+) < 0$, then the effective temperature from the horizon will be positive just like that of the sky. But if $\Delta''(r_+) > 0$, as occurs for Reissner-Nordström black holes with a charge-to-mass ratio $Q/M > \sqrt{8/9}$ and for the inner-extremal regular black holes of Eq. (4.43) with sufficiently large a_2, the outgoing effective temperature will become negative. As mentioned in Sec. 4.3.1.1, such a sign change coincides with the change in sign of the radial tidal force at the outer horizon from geodesic deviation [45] and is a commonly found semiclassical feature (see, e.g., Ref. [127] and sources therein).

At the inner horizon, the effective temperatures depend strongly on the sign of the observer's energy—note that ingoing $(E > 0)$ and outgoing $(E < 0)$ observers passing through the inner horizon will enter into causally separated sectors of the spacetime. For an ingoing, positive-energy observer passing through the left leg of the inner horizon,

$$\lim_{r \to r_-, \ E>0} \kappa_{\text{eff}}^+(r) = \frac{E \, n!}{(r-r_-)^n} \left(\frac{\kappa(r_+) - \kappa(r_-)}{\kappa^{(n-1)}(r_-)} \right) + \mathcal{O}\left(\frac{1}{(r-r_-)^{n-1}} \right), \tag{4.48a}$$

$$\lim_{r \to r_-, \ E>0} \kappa_{\text{eff}}^-(r) = \frac{\kappa(r_-)}{2E}, \tag{4.48b}$$

where n denotes the lowest non-zero order of the Taylor expansion for the horizon function $\Delta(r)$ about the inner horizon; if $\Delta(r)$ can be expanded close to a horizon $r_\pm$ as

$$\Delta(r) \approx \Delta'(r_\pm)(r-r_\pm) + \frac{1}{2}\Delta''(r_\pm)(r-r_\pm)^2 + \frac{1}{6}\Delta^{(3)}(r_\pm)(r-r_\pm)^3 + ..., \tag{4.49}$$

then, e.g., the Reissner-Nordström inner horizon corresponds to $n = 1$, while the horizon function of Eq. (4.43) corresponds to $n = 3$, since for that inner-extremal regular black hole, the first derivative $\Delta'(r_-) = 0$, the second derivative $\Delta''(r_-) = 0$, but the third derivative

$$\Delta^{(3)}(r_-) = -\frac{6(r_+ - r_-)}{2Mr_-^3 + (a_2 - 3r_-(r_+ + r_-))\, r_-^2}. \tag{4.50}$$

Conversely, an outgoing, negative-energy observer passing through the right leg of the inner

horizon has

$$\lim_{r \to r_-, \; E<0} \kappa_{\text{eff}}^+(r) = \frac{\kappa(r_+) - \kappa(r_-)}{2E}, \tag{4.51a}$$

$$\lim_{r \to r_-, \; E<0} \kappa_{\text{eff}}^-(r) = \frac{E \, n}{r - r_-} + \mathcal{O}\left((r - r_-)^0\right). \tag{4.51b}$$

Finally, in the special case $E = 0$, where the observer passes through the central intersection of the ingoing and outgoing portions of the inner horizon, κ_{eff}^+ always diverges, while κ_{eff}^- vanishes when $n > 2$, remains finite when $n = 2$, and diverges when $n = 1$.

The conclusion of the above asymptotic forms of the inner horizon effective temperatures is that at least one component of κ_{eff} will always diverge for any choice of inertial observer at the inner horizon. This occurs even when the inner horizon's surface gravity $\kappa(r_-)$ vanishes—the divergence is a direct result of the Penrose blueshift singularity (the divergence of $\omega_{\text{ob}}/\omega_{\text{em}}$ for an outgoing observer watching ingoing modes while crossing a horizon with $\Delta \to 0$), which does not depend on the surface gravity. For an inertial observer falling in from infinity, even if they reach an inner horizon with zero surface gravity, they will still encounter diverging semiclassical radiation because the surface gravity of the *outer horizon* (which governs the exponential peeling of modes from the initial collapse and can be regarded in some sense as the "source" of Hawking radiation) is non-zero.

The semiclassical instability of the inner horizon is thus seen to be an even stronger effect than the classical mass inflation instability, since the effective temperature in the Unruh vacuum from quantum radiation at the inner horizon depends not only on the inner horizon's surface gravity, but also on the outer horizon's surface gravity. Even if $\kappa(r_-)$ vanishes, a non-zero $\kappa(r_+)$ will prevent an ingoing observer's effective temperature from vanishing at the inner horizon; instead, the observer's modes will become ultraviolet-divergent. The only feasible way to prevent such a divergence for an ingoing observer is to require $\kappa(r_-) = \kappa(r_+)$, and a quick parity check shows that this can only occur if both surface gravities are identically zero.

4.3.2 Rotating black holes

In the case of rotating black holes, it was noted in Sec. 4.2 that a constant-phase constraint would be necessary for general Kerr observers sweeping across a family of horizon-limit emitters. This constraint will be utilized in the following Sec. 4.4, but for now, consider the special cases where an observer is able to stare at a single emitter throughout their entire free-fall descent. Such privileged frames give rise to feasible analytic calculations of the effective temperature, and while they are usually non-inertial and require an observer to accelerate radially or azimuthally, two exceptional cases will be considered here: on-axis observers free-falling along the $\theta = 0$ pole, and "horizostationary" observers orbiting the black hole at the same angular speed as the event horizon.

4.3.2.1 On-axis observers

Geodesics along the rotational axis of a Kerr black hole, where $\theta = 0$ and $\dot{\theta} = 0$, must have constants of motion $L = 0$ and $K = a^2$, leading to the geodesic equations

$$\dot{t} = \frac{R^2}{\Delta} E, \tag{4.52a}$$

$$\dot{r}^2 = E^2 - \frac{\Delta}{R^2}\left(\frac{r^2\delta + a^2}{R^2}\right), \tag{4.52b}$$

$$\dot{\theta}^2 = 0, \tag{4.52c}$$

$$\dot{\varphi} = \left(\frac{1}{\Delta} - \frac{1}{R^2}\right)aE, \tag{4.52d}$$

with the same notation as in Eqs. (4.14). A null particle traveling outward ($+$) or inward ($-$) along this axis will be detected by a freely falling observer ($i =$"ob") or emitter ($i =$"em") with frequency

$$\omega_i = -k^\mu \dot{x}_\mu = \frac{R^2}{\Delta}\left(E \pm \sqrt{\left(E^2 - \frac{\Delta}{R^2}\right)\left(1 - \frac{a^2\Delta}{R^4}\right)}\right), \tag{4.53}$$

normalized to the frequency seen by someone at rest asymptotically far away. This frequency is independent of the rate $\dot{\varphi}$ at which the infaller is rotating with the geometry as they make their

descent.

A freely falling observer on the symmetry axis will then detect two independent effective temperatures: if they look directly downward into the pole of the black hole they will see outgoing Hawking modes redshifting from an emitter near the past horizon, and if they look directly upward into the sky they will see ingoing Hawking modes redshifting from an emitter near past null infinity. The calculation of these effective temperatures then proceeds from an application of the chain rule to Eq. (3.33):

$$\kappa_{\text{eff}}^{\pm} = -\omega_{\text{ob}} \left(\frac{\dot{r}_{\text{ob}}}{\omega_{\text{ob}}} \frac{d \ln \omega_{\text{ob}}}{dr_{\text{ob}}} - \frac{\dot{r}_{\text{em}}}{\omega_{\text{em}}} \frac{d \ln \omega_{\text{em}}}{dr_{\text{em}}} \right), \tag{4.54}$$

which makes use of the relation

$$\frac{d\tau_{\text{em}}}{d\tau_{\text{ob}}} = \frac{\omega_{\text{ob}}}{\omega_{\text{em}}}. \tag{4.55}$$

An intermediate result is

$$\frac{d \ln \omega_i}{dr} = \frac{\frac{2r}{R^2} \left(1 - 2\omega_i E + \frac{a^2 \Delta}{R^4} \right) - \frac{\Delta'}{\Delta} \left(1 - 2\omega_i E + \frac{a^2 E^2}{R^2} \right)}{2 \left(1 - \omega_i E + \frac{a^2}{R^2} \left(E^2 - \frac{\Delta}{R^2} \right) \right)}, \tag{4.56}$$

where a prime denotes differentiation with respect to the Boyer-Lindquist radial coordinate r.

The effective temperature's dependence on the observer's position r and energy E can then be calculated with the help of Eq. (4.56). The part of Eq. (4.54) that depends on the emitter reduces to

$$\lim_{r_{\text{em}} \to \infty} \frac{\dot{r}_{\text{em}}}{\omega_{\text{em}}} \frac{d \ln \omega_{\text{em}}}{dr_{\text{em}}} = 0 \tag{4.57}$$

for ingoing modes originating from an Unruh emitter asymptotically far from the black hole (i.e., an observer looking straight up at the sky, measuring an effective temperature κ_{eff}^{-}), while it reduces to

$$\lim_{r_{\text{em}} \to r_{+}} \frac{\dot{r}_{\text{em}}}{\omega_{\text{em}}} \frac{d \ln \omega_{\text{em}}}{dr_{\text{em}}} = \kappa_{+} \tag{4.58}$$

for outgoing modes originating from an Unruh emitter asymptotically close to the past horizon (i.e.,
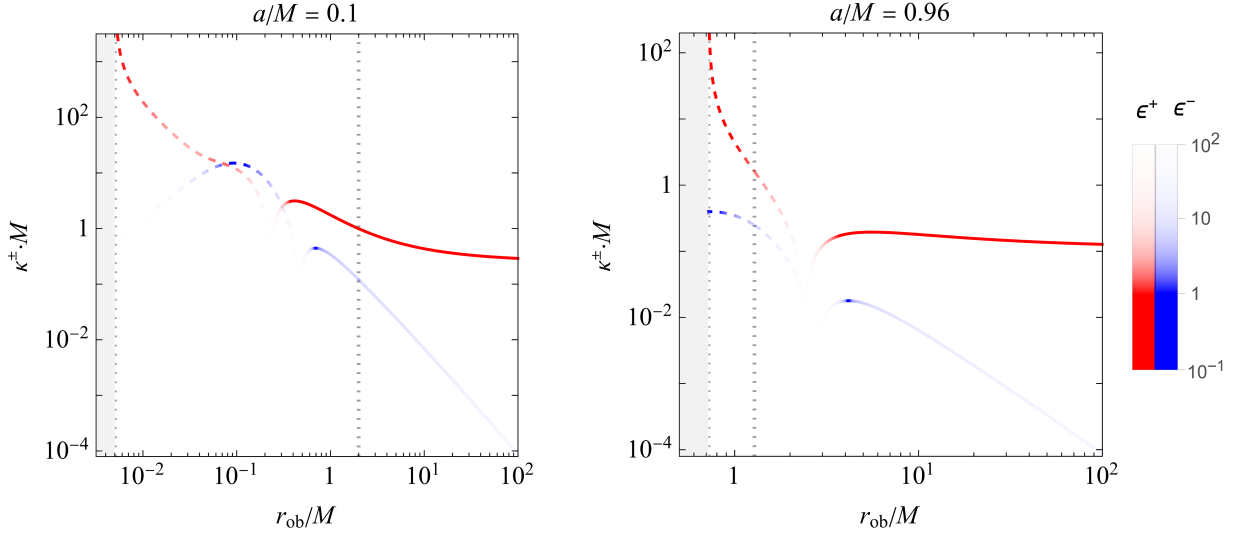
Figure 4.5: Effective Hawking temperatures $\kappa^{\pm}_{\text{eff}}$ seen by an observer freely falling along the Kerr $\theta = 0$ rotational axis looking directly inward (κ^{+}_{eff}, red curve) or outward (κ^{-}_{eff}, blue curve) at different radii r_{ob}, for two choices of the Kerr black hole spin parameter a, all in units of the black hole mass M. Solid curves indicate positive values on the log plot, and dashed curves indicate negative values. Lighter colors indicate higher values of the adiabatic control function $\epsilon^{\pm}$, which imply less confidence in the validity of the geometric optics approximation. The inner and outer horizons are shown with gray, dotted vertical lines, and the unphysical region below the inner horizon is grayed out. When the observer is asymptotically far away, the effective Hawking temperature κ^{+}_{eff} approaches a constant equal to the surface gravity, but as the observer reaches the inner horizon, the effective temperature becomes negative and diverges.

an observer looking straight down at the black hole, measuring an effective temperature κ^{+}_{eff}).

For an infalling observer with unit energy ($E = 1$) descending along the rotational axis, the effective temperatures seen above and below are shown in Fig. 4.5 for a slowly spinning black hole ($a/M = 0.1$) and a near-extremal one ($a/M = 0.96$). Some analytic limits are worth mentioning

explicitly:

$$\kappa_{\text{eff}}^+ = \begin{cases} \kappa_+, & r_{\text{ob}} \to \infty \\[2ex] \dfrac{8r_+ R_+^2 - a^2 \Delta'(r_+)}{2R_+^4} - \dfrac{2}{\Delta'(r_+)}, & r_{\text{ob}} \to r_+ , \\[2ex] -\dfrac{R_+^2 + R_-^2}{R_+^2} \dfrac{1}{r - r_-} + \mathcal{O}(1), & r_{\text{ob}} \to r_- \end{cases} \tag{4.59a}$$

$$\kappa_{\text{eff}}^- = \begin{cases} 0, & r_{\text{ob}} \to \infty \\[2ex] \dfrac{\kappa_\pm r_\pm^4 - 4a^2 r_\pm}{2R_\pm^2 (r_\pm^2 + 2a^2)}, & r_{\text{ob}} \to r_\pm \end{cases} . \tag{4.59b}$$

From Eqs. (4.59), one can see that an on-axis infaller looking downward will see a Hawking temperature proportional to the surface gravity κ_+ from Eq. (4.17) when they are asymptotically far away, as expected. However, this effective temperature will change as they approach the black hole—as they cross the event horizon, the effective temperature will generally increase by a factor of two or so, depending on the black hole's spin a (in accordance with assertion #1 in Sec. 4.1). But just as was seen for an electrically charged black hole in Sec. 4.3.1, an event horizon-crossing observer will see a negative temperature $\kappa_{\text{eff}}^+(r_+) < 0$ when the black hole is close enough to extremality (in accordance with assertion #4 in Sec. 4.1). In the Reissner-Nordström case, a radial free-faller will see a negative temperature outside the event horizon when $Q/M > \sqrt{8/9} \sim 0.943$, but in the Kerr case, an on-axis free-faller will see a negative temperature outside the event horizon when $a/M \gtrsim 0.860$.[5] This limiting value is similar but not equal to the spin $a/M = \sqrt{3}/2$ at which tidal forces change sign for an on-axis observer crossing the Kerr event horizon [116]. However, there is no reason *a priori* why the tidal forces and effective temperatures should agree (though they do in the Reissner-Nordström case)—the tidal forces are calculated from the locally measured Riemann curvature tensor and the geodesic deviation equation, which uses a different expansion order compared to the eikonal Eq. (3.28) used to calculate the effective temperature.

---

[5]From Eq. (4.59), the exact value of $(a/M)^2 \equiv \alpha$ corresponding to $\kappa_{\text{eff}}^+(r_+) = 0$ is the positive root of the polynomial $\alpha^3 + 38\alpha^2 - 7\alpha - 16$.

Once the on-axis infaller dips below the event horizon, the effective temperature κ_{eff}^+ decreases until, as shown in Eq. (4.59) and Fig. 4.5, the effective temperature diverges to negative infinity (in accordance with assertion #2 in Sec. 4.1). Such a divergence will always occur at the inner horizon of a stationary, rotating black hole in the Unruh state, as will be shown explicitly in Sec. 4.3.2.3. Even if the observer turns around inside the black hole and acquires $E < 0$, the outgoing temperature κ_{eff}^+ will become finite, but the ingoing temperature κ_{eff}^- will then diverge to negative infinity. The inner horizon is thus the surface beyond which the semiclassical approximation can absolutely no longer be trusted.

4.3.2.2   Horizostationary observers

The second class of privileged observers to be analyzed are those observers who orbit the black hole with the same angular velocity as an infaller at the event horizon. Much like a satellite in a geostationary orbit above Earth, these "horizostationary" observers will hover above the same spot on the event horizon as the black hole rotates, so that they can track the same null ray originating from an Unruh emitter as they travel along their own worldline.

Focusing on a stationary observer orbiting a Kerr black hole in the equatorial plane ($\theta = 90°$), it is known that such an observer will only be freely falling (4-acceleration $D\dot{x}^\mu/d\tau = 0$) if their angular velocity is [164]

$$\Omega \equiv \frac{d\varphi}{dt} = \frac{\sqrt{M}}{a\sqrt{M} \pm r^{3/2}}.$$ (4.60)

Geodesic horizostationary observers can thus exist only at a single spin-dependent radius, found by matching Eq. (4.60) with the angular velocity of an Unruh emitter at the event horizon, which can be found from Eqs. (4.14) to equal

$$\Omega_+ \equiv \frac{a}{R_+^2}.$$ (4.61)

While observers can orbit with this angular velocity at any radius above the event horizon, most will

be forced to accelerate radially unless they are at the radius

$$r_{\mathrm{HO}} = \left(\frac{r_+^4 M}{a^2}\right)^{1/3}.$$ (4.62)

This radius tends to infinity in the Schwarzschild $a = 0$ limit and to the event horizon in the extremal $a = M$ limit.

A horizostationary observer at radius r_{HO} in the equatorial plane will have geodesic equations of motion

$$\dot{t} = \frac{1}{r^2}\left(\frac{R^2 P_r}{\Delta} + aP_\theta\right),$$ (4.63a)

$$\dot{r}^2 = 0,$$ (4.63b)

$$\dot{\theta}^2 = 0,$$ (4.63c)

$$\dot{\varphi} = \frac{1}{r^2}\left(\frac{aP_r}{\Delta} + P_\theta\right),$$ (4.63d)

where the constants P_r and P_θ, defined by Eqs. (4.15) evaluated at $r = r_{\mathrm{HO}}$ and $\theta = 90°$, are fixed by the constraints $\Omega_+ = \dot{\varphi}/\dot{t}$ and $P_r^2 = (P_\theta^2 + r^2)\Delta$.

Since the horizostationary observer only moves along the Kerr metric's Killing fields ∂_t and ∂_φ, the frequency ω_{ob} of an outgoing null geodesic seen by the observer will not change with the observer's proper time τ_{ob}. Thus, from Eq. (3.33), the only dynamic contribution to the outgoing effective temperature κ_{eff}^+ will be from the freely falling emitter at the event horizon:

$$\kappa_{\mathrm{eff}}^+ = \frac{\omega_{\mathrm{ob}}}{\omega_{\mathrm{em}}} \frac{d\ln\omega_{\mathrm{em}}}{d\tau_{\mathrm{em}}}.$$ (4.64)

The frequency ω_{em} of an outgoing equatorial null particle with dimensionless orbital parameters $\mathcal{L}/\mathcal{E}$ and $\mathcal{K}/\mathcal{E}^2 = (a - \mathcal{L}/\mathcal{E})^2$, measured in the frame of an infalling equatorial emitter with constants

of motion E, L, and $K = (aE - L)^2$, is

$$\omega_{\text{em}} = \frac{1}{\Delta}\left(R^2 E - \mathcal{L}L + \frac{2}{r}(aE - L)(a - \mathcal{L}) + \sqrt{\left(R^2 - \mathcal{L}^2 + \frac{2}{r}(a - \mathcal{L})^2\right)\left(\frac{P_r^2}{r^2} - \left(1 + \frac{P_\theta^2}{r^2}\right)\Delta\right)}\right), \quad (4.65)$$

where the photon energy $\mathcal{E}$ is set to unity without loss of generality. Even though this frequency ω_{em} depends on the emitter's orbital parameters via E, L, P_r, and P_θ, the effective temperature κ_{eff}^+ will be independent of the emitter's motion once the emitter is taken to be asymptotically close to the event horizon, as argued in Sec. 4.2. If the Unruh emitter sends a null particle along the outgoing principal null congruence $(\mathcal{L}/\mathcal{E} = a)$, the frequency ω_{ob} seen by the observer simplifies to

$$\omega_{\text{ob}} = \dot{t} - a\,\dot{\varphi} = \frac{P_r(r_{\text{HO}})}{\Delta(r_{\text{HO}})}, \quad (4.66)$$

and the effective temperature of Eq. (4.64) becomes

$$\kappa_{\text{eff}}^+ = \omega_{\text{ob}}\frac{\Delta'(r_+)}{2r_+^2}. \quad (4.67)$$

The outgoing effective temperature seen by a horizostationary observer looking in the principal null direction, given by Eq. (4.67), depends only on the black hole's spin-to-mass ratio a/M, varying monotonically from $\kappa_{\text{eff}}^+ = 1/(4M)$ when $a = 0$ to $\kappa_{\text{eff}}^+ = \sqrt{3}/M$ when $a = M$.

Because the effective temperature given by Eq. (4.67) does not change with the observer's proper time, the adiabatic control function ϵ^+ is identically zero, so one may be assured that in the geometric optics (high frequency) limit, an inertial observer orbiting at a radius r_{HO} will see a Planckian blackbody spectrum of Hawking radiation originating from the direction of the black hole's past horizon.

The horizostationary observer may also look in a variety of other directions along the equatorial plane, by changing the photon angular momentum $\mathcal{L}$ in Eq. (4.65), to yield a straightforward change in the effective temperature (in accordance with assertion #3 in Sec. 4.1). But regardless of which direction they look along the past horizon, they will always see some non-vacuum state caused by

the exponentially redshifting Hawking modes originating from that horizon.

As a final comment, it should be noted that while the horizostationary observer has zero 4-acceleration, they will still experience a twisting force corresponding to non-Fermi-Walker transport. The only non-zero component of their 4-rotation $\mathscr{O}^\mu$ (the angular velocity of their spatial basis vectors with respect to comoving inertial gyroscopes) is the polar component [164]

$$\mathscr{O}^\theta = \frac{\dot{t}^2}{r^6} \left(M \left(1 - a\Omega_+\right) \left((3r^2 + a^2)\Omega_+ - a\right) - r^3\Omega_+ \right), \tag{4.68}$$

which is of order unity in the extremal case, falls below 0.1 in black hole mass units when $a/M \lesssim 0.9$, and vanishes as $a/M \to 0$. This rotation will in principle induce particle creation via the non-inertial Unruh effect; however, its contribution to the effective temperature calculated in Eq. (4.67) should be negligible for all black hole spins except those near enough to extremality.

4.3.2.3 Inner-extremal regular black holes

Finally, consider how the above results for Kerr black holes might be generalized in other azimuthally symmetric spacetimes, using as a case study the rotational analog of the spherical inner-extremal black holes described in Sec. 4.3.1.5. For a rotating inner-extremal regular black hole, the authors of Ref. [67] considered two modifications to the Kerr line element in Boyer-Lindquist [31] coordinates: first, a conformal factor is included so that the metric is regular at $r = 0$, and second, the radial horizon function $\Delta(r) = r^2 + a^2 - 2m(r)r$ is modified from its vacuum Kerr value $(m(r) = M)$ in order to fine-tune the inner horizon's surface gravity. The line element can be written in the same form as the standard Kerr line element [40] times a conformal factor $\Psi(r,\theta)$:

$$ds^2 = \Psi \left(\frac{1}{\Delta} dr^2 + d\theta^2 + \frac{\sin^2\theta}{\Sigma^2} \left((r^2 + a^2) \, d\varphi - a \, dt \right)^2 - \frac{\Delta}{\Sigma^2} \left(a\sin^2\theta \, d\varphi - dt \right)^2 \right), \tag{4.69}$$

where the zeros of the function

$$\Sigma(r,\theta) \equiv r^2 + a^2 \cos^2\theta \tag{4.70}$$

give the location of the Kerr ring singularity, which becomes regularized when the conformal factor

$$\Psi(r,\theta) \equiv \Sigma(r,\theta) + \frac{b}{r^{2z}} \tag{4.71}$$

contains positive, non-zero constants b and z such that $z \geq 3/2$. The horizon function $\Delta(r)$ now has dimension $[M]^2$ and in the minimal case contains a degenerate root at the inner horizon:

$$\Delta(r) = \frac{(r - r_+)(r - r_-)^3}{F(r)}, \tag{4.72}$$

where now

$$F(r) \equiv r^2 + r(2M - r_+ - 3r_-) + \frac{r_+ r_-^3}{a^2}. \tag{4.73}$$

Though the exact positions of the inner and outer horizons will not directly affect the results of the present analysis, for completion's sake, the following forms are assumed in Ref. [67] for the outer and inner horizon radii:

$$r_+ = M + \sqrt{M^2 - a^2}, \quad r_- = \frac{a^2}{M + (1 - e)\sqrt{M^2 - a^2}}, \tag{4.74}$$

such that the outer horizon radius r_+ coincides with its standard Kerr value while the inner horizon radius r_- is modified by the parameter e, which must satisfy

$$-3 - \frac{3M}{\sqrt{M^2 - a^2}} < e < 2 \tag{4.75}$$

to maintain regularity. If e is negative, the inner horizon radius will lie below its Kerr value of $M - \sqrt{M^2 - a^2}$, while if e is positive, the inner horizon radius will lie above its Kerr value.

If a test particle has Killing energy per unit mass E, Killing angular momentum along the axis of rotation per unit mass L, and Carter constant $K = Q + (aE - L)^2$ [40], its 4-velocity will take

the form

$$\dot{t} = \frac{1}{\Psi}\left(\frac{r^2 + a^2}{\Delta}P_r + aP_\theta\right), \tag{4.76a}$$

$$\dot{\varphi} = \frac{1}{\Psi}\left(\frac{aP_r}{\Delta} + \frac{P_\theta}{\sin^2\theta}\right), \tag{4.76b}$$

$$\dot{r}^2 = \frac{1}{\Psi^2}\left(P_r^2 - \left(K + \left(r^2 + \frac{b}{r^{2z}}\right)\delta\right)\Delta\right), \tag{4.76c}$$

$$\dot{\theta}^2 = \frac{1}{\Psi^2}\left(K - a^2\cos^2\theta\;\delta - \frac{P_\theta^2}{\sin^2\theta}\right) \tag{4.76d}$$

[67], where

$$P_r(r) \equiv \left(r^2 + a^2\right)E - aL, \tag{4.77a}$$

$$P_\theta(\theta) \equiv L - aE\sin^2\theta, \tag{4.77b}$$

and where $\delta = 1$ for massive particles while $\delta = 0$ for massless particles (which will be denoted with scripted constants of motion $\mathcal{E}$, $\mathcal{L}$, $\mathcal{K}$ in contrast to the massive particle's constants E, L, K).

For simplicity, consider an infalling ($\dot{r} < 0$) equatorial ($\theta = \pi/2$, $\dot{\theta} = 0$) observer, whose Carter constant must satisfy

$$K = P_\theta^2 = (L - aE)^2. \tag{4.78}$$

Additionally, as a natural generalization from the spherical case, assume the observer is looking at a photon which is purely radial in the zero angular momentum frame ($\mathcal{L}/\mathcal{E} = 0$, $\mathcal{K}/\mathcal{E}^2 = a^2$). Such a photon will be detected by the observer with a frequency normalized to the frequency $\omega_\infty = \mathcal{E}$ seen by an observer at rest at infinity, which can be written as

$$\frac{\omega}{\omega_\infty} = \frac{aP_\theta}{\Psi} + \frac{r^2 + a^2}{\Psi}\cdot\frac{P_r \pm \sqrt{\left(P_r^2 - (K + \Psi)\Delta\right)\left(1 - \frac{a^2\Delta}{(r^2 + a^2)^2}\right)}}{\Delta}, \tag{4.79}$$

where outgoing (ingoing) null geodesics are given by the upper (lower) sign.

The effective temperature of Eq. (3.33) can then be calculated with the same chain rule

expansion as in Eq. (4.32):

$$\kappa_{\text{eff}} = -\omega_{\text{ob}} \left(\frac{\dot{r}_{\text{ob}}}{\omega_{\text{ob}}} \frac{\partial \ln \omega_{\text{ob}}}{\partial r_{\text{ob}}} - \frac{\dot{r}_{\text{em}}}{\omega_{\text{em}}} \frac{\partial \ln \omega_{\text{em}}}{\partial r_{\text{em}}} \right). \tag{4.80}$$

The above form of κ_{eff} assumes that the photon's impact parameters $\mathcal{L}/\mathcal{E}$ and $\mathcal{K}/\mathcal{E}^2$ remain constant as the observer moves along their trajectory, which may induce additional non-inertial radiative effects as the observer rotates their field of view, as first discussed in Ref. [87]. However, the presence or absence of such effects will not significantly change the asymptotic behavior of κ_{eff} as the observer approaches a horizon; nor will the particular choice of the (inertial) observer's conserved angular parameters L and K. A more exhaustive analysis of all these effects will be presented in Sec. 4.4.2. For the present study, assume a freely falling zero angular momentum observer (ZAMO), with constants of motion $L = 0$, $K = a^2$, and $E = 1$ or -1 (ingoing or outgoing, respectively).

A useful intermediate result with the above simplifications (suppressing factors of ω_∞) is

$$\frac{\partial \ln \omega}{\partial r} = \frac{\omega \mp 1/2}{\omega \mp 1} \left(\left(\frac{4r}{r^2 + a^2} - \frac{\Delta'}{\Delta} \right) \left(1 - \frac{a^2 \Delta}{(r^2 + a^2)^2} \right)^{-1} - \frac{\Psi'}{\Psi} \right), \tag{4.81}$$

where primes denote differentiation with respect to r and the upper (lower) sign applies to an ingoing (outgoing) observer with positive (negative) energy E.

Just as in the spherical case, the Hawking modes contributing to the effective temperature can be divided into two sectors, the ingoing modes originating from an Unruh emitter at $r_{\text{em}} \to \infty$ in the sky above the observer, and the outgoing modes originating from an Unruh emitter at $r \to r_+$ seen at the past horizon below the observer. In the ingoing case (κ_{eff}^-), the subtracted term in Eq. (4.80) (i.e. the limit of Eq. (4.81) as an emitter's position $r = r_{\text{em}}$ asymptotically tends to infinity) vanishes, just as it does for spherically symmetric black holes. In the outgoing case (κ_{eff}^+), the subtracted term in Eq. (4.80) simplifies to

$$\lim_{r_{\text{em}} \to r_+} \frac{\dot{r}_{\text{em}}}{\omega_{\text{em}}} \frac{\partial \ln \omega_{\text{em}}}{\partial r_{\text{em}}} = \kappa(r_+), \tag{4.82}$$

where $\kappa(r)$ is the black hole's generalized surface gravity analogous to Eq. (4.42), which for a rotating

black hole with Boyer-Lindquist radius r takes the form

$$\kappa(r) \equiv \frac{1}{2(r^2 + a^2)} \frac{d\Delta}{dr}. \tag{4.83}$$

Though the full expression for the effective temperature κ_{eff} for an arbitrary observer is too complicated to be presented in a meaningful way here, some useful limits can be shown. As the observer's position is taken asymptotically far from the black hole, the observer's frequency ω_{ob} tends to unity while the first term in the parentheses of Eq. (4.80) vanishes. As a result,

$$\lim_{r \to \infty} \kappa_{\text{eff}}^+(r) = \kappa(r_+), \tag{4.84a}$$

$$\lim_{r \to \infty} \kappa_{\text{eff}}^-(r) = 0; \tag{4.84b}$$

i.e., the Hawking effect is exactly reproduced for this particular choice of observer and Unruh emitter. When this observer is taken to the event horizon at $r = r_+$, assuming the outer horizon is not degenerate,

$$\lim_{r \to r_+} \kappa_{\text{eff}}^+(r) = -\frac{r_+^2 + a^2}{\Psi(r_+)} \cdot \frac{\kappa'(r_+)}{\kappa(r_+)}, \tag{4.85a}$$

$$\lim_{r \to r_+} \kappa_{\text{eff}}^-(r) = \frac{\kappa(r_+)}{2}, \tag{4.85b}$$

in exact analog to the spherical case; compare Eqs. (4.47). The conformal factor here is defined as $\Psi(r) \equiv \Psi(r, \pi/2)$ from Eq. (4.71).

The effective temperatures seen at the inner horizon then follow suit. The choice of whether an observer enters the ingoing or outgoing portion of the inner horizon depends on the sign of the Hamilton-Jacobi parameter P_r, which for a ZAMO is equivalent to the sign of the observer's energy E. For an observer with positive energy, with the horizon function Δ and quadratic function F from

Eqs. (4.72) and (4.73), respectively, the inner horizon effective temperatures are

$$\lim_{r \to r_-,\; E>0} \kappa^+_{\text{eff}}(r) = -\frac{r_-^2 + a^2}{\Psi(r_-)} \cdot \frac{F(r_-)(r_-^2 + a^2)(r_+ - r_-)^2}{F(r_+)(r_+^2 + a^2)(r - r_-)^3} + \mathcal{O}\left(\frac{1}{(r - r_-)^2}\right), \tag{4.86a}$$

$$\lim_{r \to r_-,\; E>0} \kappa^-_{\text{eff}}(r) = 0, \tag{4.86b}$$

while for an observer with negative energy, the inner horizon effective temperatures are

$$\lim_{r \to r_-,\; E<0} \kappa^+_{\text{eff}}(r) = -\frac{(r_+ - r_-)^3}{4(r_+^2 + a^2)F(r_+)}, \tag{4.87a}$$

$$\lim_{r \to r_-,\; E<0} \kappa^-_{\text{eff}}(r) = -\frac{r_-^2 + a^2}{\Psi(r_-)} \cdot \frac{3}{r - r_-} + \mathcal{O}\left((r - r_-)^0\right). \tag{4.87b}$$

Thus, an inertial, zero angular momentum observer approaching the classically stable inner horizon of a rotating regular black hole will experience a diverging, negative effective Hawking temperature in at least one direction, just as in the spherical case. If the observer is ingoing, the divergence will be seen from the past horizon below them, and if the observer is outgoing, the divergence will be seen from the sky above them.

One may wonder about the generality of these results when different choices for observers and photon trajectories are used, especially since Eq. (4.80) does not guarantee the constant phase condition that usually warrants a numerical treatment as in Refs. [87, 127]. But as it turns out, it can be proven that regardless of the choice of observer or emitter, if the effective temperature seen at the outer horizon is finite, then the effective temperature seen at the inner horizon must diverge somewhere in the observer's field of view. To see why this is the case, a sketch of the proof is given below for an ingoing observer with positive Hamilton-Jacobi parameter P_r (a similar argument can be made for an outgoing observer, *mutatis mutandi*).

The effective temperature κ_{eff} can be written in the form

$$\kappa_{\text{eff}} = -\omega_{\text{ob}}\left(\frac{\dot{\omega}_{\text{ob}}}{\omega_{\text{ob}}^2} - \frac{\dot{\omega}_{\text{em}}}{\omega_{\text{em}}^2}\right), \tag{4.88}$$

where an overdot denotes differentiation with respect to proper time; compare Eq. (4.32). The precise assumptions about the differentiation (e.g. keeping the emitter's affine distance or the observer's viewing angles on the sky fixed) can be left arbitrary. There may in general be extra terms in the parentheses of Eq. (4.88) that nontrivially couple the observer's and emitter's motions, but one may assume that such terms (e.g. ones involving derivatives of the emitted photon's impact parameters with respect to the observer's position) can always be chosen to vanish or cancel out by a suitable choice of viewing direction in the observer's sky (e.g. in the spherical case this choice is radially inwards or outwards). The remaining terms in Eq. (4.88) will then be separable in the observer's and emitter's coordinates.

For an Unruh emitter sending outgoing modes from the outer horizon to the observer, assume that the effective temperature in the direction the observer is looking will be finite when the observer reaches the outer horizon:

$$\lim_{r_{\mathrm{ob}} \to r_+} \kappa_{\mathrm{eff}} = \mathcal{O}\left(\Delta(r_{\mathrm{ob}})^0\right). \tag{4.89}$$

The key assumption one must make is that the observer's frequency ω_{ob} for outgoing modes classically diverges at either horizon when normalized to the rest frequency at infinity. At the inner horizon, such a divergence manifests as the Penrose blueshift singularity [152, 165], while at the outer horizon, the emitter's modes will be infinitely redshifted with respect to the observer. In both cases, the effect can be attributed to the fact that the observer can pass through a horizon in finite proper time while an emitter's tortoise coordinate becomes infinite, which is a feature of any black hole spacetime regardless of the surface gravities at the horizons. The divergence of ω_{ob}, governed by the timelike component of the line element, asymptotically behaves as $\Delta(r_{\mathrm{ob}})^{-1}$.

Thus, if the frequencies of Eq. (4.88) are expressed as ratios to the rest frequency at infinity, then Eqs. (4.88) and (4.89) imply that

$$\lim_{r_{\mathrm{ob}} \to r_+} \frac{\dot{\omega}_{\mathrm{ob}}}{\omega_{\mathrm{ob}}^2} = \frac{\dot{\omega}_{\mathrm{em}}}{\omega_{\mathrm{em}}^2} + \mathcal{O}\left(\Delta(r_{\mathrm{ob}})\right). \tag{4.90}$$

Now, if the observer is taken to the inner horizon, the normalized frequency ω_{ob} will still diverge

as $\Delta(r_{\mathrm{ob}})^{-1}$, and the emitter's contribution to the effective temperature will remain unchanged. Substituting the emitter's contribution to the effective temperature from Eq. (4.90) back into Eq. (4.88) then reveals that the effective temperature at the inner horizon will always diverge unless the value of $\dot{\omega}_{\mathrm{ob}}/\omega_{\mathrm{ob}}^2$ for an infalling observer at the outer horizon is the same as that of the inner horizon:

$$\lim_{r_{\mathrm{ob}} \to r_-} \kappa_{\mathrm{eff}} = -\omega_{\mathrm{ob}}(r_-) \left(\lim_{r_{\mathrm{ob}} \to r_-} \frac{\dot{\omega}_{\mathrm{ob}}}{\omega_{\mathrm{ob}}^2} - \lim_{r_{\mathrm{ob}} \to r_+} \frac{\dot{\omega}_{\mathrm{ob}}}{\omega_{\mathrm{ob}}^2} \right), \tag{4.91}$$

since $\omega_{\mathrm{ob}}(r_-)$ is of order $\Theta(\Delta(r_{\mathrm{ob}})^{-1})$. For both spherical and rotating inner-extremal regular black holes, the term $\dot{\omega}_{\mathrm{ob}}/\omega_{\mathrm{ob}}^2$ corresponds precisely to the black hole's surface gravity at each horizon, and this quantity is assumed to be non-zero at the outer horizon. As argued for the spherical case, the only way for these quantities to be equal at the outer and inner horizons is if the black hole is extremal, so that the outer horizon is degenerate and both surface gravity terms vanish. But more generally, the sign of $\dot{\omega}_{\mathrm{ob}}/\omega_{\mathrm{ob}}^2$ at the outer horizon will always be opposite to the sign of $\dot{\omega}_{\mathrm{ob}}/\omega_{\mathrm{ob}}^2$ at the inner horizon—since the observer's normalized frequency at the outer horizon diverges as $\Delta(r_{\mathrm{ob}})^{-1}$ (which is positive as the infaller approaches r_+ and, more importantly, has a positive slope), the rate of change of this frequency with respect to the observer's proper time will also be positive at the outer horizon. But at the inner horizon, $\Delta(r_{\mathrm{ob}})$ is negative and further has a negative slope, so that the rate of change of the frequency will always be negative. Thus, the only way that $\dot{\omega}_{\mathrm{ob}}/\omega_{\mathrm{ob}}^2$ will match at both the outer and inner horizons is if it identically vanishes at both hypersurfaces, which necessarily assumes that both horizons are degenerate.

4.4   Effective Hawking temperature κ_{eff} (non-radial modes)

The results of Sec. 4.3 apply to an infaller observing modes purely in the radial direction. Since the mass inflation instability involves radial focusing of all null geodesics, one may wonder whether the diverging acceleration seen by an infaller is confined to a single radial point on the sky. An observer has an entire 4π solid angle field of view to access; what will they see when not looking straight up or down?

Observers falling into a Reissner-Nordström black hole are analyzed in Sec. 4.4.1, then observers falling into a Kerr black hole are analyzed in Sec. 4.4.2.

4.4.1   Spherical black holes

The goal of this section is to provide a generalization of Eq. (4.32) to account for photons reaching the observer from any direction. The photon's 4-momentum will now include additional angular terms with the conserved quantity $\mathcal{L}/\mathcal{E} \equiv k_\vartheta/k_t$, the photon's impact parameter, which equals 0 for radial trajectories but in general can take any real value up to infinity (in what follows, the photon energy $\mathcal{E}$ will be taken to unity without loss of generality). To translate $\mathcal{L}$ into a viewing angle on the observer's sky, it suffices to define a single parameter χ that measures the angle in the observer's local tetrad frame between the radial direction and the direction the observer is facing. This viewing angle χ ranges from 0 degrees (facing radially inward toward the past horizon) to 180 degrees (facing radially outward toward the sky above, at past null infinity). For an observer with specific energy $E_{\rm ob}$ at radius $r_{\rm ob}$, the impact parameter $\mathcal{L}$ is related to the viewing angle χ by [87]

$$\mathcal{L} = \left| \frac{r_{\rm ob} \sin \chi}{E_{\rm ob} - \sqrt{E_{\rm ob}^2 - \Delta(r_{\rm ob})} \cos \chi} \right|. \tag{4.92}$$

The frequency ω measured in the frame of an observer ($\equiv \omega_{\rm ob}$) or emitter ($\equiv \omega_{\rm em}$) with specific energy E, normalized to the frequency ω_∞ seen at rest at infinity, then generalizes to

$$\frac{\omega}{\omega_\infty} = \frac{E \pm \sqrt{(E^2 - \Delta)(1 - \mathcal{L}^2 \Delta/r^2)}}{\Delta}, \tag{4.93}$$

where, as in the radial case, the upper (lower) sign applies to outgoing (ingoing) null rays. The calculation of $\kappa_{\rm eff}$ then follows as in the radial case, though great care must be taken to account for turnaround radii and ensure the correct sign for different viewing angles and observer positions.

Since the perception of particle production is highly dependent on the choice of observer, one must take care to make an appropriate choice depending on the context of the calculation.

For example, an observer staring in a fixed direction χ as they fall inward is not the same as an observer staring at a single infalling emitter, whose position will constantly change in the observer's field of view. As argued in Ref. [87], the choice of observer that will introduce the least amount of noninertial radiative effects (e.g. from the rotation of the observer's frame) and will reveal the most "pure" Hawking radiation is an observer staring in a fixed direction χ. Such an observer will see a family of infalling emitters as they fall inward, with each emitter connected to the observer by a null path with the same phase.

If an observer stares at the sky above (corresponding to the ingoing Hawking sector, with a family of Unruh emitters at $r_{\rm em} \to \infty$), the generalization of Eq. (4.32) to account for the frequency of Eq. (4.93) seen from any viewing angle χ is sufficient to satisfy the requirement from the previous paragraph of an inertial observer with fixed χ. However, if the observer stares at the past horizon below them (corresponding to the outgoing Hawking sector, with a family of Unruh emitters at $r_{\rm em} \to r_+$), the frequency seen by the emitter or the observer will diverge, as will the affine distance of the null geodesics connecting the two infallers. In order to ensure that the observer is seeing the same emitted in-modes as they follow along a geodesic staring in a fixed direction χ, the emitted affine distance

$$\lambda_{\rm em} \equiv \omega_{\rm em} \lambda = \omega_{\rm em} \int_{r_{\rm em}}^{r_{\rm ob}} \frac{dr}{k^r} \tag{4.94}$$

(where $k^r \equiv dr/d\lambda$ is the radial component of photon's coordinate-frame 4-momentum, given by Eq. (80) of Ref. [87]) must be held constant. The resulting effective temperature then takes the form:

$$
\begin{aligned}
\kappa_{\rm eff} &= -\frac{\partial}{\partial \tau_{\rm ob}} \ln\left(\frac{\omega_{\rm ob}\lambda}{\lambda_{\rm em}}\right)\bigg|_{\chi,\lambda_{\rm em}} \\
&= -\dot{r}_{\rm ob}\left(\frac{\partial \ln \omega_{\rm ob}}{\partial r_{\rm ob}}\bigg|_{\chi} + \frac{\partial \ln \lambda}{\partial r_{\rm ob}}\bigg|_{\chi}\right) - \dot{r}_{\rm em}\frac{\omega_{\rm ob}}{\omega_{\rm em}}\frac{\partial \ln \lambda}{\partial r_{\rm em}}\bigg|_{\chi},
\end{aligned}
\tag{4.95}
$$

where the derivatives of the affine distance (at constant χ) can be expanded with the Leibniz integral

rule:

$$\left.\frac{\partial \ln \lambda}{\partial r_{\rm ob}}\right|_{\chi} = \frac{1}{\lambda}\left(\frac{1}{k_{\rm ob}^r} + \left.\frac{\partial \mathcal{L}}{\partial r_{\rm ob}}\right|_{\chi}\int_{r_{\rm em}}^{r_{\rm ob}}dr\frac{\partial}{\partial \mathcal{L}}\frac{1}{k^r}\right), \tag{4.96a}$$

$$\left.\frac{\partial \ln \lambda}{\partial r_{\rm em}}\right|_{\chi} = -\frac{1}{\lambda k_{\rm em}^r}. \tag{4.96b}$$

The numerical solution to Eq. (4.95) for various values of $r_{\rm ob}$ and Q is shown in Fig. 4.6. These plots show similar trends to that found in Ref. [87] for Schwarzschild black holes. First, the outgoing Hawking radiation seen from the past horizon (left two panels) is actually weakest in the radial direction (except when the observer is very close to the inner horizon). As χ increases from $0°$ and the observer looks farther away from the center of the black hole's shadow marking where the past horizon would be, $\kappa_{\rm eff}^+$ increases until it diverges at the edge of the shadow.[6] As the observer falls closer and closer to the inner horizon, the area of sky across which Hawking radiation is visible becomes larger (in conjunction with the growing apparent size of the black hole's shadow), and the Hawking radiation becomes more and more isotropic across the surface of the shadow. But once the observer falls close enough to the inner horizon, the apparent black hole size begins to decrease as the Hawking area shrinks to a small patch of sky ahead of the observer (this effect is most apparent in the lower left panel of Fig. 4.6, but even in the upper left panel, additional curves for smaller radii $r_{\rm ob}$ would begin to shrink since the maximum angle χ shifts down to $0°$ as $r \to r_-$).

When the black hole's charge Q is nonzero, the main effect on the outgoing effective temperature at arbitrary viewing angle is the same result found throughout Sec. 4.3; namely, an observer close enough to the inner horizon will see a negative $\kappa_{\rm eff}^+$, corresponding to modes that are exponentially blueshifting instead of redshifting. The higher the charge Q, the farther out in physical space this blueshifting zone becomes, until it extends beyond the outer horizon and reaches infinity in the extremal case (as already seen in the radial case of Fig. 4.3).

---

[6]This divergence is an artifact of the unphysical metric used; for an astrophysical black hole formed by gravitational collapse a finite time in the past, the Hawking radiation would still exponentially limb brighten but would remain finite before dropping to zero outside of the black hole's shadow [87].
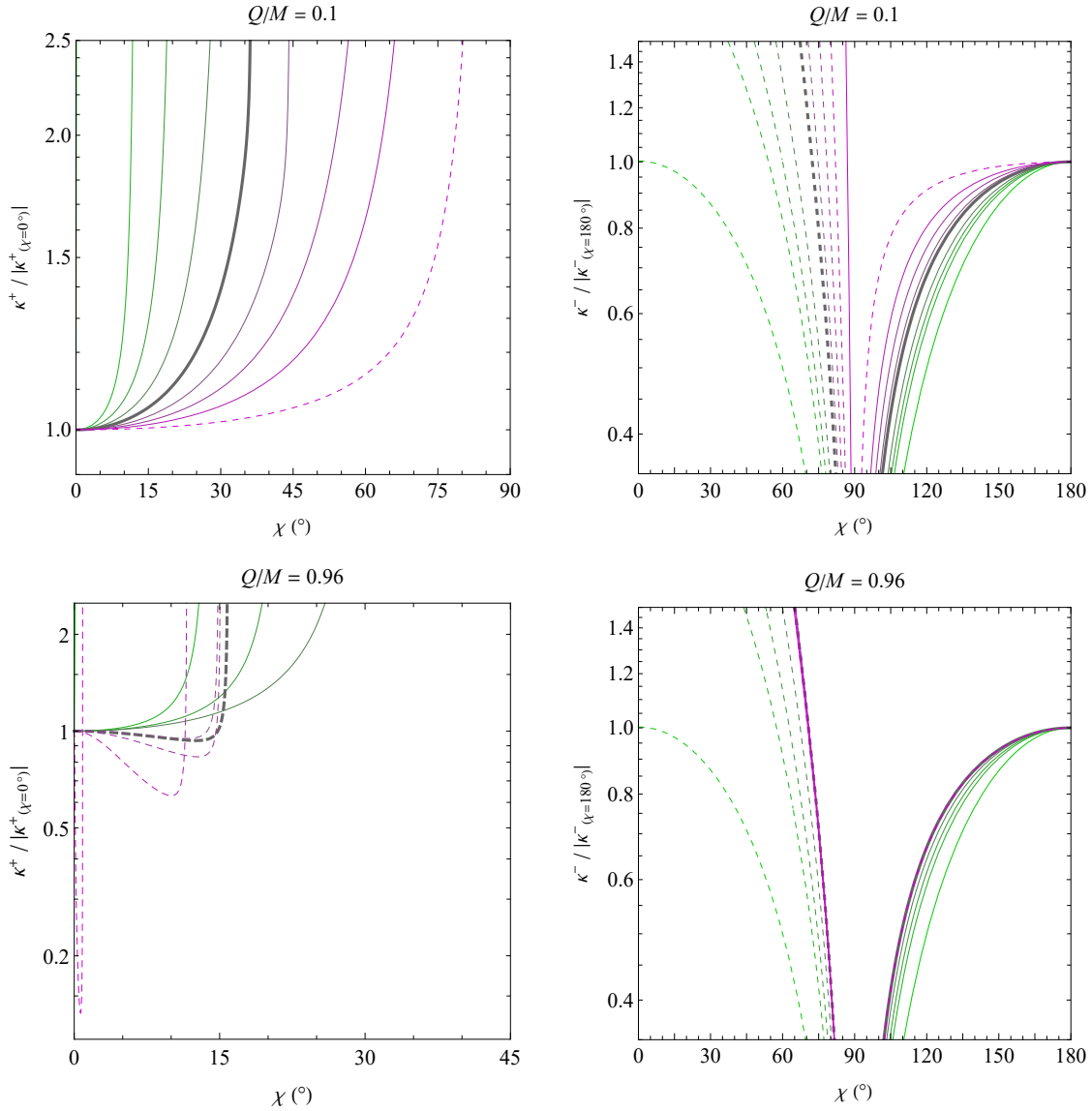
Figure 4.6: Effective temperatures κ^+_{eff} (left two panels) and κ^-_{eff} (right two panels) seen by a radial, inertial, nonrotating observer falling from infinity to the left leg of the inner horizon, as a function of the observer's viewing angle χ on the sky. Curves from green to magenta indicate radiation observed at radii $r_{\text{ob}} \to \infty$, $8r_+$, $4r_+$, $2r_+$, r_+ (thick line), $r_- + 0.5(r_+ - r_-)$, $r_- + 0.25(r_+ - r_-)$, $r_- + 10^{-1}(r_+ - r_-)$, and $r_- + 10^{-3}(r_+ - r_-)$. All curves are normalized so that the magnitude of κ^+_{eff} or κ^-_{eff} for a given radius when looking, respectively, straight down ($\chi = 0°$) or up ($\chi = 180°$), is 1. Solid curves indicate positive values on the log plot, and dashed curves indicate negative values.

Similarly, ingoing Hawking radiation seen from an observer looking up at the sky above (right two panels of Fig. 4.6) reproduces the same behavior found in Ref. [87] for the Schwarzschild case, with minimal modifications when Q is nonzero. The rate of redshifting in the upper hemisphere is

strongest when the observer looks straight up to the sky (in the outward radial direction, $\chi = 180°$), and κ_{eff}^- changes sign at $90°$, reflecting the fact that the infaller is accelerating away from the sky above (so that the upper hemisphere is redshifting) and accelerating toward the black hole below (so that the lower hemisphere is blueshifting).

However, as with the outgoing effective temperature, the ingoing effective temperature changes sign once the observer falls close enough to the inner horizon (seen, e.g., with the dashed pink line at $r_{\text{ob}} = r_- + 10^{-3}(r_+ - r_-)$ on the right half of the top right panel of Fig. 4.6), so that the upper hemisphere is blueshifting and the lower hemisphere is redshifting. But unlike the outgoing radiation, the sign change in the ingoing effective temperature is restricted only to infallers within the event horizon, regardless of the value of Q.

Aside from the sign reversal in every direction for observers close enough to the inner horizon, the main contribution that an addition of charge has on the angular distribution of Hawking radiation (for both κ_{eff}^+ and κ_{eff}^-) is to smooth out the perceived temperature gradients across the sky—the higher the charge Q, the less sharp the temperature cutoff is at the black hole shadow's boundaries, and therefore the less isotropic the temperature is across the observer's field of view for a given distance above the inner horizon.

4.4.1.1   Dependence on the observer's energy

The dependence of the ingoing and outgoing effective temperatures κ_{eff}^- and κ_{eff}^+ on the observer's specific energy E_{ob} is shown in the upper two plots of Fig. 4.7. These plots only show one choice of black hole charge ($Q/M = 0.1$) and observer position ($r_{\text{ob}}/M = 1$) so that the relevant qualitative trends can be observed.

As a check on the consistency of the upper two plots in Fig. 4.7, one can find that the presence or absence of different constant-χ curves at different observer energies exactly matches the position of the black hole silhouette in the observer's field of view. For example, for a black hole with $Q/M = 0.1$, an observer at $r_{\text{ob}}/M = 1$ with $E_{\text{ob}} = 1$ will see the past horizon below them (the black hole's "shadow") spanning from $\chi = 0°$ to its border at approximately $\chi \approx 53.2°$, and in both upper
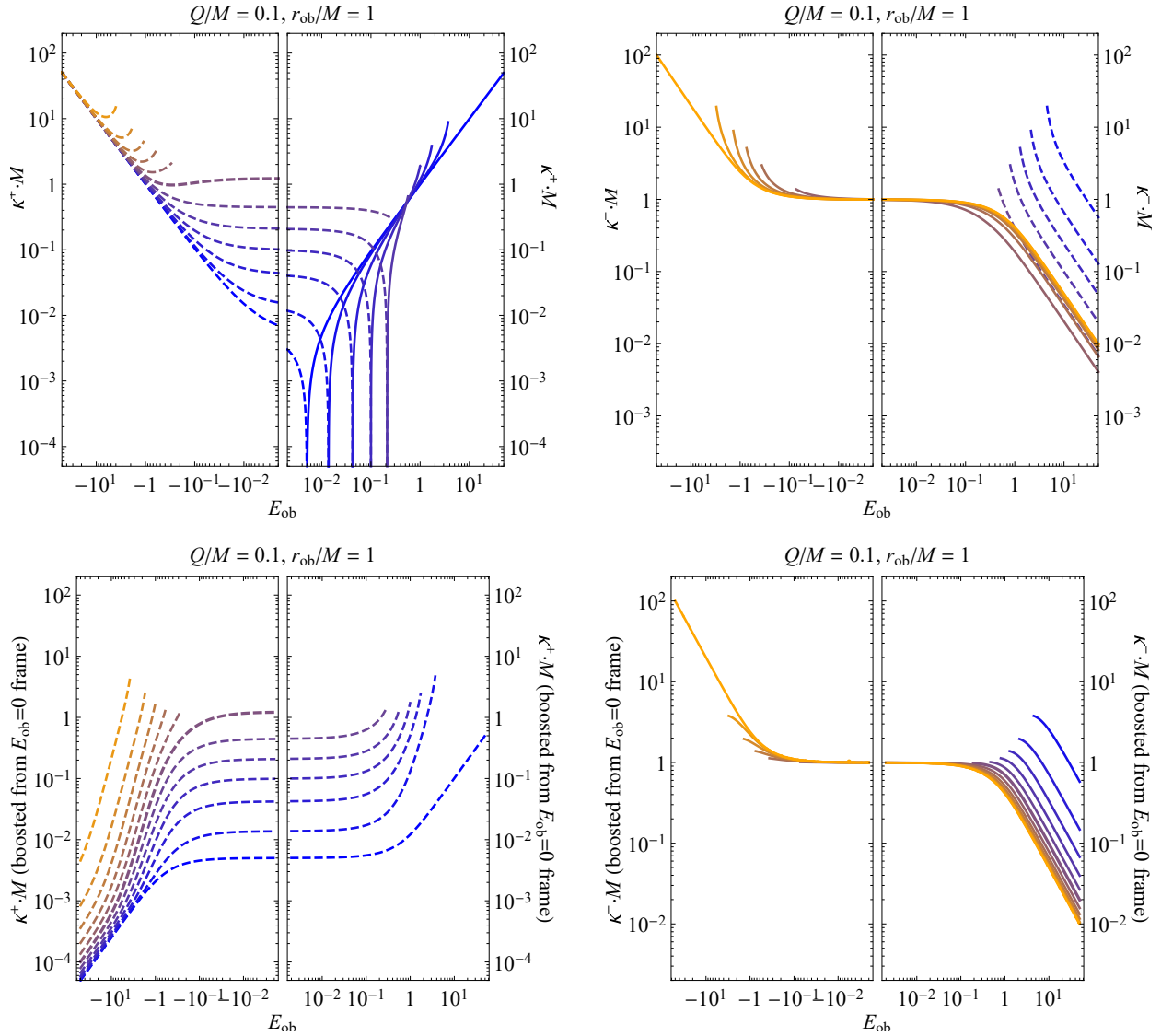
Figure 4.7: Effective temperatures κ_{eff}^+ (left plots) and κ_{eff}^- (right plots) in units of M^{-1} as a function of the observer's specific energy E_{ob}, for various choices of the observer's viewing direction χ, with intervals of 15° from $\chi = 0°$ (blue) to $\chi = 180°$ (orange) (note that the left plots contain no $\chi = 180°$ curves and the right plots contain no $\chi = 0°$ curves). Solid curves indicate positive values and dashed curves indicate negative values. The black hole's charge-to-mass ratio is $Q/M = 0.1$, and the radiation is seen from an observer halfway between the inner and outer horizons, at $r_{\mathrm{ob}}/M = 1$. The upper two plots show the effective temperatures calculated from Eq. (4.95) directly as a function of E_{ob}, while the lower two plots calculate the effective temperatures only for $E_{\mathrm{ob}} = 0$ and infer the effective temperatures at other observer energies by Lorentz-boosting to the appropriate frame.

plots at $E_{\mathrm{ob}} = 1$, the radiation κ_{eff}^- from the sky exists only for $\chi > 53.2°$ while the radiation κ_{eff}^+ from the horizon exists only for $\chi < 53.2°$. This holds true for all observer energies—as an observer is

Lorentz-boosted to $E_{\mathrm{ob}} \to \infty$, the past horizon shrinks to a single point below them, and as they are boosted in the other direction ($E_{\mathrm{ob}} \to -\infty$), the sky shrinks to a single point above them.

The lower two plots of Fig. 4.7 give a further check on the consistency of the formalism and help to show the degree to which the effective temperatures satisfy Lorentz covariance. As the observer's energy E_{ob} changes, the observer is effectively Lorentz-boosting to a different frame, even though no restriction was imposed *a priori* for the effective temperature to transform under the Lorentz group. As a test, the lower two plots of Fig. 4.7 start with the same calculations of $\kappa_{\mathrm{eff}}^{+}$ and $\kappa_{\mathrm{eff}}^{-}$ at $E_{\mathrm{ob}} = 0$, but instead of varying E_{ob} in Eq. (4.95) to find the effective temperature at other observer energies, a Lorentz boost is applied to the observer and matched to the different energies. When beginning in the $E_{\mathrm{ob}} = 0$ frame, an interior observer boosted to a frame where they have energy E_{ob}' will possess the Lorentz factor

$$\gamma = \sqrt{\frac{E_{\mathrm{ob}}'^{2} - \Delta}{\Delta}}. \tag{4.97}$$

Such a boost will entail two important effects. First, the effective temperature will be Doppler-shifted by the frequency factor ω_{ob} from Eq. (4.93), normalized to the frequency seen in the $E_{\mathrm{ob}} = 0$ frame. And second, the observer's field of view will experience relativistic aberration, such that photons arriving at an angle χ for the $E_{\mathrm{ob}} = 0$ observer will be shifted to the angle

$$\chi' = \cos^{-1}\left(\frac{\cos\chi + \beta}{1 + \beta\cos\chi}\right) \tag{4.98}$$

in the boosted frame (where $\beta = \sqrt{1 - \gamma^{-2}}$ is the observer's speed). If the Hawking radiation seen by the observer behaved purely classically and in a Lorentz-covariant fashion, the upper two plots of Fig. 4.7 would exactly match their lower counterparts.

As anticipated by the radial case (see Sec. 4.3.1.3), the Hawking radiation seen from the sky above ($\kappa_{\mathrm{eff}}^{-}$, upper right plot in Fig. 4.7) in every direction varies reciprocally with E_{ob} as the observer's energy asymptotically increases and varies approximately linearly as $E_{\mathrm{ob}} \to -\infty$. Such

a behavior is similar to what is expected for a Lorentz-boosted observer as in the lower right plot of Fig. 4.7. And just as in the radial case, changing the observer's specific energy E_{ob} for fixed χ will never change the sign of κ_{eff}^-. The ingoing effective temperature is always zero when $\chi = 90°$, always positive (with this specific choice of observer halfway between the outer and inner horizons) for larger χ, and always negative for smaller χ. Such a delineation can be noticed in the upper right plot of Fig. 4.7 from the fact that the $\chi < 90°$ curves (blue) are always negative (dashed), while the $\chi > 90°$ curves (orange) are always positive (solid). This behavior is a consequence of forcing the observer to stare in a fixed direction; such an infaller will classically always see null geodesics from infinity blueshifting below them (when $\chi < 90°$) and redshifting above them as they decrease their radius.

What about the outgoing Hawking radiation from the horizon? As shown in the upper left plot of Fig. 4.7, an interior observer can change the sign of κ_{eff}^+ by changing their energy E_{ob} enough. When $E_{\text{ob}} = 1$, the results of the upper left panel of Fig. 4.6 are reproduced; namely, a positive-temperature horizon is seen with brighter radiation at the edges (i.e. larger κ_{eff}^+ for larger χ). However, as the observer boosts to smaller and smaller energies, the temperature at the ever-growing edge of the horizon begins to decrease until it drops below zero. The negative-temperature outer portion of the black hole's shadow then begins to grow inward until the entire horizon has a negative temperature, once again with the largest magnitude at the edges. Though only one specific case is shown, an outgoing (i.e. negative-energy) observer in a black hole's interior will always see a completely negative-temperature horizon below them.

One way that the upper left plot of Fig. 4.7 differs from the results of Sec. 4.3.1.3 (and from the lower left plot of Fig. 4.7) is that κ_{eff}^+ diverges linearly as $E_{\text{ob}} \to -\infty$ instead of dropping to zero. As a reminder, the difference in the calculation done here versus that of Sec. 4.3 is that here the affine distance is kept constant so that the family of emitters seen by the observer will always have the same phase, since the emitted wave's frequency appears to diverge as the emitter is taken to the horizon. Evidently such a restriction has a big impact not just in the evaluation of the horizon temperature for nonzero χ, but also for the evaluation of the horizon temperature for negative

observer energies, even when $\chi = 0°$.

Finally, special attention will briefly be given to the case of an interior observer with $E_{\rm ob} = 0$. Classically, such an observer will begin at the event horizon seeing nothing but the past horizon in all directions, excepting a vanishingly small patch of sky directly above them at $\chi = 180°$. Then, as they fall inwards, the sky above them will grow until it almost takes up a full hemisphere of the observer's field of view, after which the sky will quickly collapse back to a single point as the horizon grows (compare the visualization in Fig. 2.6). Semiclassically, in Sec. 4.3.1.2 it was argued that the Hawking radiation in the $E_{\rm ob} = 0$ frame diverges as $z_{\rm ob}^{-1/2}$ as an observer approaches the inner horizon looking both up ($\chi = 180°$) and down ($\chi = 0°$). What happens in other directions?

When $E_{\rm ob} = 0$, the effective temperature from the sky above becomes isotropic and simplifies considerably:

$$\lim_{E_{\rm ob} \to 0} \kappa_{\rm eff}^{-}(\chi) = \frac{1}{2\sqrt{-\Delta}} \frac{d\Delta}{dr_{\rm ob}}. \tag{4.99}$$

This radiation extends across the entire sky visible to the observer, from $\chi = 180°$ to the edge of the black hole shadow at

$$\cos \chi = -\left(1 - \frac{\Delta(r)}{r^2} \frac{r_c^2}{\Delta(r_c)}\right)^{-1/2}, \tag{4.100}$$

where $r_c \equiv \frac{3M}{2}\left(1 + \sqrt{1 - \frac{8Q^2}{9M^2}}\right)$ is the critical radius of the photon sphere. This isotropicity can be seen by the convergence of all the curves in the right plots of Fig. 4.7 as $E_{\rm ob} \to 0$.

The effective temperature $\kappa_{\rm eff}^{+}$ from the horizon does not take on a simple analytic form like $\kappa_{\rm eff}^{-}$ does, but its dependence on χ for an observer with $r_{\rm ob}/M = 1$ can be ascertained from the left plots of Fig. 4.7. For various charges Q and observer positions $r_{\rm ob}$, the effective temperature is usually negative in all directions, with the smallest magnitude for $\kappa_{\rm eff}^{+}$ occurring when looking straight downward ($\chi = 0°$). Notably, as the observer reaches the inner horizon, while the temperature $\kappa_{\rm eff}^{-}$ from Eq. (4.99) diverges isotropically as $(-\Delta)^{-1/2}$ (and therefore as $z_{\rm ob}^{-1/2}$), the temperature $\kappa_{\rm eff}^{+}$ from the horizon also diverges as $(-\Delta)^{-1/2}$, with an even stronger divergence when $\chi > 0°$.

4.4.2   Rotating black holes

For an arbitrary freely falling observer in the Kerr spacetime, as mentioned in Sec. 4.2, they

must generally watch a family of Unruh emitters at different angular positions along the black hole's

past horizon. To see why this is the case, consider an equatorial infaller observing a single emitter

near the past horizon with an angular velocity asymptotically approaching Ω_+ from Eq. (4.61). This

observer must possess

$$\frac{d\varphi}{dt} = \Omega_+ - \delta\Omega, \qquad \frac{dr}{dt} = -\frac{k^r \delta\Omega}{k^\varphi}, \tag{4.101}$$

where $k^\mu \equiv dx^\mu/d\lambda$ is the 4-momentum of the null geodesic, and $\delta\Omega$ is the observer's differential

change in their angular velocity as they fall inwards and "catch up" with the azimuthally varying null

geodesic. This system of equations has no apparent solution that does not involve position-dependent

constants of motion from either the observer or the null ray. Therefore, no infalling observer can

both follow a timelike geodesic path and keep up with a single emitter's null ray.

Thus, in calculating the effective temperature seen by an observer watching a family of Unruh

emitters along the past horizon, one must impose an additional constraint so that those emitters

all lie along the same eikonal wavefront. Namely, the null affine distance, scaled by the frequency

measured in the emitter's frame, Eq. (4.28), must be held constant. Assuming in what follows that

the observer and the emitter remain fixed at the same angular position θ throughout the course of

their trajectories, variations with respect to the observer's proper time from Eq. (4.29) can come

only from the observer's and emitter's radial coordinates. Therefore,

$$\kappa_{\text{eff}} = -\dot{r}_{\text{ob}} \left(\frac{\partial \ln \omega_{\text{ob}}}{\partial r_{\text{ob}}} + \frac{\partial \ln \lambda}{\partial r_{\text{ob}}} \right) - \dot{r}_{\text{em}} \frac{\omega_{\text{ob}}}{\omega_{\text{em}}} \frac{\partial \ln \lambda}{\partial r_{\text{em}}}, \tag{4.102}$$

with the affine distance λ given by Eq. (4.27). One additional assumption, as first argued in Ref. [87],

is that the observer should stare in a fixed direction, instead of rotating their frame of reference

and inducing non-inertial effects. The direction an observer looks in their field of view can be

parameterized by two viewing angles χ and ψ, where $\chi \in (-\pi, \pi)$ is the azimuthal angle in their local

tetrad frame along the γ_1-γ_3 plane (zeroed along the positive γ_1 axis), and $\psi \in [0, \pi)$ is the polar angle from the γ_2 axis. The viewing angles (χ, ψ), in turn, can be expressed as a function of the 4-momentum of the null particle arriving at the specified point in the observer's field of view, which depends on the observer's position, the emitter's position, and the photon's energy-normalized orbital parameters $\mathcal{L}/\mathcal{E}$ and $\mathcal{K}/\mathcal{E}^2$. In what follows, as in the spherical case, it is assumed without loss of generality that $\mathcal{E} = 1$. Then, when the viewing angles (χ, ψ) are kept constant during differentiation, the λ-dependent terms in Eq. (4.102) can be expanded with the Leibniz integral rule:

$$\frac{\partial \ln \lambda}{\partial r_{\mathrm{ob}}} = \frac{1}{\lambda} \left(\frac{1}{k_{\mathrm{ob}}^r} + \frac{\partial \mathcal{L}}{\partial r_{\mathrm{ob}}} \int_{r_{\mathrm{em}}}^{r_{\mathrm{ob}}} dr \, \frac{\partial}{\partial \mathcal{L}} \frac{1}{k^r} \right), \tag{4.103a}$$

$$\frac{\partial \ln \lambda}{\partial r_{\mathrm{em}}} = -\frac{1}{\lambda k_{\mathrm{em}}^r}. \tag{4.103b}$$

Eqs. (4.103) apply to equatorial geodesics with constant polar coordinate $\theta = \pi/2$; the more general case will involve derivatives of both $\mathcal{L}$ and $\mathcal{K}$ applied to the affine distance integrands of Eq. (4.27).

If the photon's angular momentum is large enough that its trajectory contains a turning point, the integration over the affine distance must be split in two, and as a consequence, the derivatives with respect to the constants of motion $\mathcal{L}$ and $\mathcal{K}$ in Eq. (4.103a) cannot be brought inside the integral without also introducing a divergent boundary term. In these cases, the derivatives are evaluated numerically with the aid of Richardson extrapolation.

In what follows, two different classes of observers will be considered, as depicted in Fig. 4.8. The first is an equatorial observer in free-fall, with zero angular momentum (ZAMO), beginning from rest at infinity. Such an observer has equations of motion given by Eqs. (4.14) with constant of motion $E = 1$, $L = 0$, and $K = a^2$. The second observer, who can exist only in the interior portion of the black hole, is defined to be at rest in the interior Carter tetrad frame of Eqs. (2.35). Such an observer has constants of motion $E = 0$, $L = 0$, and $K = a^2 \cos^2\theta$ [125].
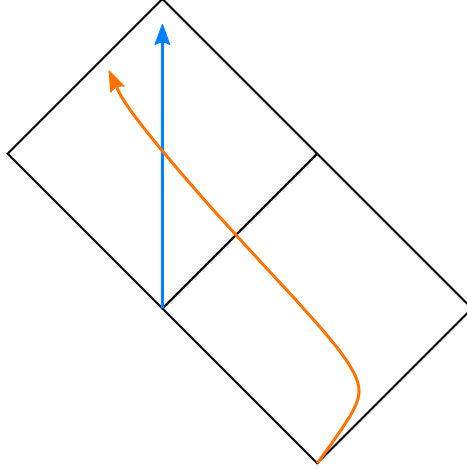
Figure 4.8: Worldlines of the two observers considered in Sec. 4.4.2: a freely falling equatorial ZAMO (orange path) beginning at rest at infinity and ending at the left portion of the inner horizon, and an interior Carter observer (blue path) beginning at the intersection of the outgoing and ingoing portions of the r_+ surface and ending at the intersection of the outgoing and ingoing portions of the r_- surface.

4.4.2.1 Freely falling equatorial ZAMO

A null particle seen in the locally orthonormal tetrad frame of an observer falling freely with zero angular momentum in the equatorial plane will have the following 4-momentum tetrad components:

$$k_{\text{ob}}^0 = \frac{1}{r^2\Delta}\left(R^2(R^2 - a\mathcal{L}) + a(\mathcal{L} - a)\Delta + \text{sgn}(k^r)\sqrt{R^2(R^2 - \Delta)\left((R^2 - a\mathcal{L})^2 - (\mathcal{L} - a)^2\Delta\right)}\right) \quad (4.104a)$$

$$k_{\text{ob}}^1 = \frac{R^2 k_{\text{obs}}^0 - (R^2 - a\mathcal{L})}{\sqrt{R^4 - r^2\Delta}} \quad (4.104b)$$

$$k_{\text{ob}}^2 = 0 \quad (4.104c)$$

$$k_{\text{ob}}^3 = \frac{1}{r\sqrt{R^4 - r^2\Delta}}\left((\mathcal{L} - a)\sqrt{R^2(R^2 - \Delta)} - \text{sgn}(k^r)\,a\sqrt{(R^2 - a\mathcal{L})^2 - (\mathcal{L} - a)^2\Delta}\right), \quad (4.104d)$$

where, as before, all quantities are normalized to unit photon energy $\mathcal{E}$.

The temporal component k_{ob}^0 of Eq. (4.104a) is equivalent to the frequency $\omega_{\text{ob}} = -k^\mu \dot{x}_\mu$ seen in the frame of the observer. The spatial components of $k_{\text{ob}}^{\hat{m}}$ give the angular position of the geodesic in the observer's field of view. This position can be expressed with the viewing angles χ and ψ,

defined by Eq. D.11. The angle χ gives the observer's azimuthal viewing angle away from the inward radial direction within the equatorial plane, while the polar angle ψ extends to the view out of the plane (here ψ is trivially constant since the observer and emitter are both restricted to the equatorial plane; this condition will be relaxed in the next subsection).

If the observer stares in a fixed direction χ, the null geodesic's angular momentum $\mathcal{L}$ will be found to vary with r as determined from the relation

$$\cos\chi = \frac{k_{\mathrm{ob}}^1}{k_{\mathrm{ob}}^0} = \frac{R^2 - (R^2 - a\mathcal{L})(k_{\mathrm{ob}}^0)^{-1}}{\sqrt{R^4 - r^2\Delta}}. \tag{4.105}$$

In the Reissner-Nordström case, the analog of Eq. (4.105) could be inverted to find an expression for the photon angular momentum $\mathcal{L}$ in terms of the viewing angle χ, Eq. (4.92). Then, the effective temperature κ_{eff} could be calculated directly as a function of χ. However, in the present case, no such analytic inversion is possible; instead, the effective temperature will be parameterized by values of $\mathcal{L}$ separately for both ingoing and outgoing photons, and any additional needed quantities like $d\mathcal{L}/dr_{\mathrm{ob}}$ will be found by implicit differentiation of Eq. (4.105).

Fig. 4.9 shows the relation between $\mathcal{L}$ and χ from Eq. (4.105) for observers at various radii when the black hole spin is fixed to $a/M = 0.96$ (different values of a/M yield qualitatively similar plots). For asymptotically distant observers (redder colored curves), the function $\mathcal{L}(\chi)$ approaches an exact sinusoid. For a Reissner-Nordström radial free-faller, this function remains odd for all radii r, but for a Kerr ZAMO free-faller, the symmetry is broken by the non-zero spin, so that null geodesics with zero angular momentum are not necessarily aligned with the observer's definition of $\chi = 0°$.

For reference, the location of the edges of the black hole shadow is indicated in Fig. 4.9 by the intersection of any given curve with the two gray horizontal lines, which lie at the values of $\mathcal{L}$ that solve the equations

$$\dot{r} = 0, \qquad \frac{d\dot{r}}{dr} = 0, \tag{4.106}$$

parameterized by the allowed prograde ($-$) and retrograde ($+$) photon orbital radii at the critical

values [22]

$$r_c = 2M \left(1 + \cos \left(\frac{2}{3} \cos^{-1}(\pm a) \right) \right). \tag{4.107}$$

In terms of the photon's orbital parameters $\mathcal{L}$ and $\mathcal{K}$, the edges of the black hole shadow occur at

$$\mathcal{L} = \frac{R^2 \Delta' - 4r\Delta}{a\Delta'}, \tag{4.108a}$$

$$\mathcal{K} = \frac{16r^2\Delta}{(\Delta')^2}. \tag{4.108b}$$

Once the observer is close enough to the black hole to pass within the outermost photon orbit, they begin receiving both outgoing and ingoing photons originating from an emitter just above the event horizon, as shown respectively by the thick and thin portions of each curve in Fig. 4.9. Then, once the observer falls within the ergosphere bounded by $r = 2M$, they begin receiving photons with divergent normalized angular momentum $\mathcal{L}/\mathcal{E}$, as shown in Fig. 4.9 by the green curves that dip to negative infinity and reappear in the positive region. In the spherically symmetric case, such
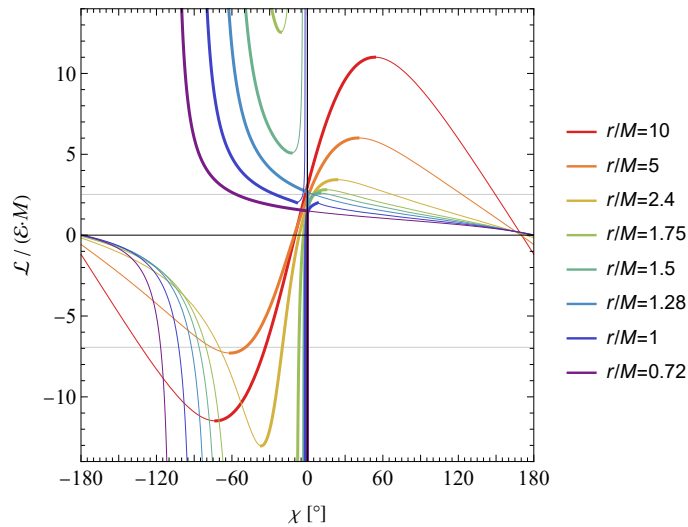
Figure 4.9: Azimuthal viewing angle χ from Eq. (4.105) for a freely falling equatorial ZAMO as a function of a null geodesic's conserved angular momentum $\mathcal{L}/\mathcal{E}$, for a black hole with spin parameter $a = 0.96M$. A selection of different observer radii r are shown, from distant observers (red) to observers crossing the event horizon at $r_+ = 1.28M$ (blue) to observers crossing the Cauchy horizon at $r_- = 0.72M$ (purple). Thick (thin) curves indicate geodesics that are outgoing (ingoing) once they reach the observer.
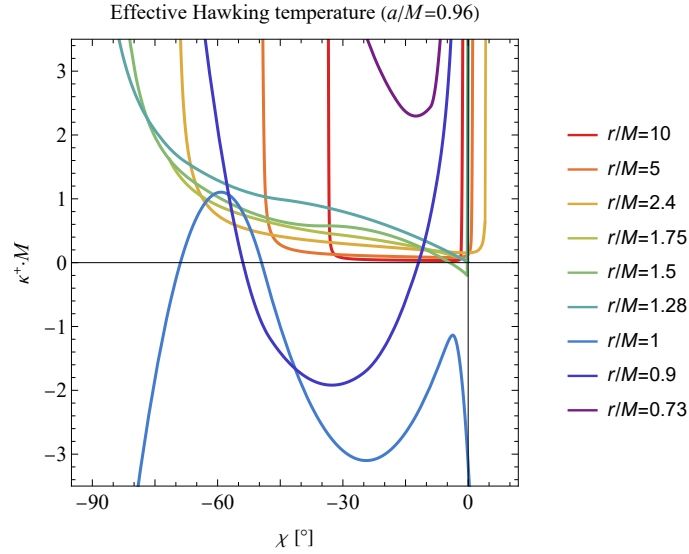
Figure 4.10: Effective Hawking temperature κ_{eff}^+ for outgoing Unruh modes as a function of a freely falling equatorial ZAMO's azimuthal viewing angle χ, for a selection of different observer radii r. The parameters are identical to that of Fig. 4.9.

divergences happen only below the event horizon and correspond only to a single cusp in χ instead of a finite swath of χ values where $\mathcal{L}/\mathcal{E}$ changes sign. Such a rich structure of allowed photon geodesics exists because the Kerr ergosphere extends above the event horizon.

Once the observer reaches the event horizon and proceeds to the inner horizon, the size of the black hole shadow in their field of view remains finite, still governed by the intersections of each colored curve with the two horizontal gray lines in Fig. 4.9. This black hole shadow marks the position of the past horizon, which sources the Unruh modes contributing to the perception of Hawking radiation.

The effective Hawking temperature seen by the freely falling equatorial ZAMO, calculated from Eq. (4.102), is plotted in Fig. 4.10 for a selection of observer positions from $r/M = 10$ down to $r/M = 0.73$ just above the inner horizon. This temperature depends strongly on the specific choice of observer and exhibits a wide range of behaviors throughout the observer's descent, but a few general trends are worth mentioning.

When the observer is far from the black hole (red curves), the effective temperature is small

but non-zero, as expected. As the observer's viewing angle χ across the equatorial plane changes, so does the effective Hawking temperature, with a minimum value near the center of the black hole shadow and maximum values at the edges. Such behavior is in accordance the limb-brightening assertion #3 in Sec. 4.1, with the only modification that in the Kerr case, the distribution is no longer symmetric about $\chi = 0°$.

As the observer approaches the black hole, the effective Hawking temperature increases in all directions across the black hole shadow, until it becomes negative for certain values of the viewing angle χ. Just as in the case of the on-axis observer of Fig. 4.5, the effective temperature can be negative even for an observer above the event horizon, as anticipated by assertion #4 in Sec. 4.1.

As the observer approaches the inner horizon, the effective temperature calculated in Fig. 4.10 diverges to positive infinity (in contrast to the on-axis observer's negative-infinite temperature from Fig. 4.5). As such, the value of κ^+_{eff} for an observer crossing through the inner horizon at $r/M = 0.72$ is not shown; instead, the value for an observer just above the inner horizon ($r/M = 0.73$) is displayed, and the effective temperature for any observer closer to the inner horizon will be inversely proportional to the distance above the horizon.

Though not shown explicitly in Fig. 4.10, as the effective temperature diverges at $r \to r_-$ (when $r/M < 0.73$ in that plot), the angular distribution across χ becomes more and more isotropic. Such behavior has been previously noted in both the Schwarzschild [87] and Reissner-Nordström [127] cases. The key takeaway here and from these prior studies is that the diverging Hawking radiation at the Cauchy horizon is not confined to the single radial point in the observer's field of view where classical radiation diverges via mass inflation, but instead, the diverging semiclassical radiation is distributed uniformly across the entire surface of the black hole's past horizon.

4.4.2.2   Interior Carter observer

The interior Carter observer, who will also be called the zero-energy observer, is the observer who is at rest in the Carter frame defined by Eqs. (2.35). This observer moves along the blue path in Fig. 4.8 and will travel along a constant latitude θ, not necessarily in the equatorial plane as in

the previous subsection. In the coordinate frame, the only non-zero component of their 4-velocity is the timelike component $\dot{r} = -\sqrt{-\Delta}/\rho$, and in their locally orthonormal tetrad frame, they will see null particles travel with the following 4-momentum components:

$$k_{\text{ob}}^0 = \frac{1}{\rho}\sqrt{\mathcal{K} - \frac{(R^2 - a\mathcal{L})^2}{\Delta}} \tag{4.109a}$$

$$k_{\text{ob}}^1 = -\frac{R^2 - a\mathcal{L}}{\rho\sqrt{-\Delta}} \tag{4.109b}$$

$$k_{\text{ob}}^2 = \frac{\text{sgn}(k^\theta)}{\rho}\sqrt{\mathcal{K} - \frac{(\mathcal{L} - a\sin^2\theta)^2}{\sin^2\theta}} \tag{4.109c}$$

$$k_{\text{ob}}^3 = -\frac{\mathcal{L} - a\sin^2\theta}{\rho\sin\theta}. \tag{4.109d}$$

As in the previous subsection, the temporal component k_{ob}^0 of Eqs. (4.109) is equivalent to the frequency $\omega_{\text{ob}} = -k^\mu \dot{x}_\mu$ seen in the frame of the observer, and the spatial components of $k_{\text{ob}}^{\hat{m}}$ give the angular position of the geodesic in the observer's field of view, parameterized by the viewing angles χ and ψ defined by Eqs. (D.11).

Eqs. (D.11) can be solved for the photons of Eqs. (4.109) to yield the following relations between the viewing angles (χ, ψ) and the photon's orbital parameters $(\mathcal{L}, \mathcal{K})$:

$$\mathcal{L} = \frac{a\sin^2\theta\sqrt{-\Delta} + R^2\sin\theta\tan\chi}{\sqrt{-\Delta} + a\sin\theta\tan\chi}, \tag{4.110a}$$

$$\mathcal{K} = \frac{\rho^4\left(\sec^2\chi\csc^2\psi - 1\right)}{\left(\sqrt{-\Delta} + a\sin\theta\tan\chi\right)^2}. \tag{4.110b}$$

Eqs. (4.110) can be used together with Eq. (4.102) to calculate the effective Hawking temperature κ_{eff} directly as a function of the observer's azimuthal and polar viewing angles χ and ψ, respectively. Before presenting the results, two modifications from the previous subsection are worth noting. First, the integration of Eq. (4.27) to calculate the affine distance will now include both r-dependent and θ-dependent terms, since the observer can now look outside of the equatorial plane. Derivatives with respect to both $\mathcal{L}$ and $\mathcal{K}$ must then be applied to both the r-dependent and θ-dependent integrands, in contrast to the simpler case of Eq. (4.103a).

Second, while the emitter's radius $r_{\rm em}$ can always be fixed at the value r_+ (for $\kappa_{\rm eff}^+$) or ∞ (for $\kappa_{\rm eff}^-$), the emitter's polar angle $\theta_{\rm em}$ will change for different values of the photon's orbital parameters $\mathcal{L}$ and $\mathcal{K}$. It must therefore be calculated via the same ray-tracing techniques used throughout this section. If the back-propagated null geodesic originating from an equatorial observer exceeds a Mino time $\tilde{\lambda}$ (defined in Eq. (4.22)) of

$$\tilde{\lambda} > K\left(\frac{1}{2} + \frac{a(a-\mathcal{L})-\mathcal{K}}{\sqrt{(\mathcal{K}+4a\mathcal{L})\mathcal{K}}}\right)((\mathcal{K}+4a\mathcal{L})\mathcal{K})^{-1/4}, \tag{4.111}$$

where K is the complete elliptic integral of the first kind, then the photon will experience a turning point at

$$\sin\theta = \frac{\sqrt{\mathcal{K}+4a\mathcal{L}}-\sqrt{\mathcal{K}}}{2a}. \tag{4.112}$$

Since the emitter's polar angle $\theta_{\rm em}$ will vary as the observer varies their proper time $\tau_{\rm ob}$ while staring in the same fixed direction parametrized by angles (χ, ψ), Eq. (4.102) will in principle include additional terms with derivatives with respect to $\theta_{\rm em}$, even if both the observer's and emitter's polar velocities $\dot{\theta}_{\rm ob}$ and $\dot{\theta}_{\rm em}$ are individually assumed to be zero (as is the case here). To address this complication, the dependence of $\theta_{\rm em}$ on $r_{\rm ob}$ and $r_{\rm em}$ is explicitly included when evaluating the r derivatives of Eq. (4.102).

A freely falling observer in the interior of a Kerr black hole with zero energy will see the black hole shadow grow over time, as shown in Fig. 4.11. As the interior Carter observer begins at $r_{\rm ob} = r_+$ at the bifurcation point of the past horizon and the event horizon, they initially see the black hole shadow emerge from a single point in their field of view along the principal null direction at $\chi = 0°$, $\psi = 90°$ (the upper-left point in Fig. 4.11). Then, the black hole shadow appears to grow in their field of view until taking on the yellow shape in Fig. 4.11 when the observer reaches the inner horizon. These are the regions that appear as the source of outgoing Hawking modes in the observer's field of view.

The calculation of the effective Hawking temperature $\kappa_{\rm eff}^+$ via Eq. (4.102) for an interior Carter observer, who follows the blue path in Fig. 4.8, is presented in Fig. 4.12. In the left panel of Fig. 4.12,
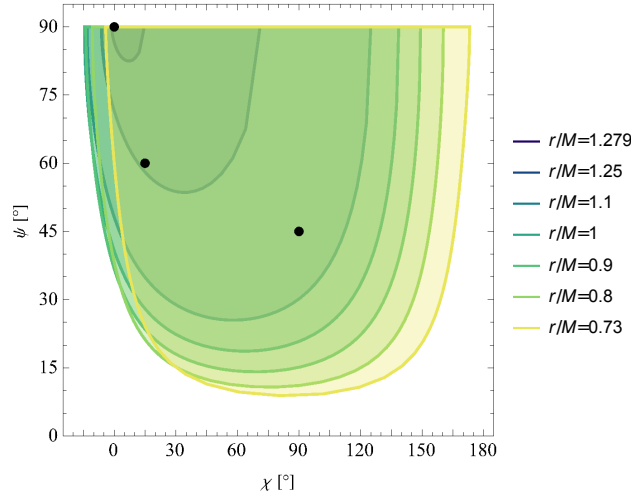
Figure 4.11: Fields of view of the black hole shadow, with edges parametrized by Eqs. (4.108), for the viewing angles χ and ψ defined by Eqs. (D.11). The view is from the perspective of a freely falling equatorial interior zero-energy observer at different radii r within a Kerr black hole with spin parameter $a = 0.96M$. The shadow initially appears as an infinitesimally small point at $(\chi, \psi) = (0°, 90°)$ when the observer is at the event horizon (dark blue), then grows along both angular directions as the observer approaches the inner horizon (yellow). The three black points correspond to the three curves shown in Fig. 4.12.

three specific viewing directions are chosen to track how κ_{eff}^+ changes as the observer travels from the event horizon to the inner horizon. These three directions are denoted by the black points in Fig. 4.11: at the approximate center of the shadow at $(\chi, \psi) = (90°, 45°)$, closer to the edge at $(\chi, \psi) = (15°, 60°)$, and at the point of emergence at $(\chi, \psi) = (0°, 90°)$.

When staring along the three directions shown in the left panel of Fig. 4.12, the observer sees a wide range of effective temperatures. The temperature appears to converge to a negative, infinite value as $r_{\text{ob}} \to r_+$, since at this point, the observer is coincident with the past horizon singularity imposed by the Unruh vacuum state. However, most directions the observer might look in the sky (in fact, all but a set of zero measure) do not actually reach this pathological divergence, since the black hole shadow falls out of their range above a certain radius.

As the interior Carter observer approaches the inner horizon, the effective temperature does not diverge in every direction, as it did for the equatorial ZAMO in the previous Sec. 4.4.2.1 and for the Reissner-Nordström radial infallers of Sec. 4.4.1. Instead, κ_{eff}^+ approaches a finite value in every
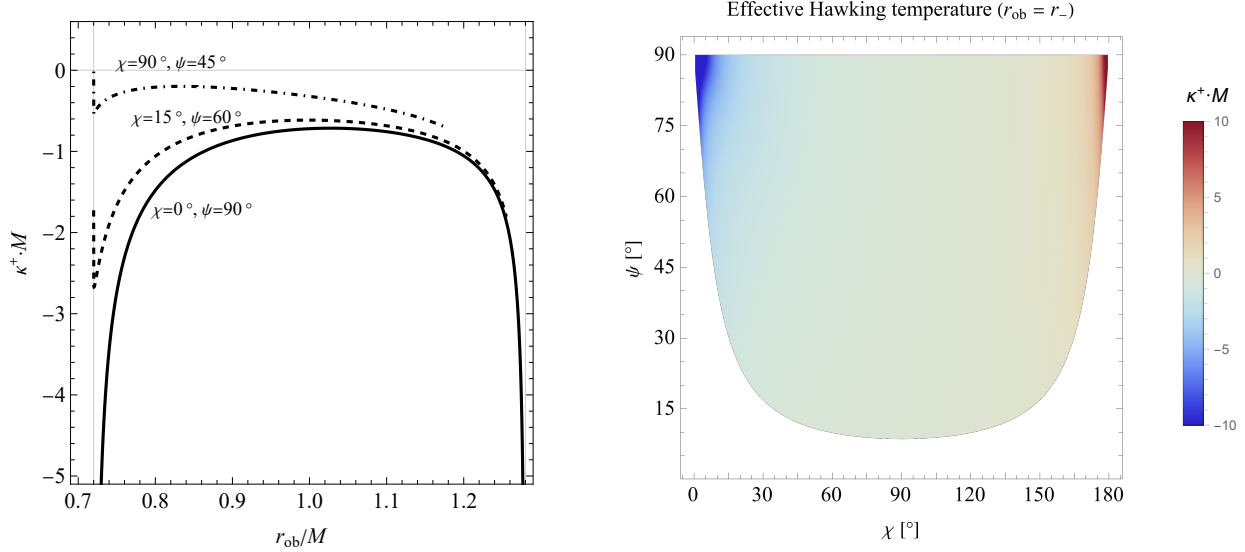
Figure 4.12: Effective Hawking temperature κ_{eff}^+ for outgoing Unruh modes seen by a freely falling zero-energy equatorial observer in the interior of a Kerr black hole with spin parameter $a = 0.96M$. Left plot: The three curves show the effective temperature when looking in the three specific directions labeled in the plot and marked by the black points in Fig. 4.11. Right plot: The effective temperature when looking in all directions in the limit as the observer approaches the inner horizon; κ_{eff}^+ is mostly (but not completely) isotropic and diverges to $\pm\infty$ along the principal null directions.

direction along the black hole shadow except along the principal null directions at $\chi = 0°$ and $\chi = 180°$, where κ_{eff}^+ does diverge to $-\infty$ and $+\infty$, respectively. One of these divergences ($\chi = 0°, \psi = 90°$) is shown in the left panel of Fig. 4.12.

The full view of the effective Hawking temperature seen just above the inner horizon is shown in the right panel of Fig. 4.12. The effective temperature becomes approximately isotropic and negligibly small across most of the surface of the past horizon, but it diverges to $\pm\infty$ and exceeds the saturation limit of the color scale along the ingoing and outgoing principal null directions at the top left and top right corners of the figure.

In conclusion, the effective temperature of Hawking radiation can be calculated in the geometric optics framework for any class of inertial observers within the Kerr spacetime, with widely varying outcomes depending on the particular choice of orbital parameters and spacetime positions. In this Sec. 4.4, several different classes of observers have been examined: freely falling radial observers in a charged black hole, equatorial infallers with zero angular momentum in a rotating black hole,

and equatorial infallers with zero energy in a rotating black hole. In all these cases, the effective temperature required an additional constraint that the emitted affine distance be kept constant, so that a family of Unruh-state emitters could be matched to the same eikonal wavefront as the observer pans across their field of view.

For all classes of observers examined here that reach the black hole's Cauchy horizon, at least one point in their field of view contains a diverging effective Hawking temperature. In accordance with prior studies of both Hawking radiation [87] and the renormalized stress-energy tensor [178], this semiclassically divergent behavior appears to be generic. Though here it has not been proved that Hawking radiation temperatures will diverge for every inner-horizon observer within the Kerr spacetime, the fact that a divergence appears for even a single inertial observer is enough to demonstrate that Kerr black holes are semiclassically singular and likely unstable at the inner horizon.

4.5   Graybody spectrum

Since a variety of choices for the observer position $r_{\rm ob}$ and black hole parameters Q or a lead to a nonadiabatic effective temperature function, one may wonder how much trust can be placed on the physical validity of the results of Secs. 4.2–4.4. Further, the effective temperature is not guaranteed to provide any information about the behavior of Hawking radiation below the high-frequency geometric optics limit. Nonetheless, as has been argued, even if the Hawking spectrum is nonthermal, there should in general still be particle production whenever $\kappa_{\rm eff}$ is nonzero. To verify this claim, here a full wave mode analysis is performed to find the particle spectrum seen by an infaller in the locations where the Klein-Gordon equation simplifies enough for such a calculation to be performed.

As in previous sections, the analysis will first be performed for spherically symmetric black holes (Sec. 4.5.1), then for azimuthally symmetric black holes (Sec. 4.5.2).

4.5.1   Spherical black holes

Consider the Bogoliubov coefficients between the vacuum state of an Unruh emitter and that of a freely falling observer in a Reissner-Nordström spacetime. In any spacetime with metric $g_{\mu\nu}$, a canonically quantized, minimally coupled, massless scalar field ϕ will satisfy the Klein-Gordon wave Eq. (3.11). Motivated by the spacetime's symmetries, this field ϕ can be decomposed into a complete set of modes $\phi_{\omega\ell m}$, each accompanied by creation and annihilation operators $\hat{a}^{\dagger}_{\omega\ell m}$ and $\hat{a}_{\omega\ell m}$, as in Eq. (3.13). If these modes are separated as

$$\phi_{\omega\ell m} = \frac{f_{\omega\ell}(t,r)Y_{\ell m}(\theta,\varphi)}{r\sqrt{4\pi\omega}}, \tag{4.113}$$

then Eq. (3.11) implies that $Y_{\ell m}$ will satisfy the spherical harmonic equation, while $f_{\omega\ell}$ must satisfy

$$\frac{\partial^2 f_{\omega\ell}}{\partial r^{*2}} - \frac{\partial^2 f_{\omega\ell}}{\partial t^2} = \Delta\left[\frac{\ell(\ell+1)}{r^2} + \frac{1}{r}\frac{d\Delta}{dr}\right]f_{\omega\ell}. \tag{4.114}$$

For convenience, the mode indices ω, ℓ, and m will hereafter be suppressed as needed. As described in Sec. 3.2, two vacuum states can be related by a Bogoliubov transformation, which aids in the calculation of the vacuum expectation value of an observer's number operator in an emitter's vacuum state (and note that there should properly be a sum of two integrals for the emitter's ingoing and outgoing states, which are omitted here for simplicity):

$$\langle 0_{\text{em}}|\hat{a}^{\dagger}_{\text{ob}}\hat{a}_{\text{ob}}|0_{\text{em}}\rangle = \int_0^{\infty} d\bar{\omega} \sum_{\bar{\ell}=0}^{\infty} \sum_{\bar{m}=-\bar{\ell}}^{\bar{\ell}} |\beta|^2 = \int_0^{\infty} d\bar{\omega} \sum_{\bar{\ell}=0}^{\infty} \sum_{\bar{m}=-\bar{\ell}}^{\bar{\ell}} |\langle\phi_{\text{em}}|\phi^*_{\text{ob}}\rangle|^2. \tag{4.115}$$

where bra-ket notation denotes the Lorentz-invariant Klein-Gordon inner product defined by Eq. (3.21). To determine the expected particle number seen by an observer, one thus needs only to specify the observer's and emitter's modes (usually via a set of boundary conditions), propagated through the spacetime via the wave equation so that they coincide on some Cauchy hypersurface.

The Unruh emitter's ingoing ($-$) and outgoing ($+$) modes are defined with the following

boundary conditions at past null infinity $\mathscr{I}^-$ and the past horizon $\mathcal{H}^+_{r_+} \equiv {}^{\text{int}}\mathcal{H}^+_{r_+} \cup {}^{\text{ext}}\mathcal{H}^+_{r_+}$ (here f is defined as in Eq. (4.113), with $\omega\ell$ indices dropped for convenience):

$$f^+_{\text{em}} \to \begin{cases} 0, & \mathscr{I}^- \\ e^{-i\omega U}, & \mathcal{H}^+_{r_+} \end{cases}, \tag{4.116}$$

$$f^-_{\text{em}} \to \begin{cases} e^{-i\omega(t+r^*)}, & \mathscr{I}^- \\ 0, & \mathcal{H}^+_{r_+} \end{cases}, \tag{4.117}$$

where U is the outgoing Kruskal-Szekeres coordinate, defined in terms of the event horizon's surface gravity κ_+ from Eq. (4.10) by

$$U \equiv \begin{cases} -e^{-\kappa_+(t-r^*)}/\kappa_+, & r_+ \leq r < \infty \\ +e^{-\kappa_+(t-r^*)}/\kappa_+, & r_- \leq r < r_+ \end{cases}. \tag{4.118}$$

The relevant surfaces to which these boundary conditions correspond are shown schematically with dotted arrows in the Penrose diagram of Fig. 4.13. Note that, as shown in the diagram, the outgoing modes can be further split into a pair of substates via $f^+ \equiv \left({}^{\text{int}}f^+\right) \cup \left({}^{\text{ext}}f^+\right)$, each of whose boundary conditions are zero except on their respective null surfaces. As argued in Sec. 4.2.1, the modes of Eqs. (4.116) and (4.117) are precisely those which are positive frequency with respect to the proper time of a freely falling observer skimming asymptotically close to those surfaces. The modes $f^\pm_{\text{em}}$ can then be extended to the entire spacetime by solving the wave Eq. (4.114).

Similarly, the observer's ingoing ($-$) and outgoing ($+$) modes can be defined via boundary conditions, in this case on the future null hypersurfaces. At future null infinity, the outgoing modes are positive frequency with respect to the outgoing Eddington-Finkelstein coordinate $u \equiv t - r^*$, since an observer asymptotically close to that surface will define positive frequency with respect to that coordinate (as argued in Sec. 4.2.1). The natural question is then how this vacuum state should be extended to the interior of the black hole. In studies of analogous acoustic black hole systems [5, 14], these interior modes are also defined with respect to the Eddington-Finkelstein coordinates, in part because the inner horizon of those systems is mimicked by a physically infinite asymptotic regime. For the Reissner-Nordström spacetime, an infaller will not reach an asymptotically steady state at the inner horizon; however, they will approach an asymptotic regime (albeit a transient one) where $\Delta \to 0$ and the scattering potential of Eq. (4.114) vanishes. In the regime where this potential vanishes, as shown in Sec. 4.2.1, freely falling observers experience a proper time proportional to the
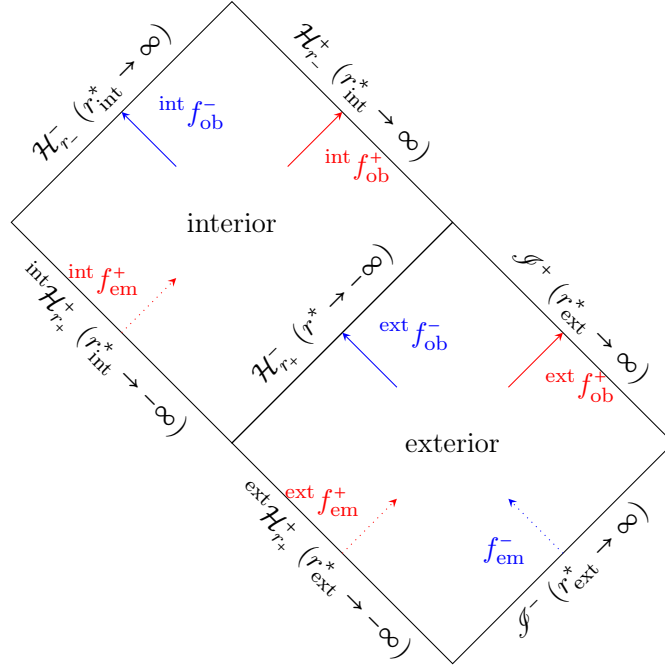
Figure 4.13: Penrose diagram showing the various boundaries for a Reissner-Nordström or Kerr black hole on which modes are defined with nonzero values. Past (future) null infinity is labeled $\mathscr{I}^-$ ($\mathscr{I}^+$), the outer (inner) horizons are labeled $\mathcal{H}_{r_+}$ ($\mathcal{H}_{r_-}$), and the superscripts $+$ ($-$) everywhere indicate whether modes traveling across a surface are outgoing (ingoing). The boundary conditions for the emitter's (observer's) modes at the locations of the dotted (solid) lines can then be propagated (backpropagated) numerically using the wave equation to define the modes throughout the entire spacetime.

Eddington-Finkelstein coordinates:

$$f_{\text{ob}}^+ \to \begin{cases} e^{-i\omega(t-r^*)}, & \mathscr{I}^+ \\ e^{-i\omega(r^*-t)}, & \mathcal{H}_{r_-}^+ \\ 0, & \mathcal{H}_{r_-}^- \end{cases}, \tag{4.119}$$

$$f_{\text{ob}}^- \to \begin{cases} 0, & \mathscr{I}^+ \cup \mathcal{H}_{r_-}^+ \\ e^{-i\omega(r^*+t)}, & \mathcal{H}_{r_-}^- \end{cases}. \tag{4.120}$$

These modes are shown with solid arrows in Fig. 4.13. They represent the experience of any inertial observer with arbitrary energy E_{ob} (up to a rescaling of the frequency ω); without loss of generality, an observer with $E_{\text{ob}} = 1$ is chosen for the left potion of the inner horizon in Fig. 4.13 ($\mathcal{H}_{r_-}^-$), while an observer with $E_{\text{ob}} = -1$ is chosen for the right portion ($\mathcal{H}_{r_-}^-$). Also, note that if the

observer is placed at the outer horizon instead of the inner horizon, a similar complete set of modes can be defined *mutatis mutandis.* In what follows, the results for both sets of modes will be presented simultaneously, though the steps of analysis for the inner horizon observers' set of modes will be the main focus.

Equipped with a complete set of modes for an Unruh emitter and an inertial observer, one may now proceed to calculate the expectation value of the particle number operator seen by the observer in the emitter's vacuum state via Eq. (4.115). To do so, consider what will subsequently be referred to as the past null Cauchy hypersurface, consisting of the union of past null infinity with the exterior and interior past horizons ($\mathscr{I}^- \cup \mathcal{H}_{r_+}^+$; see Fig. 4.13). On this surface, the emitter's modes are given by Eqs. (4.116) and (4.117), while the observer's modes can be found with scattering theory, as described below.

Since the t coordinate used to define the observer's modes defines a global timelike Killing vector for the spacetime, the field's modes $f_{\omega\ell}$ can be separated as

$$f_{\omega\ell}(t, r^*) \equiv \chi_{\omega\ell}(r^*)\, e^{\pm i\omega t}. \tag{4.121}$$

This separation puts the Klein-Gordon wave Eq. (4.114) into the form of a 1D scattering equation in r^*. In the limits as Δ approaches both 0 and 1, the scattering potential of Eq. (4.114) vanishes, leading to asymptotic eigenmode solutions of the form $\exp(\pm i\omega r^*)$. As such, the observer's modes $\chi_{\text{ob}}^{\pm}$ can be backpropagated to the past null Cauchy hypersurface—altogether, for an observer at future null infinity one has

$$^{\text{ext}}f_{\text{ob}}^+ \to e^{-i\omega t} \begin{cases} e^{i\omega r^*} + \mathcal{R}_{\text{ext}}^+ e^{-i\omega r^*}, & r_{\text{ext}}^* \to \infty \\ \mathcal{T}_{\text{ext}}^+ e^{i\omega r^*}, & r_{\text{ext}}^* \to -\infty \end{cases}, \tag{4.122}$$

for an outgoing observer at the inner horizon,

$$^{\text{int}}f_{\text{ob}}^+ \to e^{i\omega t} \begin{cases} e^{-i\omega r^*}, & r_{\text{int}}^* \to \infty \\ \mathcal{T}_{\text{int}}^+ e^{-i\omega r^*} + \mathcal{R}_{\text{int}}^+ e^{i\omega r^*}, & r_{\text{int}}^* \to -\infty \\ \mathcal{R}_{\text{int}}^+ \mathcal{T}_{\text{ext}}^- e^{i\omega r^*}, & r_{\text{ext}}^* \to \infty \\ \mathcal{R}_{\text{int}}^+ \left(e^{i\omega r^*} + \mathcal{R}_{\text{ext}}^- e^{-i\omega r^*} \right), & r_{\text{ext}}^* \to -\infty \end{cases}, \tag{4.123}$$

and for an ingoing observer at the inner horizon,

$$
{}^{\text{int}}f_{\text{ob}}^{-} \to e^{-i\omega t}
\begin{cases}
e^{-i\omega r^{*}}, & r_{\text{int}}^{*} \to \infty \\
\mathcal{T}_{\text{int}}^{-}e^{-i\omega r^{*}} + \mathcal{R}_{\text{int}}^{-}e^{i\omega r^{*}}, & r_{\text{int}}^{*} \to -\infty \\
\mathcal{T}_{\text{int}}^{-}\mathcal{T}_{\text{ext}}^{-}e^{-i\omega r^{*}}, & r_{\text{ext}}^{*} \to \infty \\
\mathcal{T}_{\text{int}}^{-}\left(e^{-i\omega r^{*}} + \mathcal{R}_{\text{ext}}^{-}e^{i\omega r^{*}}\right), & r_{\text{ext}}^{*} \to -\infty
\end{cases},
\tag{4.124}
$$

where r_{int}^{*} and r_{ext}^{*} represent the radial tortoise coordinates r^{*} for the black hole's interior and exterior, respectively. The reflection coefficients $\mathcal{R}_{\text{int,ext}}^{\pm}$ and transmission coefficients $\mathcal{T}_{\text{int,ext}}^{\pm}$, which depend on the observer's mode numbers ω and ℓ, can be computed numerically (or semianalytically with confluent Heun functions) with the above boundary conditions on the wave Eq. (4.114); see Appendix B for more details.

Defining annihilation operators ${}^{\text{int,ext}}\hat{a}_{\text{ob,em}}^{\pm}$ for each respective set of modes ${}^{\text{int,ext}}f_{\text{ob,em}}^{\pm}$, one can then calculate the particle content seen by the observer. The vacuum expectation values of the number operators associated with each choice of observer are

$$
\langle N_{\text{int,ext}}^{\pm}\rangle \equiv \left\langle 0_{\text{em}} \left| \left({}^{\text{int,ext}}\hat{a}_{\text{ob}}^{\pm}\right)^{\dagger} \left({}^{\text{int,ext}}\hat{a}_{\text{ob}}^{\pm}\right) \right| 0_{\text{em}} \right\rangle,
\tag{4.125}
$$

with $\langle N_{\text{ext}}^{+}\rangle$ for the expected particle number observed at future null infinity $\mathscr{I}^{+}$, $\langle N_{\text{ext}}^{-}\rangle$ for an observer at the event horizon $\mathcal{H}_{r_{+}}^{-}$, $\langle N_{\text{int}}^{+}\rangle$ for an outgoing observer at the inner horizon $\mathcal{H}_{r_{-}}^{+}$, and $\langle N_{\text{int}}^{-}\rangle$ for an ingoing observer at the inner horizon $\mathcal{H}_{r_{-}}^{-}$.

Using Eqs. (4.115) and (3.21) and evaluating the inner product between the emitter's modes and the observer's backpropagated modes along the past null Cauchy hypersurface, the anticipated number operators can be calculated. After summing over the angular modes, the following inner products yield nontrivial (i.e. up to an irrelevant phase) contributions to the Bogoliubov coefficients:

$$\langle N_{\text{ext}}^+ \rangle = \int_0^\infty d\bar{\omega} \left| \diamond \langle e^{-i\bar{\omega}U} | e^{i\omega u} \rangle_{\text{ext}\mathcal{H}_{r_+}^+} \right|^2, \tag{4.126a}$$

$$\langle N_{\text{ext}}^- \rangle = \int_0^\infty d\bar{\omega} \left| \diamond \langle e^{-i\bar{\omega}U} | e^{i\omega u} \rangle_{\text{ext}\mathcal{H}_{r_+}^+} \right|^2, \tag{4.126b}$$

$$\langle N_{\text{int}}^- \rangle = \int_0^\infty d\bar{\omega} \left| \diamond \langle e^{-i\bar{\omega}U} | e^{i\omega u} \rangle_{\text{ext}\mathcal{H}_{r_+}^+} + \diamond \langle e^{-i\bar{\omega}U} | e^{i\omega u} \rangle_{\text{int}\mathcal{H}_{r_+}^+} \right|^2, \tag{4.126c}$$

$$\langle N_{\text{int}}^+ \rangle = \int_0^\infty d\bar{\omega} \left| \diamond \langle e^{-i\bar{\omega}U} | e^{-i\omega u} \rangle_{\text{int}\mathcal{H}_{r_+}^+} + \diamond \langle e^{-i\bar{\omega}U} | e^{-i\omega u} \rangle_{\text{ext}\mathcal{H}_{r_+}^+} \right|^2$$

$$+ \int_0^\infty d\bar{\omega} \left| \diamond \langle e^{-i\bar{\omega}v} | e^{-i\omega v} \rangle_{\mathscr{I}^-} \right|^2, \tag{4.126d}$$

where each Penrose diagram stands in for the complex conjugate of the backscattering coefficient(s) corresponding to the path shown, e.g. the final diagram of Eq. (4.126d) represents the combination $(\mathcal{R}_{\text{int}}^+ \mathcal{T}_{\text{ext}}^-)^*$, and the subscript associated with each bra-ket indicates the null surface over which that inner product is evaluated.

Several potential pathways appear to be missing from Eqs. (4.126), such as the pathway in Eq. (4.126b) connecting the event horizon to past null infinity. However, all such pathways involve inner products of the form $\langle e^{-i\bar{\omega}v} | e^{i\omega v} \rangle$, whose modes are completely orthogonal and therefore do not contribute at all to the Bogoliubov coefficients. While the exclusion of these pathways is entirely straightforward and routine, one may wonder how these calculations relate to those of Sec. 4.3, where, for example, an observer at the event horizon *does* see nontrivial contributions from the ingoing modes from past null infinity. The discrepancy lies in the fact that adiabaticity is never satisfied for $\kappa_{\text{eff}}^-(r_+)$, and therefore the effective temperature calculations cannot be trusted at that specific location. There is a small range of black hole charges around the value $Q/M \approx 0.937$ for which it appears from Fig. 4.4 that ϵ dips below 1 at the event horizon; however, as noted in Sec. 4.3.1.4, in this range, the adiabatic control function ϵ fails to be a good estimator of the degree of adiabaticity, since higher derivatives of κ_{eff} dominate over the vanishing first derivative.

The evaluation of the inner products from Eqs. (4.126) over each relevant surface have become

a standard part of the literature (see, e.g., Refs. [20], [14], and sources therein); for example,

$$\left| \langle e^{-i\bar{\omega}U} | e^{i\omega u} \rangle_{\text{ext}\,\mathcal{H}_{r_+}^+} \right|^2 = \frac{e^{-\pi\omega/\kappa_+}}{4\pi^2\kappa_+^2} \frac{\omega}{\bar{\omega}} \left| \Gamma\left(\frac{i\omega}{\kappa_+}\right) \right|^2 \tag{4.127}$$

Using the property of gamma functions

$$\left| \Gamma(\pm ix) \right|^2 = \frac{2\pi}{x\left(e^{\pi x} - e^{-\pi x}\right)}, \tag{4.128}$$

one finds a Planckian distribution in the observer's frequency ω, and while the remaining factors of $1/(2\pi\kappa_+\bar{\omega})$ formally diverge when the integrals of Eqs. (4.126) are carried out, this divergence only occurs as a result of the unphysical usage of infinite plane waves. If one were instead to use a normalized wave packet localized in each asymptotic region with a frequency content concentrated around some frequency $\bar{\omega}_*$, the offending terms would all reduce to unity.

Since the scattering coefficients in Eqs. (4.126) are independent of the emitter's modes $\bar{\omega}$ (the emitter's modes are kept at their initial past boundaries, while the observer's modes are the ones that must be backpropagated through the spacetime's scattering potential), the final form of the number operators at each surface simplifies to (cf. the number operators of Ref. [14] evaluated for a simplified scattering potential):

$$\langle N_{\text{ext}}^+ \rangle = \frac{|\mathcal{T}_{\text{ext}}^+|^2}{e^{2\pi\omega/\kappa_+} - 1}, \tag{4.129a}$$

$$\langle N_{\text{ext}}^- \rangle = \frac{|\mathcal{R}_{\text{ext}}^-|^2}{e^{2\pi\omega/\kappa_+} - 1}, \tag{4.129b}$$

$$\langle N_{\text{int}}^- \rangle = \frac{\left| \mathcal{T}_{\text{int}}^- \mathcal{R}_{\text{ext}}^- - \mathcal{R}_{\text{int}}^- e^{\pi\omega/\kappa_+} \right|^2}{e^{2\pi\omega/\kappa_+} - 1}, \tag{4.129c}$$

$$\langle N_{\text{int}}^+ \rangle = \frac{\left| \mathcal{T}_{\text{int}}^+ - \mathcal{R}_{\text{int}}^+ \mathcal{R}_{\text{ext}}^- e^{\pi\omega/\kappa_+} \right|^2}{e^{2\pi\omega/\kappa_+} - 1} + |\mathcal{R}_{\text{int}}^+ \mathcal{T}_{\text{ext}}^-|^2. \tag{4.129d}$$

The key feature in each of the above equations is the familiar Planckian spectrum $(e^{2\pi\omega/\kappa_+} - 1)^{-1}$, modified by a frequency-dependent graybody factor associated with the appropriate set of scattering coefficients. For example, if no modes were scattered in the black hole exterior (and therefore

$\mathcal{T}^+_{\text{ext}} = 1$), Eq. (4.129a) would reduce to a completely thermal Hawking spectrum, as expected for an eikonal observer at infinity.

4.5.1.1   Spectra for s-modes

Fig. 4.14 shows the deviations from thermality for the $\ell = 0$ spectra of Eqs. (4.129). These plots are computed numerically with the help of confluent Heun functions, as outlined in Appendix B. In the top left panel, the particle spectrum seen asymptotically far from the black hole is plotted as the ratio of $\langle N^+_{\text{ext}} \rangle$ to the analogous occupation number for a fully thermal spectrum with temperature $\kappa_+/(2\pi)$ (this Planckian distribution will subsequently be referred to as a "κ_+ blackbody"). This ratio, which from Eq. (4.129a) equals the transmission probability $|\mathcal{T}^+_{\text{ext}}|^2$, approaches unity in the high frequency (geometric optics) limit, indicating a return to thermality in that regime. However, at lower frequencies, significant deviation from thermality occurs as the spectrum attains a steeper power law than that of a blackbody. The transmission probability approaches a power law index of 2, as first predicted by Starobinsky and Churilov for the analytically solvable $\omega M \ll 1$ regime [166].

For an observer crossing the event horizon, the Hawking radiation seen from ingoing modes in the sky above is shown in the top right panel of Fig. 4.14. Just as in the top left panel, values at unity indicate consistency with a κ_+ blackbody spectrum, though in this case, thermality at the surface gravity temperature mostly occurs at the lowest frequencies instead of the highest frequencies, with slight deviations for different black hole charges Q. At higher frequencies, the spectrum cuts off much sooner than it does for an asymptotically infinite observer, indicating a lower eikonal temperature. This high-frequency-limit temperature (multiplied by 2π) is approximately, but not exactly, equal to the effective temperature κ^-_{eff} from Eq. (4.35), as shown by the dotted curves in Fig. 4.14. Indeed, the modes contributing to the Bogoliubov spectrum from Eq. (4.126b) are ingoing at the event horizon and therefore tied to κ^-_{eff}, although adiabaticity is not quite satisfied there.

In principle, one may also calculate the spectrum of *outgoing* Hawking modes seen at the event horizon, corresponding to the effective temperature κ^+_{eff} there, and indeed, an infalling observer will still see an exponentially redshifting past horizon below them after they cross the event horizon.
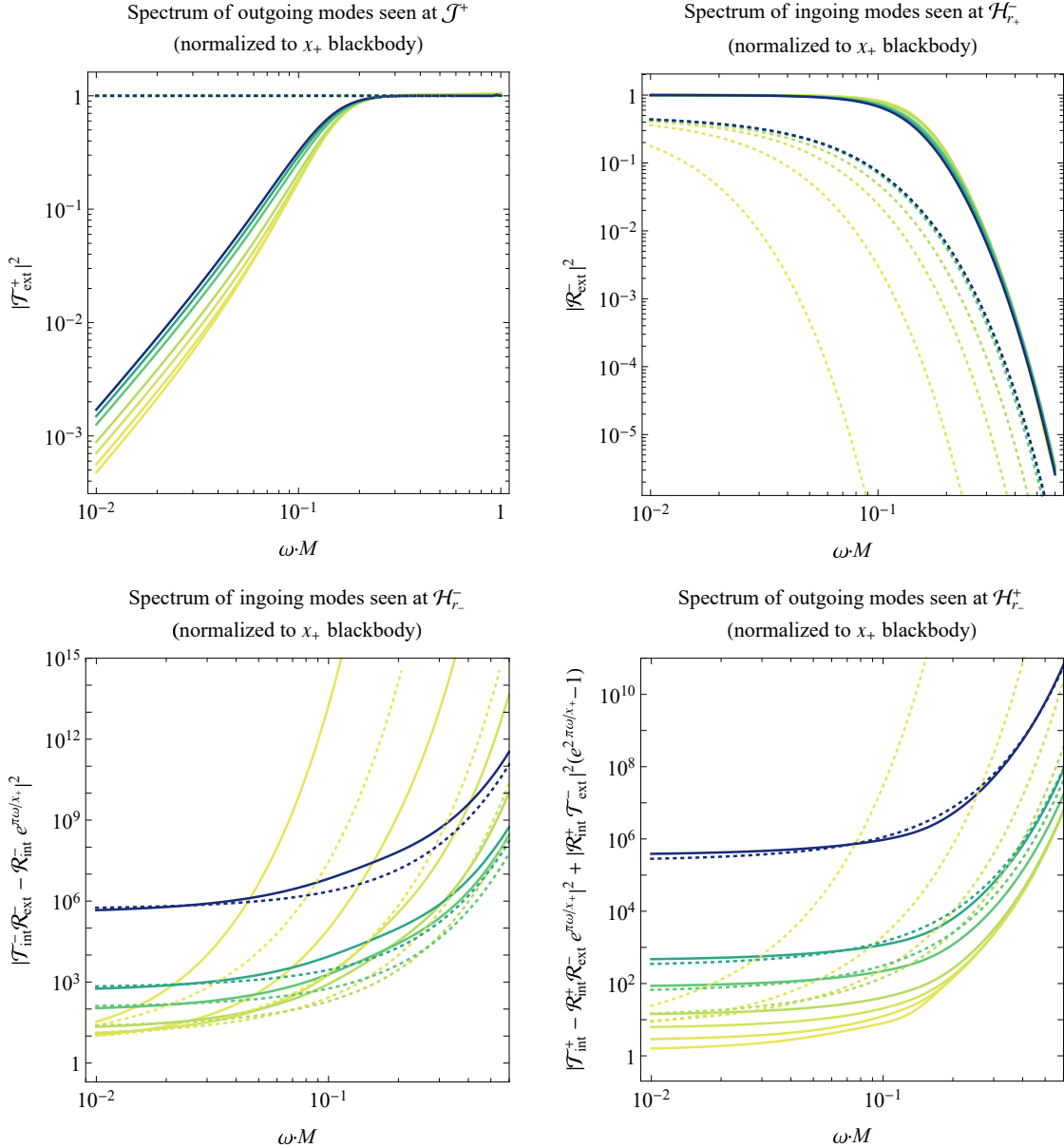
Figure 4.14: Graybody s-mode factors from Eqs. (4.129) modifying the thermal $\kappa_+/(2\pi)$-temperature Hawking spectra seen by an observer asymptotically far from the black hole looking downward at outgoing modes (top left), an ingoing observer at the event horizon looking upward at ingoing modes (top right), an ingoing observer at the inner horizon looking upward at ingoing modes (bottom left), and an outgoing observer at the inner horizon looking downward at outgoing modes (bottom right). Different black hole charges are shown with respective colors from dark blue to yellow: $Q/M = $ 0.1, 0.5, 0.7, 0.9, 0.96, 0.99, and 0.999. Solid curves show the numerically computed spectra, while dotted curves show the positive-valued spectra obtained from a completely thermal distribution with temperatures $\kappa_{\text{eff}}^+/(2\pi)$ from Eq. (4.34) (upper left), $\kappa_{\text{eff}}^-/(2\pi)$ from Eq. (4.35) (upper right), $\kappa_{\text{eff}}^-/(2\pi)$ from Eq. (4.36) (lower left), or $\kappa_{\text{eff}}^+/(2\pi)$ from Eq. (4.37) (lower right).

However, calculating the outgoing modes for an ingoing horizon observer (and vice versa) requires Fourier-decomposing the observer's modes of Eq. (4.12) so that they can be backpropagated to the past horizon, which will be deferred to a future study; for more details, see, e.g., Ref. [108].

Though only frequencies as high as $\omega M \sim 0.6$ are shown for the horizon spectra of Fig. 4.14 (the $\omega M \gg 1$ regime is beyond the code's numerical capabilities), any higher frequencies are all but irrelevant compared to the luminosity peaks of the blackbodies, which, though not shown in the normalized spectra of Fig. 4.14, occur between $\omega M \sim 0.2$ (for the lowest charge Q) and $\omega M \sim 0.01$ (for the highest charge plotted).

While the Hawking spectra seen at infinity and the event horizon contain straightforward graybody deviations from a thermal spectrum, the spectra seen at the inner horizon tell a different story. Two spectra for the left and right portions of the inner horizon are shown in the lower left and right panels of Fig. 4.14, respectively. These spectra bear little resemblance to the initial κ_+ blackbodies seen at infinity; nonetheless, the spectra are still presented normalized to the κ_+ blackbodies due to the factors in the denominators of Eqs. (4.129).

At the left leg of the inner horizon (lower left panel of Fig. 4.14), the particle spectra given by the Bogoliubov coefficient between the observer's and emitter's vacuum states all appear to be ultraviolet-divergent; if an exponential cutoff does occur, it must happen at frequencies higher than what was able to be computed. A qualitatively similar spectrum would occur for a Planckian distribution with negative temperature (albeit with an overall sign change), as anticipated in Secs. 4.3 and 4.4, and for reference, the corresponding negative-temperature κ_{eff}^- blackbodies are shown by the dotted curves in Fig. 4.14. Notably, as $Q/M \to 1$, the ultraviolet divergence grows stronger, though as $Q/M \to 0$, the entire spectrum diverges (once Q/M goes below ~ 0.01, the spectrum is too high to be seen on these lower two plots). Such a panchromatic divergence can be attributed to the fact that the inner horizon's surface gravity κ_-, and consequently the temperatures κ_{eff}^- from Eq. (4.36) and κ_{eff}^+ from Eq. (4.37), grow to infinity in the Schwarzschild limit, since $r_- \to 0$.

At the inner horizon's right leg (lower right panel of Fig. 4.14), the curves once again diverge at higher frequencies, indicating quasitemperatures much higher than the underlying κ_+ blackbodies.
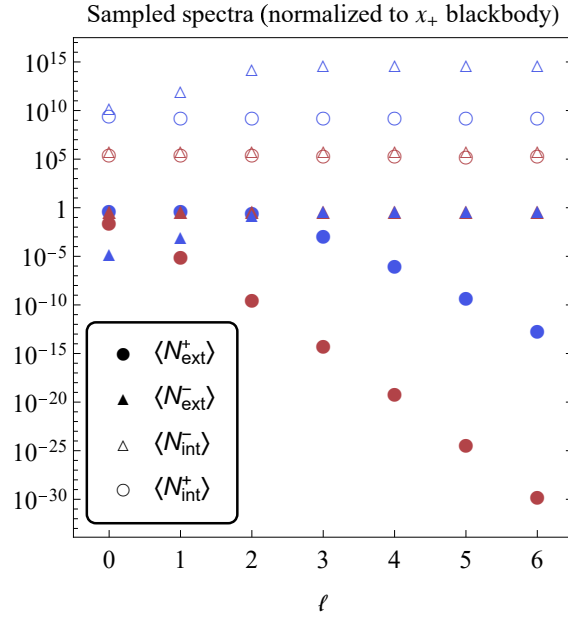
Figure 4.15: Sampled points at $\omega M = 0.5$ (blue) and $\omega M = 0.05$ (red) for the four spectra of Fig. 4.14 when generalized to higher-ℓ modes. All points use a black hole charge of $Q/M = 0.1$. The $\ell = 0$ mode dominates the spectrum $\langle N_{\text{ext}}^+ \rangle$ seen at infinity, but higher-ℓ modes make substantial contributions to the spectra seen at the horizons.

These temperatures may be high enough to be negative, though when the black hole charge is large enough, the spectra begin to deviate significantly from the dotted lines showing κ_{eff}^- blackbodies. Nonetheless, the spectrum is still everywhere nonthermal as a result of the frequency-dependent additive final term in Eq. (4.129d).

4.5.1.2   Spectra for higher spherical harmonics

The dependence of the Hawking spectra on the spherical harmonic mode number ℓ is shown in Fig. 4.15. Instead of plotting the entire spectrum for each ℓ, two points are sampled from each spectrum, one at a higher frequency ($\omega M = 0.5$, blue points) and one at a lower frequency ($\omega M = 0.05$, red points). In almost all cases (except the spectra for $\langle N_{\text{ext}}^- \rangle$; see the upper right panel of Fig. 4.14), the higher-frequency blue points exceed their lower-frequency red counterparts, indicating that the general qualitative trends of each spectrum in Fig. 4.14 remain intact for higher-ℓ modes.

For the Hawking radiation seen asymptotically far from the black hole, the $\ell = 0$ mode

dominates over any higher harmonics [144], as can be seen from the drop-off of the solid circular points in Fig. 4.15. However, for radiation seen at the outer and inner horizons, the spectra do not seem to fall off as ℓ is increased. It would appear that the ultraviolet-divergent Hawking spectra contain substantial contributions not only from the spherical $\ell = 0$ modes, but also from much higher harmonics. One important implication of this result is that semiclassical calculations of the renormalized stress-energy tensor in the (1+1)D Polyakov approximation potentially miss out on key beyond-s-wave physics near the horizons.

4.5.2   Rotating black holes

Now consider the following complementary analysis to the spherical case of Sec. 4.5.1, for Kerr black holes. An additional generalization will be made in this section to understand not only the behavior of a scalar field, but the more general case of a bosonic field with any integer spin.

Over the Kerr background one can place a canonically quantized, massless, bosonic field $_s\hat{\phi}(x)$ with spin weight[7] s. Due to the axial symmetry of the metric encoded by Eq. (4.13), the field $_s\hat{\phi}(x)$ can be decomposed into a complete set of modes $_s\phi_{\omega\ell m}(x)$ with ladder operators, as in Eq. (3.13), to yield

$$_s\phi_{\omega\ell m} = \frac{_sf_{\omega\ell}(r,t,\varphi)\ _sS_{\ell m}^{\omega}(\theta)}{R\sqrt{4\pi\omega}} \tag{4.130}$$

(the additional factor of R is included here as in Ref. [179] so that, among other reasons, the Wronskian of the wave equation will be constant in r). Focusing on the scalar (spin-0) case and dropping the spin index in what follows for clarity,[8] the quantum numbers are the frequency $\omega \in \mathbb{R}$,

---

[7]Following the notation of Teukolsky [170], the term "spin weight" is used for the parameter s, which either equals the (positive-valued) spin of the field when the ingoing component of the wave is the dominant propagating mode, or the negative of the field's spin when the outgoing component of the wave is the dominant propagating mode. However, s is *not* the same as the spin weight defined in the GHP formalism [75] as the eigenvalue of the Lorentz-invariant chiral spin operator and instead would there be called the "boost weight," the eigenvalue of the generator of Lorentz boosts. See Sec. IIIC of Ref. [89] for more details.

[8]The calculations of the Hawking spectra, and in particular the formulae of Eqs. (4.147), are valid for any bosonic field with integer spin, with the only change coming from the numerically-obtained values of the scattering coefficients for a given field's wave equation; see Appendix E for more details. In the derivation that follows, focus will be placed on the scalar (spin-0) case; non-zero spins will be analyzed in Sec. 4.5.2.2.

the multipolar number $\ell \in \mathbb{Z}_{\geq 0}$, and the azimuthal number $m \in \mathbb{Z}_{\leq \ell} \cap \mathbb{Z}_{\geq -\ell}$. Thanks to azimuthal and time translation invariance, the mode function $f_{\omega \ell}(r, t, \varphi)$ may be further separated as

$$f_{\omega \ell}(r, t, \varphi) = \psi_{\omega \ell}(r) \; e^{\pm i \omega t} \; e^{\pm i m \varphi}. \tag{4.131}$$

If the scalar field's modes $\phi_{\omega \ell m}(x)$ obey the Klein-Gordon wave equation $\Box \phi_{\omega \ell m} = 0$, then the polar function $S^{\omega}_{\ell m}(\theta)$ will satisfy the equation for spheroidal wave functions [27], while the radial function $\psi_{\omega \ell}(r)$ will satisfy the radial Teukolsky equation [170]

$$\frac{d^2 \psi_{\omega \ell}}{dr^{*2}} + V_{\omega \ell m} \psi_{\omega \ell} = 0, \tag{4.132}$$

with the scattering potential

$$V_{\omega \ell m} \equiv \left(\omega - \frac{ma}{R^2}\right)^2 - \frac{\lambda_{\omega \ell m} \tilde{\Delta}}{r} - \tilde{\Delta}^2 - \frac{d\tilde{\Delta}}{dr^*}. \tag{4.133}$$

In Eq. (4.133), the constant $\lambda_{\omega \ell m}$ is defined in Appendix E below Eq. (E.2), the tortoise coordinate r^* is defined by

$$\frac{dr}{dr^*} = \frac{\Delta}{R^2}, \tag{4.134}$$

and the function $\tilde{\Delta}$ is defined by

$$\tilde{\Delta}(r) \equiv \frac{r\Delta}{R^4}. \tag{4.135}$$

The focus of the present section will be the cases in which the scattering potential of the radial Klein-Gordon wave equation, given by Eq. (4.133), asymptotically reduces to a constant in the tortoise coordinate r^*. Such cases occur when the observer is asymptotically far away and when the observer is crossing one of the black hole's horizons:

$$V_{\omega \ell m} \to \begin{cases} \omega, & r \to \infty \\ \omega_{\pm}, & r \to r_{\pm} \end{cases}, \tag{4.136}$$

where

$$\omega_{\pm} \equiv \omega - m\Omega_{\pm} = \omega - m\frac{a}{R_{\pm}^2}. \tag{4.137}$$

In these limits, the wave equation possesses the asymptotic eigenmode solutions $\sim \exp(\pm i V_{\omega \ell m} r^*)$, and the problem of mode propagation between these limits reduces to a 1D scattering problem in r^*.

One can define the following future boundary conditions (i.e., in the limit as the timelike coordinates t_{ext} or r^*_{int} are taken to positive infinity in their respective domains) for each of four complete sets of radial mode solutions to the wave Eq. (4.132), corresponding to observers locally defining a positive frequency ω and azimuthal quantum number m:

$$^{\text{ext}}f^+_{\text{ob}} \to \begin{cases} \mathrm{e}^{im\varphi - i\omega u}, & r^*_{\text{ext}} \to \infty \\ 0, & r^*_{\text{ext}} \to -\infty \end{cases}, \tag{4.138a}$$

$$^{\text{ext}}f^-_{\text{ob}} \to \begin{cases} \mathrm{e}^{im\varphi_+ - i\omega v}, & r^*_{\text{ext}} \to -\infty \\ 0, & r^*_{\text{ext}} \to \infty \end{cases}, \tag{4.138b}$$

$$^{\text{int}}f^+_{\text{ob}} \to \begin{cases} \mathrm{e}^{-im\varphi_- + i\omega u}, & t_{\text{int}} \to \infty \\ 0, & t_{\text{int}} \to -\infty \ \cup \ r^*_{\text{ext}} \to \infty \end{cases}, \tag{4.138c}$$

$$^{\text{int}}f^-_{\text{ob}} \to \begin{cases} 0, & t_{\text{int}} \to \infty \ \cup \ r^*_{\text{ext}} \to \infty \\ \mathrm{e}^{im\varphi_- - i\omega v}, & t_{\text{int}} \to -\infty \end{cases}, \tag{4.138d}$$

where $\varphi_{\pm}$, defined in Eq. (4.19), is the azimuthal coordinate that is regular for an observer crossing the horizon at $r = r_{\pm}$. Note that these modes differ slightly from the Eddington-Finkelstein modes used in Ref. [179] in the use of ω rather than $\omega_{\pm}$ at the outer/inner horizons, since the modes here are constructed explicitly to match the positive-frequency experience of a free-falling observer rather than to provide pure eigenmode solutions to the wave equation (more details below). These initialized modes are shown by the solid arrows in Fig. 4.13. The notation for labeling these modes is the same as in Sec. 4.5.1; modes in the exterior (interior) portion of the spacetime are labeled $^{\text{ext}}f$ ($^{\text{int}}f$), and modes with canonically affine boundary conditions along a future null boundary transverse to outgoing (ingoing) null rays are labeled f^+ (f^-).

The subscript "ob" in the modes of Eqs. (4.138) is used to indicate that each mode corresponds to the waves that would be seen in the frame of an inertial observer positioned asymptotically close to its respective null boundary. To see why this is the case, consider the following analysis in analog to that performed in Sec. 4.2.2 for the modes of the emitter.

If an infalling observer is placed asymptotically far from the black hole at rest, with $E = 1$, the outgoing modes encoded by $^{\text{ext}}f_{\text{ob}}^+$ will track the same eikonal wavefront as the outgoing null congruence derived from their own proper time, since

$$\lim_{r \to \infty} \frac{du}{d\tau} = \lim_{r \to \infty} \left(\dot{t} - \frac{R^2}{\Delta} \dot{r} \right) = 1. \tag{4.139}$$

Similarly, if an infalling observer is placed asymptotically close to the event horizon, they will see the ingoing waves of $^{\text{ext}}f_{\text{ob}}^-$ tick at a rate proportional to their own proper time:

$$\lim_{r \to r_+} \frac{dv}{d\tau} = \frac{aP_\theta}{\rho^2} + \frac{R^2(K + r^2)}{2\rho^2 P_r}, \tag{4.140}$$

with the Hamilton-Jacobi parameters $P_r(r) > 0$ and $P_\theta(\theta)$ defined in Eq. (4.15). Note that while the expression on the right-hand side of Eq. (4.140) does not generally reduce to unity (although it does simplify to 1/2 for the on-axis observer considered in Sec. 4.3.2.1), the expression is nonetheless frozen at a constant value as r^* is varied, in contrast to the divergent behavior for *outgoing* waves seen by an ingoing emitter at the event horizon from Eq. (4.21).

For the remaining two interior modes $^{\text{int}}f_{\text{ob}}^\pm$, if an infalling ($\dot{r} < 0$) observer is placed at the inner horizon and is ingoing ($P_r > 0$), their proper time will be proportional to the ingoing modes $^{\text{int}}f_{\text{ob}}^-$, while if the observer is outgoing ($P_r < 0$), their proper time will be proportional to the outgoing modes $^{\text{int}}f_{\text{ob}}^+$. The constant of proportionality is the same as the right-hand side of Eq. (4.140), with r now at its inner horizon value. Thus, the modes defined by Eqs. (4.138) each correspond to the eikonal waves seen by an inertial, infalling observer passing through their respective hypersurface boundaries.

Since each set of boundaries considered in Eqs. (4.138) for each of the four sets of modes forms a complete null Cauchy hypersurface terminating at spacelike infinity, the radial wave Eq. (4.132) can be used to back-propagate each mode throughout the rest of the spacetime. Of particular importance is the behavior of these observer modes at the past null boundaries where the initial data for the emitter's Unruh modes are defined, since if both $f_{\rm ob}$ and $f_{\rm em}$ are known along the same Cauchy hypersurface, Eqs. (4.115) and (3.21) can be used to compute the scalar product between the observer's and emitter's modes and therefore the spectrum of Hawking radiation.

Equivalently, one may consider propagating the emitter's modes forward and evaluating the mode scalar product along the future null boundary where the initial data for the observer's modes are defined, instead of propagating the observer's modes backward to the past null boundary. However, this task is more difficult since the Kruskal coordinate U used to define the emitter's Unruh modes contains non-trivial coupling between t and r, so that the wave equation is not separable in these coordinates when initialized with the Unruh modes.

Fortunately, as mentioned above, the problem of finding the observer modes at the past null boundaries is a straightforward 1D scattering problem in r^*. Define reflection coefficients $\mathcal{R}_{\rm int,ext}^{\pm}$ and transmission coefficients $\mathcal{T}_{\rm int,ext}^{\pm}$ for the interior and exterior portions of the spacetime (with the same notation as in Sec. 4.5.1), depicted visually by the scattering paths in the Penrose diagrams to the right of each of the expressions below. The boundary conditions to be solved for the radial modes of Eq. (4.131), evaluated at the mode labeled with ω, ℓ, and m, are provided in Eqs. (4.141)–(4.144) below. For the modes of Eq. (4.138a) encoded by an observer asymptotically far away from the black hole, one has

$$
{}^{\rm ext}\psi_{\rm ob}^{+} \to
\begin{cases}
{\rm e}^{i\omega r^*} + \mathcal{R}_{\rm ext,\omega}^{+}\,{\rm e}^{-i\omega r^*}, & r_{\rm ext}^* \to \infty, \\[2mm]
\mathcal{T}_{\rm ext,\omega}^{+}\,{\rm e}^{i\omega_+ r^*}, & r_{\rm ext}^* \to -\infty,
\end{cases}
\tag{4.141}
$$

for the modes of Eq. (4.138b) encoded by an ingoing observer at the event horizon, one has

$$
{}^{\text{ext}}\psi_{\text{ob}}^- \to
\begin{cases}
\mathcal{T}_{\text{ext},\omega}^- e^{-i(\omega+m\Omega_+)r^*}, & r_{\text{ext}}^* \to \infty, \\[2ex]
e^{-i\omega r^*} + \mathcal{R}_{\text{ext},\omega}^- e^{i\omega r^*}, & r_{\text{ext}}^* \to -\infty,
\end{cases}
\tag{4.142}
$$

for the modes of Eq. (4.138c) encoded by an outgoing observer at the inner horizon, one has

$$
{}^{\text{int}}\psi_{\text{ob}}^+ \to
\begin{cases}
e^{-i\omega r^*}, & r_{\text{int}}^* \to \infty, \\[2ex]
\mathcal{T}_{\text{int},\omega}^+ e^{-i(\omega_+ + m\Omega_-)r^*} + \mathcal{R}_{\text{int},\omega}^+ e^{i(\omega_+ + m\Omega_-)r^*}, & r_{\text{int}}^* \to -\infty, \\[2ex]
\mathcal{R}_{\text{int},\omega}^+ \left(e^{i(\omega_+ + m\Omega_-)r^*} + \mathcal{R}_{\text{ext},\omega}^- e^{-i(\omega_+ + m\Omega_-)r^*} \right), & r_{\text{ext}}^* \to -\infty, \\[2ex]
\mathcal{R}_{\text{int},\omega}^+ \mathcal{T}_{\text{ext},\omega}^- e^{i(\omega+m\Omega_-)r^*}, & r_{\text{ext}}^* \to \infty,
\end{cases}
\tag{4.143}
$$

and for the modes of Eq. (4.138d) encoded by an ingoing observer at the inner horizon, one has

$$
{}^{\text{int}}\psi_{\text{ob}}^- \to
\begin{cases}
e^{-i\omega r^*}, & r_{\text{int}}^* \to \infty, \\[2ex]
\mathcal{T}_{\text{int},\omega}^- e^{-i(\omega_+ + m\Omega_-)r^*} + \mathcal{R}_{\text{int},\omega}^- e^{i(\omega_+ + m\Omega_-)r^*}, & r_{\text{int}}^* \to -\infty, \\[2ex]
\mathcal{T}_{\text{int},\omega}^- \left(e^{-i(\omega_+ + m\Omega_-)r^*} + \mathcal{R}_{\text{ext},\omega}^- e^{i(\omega_+ + m\Omega_-)r^*} \right), & r_{\text{ext}}^* \to -\infty, \\[2ex]
\mathcal{T}_{\text{int},\omega}^- \mathcal{T}_{\text{ext},\omega}^- e^{-i(\omega+m\Omega_-)r^*}, & r_{\text{ext}}^* \to \infty,
\end{cases}
\tag{4.144}
$$

The scattering coefficients in the above expressions can be calculated through numerical means; here the computation is performed with the help of the Teukolsky 0.3.0 package of the Black Hole Perturbation Toolkit [30]. Since this `Mathematica` package is only designed to compute exterior scattering coefficients, I have made adaptations to the code to extend computations to the spacetime region between the inner and outer horizons; details on these modifications can be found in Appendix E.

The scalar product of Eq. (3.21) can then be evaluated along the past null Cauchy hyper-surface where the Unruh state is initialized. The end goal is the computation of Eq. (4.115), the

vacuum expectation value of the particle number operator for an observer either at infinity, the event horizon, or the ingoing or outgoing portions of the inner horizon. These spectral number distributions will be labeled $\langle N_{\text{ext}}^+ \rangle_{\omega\ell m}$, $\langle N_{\text{ext}}^- \rangle_{\omega\ell m}$, $\langle N_{\text{int}}^+ \rangle_{\omega\ell m}$, and $\langle N_{\text{int}}^- \rangle_{\omega\ell m}$ for the respective modes of Eqs. (4.141)–(4.144).

The analysis proceeds almost identically to that of the spherical case in Sec. 4.5.1, with one small but crucial difference: the Kerr scattering potential of Eq. (4.133) asymptotically approaches a different constant value at infinity compared to the values at the event horizon and the inner horizon; see Eq. (4.136). Thus, observer modes that are initialized as

$$\phi_{\text{ob}} \sim \frac{\mathrm{e}^{i\omega r^*}}{R\sqrt{4\pi\omega}} \tag{4.145}$$

at future null infinity will be back-scattered into the form

$$\phi_{\text{ob}} \sim \frac{\mathrm{e}^{i\omega_+ r^*}}{R_+\sqrt{4\pi\omega}} \tag{4.146}$$

along the past horizon, and so forth.

The details for the calculation of the resulting number operator vacuum expectation values from Eq. (4.115) are given in Appendix C. The result, up to a normalization factor, is

$$\langle N_{\text{ext}}^+ \rangle_{\omega\ell m} = \left(\frac{\omega_+}{\omega}\right) \frac{\left|\mathcal{T}_{\text{ext},\omega}^+\right|^2}{\mathrm{e}^{\frac{2\pi}{\kappa_+}\omega_+} - 1}, \tag{4.147a}$$

$$\langle N_{\text{ext}}^- \rangle_{\omega\ell m} = \frac{\left|\mathcal{R}_{\text{ext},\omega}^-\right|^2}{\mathrm{e}^{\frac{2\pi}{\kappa_+}\omega} - 1}, \tag{4.147b}$$

$$\langle N_{\text{int}}^- \rangle_{\omega\ell m} = \left(\frac{\omega_+ + m\Omega_-}{\omega}\right) \frac{\left|\mathcal{T}_{\text{int},\omega}^- \mathcal{R}_{\text{ext},\omega}^- - \mathcal{R}_{\text{int},\omega}^- \mathrm{e}^{\frac{\pi}{\kappa_+}(\omega_+ + m\Omega_-)}\right|^2}{\mathrm{e}^{\frac{2\pi}{\kappa_+}(\omega_+ + m\Omega_-)} - 1}, \tag{4.147c}$$

$$\langle N_{\text{int}}^+ \rangle_{\omega\ell(-m)} = \left(\frac{\omega_+ + m\Omega_-}{\omega}\right) \frac{\left|\mathcal{T}_{\text{int},\omega}^+ - \mathcal{R}_{\text{int},\omega}^+ \mathcal{R}_{\text{ext},\omega}^- \mathrm{e}^{\frac{\pi}{\kappa_+}(\omega_+ + m\Omega_-)}\right|^2}{\mathrm{e}^{\frac{2\pi}{\kappa_+}(\omega_+ + m\Omega_-)} - 1} + \left(\frac{\omega + m\Omega_-}{\omega}\right)\left|\mathcal{R}_{\text{int},\omega}^+ \mathcal{T}_{\text{ext},\omega}^-\right|^2, \tag{4.147d}$$

with the surface gravity κ_+ of Eq. (4.17), the horizon-limit frequency ω_+ of Eq. (4.137), and the

transmission and reflection coefficients $\mathcal{T}_{\text{int,ext}}^{\pm}$ and $\mathcal{R}_{\text{int,ext}}^{\pm}$ of Eqs. (4.141)–(4.144). Note that in the limit $a \to 0$, the expressions in Eqs. (4.147) reduce to the same Schwarzschild expressions obtained in Sec. 4.5.1.

The physical interpretation of the vacuum expectation values from Eqs. (4.147) is that they measure the spectral emission rate; i.e., the mean number of quanta in the mode with frequency ω and angular mode numbers ℓ and m, seen by a freely falling observer at each respective location, per the observer's proper time τ_{ob}.

One may at first sight worry that for exterior scattering, when $\omega < m\Omega_+$ (and similarly, $\omega < m(\Omega_+ - \Omega_-)$ for the interior), the frequency prefactors in the above expressions for $\langle N_{\text{ext}}^+ \rangle_{\omega \ell m}$ and $\langle N_{\text{int}}^{\pm} \rangle_{\omega \ell m}$ become negative. This is connected to the well-known phenomenon of superradiance, in which the transmission probability in a rotating system becomes negative and the absorption probability exceeds unity, so that scattered waves gain amplitude upon reflection and extract energy from the black hole [166]. However, the aforementioned negative terms are exactly canceled by the Planckian terms in the denominator of each expression, which also become negative in the same superradiant regime. Therefore, the expected number of particles seen by the observer will always remain positive.

4.5.2.1   Spectra for scalar modes

First, consider the Hawking radiation from massless scalar mode excitations, with spin $s = 0$. The more general bosonic cases ($s = 1$ for photons and $s = 2$ for gravitons) will be considered in the next subsection.

The Hawking spectra for the lowest set of modes ($\ell = 0$, $m = 0$) are shown in Fig. 4.16. These s-wave spectra are computed numerically for a variety of black hole spin parameters seen by the four observers represented in Eqs. (4.147). First, the standard graybody spectrum seen asymptotically far from the black hole is shown in the upper left panel of Fig. 4.16. Unlike the blackbody-normalized spectra of Fig. 4.14 for Reissner-Nordström, the distributions here are plotted as spectral intensities, which scale as $\omega^3 \langle N \rangle$, so that a Planckian blackbody would appear with a quadratic power law at

the geometric optics limit). However, at low frequencies, the graybody spectra differ from their blackbody counterparts by a power law index of 2, in agreement with the analytic prediction of Starobinsky in the limit $\omega \to 0$ [166].

While the spectrum of Hawking radiation seen by someone looking inward from asymptotically far away contains entirely straightforward graybody deviations at low frequencies, the spectrum seen by someone crossing the event horizon contains graybody deviations at high frequencies, as shown in the upper right panel of Fig. 4.16. The spectral intensity is still roughly the same order of magnitude as that seen at infinity, in accordance with assertion #1 in Sec. 4.1. But at higher frequencies, the spectrum drops to zero much more quickly than one might expect from blackbody predictions. The reason for the dropoff is that in the geometric optics limit, fewer outgoing modes originating from an Unruh emitter at the horizon will be reflected and return to the observer; instead, more will escape as rays to infinity instead of being back-scattered as waves. Since the Hawking spectrum seen by an observer looking outward from the event horizon is determined entirely by these reflected modes (and not from transmitted ingoing modes originating from past null infinity, which do not exhibit the characteristic exponential peeling), Hawking radiation detected at the event horizon is suppressed at high frequencies.

Before discussing the Hawking spectrum seen by someone at the inner horizon, one feature present in all panels of Fig. 4.16 is the suppression of Hawking radiation for faster-spinning black holes. As the spin parameter a is increased and the curves change color from dark blue to yellow, one may note that the higher-a curves have overall lower intensities. The faster a black hole spins, the colder it becomes, regardless of where the observer lies within the spacetime.

The Hawking spectra seen by an observer at the Cauchy horizon are shown in the lower two panels of Fig. 4.16. The lower left panel corresponds to an ingoing observer looking outward at the sky above (crossing the null boundary $\mathcal{H}_{r_-}^-$ in Fig. 4.13), while the lower right panel corresponds to an outgoing observer looking inward at the past horizon below (crossing the null boundary $\mathcal{H}_{r_-}^+$ in Fig. 4.13). These spectra are plotted alongside the dashed blackbody curves (after taking the absolute value) for the negative temperature given by the surface gravity of the inner horizon,

$\kappa_-/(2\pi)$. At low frequencies, all the curves approach the same quadratic power law, but instead of simply falling off exponentially as the frequency ω is increased, the curves continue to climb orders of magnitude higher than any positive-temperature blackbody would allow. However, the physically measurable spectral intensity does not contain an ultraviolet divergence for non-zero rotation. Eventually, as suggested in the Reissner-Nordström case of Sec. 4.5.1, the exponential Wien tail dominates as $\omega \to \infty$ so that the spectral intensity returns to zero. But as the spin a decreases and the inner horizon approaches the $r = 0$ singularity, Hawking radiation is able to reach higher and higher frequencies before effectively experiencing an ultraviolet cutoff. The Schwarzschild limit $a/M \to 0$ is not shown in these lower two panels, since the spectral intensity in that case becomes infinite at all frequencies.

It should be noted that the Cauchy horizon Hawking spectra shown in Fig. 4.16 are not *a priori* expected to diverge. The divergent negative Hawking temperatures seen at the Cauchy horizon in Sec. 4.3.2 correspond to ingoing observers looking inward (κ_{eff}^+ for $P_r > 0$) and outgoing observers looking outward (κ_{eff}^- for $P_r < 0$). In contrast, Fig. 4.16 shows observers at the Cauchy horizon looking in the direction opposite the Penrose blueshift singularity—ingoing observers looking outward and outgoing observers looking inward. Calculations for the former two scenarios would involve the inner product of the Unruh emitter's Kruskal modes with the observer's Fourier-decomposed and back-propagated Kruskal modes [108], which is nonetheless expected to yield an infinite spectral intensity at all frequencies. What Fig. 4.16 shows is that in addition to the classical (and likely also semiclassical) blueshift singularity, an observer at the Cauchy horizon will see the entire sky around them glowing brightly with Hawking radiation.

Beyond the s-wave approximation, the Hawking spectral intensities for higher-ℓ modes are shown in Fig. 4.17. Instead of showing entire spectra as functions of the frequency ω, these spectral intensities are evaluated at a specific mid-range frequency ($\omega \cdot M = 0.1$) so that the dependence on the spin parameter a can be plotted more clearly.

For an observer asymptotically far from the black hole, the higher-ℓ spectral intensities are shown in the upper left panel of Fig. 4.17. As the black hole spin a is taken to zero, all azimuthal
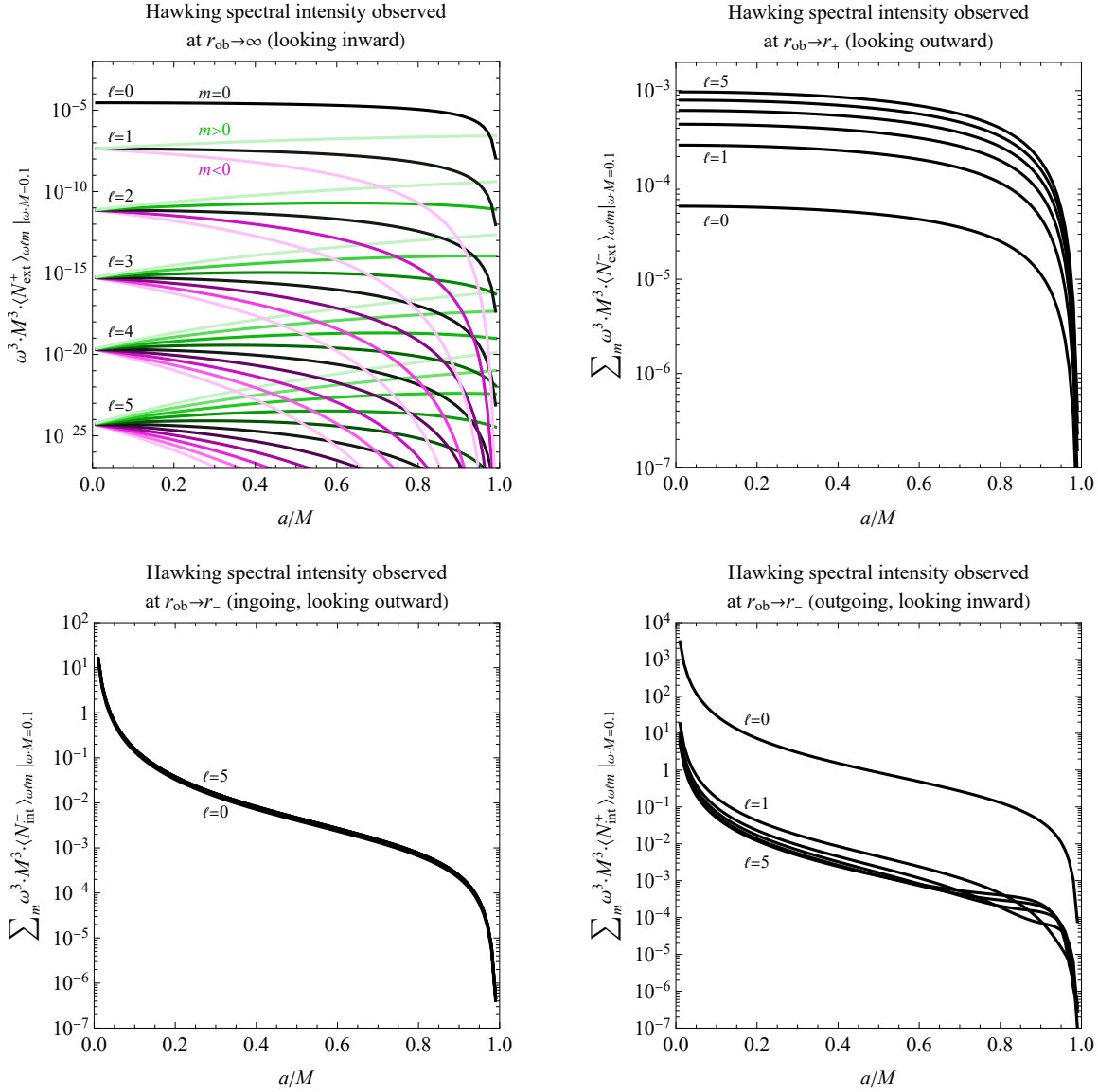
Figure 4.17: Hawking spectral intensities for higher ℓ- and m-modes, seen by an infalling observer at infinity (upper left panel), the event horizon (upper right panel), and the Cauchy horizon (lower two panels) in the Kerr spacetime as a function of the black hole spin parameter a/M. All modes are evaluated at a frequency of $\omega \cdot M = 0.1$. Each individual m-mode for a given ℓ are presented for the observer at infinity, while the m-modes are summed for each ℓ for the other three observers.

m-modes within a given ℓ mode converge to the same value, as expected. These intensities in the

low-a limit drop off as ℓ increases, so that the lowest angular mode dominates the Hawking spectrum.

In particular, the ℓ-modes are spaced apart by three to five orders of magnitude, in agreement with

the approximate behavior predicted by Starobinsky [166]:

$$|\mathcal{T}_{\text{ext}}^+|^2 \propto \frac{(\omega \cdot M)^{2\ell+1}(\ell!)^4}{[(2\ell)!]^2[(2\ell+1)!!]^2}. \tag{4.148}$$

Additionally, note that in the upper left panel of Fig. 4.17, the green curves (corresponding to positive m, with $m = \ell$ located highest in each group) always lie above the corresponding $m = 0$ curves, while the magenta curves (corresponding to negative m, with $m = -\ell$ located lowest in each group) always lie below the corresponding $m = 0$ curves. Physically, Hawking particles are always being emitted preferentially with the same angular momentum as the black hole, so that over time, the black hole will tend to spin down as the Hawking particles carry away excess angular momentum [94].

In the upper right panel of Fig. 4.17, the Hawking spectral intensity is shown for an observer crossing the event horizon, yielding quite different behavior than that of an observer far away. While the $\ell = 0$ mode dominates for an asymptotically distant observer, all higher-ℓ modes are present when the observer is in a regime where they are close enough to access more angular information than s-waves. While this panel plots the sum over all m-modes in a given ℓ-mode, it should be noted that as $\ell \to \infty$, all the modes with $m = 0$ tend to a constant value, just as quickly as all the modes with $m = 0$ for an observer at infinity tend to zero—note the relationship between $\left|\mathcal{T}_{\text{ext},\omega}^+\right|^2$ and $\left|\mathcal{R}_{\text{ext},\omega}^-\right|^2$ in Eq. (E.16).

The lower two panels of Fig. 4.17 similarly show equal contributions from all higher-ℓ modes in the full Hawking spectrum seen by an infalling observer near the Cauchy horizon. Just as expected, the spectral intensity decreases as the black hole spin a increases, and the intensity increases or decreases monotonically with ℓ, except in the near-extremal case for an outgoing observer looking inward. The higher-ℓ behavior demonstrated in Fig. 4.17 matches that of the Reissner-Nordström case in Fig. 4.15. Note that as $a \to 0$, the observed Hawking spectral intensity diverges as the inner horizon meets the $r = 0$ singularity, and as $a \to M$, the observed Hawking radiation vanishes as the inner horizon meets the outer horizon to create an extremal, zero-temperature spacetime.

Hawking spectral intensity observed
at r_{ob} for different spin modes
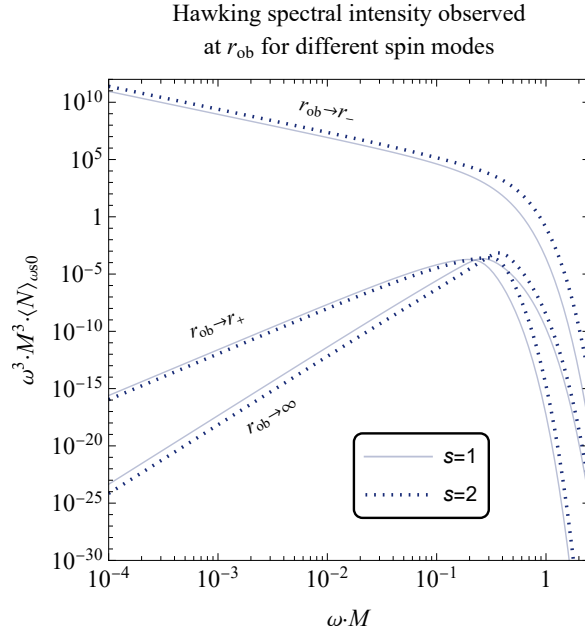
Figure 4.18: Graybody spectra for the electromagnetic (solid curves, $(s,\ell,m) = (1,1,0)$) and gravitational (dotted curves, $(s,\ell,m) = (2,2,0)$) components of the Hawking radiation seen by an inertial observer at Boyer-Lindquist radius r_{ob}. All spectra are evaluated for a Kerr black hole with angular momentum $a/M = 0.1$. These higher-spin spectra are qualitatively similar to their scalar counterparts from Fig. 4.16, except in the case of an outgoing observer at the inner horizon, who sees an infrared-divergent spectrum.

4.5.2.2 Spectra for higher-spin modes

While scalar modes (with spin 0) are commonplace in calculations of semiclassical effects in curved spacetimes due to the scalar wave equation's simplicity and the "physical enough" interpretation of modeling a single degree of freedom from a photon field, one can obtain more physically meaningful results by considering the higher-spin generalization of the wave equation given by Eq. (E.2).

The Hawking particles that will be considered here are photons from an electromagnetic field (spin-1) and gravitons from a gravitational field (spin-2). For all integer spins, the spectra of Eqs. (4.147) retain their Planckian terms, with the only modifications arising from the scattering coefficients calculated from each spin's corresponding wave equation [144].

The spectra for Hawking radiation from the lowest ℓ- and m-modes of spin-1 and spin-2 fields are shown in Fig. 4.18. In this plot, it can be seen that the higher-spin fields radiate with roughly

the same spectra as in the scalar case of Fig. 4.16 for exterior observers. When $r_{\mathrm{ob}} \to \infty$, the spin-1 and spin-2 spectra peak at a slightly higher frequency than the spin-0 spectrum (not shown), but they also trail off in the infrared regime with a steeper power-law slope than the spin-0 spectrum. Similarly, the spectra for an observer at the event horizon appear almost identical for different values of spin.

All the spectra in Fig. 4.18 are shown for a black hole with angular momentum $a/M = 0.1$. Other values of a yield qualitatively similar results (just as in Fig. 4.16), but the low value of a here is chosen since it gives the most pronounced effects, especially given the proximity of the inner horizon to the central singularity as $a \to 0$.

For an observer at the inner horizon, only the spectrum seen by an outgoing observer looking inward is shown, since the spectra seen by an ingoing observer there for positive values of the spin weight s are suppressed by the vanishing of the interior reflection coefficients dictated by the Heaviside function in Eq. (E.14). If instead one chooses $s = -1$ and $s = -2$ (i.e., the outgoing radiative parts of the field; see Footnote 7), as is common in Kerr perturbation calculations for numerical feasibility, the inner horizon spectra will appear even more ultraviolet-divergent than in the scalar case. But even for the positive spin weights shown in Fig. 4.18, the spectrum of radiation produced from electromagnetic and gravitational modes is infrared-divergent, indicating that an outgoing observer looking inward at the exponentially redshifting and dimming surface of the start that collapsed long ago will see that surface glow more and more brightly in the infrared as they approach the Cauchy horizon.

4.6   Discussion

Hawking radiation is an observer-dependent phenomenon. Here the Bogoliubov coefficient calculation of Hawking [93] has been generalized to determine the effective temperature of semiclassical radiation seen in the vacuum state of the locally inertial rest frame of an arbitrary observer within various black hole spacetimes. Hawking found that if the observer is placed asymptotically far from the black hole, they will see a small amount of approximately thermal radiation emerge from the

vacuum; here the vast parameter space of various classes of observers and types of black holes is explored. All of the observers analyzed here, outside or inside the event horizon, see a non-zero amount of Hawking radiation, sometimes thermal, sometimes not. This radiation appears to originate from the black hole shadow; i.e., the dimming, redshifting surface of the star that collapsed long ago to form the black hole.

Two of the main questions underpinning this study are as follows: how would Hawking radiation appear for someone at a black hole's inner horizon? And what is meant by a negative Hawking temperature in this context? Ultimately, one may wish to understand the full quantum backreaction near the inner horizon, and though the semiclassical quantity $\langle \hat{N}_{\omega \ell m} \rangle$ cannot provide a definitive assertion regarding the fully dynamical, quantum gravitational backreaction, the present analysis does shed further light on the nature of both Hawking radiation and semiclassical black holes with inner horizons.

To study the Hawking radiation seen anywhere near or far from a black hole, the analysis began with the effective temperature functions $\kappa_{\text{eff}}^{\pm}$ for an arbitrary inertial observer at a radius r_{ob} looking radially inward or outward [20, 21], as defined in Sec. 3.2, which reproduces Hawking's original calculation in the geometric optics limit. For a radial infaller in the Reissner-Nordström spacetime, this effective temperature is given by Eqs. (4.33) and Fig. 4.2. For an on-axis infaller in the Kerr spacetime, this effective temperature is given by Eqs. (4.59) and Fig. 4.5.

Several important conclusions can be drawn from the effective temperatures $\kappa_{\text{eff}}^{\pm}$ mentioned above for infallers with no angular momentum. First and most importantly, the effective temperature always diverges at the inner horizon, and regardless of the observer's orbital parameters, it becomes negative (indicative of modes that are blueshifting instead of redshifting) once the observer falls close enough to the inner horizon. As it turns out, this negative temperature is not merely confined to the black hole's interior that would remain inaccessible to the outside universe; instead, when the black hole is close enough to extremality, (when $Q/M \gtrsim 0.943$ for a charged black hole, and when $a/M \gtrsim 0.860$ for Kerr on-axis), the inner horizon becomes close enough to the event horizon that a negative κ_{eff}^{+} is detected *outside* the black hole.

The perception of an effective temperature for an observer looking in a non-radial direction was then analyzed in Sec. 4.4. For a charged black hole, focus was placed on a zero-angular-momentum observer (ZAMO) looking at an angle χ away from the black hole's center (Fig. 4.6). For a rotating black hole, focus was placed on two classes of observers in the equatorial plane: ZAMOs looking at an angle χ away from the principal null direction (Fig. 4.10), and zero-energy (interior Carter) observers looking an angle χ away from the principal null direction and an angle ψ away from the equatorial plane (Fig. 4.12). These observers all generically observe both positive and negative temperatures at different points along their trajectory, and they see a limb-brightened past horizon; i.e., the black hole shadow has the highest effective temperatures at its edges. But most importantly, the effective temperature κ_{eff} always diverges in at least one direction once the observer reaches the inner horizon. For the ZAMOs, the divergence occurs not just in the principal null direction, but in every direction the observer looks in their field of view. The classical phenomenon of mass inflation involves a divergence only at a single radial point in the sky (as an outgoing observer approaches the inner horizon, the sky above them will shrink to a point and become infinitely blueshifted; see Fig. 1.3), but semiclassically, Hawking radiation originating from the past horizon will fill the observer's entire field of view with diverging, negative-temperature radiation as they approach the inner horizon.

Are the approximations of the effective temperature formalism even valid whenever κ_{eff} becomes negative? By studying the adiabatic control function ϵ in Sec. 4.3.1.4, one can learn whether ϵ is small enough for the adiabatic condition to be satisfied and therefore for κ_{eff} to reproduce approximately thermal Bogoliubov coefficients. At the inner horizon, the outgoing modes for an ingoing observer are found to be sufficiently adiabatic as long as the black hole charge Q or spin a is not too small, while the ingoing modes are hardly ever fully adiabatic there.

To complement these effective temperature results and provide a more rigorous calculation in the regimes where the adiabatic condition fails, the analysis concluded in Sec. 4.5 with a full wave mode investigation to determine the Bogoliubov spectrum at each of the asymptotic regimes ($r \to \infty$, $r \to r_+$, and $r \to r_-$). To do so, the observer's wave modes were backpropagated through the spacetime to the position of the Unruh emitter using the wave equation for a massless scalar

Klein-Gordon field, and the inner product of the observer's and emitter's modes was computed. The resulting spectra for a charged black hole are shown in Fig. 4.14 and for a rotating black hole in Fig. 4.16.

Asymptotically far from the black hole, the Hawking spectrum is completely thermal for high enough frequencies (i.e., in the geometric optics limit), which is consistent with the vanishing of the outgoing adiabatic control function ϵ^+ at infinity. In contrast, for an observer at the event horizon, ϵ^+ is almost never significantly smaller than unity, and the corresponding Bogoliubov spectrum does deviate significantly from thermality in the geometric optics limit.

At the inner horizon, the spectrum of scalar particles appears quite different from that of a positive-temperature blackbody, and instead looks much more like the spectrum one would obtain (up to an overall change in sign) from a blackbody with a negative temperature. The spectra are thus mostly consistent with the effective temperature predictions, despite the general lack of adiabaticity in that regime. The familiar Rayleigh-Jeans power law is still present at lower frequencies, but at higher frequencies, the spectral intensity continues to climb even higher, though it is not fully ultraviolet-divergent.

Even if the graybody spectra at the inner horizons analyzed here are not infinitely blueshifted (as some of the effective temperatures $\kappa_{\text{eff}}^{\pm}$ are), it is important to note that the two spectra shown in the lower panels of Figs. 4.14 and 4.16 are associated with the Hawking sectors that are *not* expected to yield diverging effective temperatures (but are nonetheless negative); namely, the ingoing temperature κ_{eff}^- in Eqs. (4.36) and (4.59), and the outgoing temperature κ_{eff}^+ in Eq. (4.37). If an ingoing (or outgoing) observer at the inner horizon looks downward (or upward, respectively), they should be met with an even stronger dose of diverging Hawking radiation. But what the graybody spectra communicate is that for an outgoing observer approaching the inner horizon, while they can look upward to see the Penrose blueshift singularity forming (as in Fig. 1.3), if they look downward at the initially dimming and redshifting past horizon, even this surface will eventually begin to blueshift and produce a high-energy glow of semiclassical radiation.

The implications of these Hawking spectra are clear: the interaction of a quantum scalar field

with a black hole results in runaway particle creation detected at the inner horizon. The particle spectrum diverges at all frequencies when the black hole charge Q or spin a is taken to zero, since the inner horizon coincides with the $r = 0$ singularity that was already found to feature a diverging Hawking flux in Ref. [87]. But even for nonzero charge, the inner horizon spectrum becomes highly blueshifted and implies a substantial semiclassical backreaction.

Such a highly energetic source of radiation will quickly become amplified in the radial direction and provide an ongoing source for the Poisson-Israel mass inflation instability analyzed in Chapter 2. Even if the observer is taken to be something as simple as a two-level atom, one may speculate that the implied Hawking flux would energize the atom to such an extent that the inevitable result is a positive feedback loop resulting in the collapse of the spacetime geometry into a spacelike singularity. The Reissner-Nordström and Kerr metrics cannot remain semiclassically intact; their inner horizons must collapse into a singularity or else evolve dynamically into some potentially horizonless object.

One of the biggest outstanding questions that one may ask concerning this analysis of Hawking radiation in the framework of semiclassical gravity is how the radiation backreacts on the spacetime. Here the spacetime geometry has been kept fixed, but presumably if enough radiation is present, the particles produced will possess a gravitational field of their own that will change the underlying metric. Usually, one assumes that these backreaction effects are negligibly small and the vacuum black hole metric can still be used as a valid approximation of the spacetime geometry for astrophysical black holes. The analysis above shows that this assumption is usually true for observers outside of the event horizon. However, close to the inner horizon, the generally divergent behavior of observed Hawking radiation suggests that inner horizons are not semiclassically self-consistent. The backreaction for astrophysically relevant perturbations is likely to form a strong, spacelike singularity just above the inner horizon (as in Chapter 2), though other mathematical predictions also exist in the literature, such as a weak, null singularity [49] or a rapid implosion toward the formation of a compact horizonless object [18].

The obvious problem with attempting to analyze the effects of backreaction from Hawking radiation in the present framework is that each observer sees a different amount of Hawking radiation,

but they all exist in the same background metric. Even though the radiation is completely real from the perspective of any individual observer, the very definition of a particle depends on an observer's frame of reference, a concept which seems at first glance completely at odds with the central claim in semiclassical gravity that particles arising from quantum fields provide the source of curvature for a global, classical spacetime metric.

Which observer is the one to see the actual radiation that contributes to the underlying spacetime geometry? Is there a preferred quantum reference frame, or will each observer construct their own background based on the particular backreaction they see in their own frame? The usual approach in semiclassical gravity is to place a quantum field in a particular global state and construct an averaged version of that field's net energy-momentum, which can be cast into a Lorentz-covariant (and observer-independent) form [132, 158]. This quantity, the renormalized vacuum expectation value $\langle T^{\mu\nu}\rangle_{\text{ren}}$ of the field's stress-energy tensor (RSET), is then guaranteed to feed back into the spacetime geometry in the standard classical way. This thesis will conclude in Chapter 6 with precisely this analysis of how the RSET should backreact on the inner horizon of an arbitrary rotating black hole.

However, the RSET is only an averaged quantity and cannot provide all the information that an observer is able to access about the state of a quantum field in a curved spacetime. Classically, the stress-energy tensor involves an integral with each particle's energy-momentum over a Lorentz-invariant pseudo-scalar volume element:

$$T^{\mu\nu} = \int p^\mu p^\nu f(\boldsymbol{x}, \boldsymbol{p}) \frac{g \ d^3 p}{p^0 (2\pi\hbar)^3}, \tag{4.149}$$

where g is the number of spin states of the particle and f is the dimensionless occupation number, which specifies the number dN of particles with 4-position x^μ and 4-momentum p^μ within the Lorentz-invariant six-dimensional volume of phase space $d^3x \ d^3p$. The particle number N, directly related to this occupation number f, is precisely the object of study throughout this chapter. While the RSET is a difficult object to calculate even for the most symmetric spacetimes, one of the goals of

this chapter is to show that $\langle N \rangle$, the more elementary object, is entirely straightforward to calculate in the locally inertial frame of any observer.

In conclusion, by examining the expectation value of the number operator for a quantum field placed over a black hole spacetime, it has been shown that the same key ideas anticipated in Sec. 4.1 hold true: (1) The Hawking radiation seen by generic observers passing the vicinity of the event horizon has a negligibly weak graybody spectrum, (2) the Hawking radiation seen at the Cauchy horizon possesses a divergent effective temperature for all the classes of observers examined, (3) the Hawking radiation originating from different directions in the sky varies considerably for different classes of observers, and (4) the effective Hawking temperature for certain observers can become negative even outside of the event horizon, though an ultraviolet divergence in the Hawking spectrum is not seen for the limited cases considered here. From these results it is clear that any black hole metric with an inner horizon cannot be trusted in its full global form in the semiclassical approximation, as a result of the diverging quantum radiation that would be observed at its inner horizon.

Chapter 5

Renormalized Vacuum Polarization: $\langle \hat{\phi}^2 \rangle$

The contents of this chapter have been published as [126].

5.1   Introduction

This chapter continues to address one of the ultimate questions of this thesis: what happens inside the event horizon of a black hole? If the classical laws of general relativity are to be believed, then vacuum models of black holes with charge (Reissner-Nordström) or angular momentum (Kerr) predict that below the event horizon lies a second horizon, the Cauchy horizon, which marks the boundary of causality. Below this inner horizon, the vacuum models predict a wormhole and a naked timelike singularity, but as has been explored in depth in Chapter 2, the effects of perturbations from accretion are expected to cause the Cauchy horizon to collapse into a spacelike singularity and preclude any possibility of causality violation.

However, following the classical analysis of Chapter 2, it was shown that at high enough energies (which are easily achieved with the mass inflation instability), gravity is more appropriately treated as a quantum field, not a classical one.

As a quantized field theory (see Chapter 3), gravity is non-renormalizable, since Feynman diagram calculations at all loop orders produce divergences that only get worse the higher one goes in the perturbative expansion. Nonetheless, as an effective field theory, one-loop divergences can be absorbed by renormalization of the next-order parameters, so that quantum gravitational effects can be calculated provided the characteristic frequencies of the gravitational background do not

exceed the Planck frequency [29]. In this one-loop approach, which fits under the umbrella term *semiclassical gravity*, matter fields are quantized while the background spacetime is treated classically. Such an approach has led to many celebrated predictions in the literature, most notably concerning Hawking radiation, analyzed in detail in Chapter 4.

For calculations of quantum field theories (QFTs) in curved spacetimes, the quantity of greatest interest is the renormalized expectation value of the field's stress-energy tensor $\langle T_{\mu\nu} \rangle$, since it contributes to a backreaction to the spacetime geometry via the semiclassical field Eq. (3.9). The squared amplitude $\langle \phi^2 \rangle$ of vacuum fluctuations is often used as a proxy for the calculation of $\langle T_{\mu\nu} \rangle$, since $\langle \phi^2 \rangle$ contains fewer divergences that need to be renormalized yet still provides meaningful information about vacuum polarization effects. In particular, $\langle \phi^2 \rangle$ can be used to the determine the trace of $\langle T_{\mu\nu} \rangle$ for conformally coupled scalar fields, and $\langle \phi^2 \rangle$ additionally provides insight about spontaneous symmetry breaking in a given background spacetime [4].

In the context of semiclassical black hole interiors, most works have considered only two-dimensional or charged black holes. In the two-dimensional case, the quantum backreaction at the inner horizon leads to a divergence of the stress-energy and the formation of a spacelike singularity [65, 68]. In the charged, spherically symmetric case, early work indicated that $\langle T_{\mu\nu} \rangle$ would also likely diverge at the inner horizon to produce a spacelike singularity, but could also remain regular in certain cases [15, 28]. In the past few years, an explosion of works studying semiclassical Reissner-Nordström mass inflation have shown that the ingoing null component $\langle T_{vv} \rangle$ yields a non-zero value at the inner horizon, and switching to a time coordinate which is regular through the inner horizon shows that the renormalized stress-energy tensor does physically diverge there [18, 97, 105, 109, 169, 180, 181]. backreaction from $\langle T_{vv} \rangle$ alone is generally believed to cause a strong curvature singularity [97], though there is no complete semiclassically consistent solution to verify this yet. What has been shown is that a dynamical semiclassical inner horizon will evaporate outwards over time (along with a slower, inward-evaporating outer horizon), leading to a self-consistent steady state that inevitably contains a curvature singularity [8, 9, 18].

For the case of spinning black holes, far fewer works have been published analyzing quantum

effects at the inner horizon. In the simplified vacuum case (the Kerr metric), before mass inflation was even understood classically, Hiscock argued from symmetry and conservation conditions that $\langle T_{\mu\nu}\rangle$ must diverge on either the ingoing or outgoing inner horizon, a result confirmed in the decades following [95, 143]. More recently, $\langle T_{\mu\nu}\rangle$ was calculated for the inner horizon of rotating $(2+1)$-dimensional black holes, which was found to result in a spacelike singularity [41]. Finally, a new set of works by Zilberman et al. have shown that for a $(3+1)$-dimensional Kerr black hole, the flux components of $\langle T_{\mu\nu}\rangle$ do generically diverge at the inner horizon, with the specific choice of spin and polar angle determining whether the null flux components of $\langle T_{\mu\nu}\rangle$ are positive or negative. This analysis will be revisited in Chapter 6.

Despite the success of the aforementioned studies in calculating quantum effects in Kerr black holes, the Kerr metric is not a realistic model when describing the asymptotic regime near the inner horizon of an astrophysical black hole, which in general is modified by the perturbative effects of accretion. Instead of applying a quantum field over some vacuum spacetime solution, here focus is placed on the inflationary Kasner spacetime, the metric derived in Chapter 2 that models the near-inner-horizon geometry of a rotating black hole with accretion. The details and assumptions of this model are reviewed in Sec. 5.2.1. Then, the analysis proceeds with the calculation of the renormalized vacuum polarization $\langle \phi^2 \rangle_{\text{ren}}$. The quantization procedure is detailed in Sec. 5.2.2, while the renormalization procedure is detailed in Sec. 5.3.

Since the wave equation for this model cannot be solved analytically, a numerical framework is used, as described in Sec. 5.4. This framework is first tested on a simplified, isotropic case in Sec. 5.4.1, after which the results for the inflationary Kasner metric are presented in Sec. 5.4.2. The chapter then concludes with a discussion of the results of the calculation of $\langle \phi^2 \rangle_{\text{ren}}$ in Sec. 5.5, leaving the calculation of $\langle T_{\mu\nu}\rangle_{\text{ren}}$ to Chapter 6.

5.2   Inflationary Kasner metric revisited

A complete derivation of the inflationary Kasner metric is given in Chapter 2. Here, the key aspects of the model are presented in a slightly different form, since the different choice of coordinates

used here are more amenable to the semiclassical calculations at hand.

5.2.1   Spacetime metric

The spacetime geometry near the inner horizon of a rotating, accreting black hole can be modeled using a homogeneous metric[1] [125]:

$$ds^2 = -a_0^2(t)dt^2 + \sum_{i=1}^{3} a_i^2(t)(dx^i)^2, \tag{5.1}$$

where the time-dependent scale factors satisfy

$$a_0^2 = c_1 t\, e^{t^2}, \qquad a_1^2 = c_1 t^{-1} e^{t^2}, \qquad a_2^2 = a_3^2 = t^2, \tag{5.2}$$

for positive time t and positive constant c_1. This metric is called the *inflationary Kasner* metric because of its asymptotic resemblance to the well-known Kasner metric first proposed one hundred years earlier [99]. In particular, for t above unity, the metric approximates a Kasner metric with Kasner exponents $(p_1, p_2, p_3) = (1, 0, 0)$, and as t decreases on its way down to the spacelike singularity at $t = 0$, the spacetime "bounces" to a Kasner metric with Kasner exponents $(-1/3,\ 2/3,\ 2/3)$.

The coordinates and constants used in the line element of Eqs. (5.1)–(5.2) are chosen for their convenience for the QFT calculations done here. They are related to those of Chapter 2 by:

$$t = T^{1/2}, \qquad c_1 = \frac{1}{4\pi \Phi_0 T_0^{1/2} e^{T_0}}, \tag{5.3}$$

along with a suitable rescaling of the spatial coordinates. The astrophysical properties of the black hole (viz., the spin a, the inner horizon Boyer-Lindquist radius $r_- \equiv 1 - \sqrt{1 - a^2}$, and the initial

---

[1] Throughout this chapter, assume units where $M_\bullet = 1$.

accretion rate u) are related to these constants via:[2]

$$T_0 = \frac{r_-^3 - 3r_-^2 + a^2 r_- + a^2}{u(r_-^2 + a^2)^2}, \qquad \Phi_0 \approx \frac{u^2 T_0}{4\pi}. \qquad (5.4)$$

To comment briefly on the physical interpretation of this metric, note that the inflationary Kasner model holds only in the regime asymptotically close to the inner horizon of a rotating, accreting black hole. Above this horizon, spacetime is well-approximated by the Kerr metric. But once an observer approaches the inner horizon, they will experience the mass inflation phenomenon described in Chapter 2, corresponding to the radial collapse of the inflationary Kasner metric as t decreases from its initial value of $t_0 \equiv \sqrt{T_0}$ (which is generally quite large, since T_0 is inversely proportional to the generally tiny accretion rate u, in units where the black hole mass is 1) until reaching $t \sim \sqrt{1/2}$. Then, the inflationary Kasner model predicts a bounce in the spacetime, wherein the radial collapse reverses and the collapse in the isotropic directions proceeds towards a strong, spacelike singularity at $t = 0$.

Several key assumptions underlie the inflationary Kasner model; in particular, the near-inner-horizon spacetime is assumed to be homogeneous and sourced by the self-similar, asymptotically small accretion of a collisionless, null fluid. First, the assumption of homogeneity comes about from the fact that during mass inflation, the curvature and stress-energy exponentiate rapidly while the Boyer-Lindquist coordinates r and θ remain frozen at their inner horizon values. One should not imagine that a vast, structureless swath of homogeneous spacetime lies hidden within accreting black holes; rather, homogeneity applies locally for each near-inner-horizon observer as the entire evolution of the inflationary Kasner model passes by within a fraction of a second of their proper time. Second, the assumptions about accretion are a direct result of the process of mass inflation, which accelerates any infalling matter to relativistic velocities along the radial direction, rendering

---

[2]The initial energy density Φ_0 depends more generally on the observer's polar coordinate θ and the difference in the speed of ingoing and outgoing streams [84], but the inclusion of these parameters provides no more precision than the inflationary Kasner approximation already affords.

any other contributions to Einstein's equations irrelevant until t/t_0 reaches below $\sim \sqrt{10^{-5}}$ [125]. Finally, the assumption of a tiny accretion rate should hold for any black hole at late times (indeed, even the cosmic microwave background would source such accretion).

5.2.2 Quantum field modes

Let $\hat{\phi}(x)$ be a canonically quantized, neutral scalar field, evaluated at a spacetime point x, that satisfies the Klein-Gordon wave equation

$$\left(\Box - m^2 - \xi R\right)\phi = 0, \tag{5.5}$$

where $\Box \equiv g^{\mu\nu}\nabla_\mu\nabla_\nu$ is the d'Alembert operator, m is the mass of the field quanta, ξ is a numerical factor indicating the strength of the coupling between the scalar field and the gravitational field, and R is the Ricci scalar curvature. For the inflationary Kasner metric, $R(x) = 0$, so the calculation of $\langle\phi^2\rangle_{\text{ren}}$ here will not depend on ξ. Later, the massless case will be assumed, but in order for the adiabatic expansion of Sec. 5.3.1 to be valid, m must not be set to 0 until the end of the calculation.[3]

The homogeneity of the inflationary Kasner spacetime motivates a decomposition of the quantum field operator $\hat{\phi}$ into a set of modes indexed by wavevectors $\boldsymbol{k} \in \mathbb{R}^3$:

$$\hat{\phi} = \frac{1}{(2\pi)^{3/2}} \int d^3\boldsymbol{k} \left[\hat{A}_{\boldsymbol{k}}\psi_{\boldsymbol{k}}(t)\, \mathrm{e}^{i\boldsymbol{k}\cdot\boldsymbol{x}} + \hat{A}_{\boldsymbol{k}}^\dagger\psi_{\boldsymbol{k}}^*(t)\, \mathrm{e}^{-i\boldsymbol{k}\cdot\boldsymbol{x}}\right]. \tag{5.6}$$

The creation and annihilation operators $\hat{A}_{\boldsymbol{k}}^\dagger$ and $\hat{A}_{\boldsymbol{k}}$ (capital letters are used here in contrast to the lowercase notation introduced in Chapter 3 to avoid confusion with the metric's scale factors a_i) will then satisfy the usual commutation relations (compare Eq. (3.14))

$$[\hat{A}_{\boldsymbol{k}}, \hat{A}_{\boldsymbol{k}'}] = [\hat{A}_{\boldsymbol{k}}^\dagger, \hat{A}_{\boldsymbol{k}'}^\dagger] = 0, \qquad [\hat{A}_{\boldsymbol{k}}, \hat{A}_{\boldsymbol{k}'}^\dagger] = \delta^3(\boldsymbol{k} - \boldsymbol{k}'), \tag{5.7}$$

---

[3]Numerically, a variety of values for the mass were tested until convergence in the $m \to 0$ limit was achieved; for the present analysis, $m = 10^{-4}$ was found to be more than sufficient.

provided the mode functions $\psi_{\boldsymbol{k}}$ satisfy the Wronskian condition

$$\dot{\psi}_{\boldsymbol{k}}^* \psi_{\boldsymbol{k}} - \psi_{\boldsymbol{k}}^* \dot{\psi}_{\boldsymbol{k}} = i \frac{a_0}{a_1 a_2 a_3} = i t^{-1}. \tag{5.8}$$

Here and throughout this chapter, an overdot represents differentiation with respect to the coordinate time t. Introducing the auxiliary function

$$f_{\boldsymbol{k}}(t) \equiv \left(\frac{a_1 a_2 a_3}{a_0} \right)^{1/2} \psi_{\boldsymbol{k}}(t) = t^{1/2} \psi_{\boldsymbol{k}}(t), \tag{5.9}$$

Eq. (5.5) leads to the dynamical equation

$$\ddot{f}_{\boldsymbol{k}} + \left(\omega_{\boldsymbol{k}}^2 + \sigma \right) f_{\boldsymbol{k}} = 0, \tag{5.10}$$

where the frequency $\omega_{\boldsymbol{k}}(t)$ and $\boldsymbol{k}$-independent geometrical background term $\sigma(t)$ are defined by

$$\omega_{\boldsymbol{k}}^2(t) \equiv a_0^2 \left(\sum_{i=1}^{3} \frac{k_i^2}{a_i^2} + m^2 \right), \tag{5.11}$$

$$\sigma(t) \equiv \frac{1}{4} \left[\frac{2\ddot{a}_0}{a_0} - \frac{3\dot{a}_0^2}{a_0^2} + \sum_{i=1}^{3} \frac{\dot{a}_i^2}{a_i^2} + a_0^2 \left(4\xi - 1 \right) R \right]. \tag{5.12}$$

In the isotropic limit, $\omega_{\boldsymbol{k}}$ reduces to the standard definition of frequency used for Friedmann-Lemaître-Robertson-Walker (FLRW) universes [148]. With the scale factors of Eq. (5.2), the anisotropic background term $\sigma(t)$ simplifies to $1/(4t^2)$, and the wave Eq. (5.10) has no known solution in terms of analytic functions. Therefore, the mode functions $f_{\boldsymbol{k}}$ must be found by numerically solving the wave equation for each choice of wavevector $\boldsymbol{k}$. The boundary conditions are set by the choice of vacuum state, the discussion of which is deferred to Sec. 5.3.2.

5.2.3   Asymptotics

While the inflationary Kasner wave equation has no general closed-form solution, three asymptotic regimes are worth mentioning: the adiabatic regime $(t/t_0 \gg 1)$, where the spacetime

behaves adiabatically but is too far from the inner horizon singularity to match the behavior of a black hole; the initial inflationary regime $t/t_0 \to 1$, where both the inflationary Kasner and Kerr metrics are valid just above the inner horizon; and the final collapse regime ($t/t_0 \to 0$), where the spacetime behavior is dominated by the collapse of the metric toward the spacelike singularity.

5.2.3.1   Adiabatic regime

When t/t_0 exceeds unity, the exponential terms in the inflationary Kasner scale factors of Eq. (5.2) will dominate, provided $t_0 \gg 1$ (as is true for any astrophysical black hole below the Thorne limit [171], since t_0 scales as $u^{-1/2}$ for the generally tiny accretion rate $u \ll 1$). The resulting metric, with an exponential term over the temporal and radial sectors, has the same Rindler-type form of Lass's radar coordinates for Minkowski space (when x and $T \equiv t^2$ are swapped) [110]. As a Kasner universe, the metric asymptotically approaches the well-studied case of Kasner exponents $(1, 0, 0)$. But even more simply, the coordinate transformation

$$\tilde{T} \equiv \sqrt{\frac{c_1}{t}}\, e^{\frac{t^2}{2}} \sinh(x), \qquad \tilde{X} \equiv \sqrt{\frac{c_1}{t}}\, e^{\frac{t^2}{2}} \cosh(x), \qquad \tilde{Y} \equiv ty, \qquad \tilde{Z} \equiv tz \qquad (5.13)$$

will bring the metric to the form

$$-d\tilde{T}^2 + d\tilde{X}^2 + d\tilde{Y}^2 + d\tilde{Z}^2. \qquad (5.14)$$

in the large-t limit. Thus, the standard QFT approach to flat spacetime applies in this limit, provided the appropriate vacuum state is supplied.

5.2.3.2   Initial inflationary regime

In the massless limit, as t/t_0 approaches unity from below (in fact, for any value of t in the range $e^{-t_0^2/3} \lesssim t \lesssim t_0$, provided $t_0 \gg 1$), the frequency function in the wave equation will be dominated by the radial k_1 term, which is quadratic in t. The general solution to the wave equation in terms of

the mode functions $\psi_{\boldsymbol{k}} = f_{\boldsymbol{k}} t^{-1/2}$ can be written in terms of zeroth-order Bessel functions:

$$\psi_{\boldsymbol{k}} = A_{\boldsymbol{k}} J_0\left(\frac{1}{2}k_1 t^2\right) + B_{\boldsymbol{k}} Y_0\left(\frac{1}{2}k_1 t^2\right), \tag{5.15}$$

for complex coefficients $A_{\boldsymbol{k}}$ and $B_{\boldsymbol{k}}$.

5.2.3.3   Final collapse regime

As t/t_0 approaches zero, the exponential terms in the inflationary Kasner scale factors of Eq. (5.2) become negligible, which results in a standard Kasner metric with normalized Kasner exponents $(-1/3, \, 2/3, \, 2/3)$. Asymptotically, the wave Eq. (5.10) simplifies to

$$\ddot{f}_{\boldsymbol{k}} + \left(\frac{c_1 k_\perp^2}{t} + \frac{1}{4t^2}\right) f_{\boldsymbol{k}} = 0, \tag{5.16}$$

with a general solution to the mode functions $\psi_{\boldsymbol{k}} = f_{\boldsymbol{k}} t^{-1/2}$ given by zeroth-order Bessel functions with argument $\sqrt{4k_\perp^2 c_1 t}$. But since $t_0 \gg 1$, the constant c_1 and therefore the subleading t^{-1} term from Eq. (5.16) is exponentially suppressed by the factor $\mathrm{e}^{-t_0^2}$, so that the mode solutions further reduce to

$$\psi_{\boldsymbol{k}}(t) = A_{\boldsymbol{k}} + B_{\boldsymbol{k}} \ln(t), \tag{5.17}$$

for complex coefficients $A_{\boldsymbol{k}}$ and $B_{\boldsymbol{k}}$.

5.3   Adiabatic regularization

The quantity of interest is the probability density of vacuum fluctuations, given by the vacuum expectation value of the squared field operator, denoted $\langle 0|\phi^2(x)|0\rangle$ (or more concisely, $\langle \phi^2 \rangle$). Formally, this quantity can be defined as the coincidence limit of a suitable two-point correlation function,

$$\langle \phi^2 \rangle \equiv \frac{1}{2} \lim_{x' \to x} G^{(1)}(x, x'), \tag{5.18}$$

where

$$G^{(1)}(x, x') \equiv \langle 0 | \{ \phi(x) \phi(x') \} | 0 \rangle \tag{5.19}$$

is the Hadamard Green function, defined with anticommutator brackets $\{\}$. In the case of the mode expansion described in Sec. 5.2.2, the field variance can be naïvely calculated as

$$\langle \phi^2 \rangle_{\text{bare}} = \frac{1}{(2\pi)^3 t} \int d^3 \boldsymbol{k} \ |f_{\boldsymbol{k}}(t)|^2. \tag{5.20}$$

However, the bare integral in Eq. (5.20) is quadratically divergent. In order to obtain a physical, finite result, some renormalization procedure must be employed, as described in the next subsection.

Since the mode solutions to Eq. (5.10) cannot be expressed in an analytic form and must instead be solved numerically, most of the standard analytic renormalization techniques (such as dimensional regularization) cannot be used. One robust technique for curved spacetimes, known as point-splitting, has recently been implemented numerically by Levi and Ori under the name *pragmatic mode-sum regularization* (PMR) [112, 113]. Such a technique requires only that the background admits some symmetry (Killing field) to permit a mode expansion, and the present case of homogeneous symmetry (translational splitting) has been carried out successfully for the FLRW metric [26]. However, the x-splitting variant of PMR works well only for isotropic backgrounds—for the inflationary Kasner metric, the presence of two independent scale factors renders the PMR method ineffective or perhaps even impossible.[4] Instead, the technique of choice in this chapter is adiabatic regularization, which was introduced in Sec. 3.3 and is described in more detail below.

---

[4]In particular, whereas the generalized transform $[\mathcal{T} G_{\text{DS}}^{(1)}(\varepsilon)](k)$ in the case of isotropic x-splitting has kernel $\text{sinc}(k\varepsilon)$ and can be written explicitly, cylindrical x-splitting requires at most two transforms, with kernels proportional to $\cos(k\varepsilon)$ and $J_0(k\varepsilon)$, and no generalized Hankel transforms have been found for the divergent pieces ε^{-2} and $\ln(\varepsilon)$ that do not also diverge in k-space.

5.3.1   Derivation of the adiabatically renormalized field variance

Instead of renormalizing $\langle \phi^2 \rangle$ as a whole or at the level of the two-point function, consider what happens if the mode functions themselves are renormalized before any integration over modes is performed. In particular, the goal will be to find a Wentzel-Kramers-Brillouin-type (WKB-type) expansion of the mode solutions $f_{\boldsymbol{k}}(t)$. These solutions can then be subtracted off from the numerically-obtained solutions $f_{\boldsymbol{k}}(t)$ to yield a finite integral by construction. This procedure, known as adiabatic regularization, was developed by Parker and Fulling in the 1970s and has been found to provide a consistent means of renormalization, particularly in the case of homogeneous spacetimes [69, 70, 148].

Although adiabatic regularization lacks a manifestly covariant formulation, it is expected to be robust for spacetimes with a high degree of symmetry (such as the present case with homogeneity and 2D isotropy), and it benefits from the simplicity of its computations and the intuitive clarity of its physical interpretation. Further, the scheme has been shown to be equivalent to the DeWitt-Schwinger point-splitting method for massive scalar fields on any Bianchi Type I spacetime [120]. Nonetheless, the results presented here still may be subjected to a degree of scrutiny, since they have not been directly compared against an axiomatic, covariant construction [175]. However, the main ambiguity in the adiabatic scheme arises from the choice of the leading-order frequency of Eq. (5.23) below, and such a choice mainly corresponds to the well-known mass scale ambiguity for massless scalar fields, which should not affect the sought-after temporal dependence of $\langle \phi^2 \rangle$ [25].

Eq. (5.10) possesses the formal WKB-type solutions

$$f_{\boldsymbol{k}}(t) = \frac{\exp\left[-i \int^{t} dt' \, W_{\boldsymbol{k}}(t')\right]}{\sqrt{2 W_{\boldsymbol{k}}(t)}}, \tag{5.21}$$

where the WKB approximate frequency $W_{\boldsymbol{k}}(t)$ satisfies the nonlinear equation

$$W_{\boldsymbol{k}}^2 = \omega_{\boldsymbol{k}}^2 + \sigma - \frac{1}{2}\left(\frac{\ddot{W}_{\boldsymbol{k}}}{W_{\boldsymbol{k}}} - \frac{3}{2}\frac{\dot{W}_{\boldsymbol{k}}^2}{W_{\boldsymbol{k}}^2}\right). \tag{5.22}$$

Note that $f_{\boldsymbol{k}}$ contains an arbitrary phase factor associated with the lower bound of the integral in Eq. (5.21). At this stage, the shift from $f_{\boldsymbol{k}}$ to $W_{\boldsymbol{k}}$ is nothing more than a change of variables; the WKB-type form of Eq. (5.21) has the distinct advantage that the Wronskian condition of Eq. (5.8) is automatically satisfied if $W_{\boldsymbol{k}}$ is chosen to be real and nonnegative.

Under the adiabatic approximation, if the spacetime is slowly varying, any derivative terms in Eq. (5.22) will be small compared to the squared frequency $\omega_{\boldsymbol{k}}^2$, so a zeroth-order approximation is to substitute

$$W_{\boldsymbol{k}}^{(0)} \equiv \omega_{\boldsymbol{k}} \tag{5.23}$$

(note that the background term $\sigma(t)$, Eq. (5.12), has adiabatic order 2 (as defined below) and therefore vanishes in the zeroth-order limit along with the explicit derivative terms on the right-hand side of Eq. (5.22)). Higher-order solutions may then be derived by iteration. The next-highest order reads:

$$W_{\boldsymbol{k}}^{(2)} = \sqrt{\omega_{\boldsymbol{k}}^2 + \sigma - \frac{1}{2}\left(\frac{\ddot{\omega}_{\boldsymbol{k}}}{\omega_{\boldsymbol{k}}} - \frac{3}{2}\frac{\dot{\omega}_{\boldsymbol{k}}^2}{\omega_{\boldsymbol{k}}^2}\right)}. \tag{5.24}$$

The superscript (A) attached to the WKB approximate frequency $W_{\boldsymbol{k}}^{(A)}$ denotes the adiabatic order A of the function. The Ath adiabatic order is defined by considering the replacement $t \to \epsilon t$ (where the adiabatic parameter ϵ will be taken to 1 at the end of the calculation) and performing an expansion in powers of ϵ to obtain terms up to order ϵ^A. Practically, terms of Ath adiabatic order are those with up to A time derivatives of the metric.

The key feature of adiabatic regularization is that in the adiabatic limit $\epsilon \to 0$ (or equivalently, $\boldsymbol{k} \to \infty$), the adiabatic expansion of the mode solutions to the wave equation should match the exact mode solutions. Since this limit is precisely the regime where $\langle\phi^2\rangle$ contains ultraviolet divergences, subtracting the adiabatic term involving $W_{\boldsymbol{k}}^{(A)}$ from the term involving the exact solutions $W_{\boldsymbol{k}}$ should yield a finite, renormalized result that can be integrated.

More precisely, the renormalized field variance is

$$\langle\phi^2\rangle_{\text{ren}} = \frac{1}{(2\pi)^3 t}\int d^3\boldsymbol{k}\left[\frac{1}{2W_{\boldsymbol{k}}} - \left(\frac{1}{2W_{\boldsymbol{k}}}\right)^{(A)}\right]. \tag{5.25}$$

According to the standard prescription for $\langle \phi^2 \rangle$ renormalization [29], only terms up to adiabatic order 2 (viz., all orders containing terms that yield divergent integrals) need to be subtracted for the solution to be consistent with the results obtained from renormalization of the bare constants in the Lagrangian. Utilizing Eq. (5.24), the result is:

$$\left(\frac{1}{2W_{\boldsymbol{k}}} \right)^{(2)} = \frac{1}{2\omega_{\boldsymbol{k}}} - \frac{\sigma}{4\omega_{\boldsymbol{k}}^3} + \frac{\ddot{\omega}_{\boldsymbol{k}}}{8\omega_{\boldsymbol{k}}^4} - \frac{3\dot{\omega}_{\boldsymbol{k}}^2}{16\omega_{\boldsymbol{k}}^5}. \tag{5.26}$$

By construction, the terms in Eq. (5.26) that would diverge when integrated over $\boldsymbol{k}$ exactly cancel the divergences from the exact mode solutions $1/(2W_{\boldsymbol{k}})$.

Additionally, since the integrand is even in k_1 and isotropic in the k_2-k_3 plane, the integral simplifies in cylindrical coordinates (with $k_\perp \equiv \sqrt{k_2^2 + k_3^2}$) to

$$\langle \phi^2 \rangle_{\text{ren}} = \lim_{\Lambda \to \infty} \left(\frac{1}{2\pi^2 t} \int_0^\Lambda \int_0^\Lambda dk_1 dk_\perp k_\perp \left[\frac{1}{2W_{\boldsymbol{k}}} - \frac{1}{2\omega_{\boldsymbol{k}}} + \frac{\sigma}{4\omega_{\boldsymbol{k}}^3} - \frac{\ddot{\omega}_{\boldsymbol{k}}}{8\omega_{\boldsymbol{k}}^4} + \frac{3\dot{\omega}_{\boldsymbol{k}}^2}{16\omega_{\boldsymbol{k}}^5} \right] \right). \tag{5.27}$$

Eq. (5.27) is the expression used in Sec. 5.4 to calculate the vacuum polarization effects in the inflationary Kasner spacetime, first by numerically solving for $W_{\boldsymbol{k}}$ via Eq. (5.22) (with initial conditions provided in the next subsection) and then integrating up to a suitably large choice for the ultraviolet cutoff parameter Λ.

5.3.2   Choice of vacuum state

For any curved spacetime, the concept of "particles" will not necessarily hold the same meaning for different observers. Thus, any calculation in this framework must make the observer-dependent choice of what defines the vacuum state. Such a choice is equivalent to specifying boundary conditions for the wave equation on the spacetime.

Traditionally, the vacuum state for a stationary black hole spacetime is defined by imposing an initial condition to the wave equation along the spacetime's past null boundaries, where one can naturally specify free wave solutions with respect to some affine parameter along those boundaries.

Physically, one can then connect the vacuum state to the standard Minkowski vacuum seen by stationary observers at infinity. However, in the present case, the mode expansion for the inflationary Kasner spacetime remains valid only for observers arbitrarily close to the inner horizon. The solution to the inflationary Kasner wave equation as t approaches infinity has no physical meaning, not only because the spacetime is not stationary, but also because once t becomes larger than t_0, the metric must be replaced with the Kerr metric if one wishes to describe an astrophysical black hole.

In the absence of a clear natural choice of vacuum state within the inflationary Kasner spacetime, three options present themselves as physically viable choices:

(1) The *adiabatic vacuum* [29, 147] defined at some time t_A consists of purely positive frequency modes with respect to an adiabatic mode expansion, Eq. (5.21), given t_A lies in a regime where the spacetime is slowly varying.

(2) A *Minkowski vacuum* can be defined via the asymptotic behavior of the inflationary Kasner metric for $t/t_0 \gg 1$ (see Sec. 5.2.3.1), provided the appropriate coordinate transformation and mode decomposition that would allow for the mixing of $e^{i\boldsymbol{k}\cdot\boldsymbol{x}}$ and $e^{-i\boldsymbol{k}\cdot\boldsymbol{x}}$ waves.

(3) The *Unruh state* [173], which reproduces the predictions of Hawking radiation for stationary black holes [12, 13, 36], can be defined at the Kerr past null boundaries, propagated through the spacetime until it reaches asymptotically close to the inner horizon, then matched onto the inflationary Kasner spacetime via a suitable coordinate transformation and mode decomposition.

Since all three of these vacuum states have transparent, physical interpretations within the black hole spacetime, they all should lead to roughly similar vacuum expectation values, at least when considering the temporal dependence of the effects of particle production from the rapid evolution of the spacetime curvature during mass inflation and collapse. The vacuum state specifically tailored to study the production of physical particles (in the sense of the experiences of a comoving particle detector in a dynamic, homogeneous spacetime) is the adiabatic vacuum state of Option 1, and it is this state that will be used in the present analysis. The most physically authentic choice for the

vacuum state would likely be Option 3, especially considering its recent success in the calculation of the renormalized stress-energy tensor at the Kerr inner horizon [178, 179]. However, the transition from Unruh modes to an equivalent set of $\boldsymbol{k}$-modes in the inflationary Kasner regime is complex and nontrivial, and the authors are currently working on methods to apply the states of Options 2 and 3 in a follow-up work (now published as Ref. [89]).

The adiabatic family of vacuum states $|0^{(A)}\rangle$, which forms the focus of the present analysis, is defined at A^{th} adiabatic order such that the annihilation operator $\hat{A}_{\boldsymbol{k}}^{(A)}$ satisfies

$$\hat{A}_{\boldsymbol{k}}^{(A)}|0^{(A)}\rangle = 0 \tag{5.28}$$

and designates an exact mode decomposition of the field operator $\hat{\phi}$ akin to Eq. (5.6) [148]. The adiabatic terminology comes into play because the quantized mode solutions to the wave equation are matched to an adiabatic expansion of those modes (to order A) at a time $t = t_A$. It should be noted that despite the terminology, the adiabatic state is not merely an approximate vacuum; on the contrary, it represents an exact solution to the wave equation, with the well-defined choice of positive frequency modes motivated by the state one would get from a given adiabatic expansion.

The adiabatic vacuum has several distinct advantages as a physical vacuum state. First, it only requires a matching at a specific time t_A, which can be taken in this case to be far from the inflationary Kasner bounce so that the effects of mode distortion from the changing spacetime are minimized in the construction of the quantized field modes. Second, and more importantly, in the adiabatic limit $\epsilon \to 0$, a comoving particle detector in this vacuum will detect a spectrum that falls off faster than any inverse power of the momentum $\boldsymbol{k}$ [147, 148]. Since particle number is an adiabatic invariant, as long as

$$\omega_{\boldsymbol{k}} \gg \frac{\dot{\omega}_{\boldsymbol{k}}}{\omega_{\boldsymbol{k}}}, \tag{5.29}$$

the excitation of the large-$\boldsymbol{k}$ modes will be highly suppressed, and the adiabatic vacuum will exactly match the physical vacuum definition of particles. But even for non-adiabatic portions of a spacetime, the minimization postulate encoded by the statements above implies that the adiabatic definition

of creation operators will approximately match that of physical particles throughout the evolution of the spacetime, up to adiabatic order A. For the inflationary Kasner spacetime, the adiabatic condition (5.29) holds in the strict sense for large k_1, k_2, or k_3, and it holds more generally when $t \ll 1$ or $t \gg 1$. For large t, since $\omega_{\boldsymbol{k}} \sim e^{t^2/2}$ and $\dot{\omega}_{\boldsymbol{k}}/\omega_{\boldsymbol{k}} \sim t$, the adiabatic condition is met even for times as small as $t \sim 5$, where the frequency $\omega_{\boldsymbol{k}}$ exceeds its logarithmic derivative already by several orders of magnitude.

To demonstrate the robustness of the adiabatic state used here, Fig. 5.1 shows the computed value of $\langle \phi^2(t) \rangle_{\text{ren}}$ at a certain intermediate time ($t/t_0 \approx 0.32$) for a family of different adiabatic vacuum states parametrized by the adiabatic matching time t_A. In this plot, the renormalized field variance $\langle \phi^2 \rangle_{\text{ren}}$ is found to be exactly 0 when the adiabatic vacuum time t_A is the same as the evaluated time t (the rightmost point on the plot), since the field is in vacuum by definition. But if the adiabatic vacuum state is chosen to begin at a time t_A earlier than the point being evaluated, $\langle \phi^2 \rangle_{\text{ren}}$ obtains a nonzero value corresponding to the polarization of the vacuum accomplished by the spacetime's evolution from t_A to t. For a choice of t_A far enough into the past, the value of $\langle \phi^2 \rangle_{\text{ren}}$ asymptotes to a constant, indicating that the chosen vacuum begins in a suitably adiabatic regime. Note that for the choice of constants used throughout this chapter, t_0 (the starting time for the mass inflation epoch and the point of matching between the Kerr and inflationary Kasner metrics) takes on a value of about 3.1, which is not quite large enough to preside in the adiabatic regime. The vacuum time t_A must therefore be chosen to be distinct from (and farther in the past than) t_0 (in particular, $t_A = 5 \approx 1.6t_0$), though it is still close enough to t_0 that the inflationary Kasner model should still hold reasonably well.

In order to perform the renormalization calculations in the adiabatic vacuum state, the wave equation (in this case, Eq. (5.22)) is solved using a standard numerical integrator, with the Cauchy initial conditions

$$\frac{1}{2W_{\boldsymbol{k}}(t_0)} = \left(\frac{1}{2W_{\boldsymbol{k}}(t_0)} \right)^{(A)}, \tag{5.30a}$$

$$\partial_t \left(\frac{1}{2W_{\boldsymbol{k}}(t_0)} \right) = \partial_t \left(\frac{1}{2W_{\boldsymbol{k}}(t_0)} \right)^{(A)}, \tag{5.30b}$$
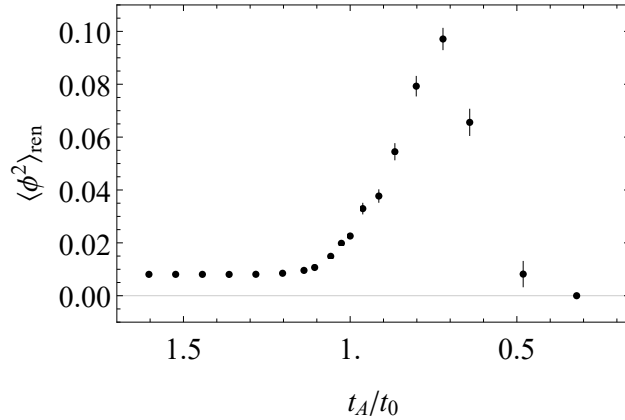
Figure 5.1: The renormalized variance $\langle \phi^2(t) \rangle_{\mathrm{ren}}$ evaluated at the inflationary Kasner time $t = 1 \approx 0.32 t_0$ for various choices of the adiabatic matching time t_A. The constants used are the black hole spin $a = 0.96$ and initial accretion rate $u = 0.02$, for which $t_0 \approx 3.1$.

where the quantities with superscript (A) are truncated at adiabatic order $A = 2$ by Eq. (5.24) to ensure consistency with the renormalization scheme. As mentioned in Sec. 5.3.1, the mode functions $W_{\boldsymbol{k}}(t)$ are used for numerical calculations instead of $f_{\boldsymbol{k}}(t)$ because the Wronskian condition of Eq. (5.8) is guaranteed to be satisfied as long as $W_{\boldsymbol{k}}(t)$ is constrained to be real and nonnegative.

5.4   Numerical results

To demonstrate how the present numerical framework of adiabatic regularization can be applied to a spacetime (and to confirm its validity), the technique is first carried out for a simplified yet comparable Bianchi Type I spacetime. The chosen spacetime (FLRW model with scale factor $t^{1/3}$) has the advantage that the renormalized variance is known analytically from several independent renormalization techniques and can also be calculated using a numerical adiabatic regularization scheme identical to the one presented here. The numerical results for this simplified case are shown in Sec. 5.4.1 to be entirely consistent with the analytic solutions. Then, the main results of the renormalization for the inflationary Kasner spacetime are presented in Sec. 5.4.2.

5.4.1 FLRW renormalization

The Friedmann-Lemaître-Robertson-Walker (FLRW) metric is a special case of the homogeneous metric of Eq. (5.1) where the scale factors are completely isotropic. For the present case, assume the scale factors

$$a_0 = 1, \ a_1 = a_2 = a_3 = t^{1/3}, \tag{5.31}$$

which correspond to a flat FLRW universe with a classical free scalar field (distinct from the quantized scalar field that will be added to this background). This choice of metric has the advantage that the formalism of Sec. 5.2.2 ff. remains completely unchanged when comparing the inflationary Kasner and FLRW calculations (in particular, $a_1 a_2 a_3/a_0 = t$).

The renormalized FLRW variance has been calculated analytically for a conformally coupled massless scalar field using both point-splitting and adiabatic techniques [7, 51, 148, 157]. Since the spacetime is isotropic, homogeneous, and spatially flat, it is conformally Minkowski. As such, in the massless, conformally coupled case, the field can be decomposed into $\boldsymbol{k}$-modes as in Eq. (5.6), with mode solutions

$$\psi_k = \frac{\exp\left(-\frac{3}{2}ikt^{2/3}\right)}{\sqrt{2kt^{2/3}}}, \qquad k \equiv |\boldsymbol{k}| = \sqrt{k_1^2 + k_2^2 + k_3^2}. \tag{5.32}$$

These modes are positive frequency with respect to the globally timelike conformal Killing vector ∂_η (where $\eta \equiv \int a(t)^{-1} dt = (3/2)t^{2/3}$). Therefore, unlike in the case of inflationary Kasner, the modes of Eq. (5.32) uniquely define a natural vacuum state. In particular, the adiabatic vacuum state of Sec. 5.3.2 is equivalent to this vacuum state for all matching points t_A, to all adiabatic orders.

On the numerical side, the corresponding initial conditions that must replace Eq. (5.30) to ensure the same conformal vacuum state as in the analytic case are those tied to the modes

$$W_k = kt^{-1/3}. \tag{5.33}$$

Otherwise, after the replacement of the scale factors of Eq. (5.31) and the inclusion of the now nonzero Ricci scalar $R = -2/(3t^2)$, the numerical scheme presented in the previous sections can be
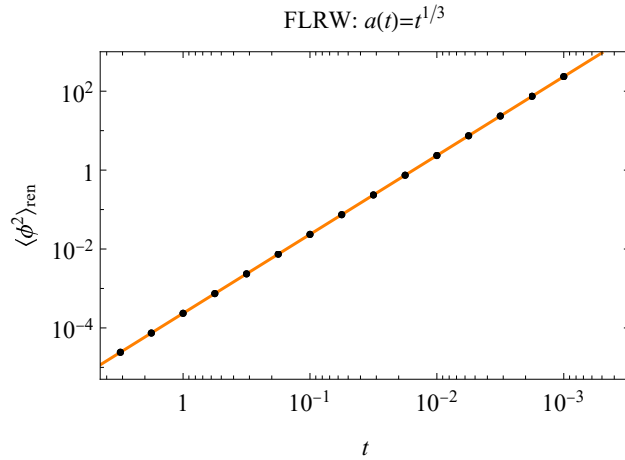
Figure 5.2: The renormalized variance in an FLRW background with scale factor power law index ⅓. The black points are computed numerically using the adiabatic regularization scheme outlined in Sec. 5.3, and the orange line indicates the analytic expression from Eq. (5.34) derived from both adiabatic and point-splitting regularization techniques.

followed exactly as in the inflationary Kasner case.

In the conformal vacuum state, the renormalized variance of a massless, conformally-coupled field over the FLRW background is [29]

$$\langle \phi^2 \rangle_{\mathrm{ren}} = -\frac{R}{288\pi^2} = \frac{1}{432\pi^2 t^2}. \tag{5.34}$$

The numerical adiabatic computation of $\langle \phi^2 \rangle_{\mathrm{ren}}$ is presented in Fig. 5.2 alongside the analytic expression from Eq. (5.34). The integrations necessary to compute each point in this figure converged to a steady value rather quickly, usually requiring an ultraviolet cutoff of no more than $\Lambda = 1$. As shown, the two methods show excellent agreement, lending credence to the validity and precision of the present adiabatic numerical scheme.

5.4.2 Inflationary Kasner renormalization

For the inflationary Kasner spacetime, the wave Eq. (5.22) subject to the boundary conditions of Eq. (5.30) is solved numerically using `Mathematica`'s parametric ODE solver. The mode solutions are then used to compute the integral of Eq. (5.27) for successively larger values of the momentum

cutoff parameter Λ until convergence is achieved. The result is the numerical value of $\langle \phi^2(t) \rangle_{\text{ren}}$ at a particular time t; this process is then repeated for different values of t until the variance's full time dependence is found.

Especially for small values of the inflationary Kasner time t, each numerical calculation of the wave equation to produce a parametric mode solution can take on the order of seconds or even minutes. As such, interpolation is used to increase the code's efficiency. A grid of points over the pertinent $\boldsymbol{k}$-space is sampled to calculate the mode solutions, and the remaining $\boldsymbol{k}$-space is estimated using third-order Hermite interpolation. To ensure that no features in the $\boldsymbol{k}$-space are overlooked by the choice of sampling grid, adaptive mesh refinement techniques are employed, such that if the errors in the interpolation function for a given region of $\boldsymbol{k}$-space are greater than a pre-determined threshold, the grid is refined to include more sampled points within that region. This process is then repeated until the integrals within all regions lie below the error threshold. An example of this process is shown in Fig. 5.3.

When the power spectrum of Fig. 5.3 is integrated over both k_1 and $k_\perp$, the result is $\langle \phi^2 \rangle_{\text{ren}}$. As k_1 or $k_\perp$ increases, the value of the integrand of Eq. (5.27) decreases until it reaches zero, since the numerically computed mode solutions $W_{\boldsymbol{k}}$ by construction will approach the same value as the adiabatic mode solutions of Eq. (5.24) in the large-$\boldsymbol{k}$ adiabatic limit. To ensure that enough of the infinite $\boldsymbol{k}$-space is being integrated over to calculate $\langle \phi^2 \rangle_{\text{ren}}$, the integral is performed for successively larger values of Λ until $\langle \phi^2 \rangle_{\text{ren}}$ converges. As an example, Fig. 5.4 shows the convergence of $\langle \phi^2(t) \rangle_{\text{ren}}$ for the same time used in Fig. 5.3 ($t = t_0$). That is, the integral of the region shown in Fig. 5.3 corresponds to the point at $\Lambda = 10$ in Fig. 5.4.

Since the time t in Figs. 5.3 and 5.4 is close to the adiabatic vacuum time t_A, only the lowest $\boldsymbol{k}$-modes are occupied, and the integral converges quickly. But as t advances from t_0 to 0 and the spacetime evolves through the inflationary Kasner bounce, higher modes are expected to be occupied as the strong gravitational field seeds further particle production. Throughout the first Kasner epoch from $t \sim t_0$ to $t \sim \sqrt{1/2}$ signaling mass inflation, the transverse modes ($k_\perp$) become progressively more occupied, and during the second Kasner epoch from $t \sim \sqrt{1/2}$ to $t \sim 0$ signaling spacelike collapse,
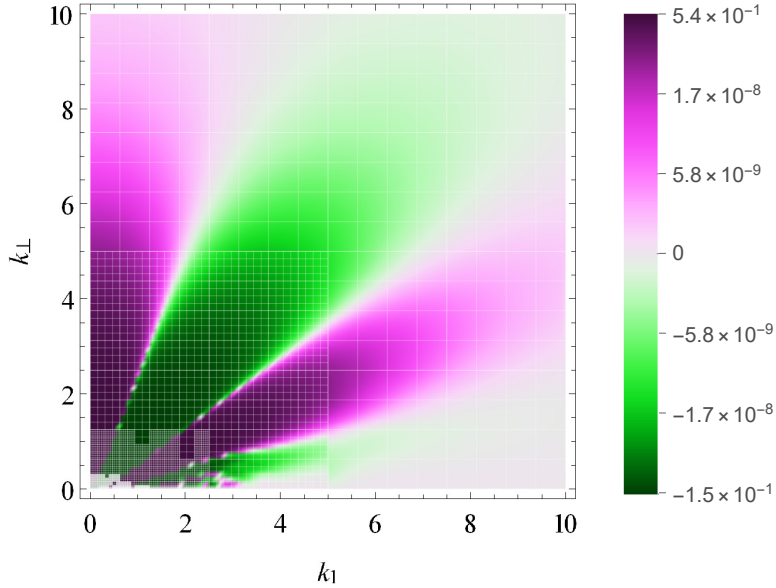
Figure 5.3: Power spectrum (the integrand of Eq. (5.27)) over a portion of $\boldsymbol{k}$-space, evaluated at time $t = t_0$ (as defined in Sec. 5.2.1). Gridlines reveal the steps of adaptive mesh refinement, with an error threshold of 10^{-8} and grid sizes varying from 0.625 to 2×10^{-5}. The constants used are the black hole spin $a = 0.96$, initial accretion rate $u = 0.02$, and adiabatic matching time $t_A = 5$.
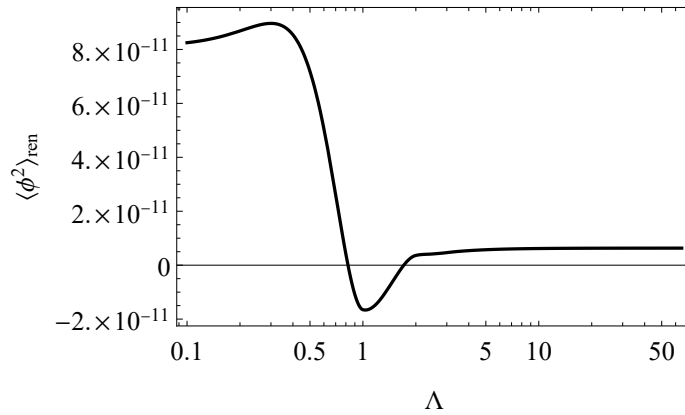
Figure 5.4: Convergence of the integral in Eq. (5.27) at time $t = t_0$ as a function of the cutoff parameter Λ. The choice of constants is the same as in Fig. 5.3.

energy from the transverse modes passes over into the higher radial modes (k_1).

The time evolution of $\langle \phi^2 \rangle_{\text{ren}}$ for a massless scalar field in the adiabatic vacuum in the inflationary Kasner spacetime is shown in Fig. 5.5. Since t begins close to the adiabatic vacuum

time t_A (t_0 is about 3.1 for the choice of constants used here, while $t_A = 5$), the vacuum polarization $\langle \phi^2(t_0) \rangle_{\text{ren}}$ begins very close to 0 (the precision-limited calculation done here for $t = t_0$ has error bars crossing through 0). But as mass inflation progresses, $\langle \phi^2 \rangle_{\text{ren}}$ increases as more and more quantized field modes become occupied by the changing gravitational potential.

After the inflationary Kasner spacetime undergoes a bounce and proceeds to collapse towards the strong, spacelike singularity, the renormalized variance continues to increase, spanning several orders of magnitude as it approaches a divergence at $t = 0$. Throughout the duration of the collapse epoch, $\langle \phi^2 \rangle_{\text{ren}}$ seems to follow a quasi-power law in time, with an index of -3. Qualitatively, the vacuum polarization follows a similar trend to that of the inflationary Kasner spacetime's classical stress-energy tensor, whose density and radial flux components in a locally orthonormal tetrad frame are [125]

$$T_{00} = T_{11} = \frac{1}{4\pi c_1 t \; e^{t^2}},$$ (5.35)

which also asymptote to a power law in t during the final collapse regime. The main difference is that the power law divergence in $\langle \phi^2 \rangle_{\text{ren}}$ is even steeper than that of the classical stress-energy tensor.

Figure 5.5: Renormalized adiabatic vacuum expectation value of the quantized field variance as a function of time in the inflationary Kasner spacetime. The vertical line signals the bounce transition from the mass inflation epoch to the spacelike collapse epoch, and the dashed line shows a t^{-3} power law. The black hole spin is $a = 0.96$, the initial accretion rate is $u = 0.02$, and the adiabatic matching time is $t_A = 5$.

5.5   Discussion

The results from Sec. 5.4.2 suggest that as an observer falls into a rotating, accreting black hole and approaches the inner horizon, the classical picture of mass inflation and subsequent spacelike collapse is reinforced when semiclassical effects are taken into account. In particular, when a quantized, massless, neutral, scalar field in the adiabatic vacuum state is coupled to the inflationary Kasner spacetime, to first-loop order, that field acquires a nonzero variance, shown in Fig. 5.5, that follows a similar trend to that of the classical stress-energy of the spacetime, asymptotically approaching a power law divergence.

Since the vacuum polarization $\langle \phi^2 \rangle_{\mathrm{ren}}$ can be seen as a tracer for the behavior of the renormalized stress-energy tensor $\langle T_{\mu\nu} \rangle_{\mathrm{ren}}$, which feeds back into the geometry of the spacetime via the semiclassical Einstein Eq. (3.9), the picture that emerges is a quantum backreaction that acts to amplify the strength of the curvature singularity at the inner horizon. Locally, particle production occurs near the inner horizon as the vacuum interacts with the inflating and collapsing spacetime curvature, and these particles seed further accretion that should feed back into the same classical inflationary Kasner spacetime.

The choice of constants used throughout this study is made both for numerical convenience and astrophysical relevance. As mentioned in Sec. 5.3.2, the choice of the adiabatic matching time t_A should not change the results of the renormalization much, as long as that time lies within the adiabatic regime. The only other independent constant in this model is c_1, the metric coefficient for the radial scale factor, which is determined by two physical constants via Eqs. (5.3) and (5.4), the black hole spin a and the initial accretion rate u. Though the spin parameter a can take on any value between 0 and 1, only a small range of values near 1 lead to numerically tractable values for c_1 with the present choice of coordinates (for example, when $a = 0.5$, the presence of an exponential term in the conversion factor leads to $c_1 \sim 10^{-70}$). However, within this range, changing the spin does not change the qualitative behavior of Fig. 5.5 (only the overall magnitude), and many astrophysical black holes have been observed with spins consistent with what has been used for this analysis [73,

$a\ (u{=}0.02)$

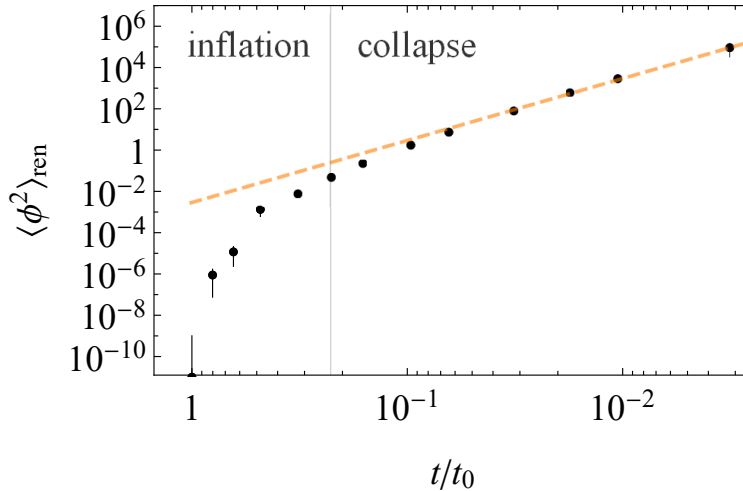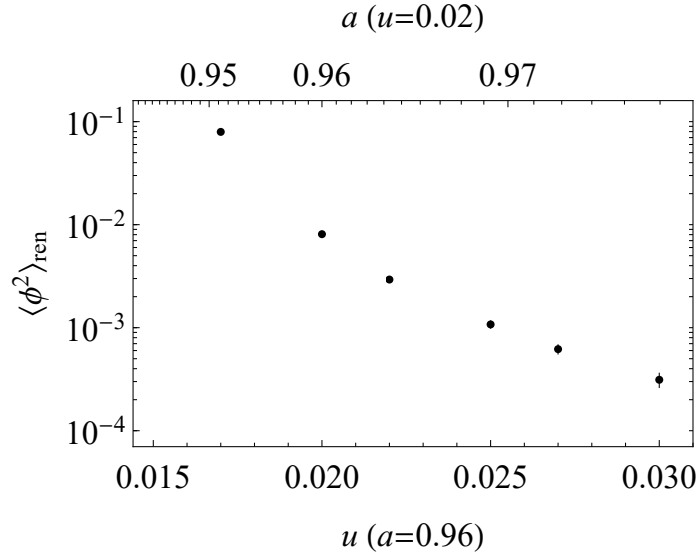
Figure 5.6: Renormalized adiabatic vacuum expectation value of the quantized field variance as a function of the inflationary Kasner metric coefficient c_1, which depends on both the initial accretion rate u and the black hole spin a. All the values shown are calculated at a time $t/t_0 \approx 0.32$.

77].

Regardless, the picture presented here is expected to hold for all astrophysically relevant ranges of spin and accretion; as either a or u increases, the overall magnitude of $\langle\phi^2\rangle_{\mathrm{ren}}$ decreases nonlinearly while preserving its general qualitative trend in t. The dependence of $\langle\phi^2\rangle_{\mathrm{ren}}$ on these parameters for a fixed time $t = 1 \approx 0.32t_0$ (in the intermediate regime between inflation and collapse) is shown in Fig. 5.6. For a fixed initial accretion rate u, as the spin a increases, $\langle\phi^2\rangle_{\mathrm{ren}}$ decreases, and similarly, for a fixed spin a, as the initial accretion rate u increases, $\langle\phi^2\rangle_{\mathrm{ren}}$ decreases. Classically, the tinier the accretion rate, the more powerful mass inflation becomes, and here it is found that the same holds true for the semiclassical backreaction to mass inflation.

To ensure the robustness of the results presented here, the next natural step is to build on this framework and calculate the renormalized quantum stress-energy tensor $\langle T_{\mu\nu}\rangle_{\mathrm{ren}}$. Such a calculation involves derivatives of the mode functions and contains stronger divergences to be renormalized than those of $\langle\phi^2\rangle_{\mathrm{ren}}$, but knowing $\langle T_{\mu\nu}\rangle_{\mathrm{ren}}$ will allow for a more direct understanding of the quantum backreaction at the inner horizon of rotating, accreting black holes.

Chapter 6

Renormalized Stress-Energy Tensor: $\langle \hat{T}_{\mu\nu} \rangle$

The contents of Sec. 6.1 have been published as part of [123], and the contents of Secs. 6.2-6.3 have been submitted for publication [124].

In this chapter, the inevitability of divergent semiclassical behavior at inner horizons will be confirmed by analyzing the behavior of the vacuum expectation value of the renormalized stress-energy tensor $\langle T_{\mu\nu} \rangle$. This quantity is not only free of assumptions about adiabaticity and eikonality, but it is also more directly tied to the effects of quantum backreaction on the underlying spacetime geometry (via the semiclassical Einstein field Eq. 3.9).

This chapter is divided into three sections; first, in Sec. 6.1 the renormalized stress-energy tensor (RSET) is calculated at the inner horizon for black holes with spherical symmetry. The specific model under consideration is the inner-extremal regular black hole introduced in Sec. 4.3.1.5, with a line element given by Eqs. (4.1) and (4.43). This black hole is similar to the Reissner-Nordström solution but has an inner horizon with zero surface gravity κ_-; if there was a non-extremal spherical black hole solution without a diverging inner-horizon RSET, this would be the most promising candidate. However, it will be shown using two different renormalization techniques (the Polyakov approximation in Sec. 6.1.1 and point-splitting in Sec. 6.1.2) that the RSET does indeed diverge at the inner horizon of inner-extremal regular black holes, so that they are actually not regular in the semiclassical sense.

In the second section of this chapter (Sec. 6.2), the RSET is calculated at the inner horizon

of a Kerr black hole for a large range of parameters. The conclusion is once again that at least one component of the RSET always diverges at the inner horizon, and therefore the semiclassical backreaction to the spacetime metric cannot be neglected. Therefore, in the final section (Sec. 6.3), an analysis of the semiclassical field equations is carried out to determine how the RSET should backreact on the near-inner-horizon geometry. The resulting predictions end up bearing a striking resemblance to the classical behavior of the inflationary Kasner metric derived in Chapter 2, with some additional surprises.

6.1   Spherical black holes

As a primer, consider the trace anomaly, which helped form the foundations of semiclassical gravity in the early days of quantum field theory in curved spacetimes [56]. While the trace of the stress-energy tensor for a classical field with conformal invariance must vanish, the trace of the expectation value of the renormalized stress-energy tensor for a quantum theory with an ultraviolet regulator is generically non-zero—for a conformal field in four spacetime dimensions, this trace anomaly can be written as

$$\langle T_\mu^\mu \rangle = \alpha_F F + \alpha_E E + \alpha_R \Box R \tag{6.1}$$

[56], where F is the squared Weyl tensor, E is the squared Riemann dual tensor (known as the Euler density), and $\Box R$ is the d'Alembertian of the Ricci scalar R. These quantities can be expressed in terms of the Riemann tensor $R_{\mu\nu\rho\sigma}$ and the Ricci tensor $R_{\mu\nu}$ as

$$F = R_{\mu\nu\rho\sigma}R^{\mu\nu\rho\sigma} - 2R_{\mu\nu}R^{\mu\nu} + \frac{1}{3}R^2, \tag{6.2a}$$

$$E = R_{\mu\nu\rho\sigma}R^{\mu\nu\rho\sigma} - 4R_{\mu\nu}R^{\mu\nu} + R^2. \tag{6.2b}$$

The coefficients α_F, α_E, and α_R depend only on the number of fields and their spins, so that the entire trace anomaly is independent of the vacuum state in which the renormalized stress-energy tensor is evaluated. The form of Eq. (6.1) may also contain additional additive terms if the massless

fields are coupled to additional background gauge fields.

For a Reissner-Nordström black hole, the Ricci scalar and its d'Alembertian vanish everywhere, but the squared Weyl tensor and Euler density remain non-zero, so that at the inner horizon, the trace anomaly becomes

$$\langle T_\mu^\mu \rangle^{\text{RN}}(r_-) = (\alpha_F + \alpha_E)\frac{12(r_+ - r_-)^2}{r_-^6} - \alpha_E \frac{8r_+^2}{r_-^6}. \tag{6.3}$$

For a spherical inner-extremal regular black hole, while the Ricci scalar does not vanish (at the inner horizon, $R = 2/r_-^2$), both $\Box R$ and E do vanish at the inner horizon, so that the trace anomaly simplifies to

$$\langle T_\mu^\mu \rangle^{\text{IE}}(r_-) = \alpha_F \; \frac{4}{3r_-^4}. \tag{6.4}$$

Note that a finite, non-zero conformal anomaly does not necessarily imply that individual components of a physically realizable renormalized stress-energy tensor will remain well-behaved—for example, for a Reissner-Nordström black hole, though $\langle T_\mu^\mu \rangle$ from Eq. (6.3) is finite and non-zero at the inner horizon, the flux components (as well as the trace) of $\langle T_{\mu\nu} \rangle^{\text{ren}}$ are well-known to exhibit an inner horizon divergence when a physically realistic vacuum state is used in place of the conformal vacuum [97, 180].

In principle, one may use the trace anomaly to derive an effective action for a set of auxiliary fields that can be used to define the full covariantly conserved stress-energy tensor $\langle T_{\mu\nu} \rangle^{\text{ren}}$ [6]. However, since inner-extremal regular black holes are not Ricci-flat, the resulting fourth-order differential equations to define $\langle T_{\mu\nu} \rangle^{\text{ren}}$ this way do not have analytic solutions in closed form. Further, if the quantum field $\hat{\phi}$ over the spacetime is not conformally invariant, an additional $\Box\langle \phi^2 \rangle^{\text{ren}}$ term must be included in the calculation of the renormalized stress-energy tensor's trace [163]. Thus, instead, the renormalized stress-energy tensor will be evaluated two different ways here: first, integrating over the angular degrees of freedom allows for $\langle T_{\mu\nu} \rangle^{\text{ren}}$ to be calculated exactly in 1+1 dimensions via the so-called Polyakov approximation (Sec. 6.1.1), and secondly, a pragmatic mode-sum analysis allows for $\langle T_{\mu\nu} \rangle^{\text{ren}}$ to be calculated numerically via point-splitting at the inner

horizon in the full 3+1 dimensions (Sec. 6.1.2).

6.1.1   Polyakov approximation

If the static, spherically symmetric black hole spacetime described by Eq. (4.1) is restricted to the (t, r) sector, the stress-energy tensor of a quantized field in the resulting 1+1D spacetime can be uniquely renormalized to yield an exact expression, since the equations of motion for the field are conformally invariant [19]. If one converts to a set of double null coordinates (u, v) that define the vacuum state, so that the line element becomes

$$ds^2 = -C(u, v)\ du\ dv \tag{6.5}$$

for some conformal factor C, the vacuum expectation value of the renormalized stress-energy tensor for a massless, scalar quantum field will be

$$\langle T_{uu} \rangle^{\text{ren}} = \frac{1}{24\pi} \left(\frac{1}{C} \frac{\partial^2 C}{\partial u^2} - \frac{3}{2C^2} \left(\frac{\partial C}{\partial u} \right)^2 \right), \tag{6.6a}$$

$$\langle T_{vv} \rangle^{\text{ren}} = \frac{1}{24\pi} \left(\frac{1}{C} \frac{\partial^2 C}{\partial v^2} - \frac{3}{2C^2} \left(\frac{\partial C}{\partial v} \right)^2 \right), \tag{6.6b}$$

$$\langle T_{uv} \rangle^{\text{ren}} = \frac{1}{24\pi} \left(\frac{1}{C^2} \frac{\partial C}{\partial u} \frac{\partial C}{\partial v} - \frac{1}{C} \frac{\partial^2 C}{\partial u \partial v} \right). \tag{6.6c}$$

The contribution made by Polyakov (working in the context of bosonic string theory) was that an effective action for a higher-dimensional theory can be reduced to a two-dimensional, renormalizable, completely integrable theory by performing an averaging sum over all the remaining surfaces [155]. In the present context, Polyakov's approximation manifests by averaging over the 2-sphere so that the renormalized stress-energy tensor in 3+1 dimensions is simply given by the expressions of Eqs. (6.6), each divided by the factor $4\pi r^2$. While such a choice implies that $\langle T_{\mu\nu} \rangle^{\text{ren}}$ will behave in a singular fashion at $r = 0$, this $r = 0$ singularity at least in the rotating case can only be reached in an infinite proper time [67], but more importantly, it is understood that the renormalized stress-energy tensor in the Polyakov approximation should be further regularized at small r [9].

6.1.1.1 Boulware vacuum

The calculation of $\langle T_{\mu\nu}\rangle^{\mathrm{ren}}$ depends heavily on the choice of vacuum state, which, as mentioned, is dictated by the specification of the conformal factor $C(u,v)$ of Eq. (6.5). One simple choice is to set $C = \Delta$ from Eq. (4.43), so that the double null coordinates (u,v) coincide with the usual static Eddington-Finkelstein coordinates. The corresponding vacuum state $|0\rangle_{\mathrm{B}}$ is known as the Boulware vacuum, which describes an asymptotically radiation-free black hole as viewed by a static observer in the exterior (and a similar state can be defined for a zero-energy observer in the black hole interior). As a result, the state is not well-defined for an observer at either horizon, and an infaller will see a diverging stress-energy flux at the outer horizon:

$$\langle T_{uu}\rangle^{\mathrm{ren}}_{\mathrm{B}} = \langle T_{vv}\rangle^{\mathrm{ren}}_{\mathrm{B}} = \frac{1}{192\pi^2 r^2}\left(\kappa'(r)\Delta(r) - \kappa(r)^2\right), \tag{6.7a}$$

$$\langle T_{uv}\rangle^{\mathrm{ren}}_{\mathrm{B}} = \langle T_{vu}\rangle^{\mathrm{ren}}_{\mathrm{B}} = \frac{1}{192\pi^2 r^2}\kappa'(r)\Delta(r), \tag{6.7b}$$

where $\kappa(r)$ is the generalized surface gravity given by Eq. (4.42). While these null components of $\langle T_{\mu\nu}\rangle^{\mathrm{ren}}$ do not diverge at either horizon, the coordinate system does. Changing to a coordinate system that behaves regularly at the horizons, such as the Kruskal-Szekeres coordinates (U,V) defined by

$$\frac{dU}{du} = \mathrm{e}^{-\kappa(r_+)u}, \qquad \frac{dV}{dv} = \mathrm{e}^{\kappa(r_+)v}, \tag{6.8}$$

reveals that as long as $\langle T_{uu}\rangle^{\mathrm{ren}}_{\mathrm{B}}$ is non-zero at the outer horizon, $\langle T_{UU}\rangle^{\mathrm{ren}}_{\mathrm{B}}$ will diverge as $\mathrm{e}^{2\kappa(r_+)u}$ as the horizon at $u \to \infty$ is approached. At the outer horizon, the surface gravity $\kappa(r_+)$ contributing to Eq. (6.7a) remains non-zero, so the Boulware vacuum stress-energy will always diverge in that limit. In accordance with the Fulling-Sweeny-Wald theorem [71], since any Hadamard state should yield finite quantities at the outer horizon, a more astrophysically relevant vacuum state must be sought after.

The two vacuum states that will be used here to find the renormalized stress-energy tensor at the inner horizon are the "in" Minkowski vacuum $|0\rangle_{\mathrm{in}}$ and the Unruh vacuum $|0\rangle_{\mathrm{U}}$.

6.1.1.2   Minkowski "in" vacuum

The "in" vacuum state assumes that asymptotically far into the past, the spacetime is completely flat, with the standard Minkowski vacuum. Then, at a time $v = v_0$, an ingoing null shell forms a black hole so that the conformal factor of Eq. (6.5) transitions from $C(u_{\text{in}}, v_{\text{in}}) = 1$ in the "in" region $(v < v_0)$ to $C(u_{\text{out}}, v_{\text{out}}) = \Delta$ in the "out" region $(v > v_0)$. The corresponding conformal factor of the "in" vacuum state to be substituted into Eq. (6.6) is

$$C = \frac{du_{\text{out}}}{du_{\text{in}}}\Delta, \tag{6.9}$$

where the relation between the "in" and "out" coordinates can be found by matching metrics through the collapsing null shell, as detailed below.

The authors of Ref. [18] performed such a matching with sufficient generality by focusing on the asymptotic behavior of $\langle T_{\mu\nu}\rangle_{\text{in}}^{\text{ren}}$ at the inner and outer horizons. By expanding the horizon function Δ about either horizon at $r_\pm$ via the series of Eq. (4.49), the stress-energy tensor at $r_\pm$ reduces to

$$\langle T_{uu}\rangle_{\text{in}}^{\text{ren}} \approx \frac{1}{96\pi^2 r_\pm^2} \frac{\kappa''(r_\pm)}{8\kappa(r_\pm)}\left(e^{2\kappa(r_\pm)(v-v_0)} - 1\right) + \mathcal{O}\left(r - r_\pm\right), \tag{6.10a}$$

$$\langle T_{vv}\rangle_{\text{in}}^{\text{ren}} \approx -\frac{1}{96\pi^2 r_\pm^2} \frac{\kappa(r_\pm)^2}{2} + \mathcal{O}\left((r - r_\pm)^2\right), \tag{6.10b}$$

$$\langle T_{uv}\rangle_{\text{in}}^{\text{ren}} = \langle T_{vu}\rangle_{\text{in}}^{\text{ren}} \approx \frac{1}{96\pi^2 r_\pm^2} \frac{\kappa'(r_\pm)}{2}e^{\kappa(r_\pm)(v-v_0)} + \mathcal{O}\left(r - r_\pm\right). \tag{6.10c}$$

For the inner-extremal regular black holes in which $\kappa(r_-) = 0$, the modified series expansion and subsequent matching procedure lead to the same form for the stress-energy tensor components as that inferred from Eqs. (6.10). In particular, the uu-component of the stress-energy tensor at the inner horizon diverges as $\kappa''(r_-)(v - v_0)$, while the vv-component vanishes. Converting to a set of regular coordinates across the horizon (such as $\langle T_{rr}\rangle_{\text{in}}^{\text{ren}}$) yields a similar divergence in v. However, as the authors of Ref. [18] note, higher-order terms in the series expansion also contain similar

time-dependent divergent factors (except in the expansion of $\langle T_{vv} \rangle_{\text{in}}^{\text{ren}}$), so that the truncated series expansion about the inner horizon becomes less and less of a good approximation as v increases. The opposite happens at the outer horizon, where higher-order time-dependent terms are exponentially damped in accordance with the change in sign of the surface gravity.

To alleviate this problem, instead of performing a series expansion about a general horizon function Δ, consider the exact form of the "in" vacuum stress-energy tensor for the specific case of the horizon function of Eq. (4.43). At the null shell boundary, outgoing null geodesics in the "in" region satisfy

$$r = \frac{v_0 - u_{\text{in}}}{2},$$

(6.11)

while outgoing null geodesics in the "out" region satisfy

$$\frac{v_0 - u_{\text{out}}}{2} = r + \frac{A}{(r - r_-)} + \frac{B}{(r - r_-)^2} + C \ln \left| \frac{r - r_-}{r_-} \right| + D \ln \left| \frac{r - r_+}{r_+} \right|,$$

(6.12)

where the constants A, B, C, and D define a tortoise coordinate (via $dr/dr^* = \Delta$); their exact form in terms of the parameters r_+, r_-, a_2, and M is not too enlightening and will not be given here. After matching these solutions at the null boundary, the resulting stress-energy tensor can then be calculated through Eqs. (6.6) and (6.9). Instead of calculating the full u- and v-dependence of the conformal factor C, one may note that each term on the right-hand side of Eq. (6.9) will contribute a separate additive term to the total stress-energy tensor: the contribution from the horizon function Δ has already been calculated as the static Boulware term of Eqs. 6.7, and the second state-dependent term will approximately equal the Schwarzian derivative of $u_{\text{in}}(u_{\text{out}})$, divided by -24π [61].

The result for the normal stress components (for simplicity the shear stress components are ignored in what follows, since they will generally vanish in the horizon limit) of the renormalized stress-energy tensor in the "in" vacuum state, evaluated at the outer horizon (where $u_{\text{in}} = v_0 - 2r_+$

and $r = r_+$), is

$$\lim_{r \to r_+} \langle T_{uu} \rangle_{\text{in}}^{\text{ren}} = 0, \tag{6.13a}$$

$$\lim_{r \to r_+} \langle T_{vv} \rangle_{\text{in}}^{\text{ren}} = -\frac{1}{96\pi^2 r_+^2} \frac{\kappa(r_+)^2}{2}, \tag{6.13b}$$

while the same components evaluated at the left leg of the inner horizon (where $u_{\text{in}} = v_0$ and $r = r_-$) simplify to

$$\lim_{r \to r_-} \langle T_{uu} \rangle_{\text{in}}^{\text{ren}} = \frac{1}{96\pi^2 r_-^2} \frac{a_2 - 3r_-(r_+ + r_-)}{2r_+ r_-^3}, \tag{6.14a}$$

$$\lim_{r \to r_-} \langle T_{vv} \rangle_{\text{in}}^{\text{ren}} = 0. \tag{6.14b}$$

The outer horizon value of $\langle T_{uu} \rangle_{\text{in}}^{\text{ren}}$ vanishes because the state-dependent term is proportional to $\kappa(r_+)^2$, which exactly cancels the same factor in the Boulware term of Eq. (6.7a), while the inner horizon value of $\langle T_{vv} \rangle_{\text{in}}^{\text{ren}}$ vanishes because both the state-dependent and Boulware terms are identically zero.

At the outer horizon, the interpretation of Eqs. (6.13) is that a steady negative ingoing flux counters the outgoing Hawking radiation at infinity and causes the outer horizon to shrink over time, while no outgoing flux is observed at the outer horizon (otherwise, the stress-energy would diverge there when written in coordinates that are regular across the horizon).

At the left leg of the inner horizon, the interpretation of Eqs. (6.14) is that the vanishing surface gravity removes any ingoing flux that might shift the position of the inner horizon, but the outgoing flux from the collapse vacuum is non-zero and therefore causes divergent, singular behavior when switching over to Kruskalized coordinates that are regular across the inner horizon.

6.1.1.3   Unruh vacuum

The final vacuum state that will be considered here is the (past) Unruh vacuum $|0\rangle_{\text{U}}$ [173], which is the late-time ($u \to \infty$) limit of the "in" Minkowski state. This state describes the steady-state

collapse dynamics of a black hole by replacing the past horizon of an eternal black hole spacetime (such as the inner-extremal regular black hole model) with a semiclassically singular surface that sources exponentially redshifting modes.

The appropriate conformal factor for the Unruh state is

$$C = \frac{du}{dU}\Delta, \tag{6.15}$$

where u is the standard outgoing Eddington-Finkelstein coordinate and U is the outgoing Kruskal-Szekeres coordinate of Eq. (6.8). The resulting components of the renormalized stress-energy tensor are

$$\langle T_{uu}\rangle_{\mathrm{U}}^{\mathrm{ren}} = \frac{1}{192\pi^2 r^2}\left(\kappa'(r)\Delta(r) - \kappa(r)^2 + \kappa(r_+)^2\right), \tag{6.16a}$$

$$\langle T_{vv}\rangle_{\mathrm{U}}^{\mathrm{ren}} = \frac{1}{192\pi^2 r^2}\left(\kappa'(r)\Delta(r) - \kappa(r)^2\right), \tag{6.16b}$$

$$\langle T_{uv}\rangle_{\mathrm{U}}^{\mathrm{ren}} = \langle T_{vu}\rangle_{\mathrm{U}}^{\mathrm{ren}} = \frac{1}{192\pi^2 r^2}\kappa'(r)\Delta(r). \tag{6.16c}$$

Consider the behavior of Eqs. (6.16) for the horizon function of Eq. (4.43). At the outer horizon, the only non-zero double-null component of $\langle T_{\mu\nu}\rangle_{\mathrm{U}}^{\mathrm{ren}}$ is the usual ingoing vv term contributing to the shrinking of that horizon. However, at the inner horizon, the only non-vanishing component is the uu component, which is proportional to the square of the *outer* horizon's surface gravity. As a result, conversion to a set of coordinates that are regular across horizons will yield a physical divergence in $\langle T_{\mu\nu}\rangle_{\mathrm{U}}^{\mathrm{ren}}$ along the left leg of the inner horizon. This divergence is of the exact same form as that found in the effective temperature calculations of Eq. (4.48a)—even though the inner horizon's surface gravity may vanish, the semiclassical flux diverges at the inner horizon because the surface gravity of the outer horizon (which determines the quantum modes' exponential peeling rates) is non-zero.

6.1.2   Pragmatic mode-sum renormalization

One may wonder whether the divergence of the renormalized stress-energy tensor at the inner horizon is simply an artifact of the Polyakov restriction to 1+1 dimensions, which does not account for the back-scattering of angular modes. To test whether this is the case, the inner-horizon limit of the 3+1D renormalized stress-energy tensor will be calculated numerically using a prescription developed by Levi and Ori known as pragmatic mode-sum renormalization (PMR) [111, 112, 114].

In the PMR prescription, $\langle T_{\mu\nu} \rangle$ is renormalized with covariant point-splitting, where the stress-energy tensor is built out of the field's two-point function and its derivatives. The resulting quantity will formally diverge when the coincidence limit is taken, but it will remain finite when a geometrically constructed counterterm is subtracted from the bare stress-energy tensor. Covariant point-splitting renormalization usually has the numerical difficulty that both the bare stress-energy and the subtracted counterterm formally diverge, so that a finite result can only be obtained when both quantities are regularized to yield analytic closed forms that can be subtracted. The way PMR overcomes this obstacle is by bringing both the bare term and the counterterm under the same mode sum, so that the subtraction can be carried out in a finite fashion mode-by-mode.

If a massless, minimally coupled scalar field $\hat{\phi}$ is placed over the spherically symmetric spacetime of Eq. (4.1) with the inner-extremal regular horizon function of Eq. (4.43), that field will obey the wave equation $\Box\phi = 0$. Decomposing the field into a sum of modes via

$$\phi(x) = \sum_{\ell=0}^{\infty} \sum_{m=-\ell}^{\ell} \int_0^{\infty} d\omega \; e^{-i\omega t} Y_{\ell m}(\theta, \varphi) \psi_{\omega\ell}(r) \tag{6.17}$$

leads to the following wave equation for the radial mode functions $\psi_{\omega\ell}$:

$$\frac{d\psi_{\omega\ell}}{dr^{*2}} + \left(\omega^2 - \left(\frac{\ell(\ell+1)}{r^2} + \frac{2\kappa}{r} \right) \Delta \right) \psi_{\omega\ell} = 0, \tag{6.18}$$

where r^* is the tortoise coordinate defined by $dr/dr^* = \Delta$ as in Eq. (6.12), and $\kappa(r)$ is the generalized surface gravity of Eq. (4.42).

The Unruh state for this field $\hat{\phi}$ is specified by the following boundary conditions on the set of ingoing modes $\phi_{\omega\ell}^{\mathrm{in}} \equiv \mathrm{e}^{-i\omega t}\psi_{\omega\ell}^{\mathrm{in}}$ and outgoing modes $\phi_{\omega\ell}^{\mathrm{up}} \equiv \mathrm{e}^{-i\omega t}\psi_{\omega\ell}^{\mathrm{up}}$:

$$\phi_{\omega\ell}^{\mathrm{in}} \to \begin{cases} 0, & \text{past null infinity} \\ \mathrm{e}^{-i\omega U}, & \text{past horizon} \end{cases}, \tag{6.19a}$$

$$\phi_{\omega\ell}^{\mathrm{up}} \to \begin{cases} \mathrm{e}^{-i\omega v}, & \text{past null infinity} \\ 0, & \text{past horizon} \end{cases}, \tag{6.19b}$$

with the Kruskal-Szekeres coordinate U of Eq. (6.8), the Eddington-Finkelstein coordinate $u \equiv t - r^*$ (both in the interior and the exterior), and where the "past horizon" denotes the surface for which $r^* \to -\infty$ and $t \to -\infty$ (both in the interior and the exterior).

In this vacuum state, renormalization of the stress-energy tensor by θ-splitting PMR yields the following formulas for the normal stress components evaluated at the inner horizon:

$$\langle T_{uu} \rangle_{\mathrm{U}}^{\mathrm{ren}}(r_-) = \sum_{\ell=0}^{\infty} \frac{2\ell+1}{8\pi} \left(\int_0^{\infty} d\omega \ \hat{E}_{\omega\ell}^{\mathrm{U}} - \beta \right), \tag{6.20a}$$

$$\langle T_{vv} \rangle_{\mathrm{U}}^{\mathrm{ren}}(r_-) = \langle T_{uu} \rangle_{\mathrm{U}}^{\mathrm{ren}}(r_-) - \frac{1}{4\pi r_-^2} \sum_{\ell=0}^{\infty} L_\ell^{\mathrm{U}} \tag{6.20b}$$

[180], where

$$\hat{E}_{\omega\ell}^{\mathrm{U}} = \frac{\omega}{4\pi r_-^2} \left(|A_{\omega\ell}|^2 \left(1 + (\coth\widetilde{\omega} - 1)\,|\rho_{\omega\ell}^{\mathrm{up}}|^2 \right) + \operatorname{csch}\widetilde{\omega} \ \mathfrak{Re}\left(\rho_{\omega\ell}^{\mathrm{up}} A_{\omega\ell} B_{\omega\ell} \right) \right), \tag{6.21a}$$

$$L_\ell^{\mathrm{U}} = \frac{2\ell+1}{4\pi} \int_0^{\infty} d\omega \ \omega \left(\coth\widetilde{\omega} - 1 \right) |\tau_{\omega\ell}^{\mathrm{up}}|^2, \tag{6.21b}$$

where $\widetilde{\omega} \equiv \pi\omega/\kappa(r_+)$, and where $\rho_{\omega\ell}^{\mathrm{up}}$, $\tau_{\omega\ell}^{\mathrm{up}}$, $A_{\omega\ell}$, and $B_{\omega\ell}$ are scattering coefficients described in more detail below.

The above expressions for the components of the renormalized stress-energy tensor at the inner horizon were originally derived for Reissner-Nordström black holes, but the derivation was carried out with sufficient generality so that it also can be applied to the present case of spherical inner-extremal regular black holes with minimal changes. The most noticeable difference aside from

the alternative specification of the horizon function Δ is in the form of the blind-spot counterterm β in Eq. (6.20a), which represents the asymptotic large-ℓ plateau value of the integral immediately preceding it. In Reissner-Nordström, one has $\beta = \left(\kappa(r_-)^2 - \kappa(r_+)^2\right)/(24\pi r_-^2)$ [180], but the derivation of this analytic expression (in particular, the large-ℓ forms of the scattering coefficients derived in Ref. [163]) relies on the Reissner-Nordström form of the horizon function in several crucial ways. When the inner-extremal horizon function of Eq. (4.43) instead is used in the radial wave Eq. (6.18), the relevant asymptotic solutions can no longer be written in terms of Bessel functions near the inner horizon (nor any other well-understood special functions). An analytic form for β may still be possible for the inner-extremal case through a form of Frobenius matching; however, here it suffices to compute β numerically, since the sum of Eq. (6.20a) quickly reaches a plateau value within the desired precision after only a few of the lowest-ℓ terms are included. Regardless, as will be seen, the divergence of at least one component of $\langle T_{\mu\nu}\rangle^{\mathrm{ren}}$ can be shown without making any assumptions about β.

The scattering coefficients $\rho_{\omega\ell}^{\mathrm{up}}$, $\tau_{\omega\ell}^{\mathrm{up}}$, $A_{\omega\ell}$, and $B_{\omega\ell}$ are computed by numerically integrating the radial wave Eq. (6.18) for a set of Eddington-Finkelstein modes propagating between the asymptotic boundaries for both the exterior and interior black hole sectors. In the exterior sector, the reflection coefficient $\rho_{\omega\ell}^{\mathrm{up}}$ gives the fraction of outgoing waves emitted from the outer horizon in the asymptotic past that reflect back to the outer horizon, while the transmission coefficient $\tau_{\omega\ell}^{\mathrm{up}}$ gives the remaining portion of waves that reach infinity:

$$\psi_{\omega\ell}^{\mathrm{up}} \to \begin{cases} \mathrm{e}^{i\omega r^*} + \rho_{\omega\ell}^{\mathrm{up}}\,\mathrm{e}^{-i\omega r^*}, & r^* \to -\infty \\ \tau_{\omega\ell}^{\mathrm{up}}\,\mathrm{e}^{i\omega r^*}, & r^* \to \infty \end{cases}. \tag{6.22}$$

The reflection coefficient $\rho_{\omega\ell}^{\mathrm{up}}$ is related to the transmission coefficient $\tau_{\omega\ell}^{\mathrm{up}}$ through the condition $|\rho_{\omega\ell}^{\mathrm{up}}|^2 + |\tau_{\omega\ell}^{\mathrm{up}}|^2 = 1$ resulting from Wronskian conservation of solutions for the radial wave Eq. (6.18).

In the interior sector, where r^* becomes a timelike coordinate, free incoming waves at the outer horizon scatter into a superposition of ingoing and outgoing waves at the inner horizon with the corresponding reflection and transmission coefficients $A_{\omega\ell}$ and $B_{\omega\ell}$:

$$\psi_{\omega\ell}^{\mathrm{up}} \rightarrow \begin{cases} \mathrm{e}^{-i\omega r^*}, & r^* \rightarrow -\infty \\ A_{\omega\ell}\ \mathrm{e}^{i\omega r^*} + B_{\omega\ell}\ \mathrm{e}^{-i\omega r^*}, & r^* \rightarrow \infty \end{cases}. \tag{6.23}$$

For these interior scattering coefficients, which need not remain bounded, the Wronskian condition implies that $|B_{\omega\ell}|^2 - |A_{\omega\ell}|^2 = 1$.

Once these scattering coefficients are computed numerically for each set of modes specified by ω and ℓ, the quantity $\hat{E}_{\omega\ell}^{\mathrm{U}}$ from Eq. (6.20a) can be integrated over a sampled set of frequencies with the help of third-order Hermite interpolation built into the software package `Mathematica`. In practice, instead of sampling points all the way out to $\omega \rightarrow \infty$, computations of the integrand $\hat{E}_{\omega\ell}^{\mathrm{U}}$ are terminated once it enters deep into the regime in which it decays as $\omega \cdot \mathrm{e}^{-\omega/k}$ for some positive k, after which the integrand is analytically extended to infinity with the appropriate extrapolation. The values of this integrand for the $\ell = 0$ and $\ell = 1$ modes are shown in the left panel of Fig. 6.1.

For numerical computations, the outer and inner horizons are chosen to lie at the following radii:

$$r_+ = 2M, \qquad r_- = l\left(1 + \alpha\frac{l}{M} + \mathcal{O}\left(\frac{l^2}{M^2}\right)\right), \tag{6.24}$$

where M is the mass of the black hole, α is an order-unity parameter, and l is a regularization length scale often identified as the Planck length, where semiclassical gravity breaks down (though it should be noted that for the present choice of constants such an identification cannot be upheld as it would imply that the black hole weighs less than a single grain of sand). The numerical computations done here use the same choices for these constants as in Ref. [38]: $\alpha = 1$ and $M/l = 100$.

In the left panel of Fig. 6.1, though the spectra for only the lowest two angular modes ($\ell = 0$ and $\ell = 1$) are shown, all higher-ℓ modes appear visually similar to the $\ell = 1$ spectrum on that plot, as the integrated spectrum quickly plateaus to the value β as ℓ is increased. This constant is numerically found to equal approximately $1.4 \times 10^4 M^{-4}$, which is consistent with the parameter range one might expect from an analysis of Reissner-Nordström black holes (in particular, the inner-extremal β for this choice of parameters coincides with the Reissner-Nordström β for a black hole with charge-to-mass
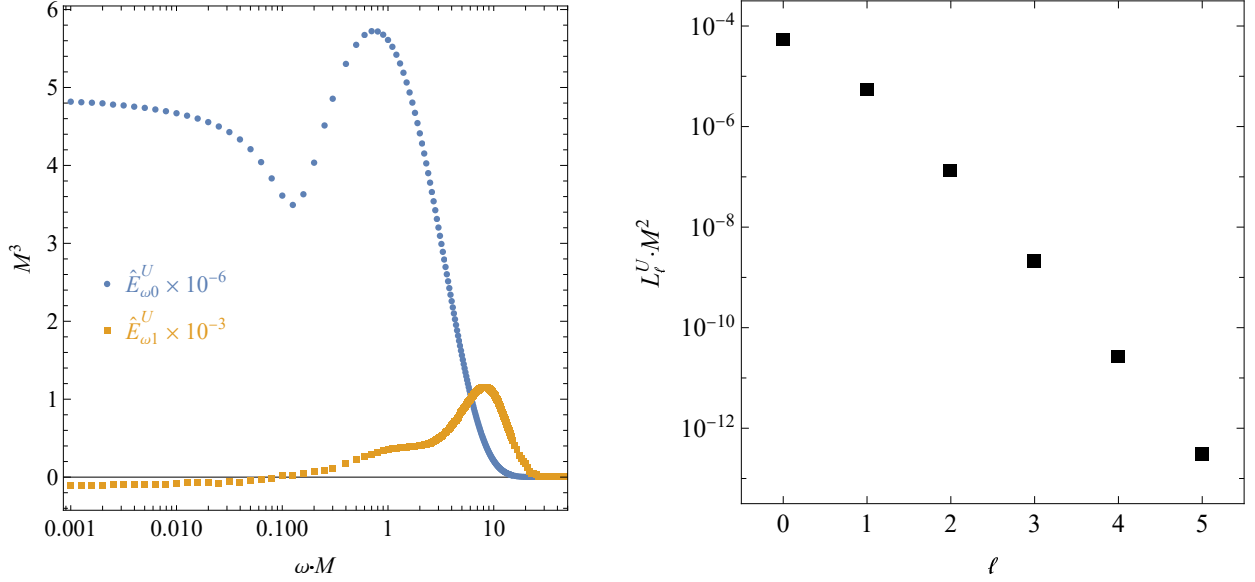
Figure 6.1: *(Left panel)* Numerically computed values of the integrand $\hat{E}^{\mathrm{U}}_{\omega\ell}$ from Eq. (6.20a) for the $\ell = 0$ (blue) and $\ell = 1$ (orange) modes. The area under each of these curves (which approaches the constant β as $\ell \to \infty$) is used to calculate the Unruh-state renormalized stress-energy component $\langle T_{uu}\rangle^{\mathrm{ren}}_{\mathrm{U}}$ evaluated at the inner horizon.
(Right panel) Numerically computed values of luminosity ℓ-modes L^{U}_{ℓ} from Eq. (6.21b). The sum of all these values from $\ell = 0$ to $\ell = \infty$ yields the Hawking outflux $4\pi r^2_- \left(\langle T_{uu}\rangle^{\mathrm{ren}}_{\mathrm{U}} - \langle T_{vv}\rangle^{\mathrm{ren}}_{\mathrm{U}}\right)$ of Eq. (6.20b). All modes are positive and drop to zero exponentially as ℓ increases. The fact that the sum over all these points yields a non-zero value indicates that at least one (Kruskalized) component of the renormalized stress-energy tensor diverges at the inner horizon of spherical inner-extremal regular black holes. The constants used for both the left and right panels are $\alpha = 1$, $l/M = 1/100$, and $a_2/M^2 = 1/10$.

ratio $Q/M \approx 0.427$). As a result, the uu-component of the Unruh-state renormalized stress-energy tensor at the inner horizon from Eq. (6.20a) is calculated to be $8.9 \times 10^5 M^{-4}$. Since this value is non-zero, the corresponding stress-energy component for a set of coordinates that are regular through the inner horizon, such as the Kruskal coordinates of Eq. (6.8), will diverge.

Since the inner-extremal regular black hole spacetime under consideration here is spherically symmetric and static, energy-momentum conservation implies that in spherically symmetric, static quantum states like the Unruh state, the quantity

$$4\pi r^2\left(\langle T_{uu}\rangle^{\mathrm{ren}}_{\mathrm{U}} - \langle T_{vv}\rangle^{\mathrm{ren}}_{\mathrm{U}}\right) \tag{6.25}$$

must be conserved everywhere in the spacetime [180]. For some vacuum states like the Hartle-Hawking state, this constant trivially vanishes, but for the Unruh state, it can be evaluated at the inner horizon as the sum $\sum_{\ell=0}^{\infty} L_\ell^{\mathrm{U}}$ from Eqs. (6.20b) and (6.21b). For the Unruh state, this luminosity coincides precisely with the Hawking outflux. For the choice of inner-extremal parameters used throughout this section, the computed Hawking outflux equals $6.81142 \times 10^{-5} M^{-2}$. To obtain this value, similar to the methodologies described above, the external scattering coefficient is sampled for a set of frequencies and extrapolated with the knowledge that at high frequencies, the integrand of Eq. (6.21b) behaves as $\omega \cdot \mathrm{e}^{-2\widetilde{\omega}}$, while at low frequencies, it behaves as a power law in ω. Then, the spectrum is integrated over all frequencies and summed over larger and larger values of ℓ until convergence is reached, as shown in the right panel of Fig. 6.1.

The fact that the Hawking outflux does not vanish at the inner horizon indicates that $\langle T_{uu} \rangle_{\mathrm{U}}^{\mathrm{ren}}$ and $\langle T_{vv} \rangle_{\mathrm{U}}^{\mathrm{ren}}$ can never simultaneously equal zero and therefore that at least one component (in coordinates that are regular across the inner horizon) of the renormalized stress-energy tensor will always diverge there. The remarkable aspect of this result is that the semiclassical divergence occurs regardless of anything happening in the interior, such as a vanishing surface gravity at the inner horizon or some anomalous scattering governed by $A_{\omega\ell}$ and $B_{\omega\ell}$. Rather, from Eq. (6.21b), this divergence depends only on the external portion of the spacetime, characterized by the outer horizon's surface gravity $\kappa(r_+)$ and the external transmission coefficient $\tau_{\omega\ell}^{\mathrm{up}}$.

6.1.3   Outlook

In the absence of a full theory of quantum gravity, one may hope that using an effective field theory to describe the semiclassical behavior of gravity (valid up the the Planck energy) would be enough to provide a complete model of astrophysical black holes formed from collapse. If this were true, one should be able to write down a completely classical, singularity-free metric to describe the black hole, sourced by semiclassical stress-energy via Eq. (3.9). The inner-extremal regular black hole metric of Eq. (4.1) potentially provides such a model, especially promising due to its avoidance of the classical mass inflation instability.

The key takeaway of the present analysis is that for black holes formed from astrophysical collapse, no regular black hole models with an inner horizon will be semiclassically stable and regular, regardless of whether or not the inner horizon is fine-tuned so that its surface gravity vanishes (like in the inner-extremal models). An Unruh-state semiclassical divergence at the inner horizon is driven by both the inner and outer horizons' surface gravities, so that the only singularity-free black holes models that can avoid the semiclassical instability are extremal black holes.

The semiclassical divergence present at the inner horizon of inner-extremal regular black holes has here been demonstrated with the calculation of the renormalized stress-energy tensor for a quantized massless scalar field. In Sec. 6.1.1, the RSET was evaluated using the Polyakov approximation (i.e., averaging over the angular degrees of freedom so that an exact answer can be obtained in 1+1 dimensions). The normal stress component of this tensor in outgoing Eddington-Finkelstein coordinates ($\langle T_{uu} \rangle^{\mathrm{ren}}$) remains non-zero at the inner horizon in both the Unruh and Minkowski "in" vacuum states, which indicates that the physical stress-energy will diverge when one transforms to a set of coordinates that are regular across that surface.

Then, to confirm that the 1+1D calculations of Sec. 6.1.1 are not missing any crucial information from the scattering of higher-ℓ angular modes in the full 3+1 dimensions, the renormalized stress-energy tensor has been calculated numerically for a specific choice of parameters in Sec. 6.1.2 using pragmatic mode-sum renormalization. To do so requires finding the exterior and interior scattering coefficients for free waves traveling from infinity to the outer horizon and from the outer horizon to the inner horizon, respectively. The result is the same as in the 1+1D case: the renormalized stress-energy in outgoing Eddington-Finkelstein coordinates do not vanish at the inner horizon, so that a semiclassical singularity will emerge there if the spacetime remains static. This divergence will always occur for at least one leg of the inner horizon, since the difference $\langle T_{uu} \rangle^{\mathrm{ren}}_{\mathrm{U}} - \langle T_{vv} \rangle^{\mathrm{ren}}_{\mathrm{U}}$ in the Unruh state is always proportional to the non-zero Hawking outflux.

It would thus appear that any semiclassically self-consistent model of a regular black hole one may come up with cannot have an inner horizon that is spatially separated from the outer horizon, no matter how degenerate it may be. It would be interesting to analyze how the semiclassical

backreaction dynamically affects the inner-extremal geometry if the constraints of staticity are relaxed—the inner horizon may evaporate outward to meet the outer horizon and perhaps evolve to a new, non-black-hole geometry, for example. However, the vanishing of $\langle T_{vv}\rangle^{\text{ren}}$ in Eqs. (6.14) and (6.16) at the inner horizon offers an indication that forcing the inner horizon's surface gravity to vanish only strengthens the semiclassical divergence, since it is precisely this surface gravity that would cause the inner horizon to evaporate. Instead, it is likely that the semiclassical inflation near the inner horizon will occur too rapidly for the geometry to have time to react, so that a curvature singularity forms. One must then appeal to higher-order theories of quantum gravity to understand how spacetime evolves further [46].

6.2   Rotating black holes

Now, consider the evaluation of the RSET at the inner horizon of a rotating black hole, specifically in the case of the Kerr metric. What is the fate of the inner horizon and its traversability if a Kerr black hole is subject to semiclassical perturbations?

The computation of this renormalized stress-energy tensor (RSET) is a difficult task for physically realistic vacuum states in even the most symmetric spacetimes. But in recent years, novel computational methods have led to a resurgence of interest, and most relevant to the present analysis, Ref. [178] made use of state subtraction to calculate the mode-summed RSET of a scalar field at the inner horizon of a four-dimensional (4D) Kerr black hole (see [179] for a thorough derivation and Fig. 6.2 for the parameter space covered by the study). The main conclusion of the study was that the ingoing double-null flux component of the RSET (the vv-component, in Eddington-Finkelstein coordinates) is generically nonvanishing, implying that the semiclassical stress-energy will diverge when cast into coordinates that are regular across the inner horizon (as seen, for example, in the local frame of an infalling, outgoing[1] observer reaching the inner horizon). The implications are

---

[1]Infalling (outfalling) here means that the radial component of the observer's 4-velocity satisfies $\dot{r} < 0$ ($\dot{r} > 0$), while ingoing (outgoing) refers to a left-moving (right-moving) observer on a traditional Penrose diagram. Ingoing observers are not considered here, since the Unruh state differs substantially from the more realistic Minkowski in-state along
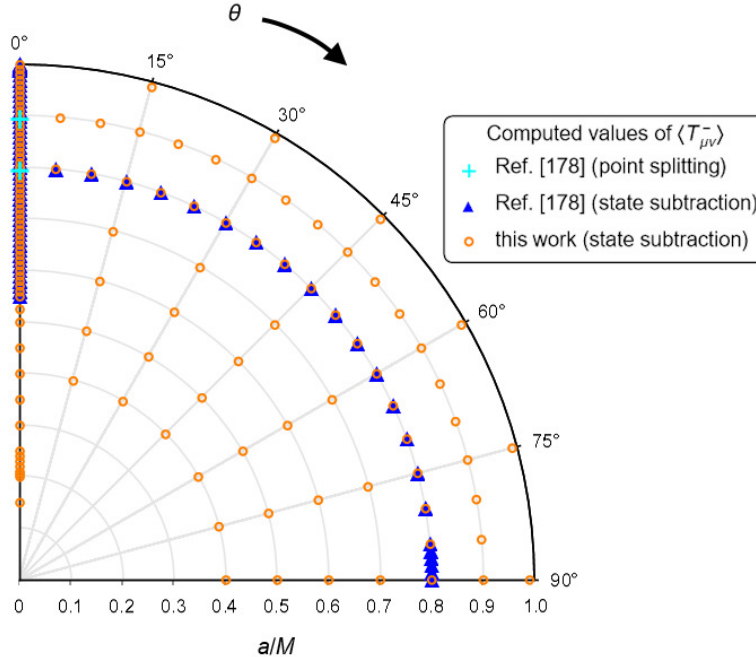
Figure 6.2: Parameter space of Kerr spin-to-mass ratios a/M and polar angles θ for which the dominant components of the RSET $\langle T^-_{\mu\nu} \rangle$ have been calculated for a scalar field at the inner horizon. Cyan plus signs indicate values calculated in Ref. [178] via point splitting, solid blue triangles indicate values calculated in Ref. [178] via state subtraction, and hollow orange circles show the values calculated in the present study via state subtraction.

much stronger than the classical case—even in the complete absence of external matter or radiation tails, the mere presence of an initially empty quantum field is enough to interrupt the gravitational collapse toward the full Kerr spacetime once the inner horizon is reached.

The divergence of the RSET at the inner horizon implies that the full geometry of the Kerr metric is not semiclassically self-consistent and must be substantially modified by the field's backreaction. Ref. [178] suggested that the backreaction should depend crucially on the signs of the RSET's null flux components, based on prior results from the spherically symmetric case [180]: if the RSET's vv-component at the inner horizon is positive (negative), an observer approaching the inner horizon would experience an abrupt contraction (expansion). Since this component was generically found to change signs for different latitudes along the inner horizon and for different

that portion of the inner horizon.

black hole spins, the result to first order is a chaotic inner-horizon singularity with local patches of abrupt contraction or expansion.

A more comprehensive analysis of the semiclassical backreaction in rotating black holes was recently carried out in the context of the Kerr-de Sitter spacetime, confirming the postulations of Ref. [178] that the RSET's vv-component dominates the evolution [103]. But if the RSET's vv-component changes sign across different latitudes, this would imply that some portions of the inner horizon would necessarily remain unscathed by any quantum null fluxes. Could a finely-tuned observer evade the semiclassical singularity at the inner horizon? Not quite—Ref. [103] found that even in these regions, a subdominant divergence in the RSET's $v\varphi$-component causes the local patch of geometry to experience a diverging amount of relative twist.

The goal of the present study is to provide independent validation of the prior studies' numerical work, extend the parameter space of known RSET values (see Fig. 6.2), and understand as much as can be possibly gleaned about the Kerr metric's semiclassical evolution out of equilibrium. There is a hope that the semiclassical gravity framework may be sufficient to describe the (meta)stable endpoint of evolution from a gravitational collapse toward a black hole [64]—though the black hole may evaporate on super-cosmological timescales, the mass-inflation and semiclassical instabilities operate on light-crossing timescales and may push the black hole toward a stable configuration with extremal horizons, a regular core, a wormhole throat, or no horizon at all (such as a gravastar). However, here evidence is given against the formation of such objects from Kerr-like initial conditions. Instead, an analysis of the backreaction using the mass-inflationary framework of Refs. [84, 85, 90] suggests that the local geometry near the would-be inner horizon should evolve in a Belinskii-Khalatnikov-Lifschitz (BKL)-like fashion [24] toward a strong, spacelike singularity.

The derivation of the key details in the calculation of the RSET is presented in Sec. 6.2.1, the numerical results of the calculations are presented in Sec. 6.2.2, and the analysis of the backreaction is given in Sec. 6.3. In this analysis, it should be noted here that one cannot actually conclude definitively that a spacelike singularity is the generic outcome of the semiclassical instability near the inner horizon. The backreaction of the Kerr RSET is only valid while the geometry can still be

well-approximated by the vacuum Kerr metric, and as soon as the spacetime begins to evolve away from equilibrium, a new, non-vacuum RSET would need to be found. Most prior studies remain silent on the search for a path forward in our understanding other than an admission to the necessity of a full theory of quantum gravity. But here, another path is suggested: the local inner-horizon geometry under some mild assumptions becomes elegantly simple during the initial stages of mass inflation, and it thus may be possible in the future to compute the RSET in this simplified spacetime to determine the full semiclassical evolution of the near-inner-horizon geometry until the curvature reaches the Planck scale.

6.2.1   Derivation of the renormalized Kerr RSET

The Kerr RSET at the inner horizon is here computed using the state subtraction method employed in Refs. [178, 179]. The key details are outlined in what follows.

The Kerr line element for a black hole with mass M and angular momentum $J \equiv aM$ can be written in Boyer-Lindquist coordinates as

$$ds^2 = \rho^2 \left(\frac{dr^2}{(r^2 + a^2)^2 \Delta_r} + \frac{\sin^2\theta \; d\theta^2}{\Delta_\theta} + \frac{\Delta_\theta(d\varphi - \Omega_r dt)^2 - \Delta_r(dt - \Omega_\theta d\varphi)^2}{(1 - \Omega_r \Omega_\theta)^2} \right), \qquad (6.26)$$

with the conformal factor $\rho^2 \equiv r^2 + a^2 \cos^2\theta$, the horizon function $\Delta_r \equiv (r^2 + a^2 - 2Mr)/(r^2 + a^2)^2$ (with two roots at the outer and inner horizon radii $r_\pm \equiv M \pm \sqrt{M^2 - a^2}$), the polar function $\Delta_\theta \equiv \sin^2\theta$, the angular velocity $\Omega_r \equiv a/(r^2 + a^2)$ of the principal frame through the coordinates, and the specific angular momentum $\Omega_\theta \equiv a \sin^2\theta$ of principal null congruence photons.

If a massless scalar test field $\hat{\phi}$ is minimally coupled to the Einstein-Hilbert action and canonically quantized, the resulting Klein-Gordon wave equation $\Box\phi_{\omega\ell m} = 0$ for the field's modes is separable [40, 170] and lends itself to the following decomposition:

$$\phi_{\omega\ell m}(t, r, \theta, \varphi) = e^{im\varphi - i\omega t} S_{\ell m}^\omega(\theta) R_{\omega\ell m}(r), \qquad (6.27)$$

where $S^{\omega}_{\ell m}(\theta)$ are prolate spheroidal harmonics, normalized on the two-sphere according to the Meixner-Schäfke scheme (such a normalization adds some extra factors to the calculation but is the scheme of choice for the functions provided in `Mathematica`) [129].

The field $\hat{\phi}$ is then equipped with an Unruh-type vacuum state $|U\rangle$ [106, 173] to mimic the effects of a physically realistic gravitational collapse, with positive frequencies along the past null boundaries defined with respect to the proper time of an infalling observer asymptotically approaching those radii [128].

In order to calculate the Unruh-state RSET at the inner horizon, Ref. [178] constructed a bare mode sum composed of the appropriate differential operator acting on the Hadamard two-point function. Since this sum is formally divergent, the summand was then subtracted from that of another bare mode sum equipped with a vacuum state known to lead to a vanishing RSET at the inner horizon, in order to yield a finite RSET. This latter vacuum state, constructed from a time-reversed, negative-mass Kerr spacetime, may appear unconventional but nonetheless agrees with the Unruh-state RSET obtained from a "comparison" state subtraction [103] as well as from a traditional point splitting approach [178] (at least for two different values of the black hole spin parameter on the polar axis; see Fig. 6.2).

Computing the two-point function at the inner horizon for a field initialized at the past null boundaries necessitates solving a relativistic scattering problem. Although the Unruh-state modes at the past horizon are not eigenmodes of the radial Teukolsky equation, they can nonetheless be Fourier-decomposed into an orthonormal set of eigenmodes $R^{\text{in}}_{\omega\ell m}$ (originating from past null infinity) and $R^{\text{up}}_{\omega\ell m}$ (originating from the past horizon) so that the two-point function and therefore the RSET at the inner horizon can be expressed in terms of numerically attainable 1D scattering coefficients [179]. These coefficients are calculated using the Mano-Suzuki-Takasugi (MST) method [118, 119], using a version of the Black Hole Perturbation Toolkit (BHPT) [30] adapted by the author; see Appendix E for details. In the notation of MST,[2] these scattering coefficients satisfy the asymptotic

---

[2]The translation from the notation of MST, BHPT, and the present work to that of Ref. [178] can be accomplished

conditions

$$
R_{\omega\ell m}^{\text{in}} \rightarrow
\begin{cases}
B_{\text{ext}}^{\text{ref}} r^{-1} \mathrm{e}^{i\omega r^*} + B_{\text{ext}}^{\text{inc}} r^{-1} \mathrm{e}^{-i\omega r^*}, & r \rightarrow \infty \\
B_{\text{ext}}^{\text{trans}} \mathrm{e}^{-i\omega_+ r^*}, & r \rightarrow r_+ , \\
B_{\text{int}}^{\text{ref}}\ \mathrm{e}^{i\omega_- r^*} + B_{\text{int}}^{\text{trans}} \mathrm{e}^{-i\omega_- r^*}, & r \rightarrow r_-
\end{cases}
\tag{6.28a}
$$

$$
R_{\omega\ell m}^{\text{up}} \rightarrow
\begin{cases}
C_{\text{ext}}^{\text{trans}} r^{-1} \mathrm{e}^{i\omega r^*}, & r \rightarrow \infty \\
C_{\text{ext}}^{\text{inc}}\ \mathrm{e}^{i\omega_+ r^*} + C_{\text{ext}}^{\text{ref}} \mathrm{e}^{-i\omega_+ r^*}, & r \rightarrow r_+ , \\
C_{\text{int}}^{\text{trans}}\ \mathrm{e}^{i\omega_- r^*} + C_{\text{int}}^{\text{ref}} \mathrm{e}^{-i\omega_- r^*}, & r \rightarrow r_-
\end{cases}
\tag{6.28b}
$$

where $\omega_\pm \equiv \omega - m\Omega_{r_\pm}$ and the tortoise coordinate r^* is chosen to be

$$
r^* \equiv r + \frac{1}{2\kappa_+} \ln\left|\frac{r - r_+}{2M}\right| + \frac{1}{2\kappa_-} \ln\left|\frac{r - r_-}{2M}\right|,
\tag{6.29}
$$

with the surface gravity $\kappa_\pm \equiv M r_\pm \Delta_r'(r_\pm)$ (where a prime denotes differentiation with respect to r), defined to be negative at the inner horizon.

In terms of these scattering coefficients, the state-subtracted mode sum yielding the RSET at the inner horizon can be written explicitly [103, 179]. In terms of the interior Eddington-Finkelstein coordinates $u \equiv r^* - t$ and $v \equiv r^* + t$, the three most relevant components of the RSET are the vv-, $v\varphi$-, and uu-components, which are given by the equations [103, 178]

$$
\langle T_{vv}^- \rangle = \oint \left(E_{vv(\omega\ell m)}^{U-} - \coth\frac{\pi\omega_-}{-\kappa_-} \right),
\tag{6.30a}
$$

$$
\langle T_{v\varphi}^- \rangle = \oint \frac{-m}{\omega_-} \left(E_{vv(\omega\ell m)}^{U-} - \coth\frac{\pi\omega_-}{-\kappa_-} \right),
\tag{6.30b}
$$

$$
\langle T_{uu}^- \rangle - \langle T_{vv}^- \rangle = \oint \left(\coth\frac{\pi\omega_+}{\kappa_+} - 1 \right) \left(1 - \left|\frac{C_{\text{ext}}^{\text{ref}}}{C_{\text{ext}}^{\text{inc}}}\right|^2 \right).
\tag{6.30c}
$$

Here and throughout, each RSET component is written as $\langle T_{\mu\nu}^\pm \rangle \equiv \langle U|\hat{T}_{\mu\nu}|U\rangle_{\text{ren}}|_{r_\pm}$, and the symbols

---

by setting $\rho_{\omega\ell m}^{\text{up}} = (1-a^2)^{-2i\omega_+(1-a^2)^{-1/2}} C_{\text{ext}}^{\text{ref}}/C_{\text{ext}}^{\text{inc}}$ and $B_{\omega\ell m} = (1-a^2)^{im/a}(r_-/r_+)^{1/2} B_{\text{int}}^{\text{trans}}/B_{\text{ext}}^{\text{trans}}$, with the remaining coefficients obtained from the Wronskian conditions of Appendix E.

$\displaystyle\oint$ and $E^{U_-}_{vv(\omega\ell m)}$ are defined by

$$\oint (X) \equiv \int_0^\infty \sum_{\ell=0}^\infty \sum_{m=-\ell}^\ell \frac{(2\ell+1)(\ell-m)!}{(\ell+m)!} \frac{\omega_- |S^\omega_{\ell m}(\theta)|^2}{32\pi^2 M r_-}(X)\, d\omega, \tag{6.31}$$

$$E^{U_-}_{vv(\omega\ell m)} = \frac{r_-\omega_-}{r_+\omega_+}\left[\coth\frac{\pi\omega_+}{\kappa_+}\left(\left|\frac{B^{\text{ref}}_{\text{int}}}{B^{\text{trans}}_{\text{ext}}}\right|^2 + \left|\frac{C^{\text{ref}}_{\text{ext}}}{C^{\text{inc}}_{\text{ext}}}\right|^2 \left|\frac{B^{\text{trans}}_{\text{int}}}{B^{\text{trans}}_{\text{ext}}}\right|^2 \right) \right.$$
$$\left. + 2\operatorname{csch}\frac{\pi\omega_+}{\kappa_+}\Re\left(\frac{C^{\text{ref}}_{\text{ext}} B^{\text{ref}}_{\text{int}} B^{\text{trans}}_{\text{int}}}{C^{\text{inc}}_{\text{ext}}(B^{\text{trans}}_{\text{ext}})^2} \right) + \left(1 - \left|\frac{C^{\text{ref}}_{\text{ext}}}{C^{\text{inc}}_{\text{ext}}}\right|^2 \right)\left|\frac{B^{\text{trans}}_{\text{int}}}{B^{\text{trans}}_{\text{ext}}}\right|^2 \right]. \tag{6.32}$$

Thus, the RSET at the Kerr inner horizon can be calculated in a straightforward manner by numerically solving the radial and angular Teukolsky equations and applying their eigenmode solutions to Eqs. (6.30a)–(6.30c).

6.2.2 Numerical results

In order to make the calculation of the RSET as efficient as possible, integration is performed in the present work using an adaptive quadrature algorithm, which has the advantages of both rapid convergence for preferably sparse domain sampling and fine control over error estimation. An example of the output of this scheme for a particular choice of parameters can be seen in Fig. 6.3. The ultimate goal is to integrate and sum Eqs. (6.30a)–(6.30c) over all possible ω-, ℓ-, and m-modes, which for brevity are written with the notation

$$\langle T^-_{\mu\nu}\rangle \equiv \int_0^\infty \langle T^-_{\mu\nu}\rangle_{(\omega)} d\omega \equiv \int_0^\infty \sum_{\ell=0}^\infty \sum_{m=-\ell}^\ell \langle T^-_{\mu\nu}\rangle_{(\omega\ell m)} d\omega. \tag{6.33}$$

Each point in the main panel of Fig. 6.3 corresponds to the integrand $\langle T^-_{vv}\rangle_{(\omega)}$ for a particular value of the frequency ω, and each of these points is computed by summing over all possible ℓ- and m-modes (see inset of Fig. 6.3). These sums converge exponentially and usually require only modes with $\ell \leq 2$ for the error threshold to be vastly dwarfed by the error in the ω integration, though in some cases like the one shown in the figure, a larger number of angular modes are needed.
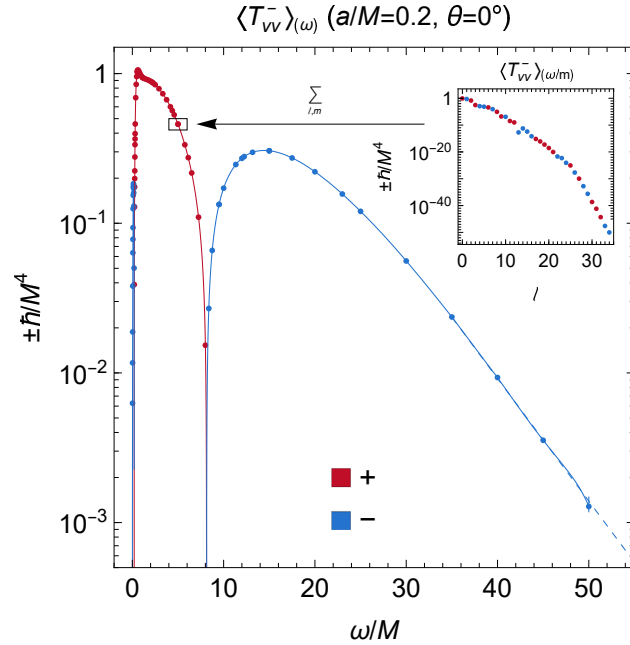
Figure 6.3: Spectrum of $\langle T_{vv}^- \rangle$ at the north or south pole ($\theta = 0°$) for a Kerr black hole with $a/M = 0.2$. The sum over the ℓ- and m-modes in the inset panel yields each point in main panel (note that only the $m = 0$ modes contribute when $\theta = 0°$), and the integral over the ω-modes in the main panel yields the total RSET $\langle T_{vv}^- \rangle$ (i.e., the point at $a/M = 0.2$ in Fig. 6.4). Positive (negative) values on the log plots are given by the red (blue) points. The sampling and integration is performed using the adaptive quadrature algorithm described in the text.

Then, the algorithm proceeds by (i) computing four $\langle T_{\mu\nu}^- \rangle_{(\omega)}$ points subdivided evenly in a closed frequency domain, (ii) interpolating between these points with a cubic B-spline, (iii) computing a fifth sample point in the center of the domain, (iv) calculating the difference between this sample point and the center point of the spline, and (v) if this difference lies above a set error threshold, the domain is divided evenly in half and the algorithm is repeated from step (i) for each new domain. This approach leads to a speedup of up to a factor of 10 in the total computational runtime compared to a fixed linear integration method and additionally allows for more precise error control.

Adaptive quadrature approaches perform most poorly in regimes where the integrand cannot be well-approximated by polynomial functions, which for the integrands of Eqs. (6.30a)–(6.30c) occurs in the exponential decay regime at high frequencies (notice in Fig. 6.3 the slight difference at $\omega/M \sim 50$ between the interpolating function and the dashed exponential fit). In these cases, two

options were tested, both yielding similar convergent results: either the splines can be computed over log-frequency space and the domain extended until convergence is reached, or enough points can be sampled so that the remaining portion of the integrand can be fitted to an exponentially decaying function and the integral extrapolated to infinity.

Two main sources of error are accounted for in the numerical calculations of the RSET performed here. The first is truncation error, which is minimized in the ℓ- and m-sums by cutting off the sum only when the next term returns zero with the specified numerical precision, and which is controlled in the ω-integrals by the degree of confidence in the exponential decay fit that is integrated to infinity. The second source of error is the global discretization error from the numerical integration scheme, which is controlled by specifying an error bound in the algorithm described above. Accounting for both of these sources of uncertainty, the points in Figs. 6.3–6.5 are computed to a high enough precision that their error bars are smaller than the points themselves in all but a couple edge cases.
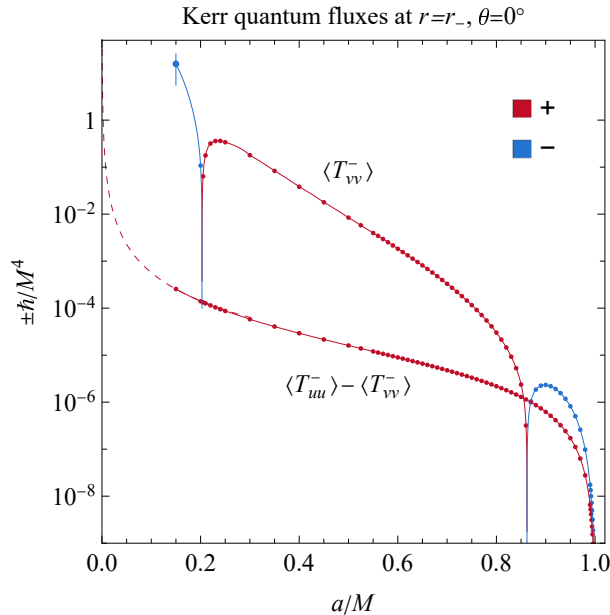

Figure 6.4: Computed values of the vv- and uu-components of the RSET at the Kerr inner horizon along the axis of rotation for different values of the black hole spin-to-mass ratio a/M. Positive (negative) values on the log plot are given by the red (blue) points. Solid curves interpolate between the numerically-computed points, and the dashed curve shows a $1/a^2$ fit at low spins.
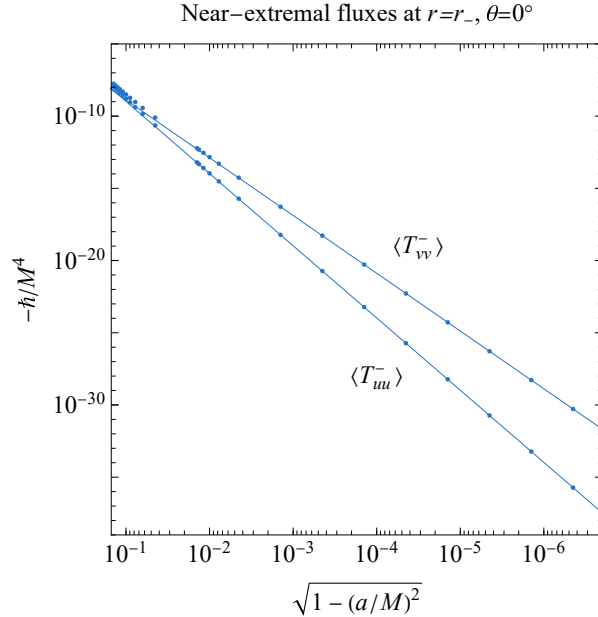
Near−extremal fluxes at $r=r_-$, $\theta=0°$

Figure 6.5: Same setup as Fig. 6.4 but for black hole spins near extremality, with the near-zero parameter $\epsilon \equiv \sqrt{1-(a/M)^2}$. The two lines show the asymptotic behavior of the RSET's double-null components near extremality, given by the analytic expressions $\langle T_{vv}^- \rangle \to \epsilon^4/(7680\pi^2)$ and $\langle T_{uu}^- \rangle \to \epsilon^5/(960\pi^2)$.

First, consider the inner-horizon RSET at the north or south pole, where $\theta = 0°$. There only the modes with $m = 0$ contribute to the RSET, so that $\langle T_{v\varphi}^- \rangle$ vanishes and the calculation of the other null components simplify considerably. The two double-null flux components of the RSET are plotted as a function of the black hole's angular momentum a in Figs. 6.4 and 6.5. Fig. 6.4 shows computed values for spins from $a/M = 0.15$ to $a/M \approx 0.997$, yielding excellent quantitative agreement with Fig. 2 of Ref. [178] and qualitative agreement with the Kerr-de Sitter case in Fig. 4 of Ref. [103] (both of which only reach a minimum of $a/M = 0.55$). The vv-component of the RSET is negative and vanishingly small at high spins, and as the rotation of the black hole slows, this component increases until reaching zero at $a/M \approx 0.862$ and continuing to increase exponentially in a/M. However, at slow enough spins, $\langle T_{vv}^- \rangle$ once again changes signs.

Both $\langle T_{vv}^- \rangle$ and $\langle T_{uu}^- \rangle$ are expected to diverge as $a \to 0$, since in that limit the inner horizon coincides with the $r = 0$ singularity. In particular, the quantity $\langle T_{uu}^- \rangle - \langle T_{vv}^- \rangle$, related to the Hawking outflux per surface area $4\pi r_-^2$ [180], should diverge as a^{-2} (compare the dashed curve in Fig. 6.4)

owing to the factor of r_- in the denominator of Eq. (6.31). An even stronger divergence is expected to be present in $\langle T_{vv}^- \rangle$ as $a \to 0$, since the scattering coefficients $|B_{\text{int}}^{\text{ref}}|^2$ and $|B_{\text{int}}^{\text{trans}}|^2$ from Eq. (6.28a) both diverge as a^{-2}. However, the exact nature of the low-spin divergence of $\langle T_{vv}^- \rangle$ is not easily found, since the spectrum includes non-trivial contributions from successively higher frequencies ω as the spin a decreases, so that for $a/M < 0.15$, $\langle T_{vv}^- \rangle$ could be either positive or negative (or even vanish in a highly fine-tuned case).

While the double-null components of the RSET are expected to diverge at the inner horizon as $a/M \to 0$, they will vanish as $a/M \to 1$, as shown in Fig. 6.5 (compare Fig. 3 in the Supplemental Materials of Ref. [178]). In particular, through an analysis of the asymptotic behavior of the near-extremal scattering coefficients, it can be shown that in terms of a near-extremal spin parameter $\epsilon \equiv \sqrt{1 - (a/M)^2}$, the vv-component of the RSET will vanish as $\langle T_{vv}^- \rangle \to \epsilon^4/(7680\pi^2)$, while the uu-component will vanish as $\langle T_{uu}^- \rangle \to \epsilon^5/(960\pi^2)$.

Off the axis of rotation, the computation of the inner-horizon RSET is less clean. Even in the near-extremal limit, while the on-axis scattering coefficients are dominated by low-frequency $\ell = 0$ modes that create a simple negative, exponentially decaying spectrum, the off-axis spectrum generally contains both positive and negative peaks at low frequencies. Nevertheless, in the limit as $a/M \to 1$ for all polar angles θ, all three components of the RSET analyzed here vanish.

The behavior of $\langle T_{vv}^- \rangle$ as a function of both spin a and polar angle θ is shown in Fig. 6.6. As can be seen, while the sign of $\langle T_{vv}^- \rangle$ changes as the spin of the black hole is varied, even for a single black hole with a given spin, $\langle T_{vv}^- \rangle$ will necessarily change signs at different latitudes along the inner horizon. For $a/M \gtrsim 0.862$, $\langle T_{vv}^- \rangle$ is negative near the pole and reaches zero exactly once between the pole and the equator. For smaller spins, $\langle T_{vv}^- \rangle$ may change signs twice, though it should be noted that the behavior of the RSET for large θ and very small spins in Fig. 6.6 is only an extrapolated estimation.

Though not plotted here, the $v\varphi$-component of the RSET has also been computed and is generically non-zero throughout the 2D parameter space, except for at least one 1D zero-valued
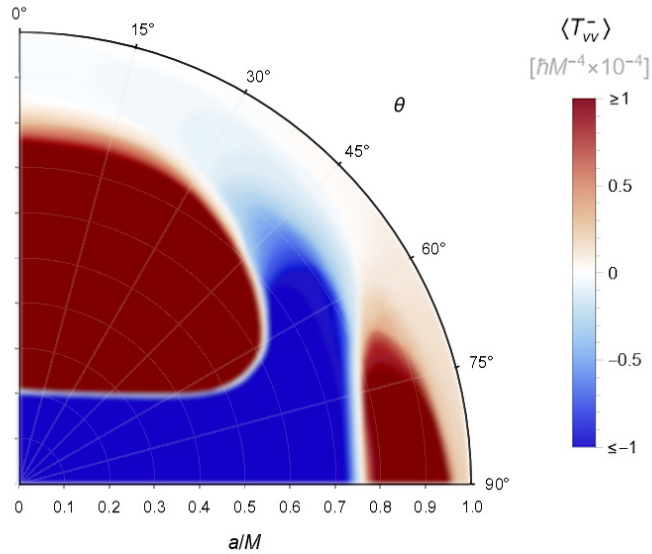
Figure 6.6: Parameter space for the vv-component of the Kerr RSET at the inner horizon as a function of both the black hole spin-to-mass ratio a/M and the polar angle θ. The points at the locations given in Fig. 6.2 were computed explicitly using the techniques described in the text, and the remaining portion of the parameter space was filled in via interpolation.

contour (just as $\langle T^-_{vv} \rangle$ in Fig. 6.6 contains two[3] zero-valued contours given by the white regions). Though the divergence associated with $\langle T^-_{v\varphi} \rangle$ is subdominant compared to $\langle T^-_{vv} \rangle$, the presence of a sign flip in $\langle T^-_{vv} \rangle$ implies that $\langle T^-_{v\varphi} \rangle$ will dominate the backreaction for at least one latitude, leading to a divergent twisting of the geometry separating regions of local expansion and contraction [103].

In conclusion, the renormalized stress-energy of a scalar quantum field in the Unruh state has been calculated for most of the physically relevant parameter space in the Kerr spacetime at the inner horizon. The results indicate that in a locally inertial frame reaching the inner horizon, the field's flux generically diverges, and thus that the Kerr metric is not semiclassically self-consistent at or beyond the inner horizon. To understand how the geometry backreacts to this semiclassical instability, one must analyze the field equations, as shown in the next section.

---

[3]Or three, if you count the θ-parametrized contour at $a/M = 1$, though in this work the extremal case is not treated.

6.3   Backreaction

Analyses of semiclassical backreactions carry with them intricate subtleties. Ideally, one would like to find a solution to the Møller-Rosenfeld semiclassical field equations, Eq. (3.9), to see how the geometry and the quantum field coevolve over time. However, as can be gleaned from the calculations of the previous sections, the RSET is difficult to calculate and currently is only known for a select handful of highly symmetric vacuum spacetimes. Thus, the present calculations will apply only to a *weak backreaction domain*, where one is still far enough from the inner horizon that the geometry can be well-approximated by the vacuum black hole spacetime but close enough that the semiclassical backreaction, of order $(\mathrm{e}^{\kappa_- v}\, m_P/M)^2$ (where m_P denotes the Planck mass), is not negligible.

6.3.1   Spherical symmetry

The conclusions of any backreaction analysis are limited by the choice of assumptions about how the metric in question should be generalized. In the case of spherical symmetry (when $a = 0$), such generalizations can be made comprehensively. If double-null coordinates u and v are gauge-fixed to match those of the vacuum RSET $\langle T_{\mu\nu}^-\rangle$, then the remaining two functional degrees of freedom in the line element can be written as $-\mathrm{e}^{\sigma(u,v)}dudv + r(u,v)^2 d\Omega^2$. The resulting field equations imply that near the inner horizon,

$$\partial_v r \approx \frac{4\pi r_-}{\kappa_-}\langle T_{vv}^-\rangle + \mathcal{O}(\mathrm{e}^{-\kappa_- v}). \tag{6.34}$$

Recalling that the inner-horizon surface gravity κ_- is defined here to be negative, one would then conclude that an infalling observer near the inner horizon would experience an abrupt contraction (expansion) in the geometry's area element when $\langle T_{vv}^-\rangle$ is positive (negative) [180].

However, if instead the radial coordinate r is gauge-fixed to match that of the vacuum RSET and the remaining two metric degrees of freedom are encoded by, for example, the positions of the black hole's inner and outer horizons, the same field equations then imply dynamical behavior in the horizon structure rather than in the local area element. In particular, the outer horizon will evaporate inward slowly over time, as per Hawking's famous result (as long as $\langle T_{vv}^+\rangle < 0$, which is

always true in the 2D case) [18, 50, 93], while the inner horizon will evaporate rapidly outward (inward) when $\langle T_{vv}^- \rangle$ is negative (positive). The inner horizon in this case will move extremely quickly, at a timescale on the order of the black hole's light-crossing time [18].

While the two options described above for the spherically symmetric case might seem distinct or even at odds with one another, they are actually completely compatible. Extrapolating and reinterpreting those results as statements about the dominant contributions to global, long-term dynamics, "which is irresistible but not allowed" [15], would lead to the conclusion that black holes with $\langle T_{vv}^- \rangle > 0$ have interiors that contract until a spacelike singularity is formed at $r = 0$, while black holes with $\langle T_{vv}^- \rangle < 0$ would explode from the inside out to form extremal or horizonless objects. However, since the RSET calculated here only remains valid in the weak backreaction domain, absolutely no conclusions can be made about long-term dynamics until the RSET is computed for the more general form of the spacetime.

6.3.2 Axisymmetry: initial tendencies

Now consider the case of black holes with non-zero rotation. Here it is clear that the outcome must be more complicated than in the spherically symmetric case, since the local interior geometry will no longer uniformly contract or expand across the entire inner horizon; instead, $\langle T_{vv}^- \rangle$ is both positive and negative across different latitudes of the same black hole (see Fig. 6.6). An excellent backreaction analysis for the case of Kerr-de Sitter black holes was recently [103] carried out by decomposing the spacetime into a set of double-null hypersurfaces gauge-fixed to match the null coordinates in $\langle T_{\mu\nu}^- \rangle$.[4] Along each hypersurface, the induced metric can be written in a completely general form as

$$g_{AB}dx^A dx^B = \gamma^2 \left[\alpha^{-2} d\theta^2 + \alpha^2 \left(d\varphi + \tau d\theta \right)^2 \right], \tag{6.35}$$

---

[4]The fixing comes in the identification of the affine parameter λ, taken to be constant along each hypersurface, with the Kruskal coordinate $V_- \propto \mathrm{e}^{-\kappa_- v}$.

for the area element γ^2 and the arbitrary functions α and τ that physically relate to notions of shear and twisting of null geodesics as the hypersurface is moved toward the would-be inner horizon at $\lambda \to 0$, or equivalently, $v \to \infty$. The semiclassical Einstein equations and Raychaudhuri equations can then be analyzed to yield

$$\partial_\lambda^2 \gamma = -\gamma \left[4\pi \langle T_{\lambda\lambda}^- \rangle + 4(\partial_\lambda \ln \alpha)^2 + \alpha^4 (\partial_\lambda \tau)^2 \right], \tag{6.36a}$$

$$\partial_\theta (\gamma^2 \alpha^4 \partial_\lambda \tau) = 8\pi \gamma^2 \langle T_{\lambda\varphi}^- \rangle + \partial_\lambda (\gamma^2 \beta), \tag{6.36b}$$

where β measures the amount of twisting in the φ-direction for light rays perpendicular to the surfaces of constant λ as $\lambda \to 0$.

From Eq. (6.36a) it can be gleaned that for positive (negative) $\langle T_{vv}^- \rangle$, the divergent RSET component $\langle T_{\lambda\lambda}^- \rangle \sim \lambda^{-2}$ will also be positive (negative) and will cause γ to contract (expand) as $\lambda \to 0$. In the inevitable intermediate cases where γ neither contracts nor expands, Eq. (6.36b) then predicts that a non-zero $\langle T_{v\varphi}^- \rangle$ will cause an infinite local twisting. Thus, one reproduces the same behaviors predicted in the spherically symmetric case (i.e., the local blow-up or shrinking of the geometry near the inner horizon dictated by the sign of $\langle T_{vv}^- \rangle$), with the addendum that even in the cases where the geometry neither contracts nor expands, a subdominant component of the RSET will still generically cause the local geometry to diverge in a shearing manner.

Two comments concerning the above analysis are worth mentioning. First, while the backreaction is performed with sufficient generality to reproduce the effects predicted in the spherical case and predict additional rotational effects, the restriction of the metric to null hypersurface cuts of constant v does not allow for a full global analysis of the spacetime's evolution and does not encompass the most general axisymmetric geometry possible (it for example washes out any dynamical information related to the outgoing u coordinate and its coupling with the other degrees of freedom). But more importantly, the analysis does not invite any obvious path forward to understand how the spacetime evolves beyond these initial tendencies. Does the semiclassical inner-horizon instability remain confined to a (meta)stable interior singularity (or even a regular configuration), or will inflationary

perturbations spread like a wildfire until they destroy the black hole from the inside out? To address these problems at least partially, consider the complementary analysis below.

Generalizations of the Kerr metric abound. Starting from the line element of Eq. (6.26), one may, for example, promote the mass M to an arbitrary function $M(r,\theta)$ [62], or allow dynamical behavior via $M \to M(v)$ and $a \to a(v)$ [177], or leave all the functions $\Delta_r(r)$, $\Delta_\theta(\theta)$, $\Omega_r(r)$, $\Omega_\theta(\theta)$, and $\rho^2 = \rho_r^2(r) + \rho_\theta^2(\theta)$ arbitrary for full Hamilton-Jacobi separability [40]. Additional generalizations beyond the form of Eq. (6.26) also exist; imposing Klein-Gordon and timelike Hamilton-Jacobi separability yields a 3-function class of metrics that reproduces a wide variety of regular and singular spacetime candidates [10], and imposing only asymptotic flatness and the preservation of the Carter constant leads to a 10-function class of general axisymmetric metrics [145]. Amidst all these options, one thus desires a trade-off between generality and tractability in capturing the most important physical behaviors to be modeled and understood.

The properties of the semiclassical radiation produced from a quantum scalar field in the vacuum Kerr spacetime already seem to rule out a number of Kerr generalizations. For example, the 3-function class of metrics put forward in Ref. [10] claims to encompass a majority of the currently-proposed stable endpoints of black hole evolution (aside from complete evaporation or gravastar-like objects); however, the Einstein tensor for these metrics always contains a vanishing rt-component, despite the fact that the semiclassical RSET calculated here possesses a non-vanishing (and in fact diverging) rt-component $\langle T_{rt}^- \rangle = (\langle T_{vv}^- \rangle - \langle T_{uu}^- \rangle) R^{-2} \Delta_r^{-1}$. Presumably such black hole solutions that are regular and instability-free cannot form from an initial Kerr-like collapse.

6.3.3 Axisymmetry: mass inflationary approach

To generalize the Kerr metric in order to allow for the dynamics anticipated from the vacuum RSET, the following assumptions will be made:

(i) The spacetime is axisymmetric, motivated both by simplicity and by the preservation of this symmetry in the past Unruh state.

(ii) The spacetime is asymptotically flat at spatial infinity, as in the case of the original Kerr metric.

(iii) The spacetime is initialized with a Kerr vacuum geometry, and the quantum scalar field is initialized with an Unruh vacuum state mimicking the effects of a gravitational collapse sufficiently far in the past.

(iv) The spacetime maintains conformal Hamilton-Jacobi separability [84]; i.e., the equations of motion for massless particles are separable in spheroidal coordinates (but not necessarily for massive particles, as in the case of strict separability seen for Kerr).

Unfortunately, none of these assumptions are actually true for astrophysically realistic black holes. The accretion flows observed by the GRAVITY instrument [78] and the Event Horizon Telescope Collaboration [60] feature asymmetries in φ, though in the stationary limit, rigidity theorems suggest that any non-axisymmetric perturbations are part of the "hair" that a black hole will eventually shed [92, 96]. In regard to Assumption (ii), the lack of asymptotic flatness in the Universe has been measured with great precision [153], but any effects from a cosmological horizon on the inner-horizon instability are expected to be negligible, both due to the similarity in the RSET calculations here to those of the Kerr-de Sitter case [103], and because the cosmological constant is currently measured to be $\Lambda \sim 10^{-46} \, M_{\odot}^{-2}$ in geometrized units, much too small to have any practical influence. As for Assumption (iii), black holes (and therefore near-inner-horizon geometries) form under chaotic, rapidly evolving conditions, and even after settling down, the most quiescent black holes are still non-vacuum and accrete more than enough radiation to trigger the mass inflation instability and destroy any vacuum inner horizon [125]. Additionally, physically relevant fields in the Standard Model are those with spin 1 (electromagnetic), 1/2 (fermionic), or 2 (gravitational), so using a massless scalar field with spin 0 is a simplification seen as a proxy for, e.g., a single photonic degree of freedom. Even regarding Assumption (iv), which provides a more general notion than the strict separability that itself is justified by the observation of long-lived accretion disks (lack of separability implies chaotic, destabilizing particle orbits [10]), it will be seen in what follows that

conformal separability, while valid in the weak backreaction domain, eventually breaks down once the vierbein of Eq. (6.40) ceases to be diagonal.

Under Assumptions (i)–(iv), the spacetime's line element takes the form of Eq. (6.26), except that the functions $\Delta_r(r)$, $\Delta_\theta(\theta)$, $\Omega_r(r)$, $\Omega_\theta(\theta)$, and $\rho(r,\theta,t)$ are left arbitrary. Assumption (ii) of asymptotic flatness, while not strictly required for any aspect of this analysis (any cosmological contribution to the near-inner-horizon geometry will be completely overwhelmed by the ignition of both classical and semiclassical streams [84]), will impose the additional conditions $\Delta_r \sim \Omega_r \sim r^{-2}$ and $\rho \sim r$.

The form of the line element of Eq. (6.26) naturally encodes an orthonormal tetrad basis first written down by Carter [40]. This basis can be constructed in the Newman-Penrose formalism by performing a null rotation on the Kinnersley tetrad so that the resulting frame is symmetric with respect to the ingoing and outgoing principal null directions [182]. The corresponding vierbein $e^{\hat{m}}{}_\mu$, defined through

$$ds^2 = g_{\mu\nu}dx^\mu dx^\nu = \eta_{\hat{m}\hat{n}}e^{\hat{m}}{}_\mu e^{\hat{n}}{}_\nu dx^\mu dx^\nu \tag{6.37}$$

for the Minkowski metric tensor $\eta_{\hat{m}\hat{n}}$, can be written as the product [86]

$$e_{\hat{m}\mu} = (e_{\text{dyn}})_{\hat{m}\kappa} \, (e_{\text{fix}})^\kappa{}_\mu, \tag{6.38}$$

where $(e_{\text{dyn}})_{\hat{m}\kappa}$ is a dynamical vierbein that is only a function of the variable r (which is timelike in the interior), and $(e_{\text{fix}})^\kappa{}_\mu$ is a fixed vierbein whose elements should remain frozen at their inner-horizon values throughout the evolution of the instability induced by the semiclassical backreaction.

In terms of Boyer-Lindquist coordinates, the fixed vierbein contains the basis vectors

$$(e_{\text{fix}})^0 = \rho \, \partial_r, \tag{6.39a}$$

$$(e_{\text{fix}})^1 = \frac{\rho}{1 - \Omega_r \Omega_\theta} \left(\partial_t - \Omega_\theta \partial_\varphi \right), \tag{6.39b}$$

$$(e_{\text{fix}})^2 = \rho \, \partial_\theta, \tag{6.39c}$$

$$(e_{\text{fix}})^3 = \frac{\rho \sqrt{\Delta_\theta}}{1 - \Omega_r \Omega_\theta} \left(\partial_\varphi - \Omega_r \partial_t \right), \tag{6.39d}$$

which serves to align the tetrad with the principal null directions of the black hole. The dynamical vierbein then is purely diagonal:

$$(e_{\text{dyn}})_0 = \frac{e^{-5\xi/2}}{R^2 \sqrt{|\Delta_r|}} \, \partial_0, \tag{6.40a}$$

$$(e_{\text{dyn}})_1 = e^{\xi/2} \sqrt{|\Delta_r|} \, \partial_1, \tag{6.40b}$$

$$(e_{\text{dyn}})_2 = e^{-\xi} \, \partial_2, \tag{6.40c}$$

$$(e_{\text{dyn}})_3 = e^{-\xi} \, \partial_3, \tag{6.40d}$$

where the redefinitions $\rho(r,\theta,t) \to e^{-\xi(r)}\rho(r,\theta,t)$ and $\Delta_r(r) \to e^{3\xi(r)}\Delta_r(r)$ have been made for an arbitrary radial function $\xi(r)$, which is brought to the dynamical vierbein so that the vierbein may undergo a conformal expansion or contraction under backreaction.

The Einstein tensor corresponding to this spacetime is far too intricate to be presented here in any complete, meaningful way. However, at least in the quasi-stationary limit (in particular, if the redefined conformal piece ρ is written as $\rho(r,\theta,t) = e^{\tilde{v}t}\sqrt{r^2 + a^2 \cos^2\theta}$ for some vanishing small accretion parameter $\tilde{v}$), the field equations have already been analyzed in detail in Refs. [84, 85, 90] (this is the conformally separable Kerr solution described in Sec. 2.3.1). The resulting behavior provides classical justification for the decomposition of Eq. (6.38), since near the inner horizon, the functions Δ_θ, Ω_r, and Ω_θ remain approximately fixed at their Kerr values near the inner horizon, while the horizon function Δ_r and the inflationary function ξ become the dominant contributors to

the evolution of the Einstein tensor. The resulting tensor behaves at least initially like a perfect fluid with equal ingoing and outgoing streams, with dominant inflating tetrad-frame components $G_{00} \sim G_{11} \sim G_{01} \sim \Delta_r^{-1}$, where the off-diagonal component G_{01} is suppressed by a factor of $\tilde{v}$. Classically, the evolution can then be continued to show that Δ_r eventually stalls out at some tiny value [84], after which ξ grows large and the spacetime undergoes a series of BKL-like bounces toward a strong, spacelike singularity [86].

How might semiclassical effects modify this picture? The tetrad-frame components of the RSET can be re-expressed in terms of the double-null Eddington-Finkelstein coordinates used throughout this paper:

$$\langle T_{00} \rangle = \frac{e^{5\xi}}{\rho^2 |\Delta_r|} \left[\langle T_{uu} \rangle + \langle T_{vv} \rangle + 2\langle T_{uv} \rangle \right], \tag{6.41a}$$

$$\langle T_{11} \rangle = \frac{e^{-\xi}}{\rho^2 |\Delta_r|} \left[\langle T_{uu} \rangle + \langle T_{vv} \rangle - 2\langle T_{uv} \rangle - 2\Omega_r \left(\langle T_{u\varphi} \rangle - \langle T_{v\varphi} \rangle \right) + \Omega_r^2 \langle T_{\varphi\varphi} \rangle \right], \tag{6.41b}$$

$$\langle T_{01} \rangle = \frac{2e^{2\xi}}{\rho^2 |\Delta_r|} \left[\langle T_{uu} \rangle - \langle T_{vv} \rangle - \Omega_r \left(\langle T_{u\varphi} \rangle + \langle T_{v\varphi} \rangle \right) \right], \tag{6.41c}$$

$$\langle T_{13} \rangle = \frac{e^{\xi/2}}{\rho^2 \sqrt{|\Delta_r|\Delta_\theta}} \left[\Omega_\theta \left(\langle T_{uu} \rangle + \langle T_{vv} \rangle - 2\langle T_{uv} \rangle \right) + \left(1 + \Omega_r \Omega_\theta \right) \left(\langle T_{v\varphi} \rangle - \langle T_{u\varphi} \rangle \right) + \Omega_r \langle T_{\varphi\varphi} \rangle \right], \tag{6.41d}$$

$$\langle T_{22} \rangle = \frac{e^{2\xi}\Delta_\theta}{\rho^2 \sin^2\theta} \langle T_{\theta\theta} \rangle, \tag{6.41e}$$

$$\langle T_{33} \rangle = \frac{e^{2\xi}}{\rho^2 \Delta_\theta} \left[\Omega_\theta^2 \left(\langle T_{uu} \rangle + \langle T_{vv} \rangle - 2\langle T_{uv} \rangle \right) + 2\Omega_\theta \left(\langle T_{v\varphi} \rangle - \langle T_{u\varphi} \rangle \right) + \langle T_{\varphi\varphi} \rangle \right]. \tag{6.41f}$$

Far enough away from the inner horizon, all components of the RSET should be completely negligible, as they are suppressed by the Planck scale. Thus, everywhere outside the black hole as well as inside when v is not large, a vacuum source should recover the standard Kerr solution with $\xi = 0$ and $\Delta_r = (r^2 + a^2 - 2Mr)/(r^2 + a^2)^2$. However, in the weak backreaction domain, once the null components of the RSET cease to be vanishingly small, Eqs. (6.41) indicate that the radial- and time-components of the tetrad-frame Einstein tensor will begin to diverge as Δ_r^{-1} as one takes $\Delta_r \to 0$.

Though the RSET components $\langle T_{uv}^- \rangle$, $\langle T_{u\varphi}^- \rangle$, and $\langle T_{\varphi\varphi}^- \rangle$ have not been computed explicitly,

one can make the assumption that their contributions to Eqs. (6.41) will be subdominant compared to that of the double-null components, and more importantly, that they will not contrive to cause any of the specific combinations in the equations above to cancel exactly. Even if they do, then the classical mass inflation phenomenon described in Refs. [84, 85, 90] will take over the evolution and a spacelike singularity will form. But based on the numerical results in Sec. 6.2.2, it is apparent that $\langle T_{00}^- \rangle$ and $\langle T_{11}^- \rangle$ are the dominant contributors to the evolution in the weak backreaction domain, while the off-diagonal components $\langle T_{01}^- \rangle$ are also important but initially much smaller than their diagonal counterparts (recall from Fig. 6.4 that the difference $\langle T_{uu}^- \rangle - \langle T_{vv}^- \rangle$ is almost always several orders of magnitude smaller than either individual component).

The Einstein tensor combination $G_{00} + G_{11}$ for the tetrad frame of Eq. (6.38) can be written as

$$G_{00} + G_{11} = -\frac{2\Delta_r}{\rho^2}\left(\partial_{r_*}^2 \xi + (\partial_{r_*}\xi)^2 - 2\partial_{r_*}\ln\left(\frac{\rho}{1 - \Omega_r\Omega_\theta}\right)\partial_{r_*}\xi\right) + F_{rt}, \tag{6.42}$$

where the tortoise coordinate r_* is defined by $dr/dr_* = \mathrm{e}^{3\xi}R^2\Delta_r$, and the function F_{rt} encompasses subdominant terms related to the precise nature of any classical accretion contributing to non-stationary conformal dynamics.

The dominant term in Eq. (6.42) is the one involving the second derivative of the inflationary exponent ξ [84]. Equating this term to the semiclassical source from Eq. (6.41), which behaves as Δ_r^{-1} near the inner horizon, yields after integration the approximate solution

$$\partial_{r_*}\xi \approx \frac{8\pi}{-\Delta_r}\left(\langle T_{uu}^- \rangle + \langle T_{vv}^- \rangle - 2\Omega_r(\langle T_{u\varphi}^- \rangle - \langle T_{v\varphi}^- \rangle) + \Omega_r^2\langle T_{\varphi\varphi}^- \rangle\right), \tag{6.43}$$

as long as ξ remains smaller than its derivatives. In the regime where the double-null components of the RSET dominate over the shearing components, Eq. (6.43) thus predicts that when the sum $\langle T_{uu}^- \rangle + \langle T_{vv}^- \rangle$ is positive (negative), the spacetime's conformal factor $\mathrm{e}^{-\xi}$ will abruptly contract (expand) as the inner horizon is approached at $\Delta_r \to 0_-$. These initial tendencies align precisely with that of the spherically symmetric case, since $\langle T_{uu}^- \rangle + \langle T_{vv}^- \rangle$ is usually the same sign as $\langle T_{vv}^- \rangle$.

One can continue the evolution of the spacetime by examining the behavior of the dynamical vierbein of Eqs. (6.40a)–(6.40d). Under the assumption that the fixed vierbein of Eqs. (6.39a)–(6.39d) remains stable as the initial backreaction ignites the inflationary tendencies described above, the geometry will be governed solely by a diagonal, dynamical, homogeneous line element sourced by inflating streams of semiclassical matter. The classical counterpart of this analysis has already been carried out in detail in Chapter 2, yielding the inflationary Kasner metric: as one might anticipate, the streams of matter are amplified in energy density as Δ_r plunges to zero and ξ increases rapidly. Then, the spacetime undergoes a bounce as Δ_r freezes out at a small value and the $e^{\xi/2}$ term in Eq. (6.40b) takes over and causes a radial expansion. The solution works for both positive and negative sources of stress-energy, generically producing a series of inflating Kasner-like bounces toward a spacelike singularity.

Eventually, the approximations made in this section will break down, and the final evolution of the geometry near the spacelike singularity must be relinquished to a higher-order theory of quantum gravity. However, the results remain robust in the weak backreaction domain, and even in the presence of additional non-negligible stress-energy sources not accounted for in the analysis above, it has been shown [84] that the dominant double-null contributors to the geometry's initial inflation remain dominant to the next-highest order, as long as one still has $|\Delta_r| \ll \partial_{r_*}\xi$ or $\partial_{r_*}\xi \ll 1$. If anything, the semiclassical contribution to the classical mass inflation instability will cause the conformally separable solution to break down faster than it otherwise would (due to the presence of shearing terms that act to rotate the dynamical vierbein away from its initial configuration). But numerical work in the classical case serves to indicate that even with such perturbations, the generic result should still be a chaotic, BKL-like collapse toward a spacelike singularity [86].

6.3.4 Discussion

By now it is clear in the literature that quantum fields do not jive well with vacuum black hole spacetimes. If the Kerr metric (the axisymmetric solution to Einstein's equations for a rotating black hole in an empty spacetime) is immersed within a scalar quantum field, then even if that field

begins in an empty vacuum state, the gravitational collapse leading to the formation of the black hole will cause a mixing of positive- and negative-frequency modes that leads to the spontaneous production of particles. Usually, this semiclassical flux of particles will be suppressed on the order of the Planck mass m_P^2 divided by the black hole's mass M^2, and the Kerr structure will remain intact, but close enough to the inner horizon, this study confirms the conclusion of previous studies [103, 178] that semiclassical radiation will diverge at the Kerr inner horizon.

To understand how the Kerr geometry will react to the diverging quantum field near the inner horizon, it is natural to work in the framework of the semiclassical Einstein field Eqs. (3.9), wherein the spacetime's curvature is sourced by the vacuum expectation value of the renormalized stress-energy tensor (RSET) of the quantum field. The potential problems (mathematical, physical, and philosophical) associated with such an approach have been debated again and again over the years [2, 63, 104, 137], but it nonetheless remains true that the semiclassical approach is perfectly valid as an effective field theory of quantum gravity, as long as the RSET remains below Planck-scale energies (at 10^{19} GeV, which is already orders of magnitude above the grand unified scale, beyond the point where every atomic nucleus has been dissociated and the very notion of particles and interactions is called into question).

Here it is found that the RSET in double-null coordinates contains a non-zero component $\langle U|\hat{T}_{vv}|U\rangle_{\mathrm{ren}}$ near the inner horizons of both spherical and rotating black holes, which, when converted to coordinates that are regular across that horizon, yields an exponential divergence in the quantum flux. Such behavior was also found in Refs. [103, 178]; the additional contributions here were to compute more inner-horizon RSET components over the full parameter space (a, θ) (Fig. 6.6), find the asymptotic behavior at both high and low black hole spins (Figs. 6.4, 6.5), and analyze the backreaction that the RSET elicits.

The most striking feature of the inner-horizon RSET is that, in contrast to the classical case (or even the semiclassical 2D case), the double-null components of the RSET can be either positive or negative at different points along the inner horizon. The semiclassical Einstein equations then suggest that as an initial tendency, the local geometry as one approaches the inner horizon will

rapidly contract (expand) wherever $\langle T_{vv}^- \rangle$ is positive (negative).

In semiclassical backreaction analyses, the above statement is usually the end of the story. Ref. [103] takes it one step further to show that in the inevitable regions where the local geometry neither contracts nor expands, the $v\varphi$-component of the RSET will cause an initial tendency for the geometry to undergo an infinite twisting. However, the question of whether anything more can be ascertained from the RSET about the geometry's evolution and the black hole's final configuration is either left to speculation or completely ignored, and for good reason—as soon as the inner horizon is pushed even slightly away from its Kerr value, the Kerr vacuum RSET is no longer valid and a new RSET in a more general spacetime would need to be found to continue the evolution any further. Nonetheless, the goal of the current work is to provide a path forward to do exactly that, so that one may determine whether or not the semiclassical inner-horizon instability generically leads to a spacelike singularity.

The backreaction analysis of Sec. 6.3.3 employed the conformally separable framework of Refs. [84–86, 90] to determine how semiclassical fluxes can be understood together with the classical fluxes that lead to mass inflation near the inner horizon. One can immediately gather from the presence of a non-vanishing RSET component $\langle T_{rt}^- \rangle = (\langle T_{vv}^- \rangle - \langle T_{uu}^- \rangle)\, R^{-2}\Delta_r^{-1}$ that the semiclassical backreaction drives the evolution away from many of the potential (meta)stable geometries proposed as potential endpoints of black hole evolution, like the regular "eye of the storm" geometry or the Kerr "black-bounce" geometry (see the end of Sec. 6.3.2). In contrast, the conformally separable model generically predicts the presence of a strong, spacelike singularity that is stable over astrophysical time scales.

In particular, in Sec. 6.3.3, the metric is generalized to allow for all the functions in the Kerr line element of Eq. (6.26) to respond freely to the presence of semiclassical stress-energy. The dominant evolution near the inner horizon comes from the horizon function $\Delta_r(r)$ and the conformal factor $\rho(r, \theta, t)$, and thus it becomes useful to analyze the spacetime in a tetrad frame rotated to align with the principal null directions so that the Δ_r- and ρ-dependent portions of the vierbein are purely diagonal, Eqs. (6.40a)–(6.40d).

In this Carter tetrad frame, the RSET's dominant components are the diagonals $\langle T_{00}^- \rangle$ and $\langle T_{11}^- \rangle$, Eqs. (6.41), while the off-diagonal $\langle T_{01}^- \rangle$ also diverges as Δ_r^{-1} but is numerically seen to be usually several orders of magnitude smaller than the diagonal components. As such, one is justified in treating the initial semiclassical evolution with the inflationary Kasner spacetime of Chapter 2, which uses precisely the dynamical vierbein of Eqs. (6.40a)–(6.40d) sourced by stress-energy components T_{00} and T_{11}. Eventually (or even initially, in the latitudes of infinite quantum twisting), this solution will break down once the RSET's angular components become non-negligible, but even once the inflationary Kasner model breaks down, the full conformally separable model can still be continued (albeit with less symmetry), as it has been shown to be robust for a wide variety of stress-energy sources [84].

The advantage of the conformally separable model at describing the inner-horizon backreaction is not only in its ability to encompass a wide range of behaviors related to the mass inflation phenomenon, but also in its potential to take the semiclassical evolution even deeper. It is almost miraculous that such a chaotic instability leads at least initially to a spacetime (the inflationary Kasner metric) that is so simple, elegant, and possesses a high degree of symmetry. The RSET in this new homogeneous spacetime should be relatively straightforward to compute, with the only difficulty coming from mode-matching to the Kerr Unruh state (though the relevant mathematical details have already been worked out in Ref. [89]). The renormalized vacuum polarization $\langle \hat{\phi}^2 \rangle_{\mathrm{ren}}$ has already been calculated in the inflationary Kasner spacetime in an adiabatic vacuum state (Chapter 5), with the conclusion that the semiclassical contribution follows the same qualitative behavior as the classical stress-energy.

It is time to take RSET calculations beyond vacuum black holes. From this work it can be gleaned that the semiclassical inner-horizon instability causes the local Kerr spacetime to be filled with diverging streams of radiation, and while this work provides evidence that those streams should generically lead to an astrophysically stable, chaotic, spacelike singularity, their exact semiclassical evolution remains an open but tractable question.

Chapter 7

Concluding Remarks

This thesis is a jam-packed conglomeration of six separate works published over the course of four years. However, hopefully it is clear to any reader (whether skimming, seeking out sections of interest, or analyzing everything with a fine-toothed comb) that these works are all brought together under a central, unifying theme—astrophysical black holes cannot possess an inner horizon.

The thesis uses two physical frameworks to address the topic at hand: first, classical gravity as described by Einstein's theory of general relativity (Chapters 1–2), and second, semiclassical gravity as described by one-loop quantum field theory over a curved spacetime (Chapters 3–6).

In the context of the framework of classical gravity, inner horizons are commonplace features of black hole spacetimes in general relativity, and beyond these inner horizons one may expect to find a regular star-like core, a timelike singularity, or even a wormhole to a new universe. However, the analysis of Chapter 2 revealed that if a black hole is not empty but instead is subject to a constant, tiny source of accretion (like the radiation penetrating every black hole in the current Universe), the geometry near the would-be inner horizon will be replaced with the inflationary Kasner metric, Eq. (2.5). This metric predicts the dynamical evolution of the spacetime through a *mass inflation* stage (where the streams of fluid focus along the principal null directions and increase exponentially in energy) into a *collapse* stage (where the geometry bounces and proceeds toward a spaghettifying, Schwarzschild-like singularity). The phenomenon of mass inflation has been predicted as a robust outcome since at least the early 1990s [154], but here it was shown that it is not the end of the story—the mass inflation instability eventually stalls out and gives way to a BKL-like collapse toward

a spacelike singularity, as a result of the continued presence of accretion.

In the context of the framework of semiclassical gravity, the goal was to understand what quantum effects an inertial observer would experience as they fall into a black hole. The most obvious effect is Hawking radiation, which, contrary to the common lore, will continue to be detected as a bath of outgoing particles even after an observer falls below the event horizon. While the analysis of Chapter 4 did not make use of a local particle picture and instead worked with the global scattering framework originally used by Hawking [94], heuristically, one could imagine that particle-antiparticle pairs are always being spontaneously produced from the quantum vacuum. Usually, these pairs cannot exist on-shell because one member must have a (classically forbidden) negative energy, but in the presence of a black hole interior where the global time coordinate becomes spacelike, energies can be positive or negative, and Hawking pairs are free to roam as real radiation anywhere they please. These particles become more and more numerous and energetic as one approaches the inner horizon, until the effective Hawking temperature (defined in Sec. 3.2) diverges at the inner horizon. Curiously, this effective temperature is negative, which was interpreted either as an indication that the spectrum is ultraviolet-divergent in response to the blueshifting of modes, or as a consequence of the fact that the spaghettifying tidal forces ripping apart Hawking pairs switch signs to become "pancakifying" close enough to the inner horizon [122].

Though other important quantum effects were analyzed in this thesis, Hawking radiation was the main semiclassical effect that deserved the most focus, as it had not previously been explored for black hole interiors. The effective temperature formalism used in Sec. 4.2–4.4 clearly shows how the perception of Hawking radiation changes along any inertial trajectory outside or inside a black hole, and more conclusively, the full Bogoliubov coefficient calculations of Sec. 4.5 show how the entire graybody spectrum of Hawking radiation will appear at each horizon.

Perhaps the most important semiclassical quantity analyzed in this thesis is the renormalized stress-energy tensor of Chapter 6, since this quantity provides direct information about backreaction and brings us one step closer to answering the deeper question of whether one can construct a semiclassically self-consistent black hole model. The conclusion here is that such a model likely

cannot contain an inner horizon, since such a hypersurface always appears to excite a quantum field's stress-energy content an infinite amount. However, it is still not known what the generic outcome of this semiclassical instability will be—this thesis supports the conclusion that astrophysical black holes will host chaotic, oscillatory, spacelike singularities (i.e., regions where ultraviolet-complete theories of quantum gravity reign supreme) that remain semiclassically stable over cosmological timescales, but since a fully self-consistent backreaction analysis is still nonexistent, one could also imagine any number of other scenarios in which a black hole's core becomes regularized or rapidly evaporates from the inside out to form a compact, horizonless object.

Why care about these fascinating classical and quantum effects happening inside astrophysical black holes? For the astronomer, we wish to understand what these objects whose gravitational and radiative effects we observe actually are—should we be looking for compact, horizonless objects, does the interior instability substantially modify the external parameters of the black hole, or is mass inflation semiclassically stable so that the Kerr metric remains completely valid in all observable portions of the spacetime?

For the high energy physicist, this semiclassical instability is a theoretical testbed that provides one of our best chances for understanding quantum gravity. Particle energies close to the would-be inner horizon can very quickly reach far above the grand unified scale, and yet these phenomena have remained largely unexplored up to this point.

For the mathematician, a plethora of problems related to robust construction of an Unruh state, the monodromy of confluent Heun eigenmodes, and the validity of the cosmic censorship hypothesis still remain to be solved.

For the quantum information theorist, while great strides have been made toward understanding the unitary of black hole systems as a whole and their connections to holography and computational complexity, we still are lacking a firm answer as to what happens on the side of semiclassical physics.

And for the dreamer, the study of black hole interiors is bound to lead to new, unexpected discoveries that will transform physics as we know it. Black holes, quantum vacuum fluctuations, wormholes, and warp drives lie at the very forefront of the imagined world of science fiction, and my

hope is that the analysis in this thesis of robust semiclassical effects in astrophysical models of black holes has pushed some of these phenomena just a little bit closer to science reality.

References

[1] B. P. Abbott et al. (LIGO Scientific Collaboration and Virgo Collaboration), "Observation of gravitational waves from a binary black hole merger", Phys. Rev. Lett. **116**, 061102 (2016) (Cited on p. 2).

[2] Y. Aharonov and D. Rohrlich, *Quantum paradoxes: quantum theory for the perplexed* (Wiley-VCH Verlag, Weinheim, Germany, 2003), pp. 212–213 (Cited on p. 237).

[3] A. Almheiri, N. Engelhardt, D. Marolf, and H. Maxfield, "The entropy of bulk quantum fields and the entanglement wedge of an evaporating black hole", Journal of High Energy Physics **2019**, 63 (2019) (Cited on p. 2).

[4] P. R. Anderson, "$\langle\varphi^2\rangle$ for massive fields in Schwarzschild spacetime", Phys. Rev. D **39**, 3785 (1989) (Cited on p. 176).

[5] P. R. Anderson, R. Balbinot, A. Fabbri, and R. Parentani, "Hawking radiation correlations in Bose-Einstein condensates using quantum field theory in curved space", Phys. Rev. D **87**, 124018 (2013) (Cited on p. 144).

[6] P. R. Anderson, E. Mottola, and R. Vaulin, "Stress tensor from the trace anomaly in Reissner-Nordström spacetimes", Phys. Rev. D **76**, 124028 (2007) (Cited on p. 201).

[7] P. R. Anderson and L. Parker, "Adiabatic regularization in closed Robertson-Walker universes", Phys. Rev. D **36**, 2963 (1987) (Cited on p. 192).

[8] J. Arrechea, C. Barceló, V. Boyanov, and L. J. Garay, "Vacuum semiclassical gravity does not leave space for safe singularities", Universe **7**, 10.3390/universe7080281 (2021) (Cited on p. 176).

[9] J. Arrechea, C. Barceló, R. Carballo-Rubio, and L. J. Garay, "Reissner–Nordström geometry counterpart in semiclassical gravity", Class. Quant. Grav. **38**, 115014 (2021) (Cited on pp. 176, 202).

[10] J. Baines and M. Visser, "Killing horizons and surface gravities for a well-behaved three-function generalization of the Kerr spacetime", Universe **9**, 10.3390/universe9050223 (2023) (Cited on pp. 230, 231).

[11] V. Balasubramanian, A. Kar, and G. Sárosi, "Holographic probes of inner horizons", Journal of High Energy Physics **2020**, 54 (2020) (Cited on p. 3).

[12] R. Balbinot, "Hawking radiation and the back reaction-a first approach", Classical and Quantum Gravity **1**, 573 (1984) (Cited on p. 188).

[13] R. Balbinot, A. Fabbri, P. Nicolini, V. Frolov, P. Sutton, and A. Zelnikov, "Vacuum polarization in the Schwarzschild spacetime and dimensional reduction", Phys. Rev. D **63**, 084029 (2001) (Cited on p. 188).

[14] R. Balbinot, A. Fabbri, R. A. Dudley, and P. R. Anderson, "Particle production in the interiors of acoustic black holes", Phys. Rev. D **100**, 105021 (2019) (Cited on pp. 144, 149).

[15] R. Balbinot and E. Poisson, "Mass inflation: the semiclassical regime", Phys. Rev. Lett. **70**, 13 (1993) (Cited on pp. 176, 228).

[16] L. C. Barbado, C. Barceló, and L. J. Garay, "Hawking radiation as perceived by different observers", Classical and Quantum Gravity **28**, 125021 (2011) (Cited on pp. 67, 68, 76, 85).

[17] L. C. Barbado, C. Barceló, L. J. Garay, and G. Jannes, "A tensorial description of particle perception in black-hole physics", Phys. Rev. D **94**, 064004 (2016) (Cited on p. 99).

[18] C. Barcelo, V. Boyanov, R. Carballo-Rubio, and L. J. Garay, "Black hole inner horizon evaporation in semiclassical gravity", Class. Quant. Grav. **38**, 125003 (2021) (Cited on pp. 20, 77, 172, 176, 204, 228).

[19] C. Barceló, R. Carballo, and L. J. Garay, "Two formalisms, one renormalized stress-energy tensor", Phys. Rev. D **85**, 084001 (2012) (Cited on p. 202).

[20] C. Barceló, S. Liberati, S. Sonego, and M. Visser, "Hawking-like radiation from evolving black holes and compact horizonless objects", Journal of High Energy Physics **2011**, 1 (2011) (Cited on pp. 66, 68, 75, 76, 100, 101, 149, 169, 270).

[21] C. Barceló, S. Liberati, S. Sonego, and M. Visser, "Minimal conditions for the existence of a Hawking-like flux", Phys. Rev. D **83**, 041501 (2011) (Cited on pp. 66, 75, 76, 100, 169).

[22] J. M. Bardeen, W. H. Press, and S. A. Teukolsky, "Rotating black holes: locally nonrotating frames, energy extraction, and scalar synchrotron radiation", The Astrophysical Journal **178**, 347 (1972) (Cited on pp. 48, 135).

[23] C. Barrabes, W. Israel, and E. Poisson, "Collision of light-like shells and mass inflation in rotating black holes", Class. Quant. Grav. **7**, L273 (1990) (Cited on p. 18).

[24] V. Belinskii, I. Khalatnikov, and E. Lifshitz, "Oscillatory approach to a singular point in the relativistic cosmology", Advances in Physics **19**, 525 (1970) (Cited on pp. 17, 29, 217).

[25] P. Beltrán-Palau, J. Navarro-Salas, and S. Pla, "Adiabatic regularization for Dirac fields in time-varying electric backgrounds", Phys. Rev. D **101**, 105014 (2020) (Cited on p. 185).

[26] P. Beltrán-Palau, A. del Río, S. Nadal-Gisbert, and J. Navarro-Salas, "Note on the pragmatic mode-sum regularization method: translational-splitting in a cosmological background", Phys. Rev. D **103**, 105002 (2021) (Cited on p. 184).

[27] E. Berti, V. Cardoso, and M. Casals, "Eigenvalues and eigenfunctions of spin-weighted spheroidal harmonics in four and higher dimensions", Phys. Rev. D **73**, 024013 (2006) (Cited on pp. 155, 279).

[28] N. D. Birrell and P. C. W. Davies, "On falling through a black hole into another universe", Nature **272**, 35 (1978) (Cited on p. 176).

[29] N. D. Birrell and P. C. W. Davies, *Quantum fields in curved space*, Cambridge Monographs on Mathematical Physics (Cambridge University Press, 1982) (Cited on pp. 58, 60, 62, 176, 187, 188, 193).

[30] *Black Hole Perturbation Toolkit*, bhptoolkit.org, 2022 (Cited on pp. 159, 219, 279).

[31] R. H. Boyer and R. W. Lindquist, "Maximal analytic extension of the Kerr metric", Journal of Mathematical Physics **8**, 265 (1967) (Cited on p. 114).

[32] P. R. Brady and C. M. Chambers, "Nonlinear instability of Kerr-type Cauchy horizons", Phys. Rev. D **51**, 4177 (1995) (Cited on p. 18).

[33] E. J. Brynjolfsson and L. Thorlacius, "Taking the temperature of a black hole", Journal of High Energy Physics **2008**, 066 (2008) (Cited on p. 96).

[34] L. M. Burko, "Survival of the black hole's Cauchy horizon under noncompact perturbations", Phys. Rev. D **66**, 024046 (2002) (Cited on p. 19).

[35] L. M. Burko, "Black-hole singularities: a new critical phenomenon", Phys. Rev. Lett. **90**, 121101 (2003) (Cited on p. 19).

[36] P. Candelas and K. W. Howard, "Vacuum $\langle \varphi^2 \rangle$ in Schwarzschild spacetime", Phys. Rev. D **29**, 1618 (1984) (Cited on p. 188).

[37] R. Carballo-Rubio, F. Di Filippo, S. Liberati, C. Pacilio, and M. Visser, "Inner horizon instability and the unstable cores of regular black holes", Journal of High Energy Physics **2021**, 132 (2021) (Cited on p. 19).

[38] R. Carballo-Rubio, F. Di Filippo, S. Liberati, C. Pacilio, and M. Visser, "Regular black holes without mass inflation instability", Journal of High Energy Physics **2022**, 118 (2022) (Cited on pp. 102–104, 211).

[39] R. Carballo-Rubio, F. D. Filippo, S. Liberati, and M. Visser, "Mass inflation without Cauchy horizons", `10.48550/arXiv.2402.14913` (2024) (Cited on p. 13).

[40] B. Carter, "Global structure of the Kerr family of gravitational fields", Phys. Rev. **174**, 1559 (1968) (Cited on pp. 32, 85, 114, 115, 218, 230, 232).

[41] M. Casals, A. Fabbri, C. Martínez, and J. Zanelli, "Quantum-corrected rotating black holes and naked singularities in $(2 + 1)$ dimensions", Phys. Rev. D **99**, 104023 (2019) (Cited on p. 177).

[42] S. Chandrasekhar, *The mathematical theory of black holes* (Clarendon Press, Oxford, England, 1983), 646 pp. (Cited on p. 22).

[43] S. M. Christensen, "Vacuum expectation value of the stress tensor in an arbitrary curved background: The covariant point-separation method", Phys. Rev. D **14**, 2490 (1976) (Cited on p. 72).

[44] S. M. Christensen, "Regularization, renormalization, and covariant geodesic point separation", Phys. Rev. D **17**, 946 (1978) (Cited on p. 72).

[45] L. C. B. Crispino, A. Higuchi, L. A. Oliveira, and E. S. de Oliveira, "Tidal forces in Reissner–Nordström spacetimes", The European Physical Journal C **76**, 168 (2016) (Cited on pp. 78, 96, 105).

[46] K. Crowther and S. D. Haro, "Four attitudes towards singularities in the search for a theory of quantum gravity", `10.48550/arXiv.2112.08531` (2021) (Cited on p. 215).

[47] A. Curir, "Spin entropy of a rotating black hole", Il Nuovo Cimento B (1971-1996) **51**, 262 (1979) (Cited on p. 79).

[48] M. Cvetič, G. W. Gibbons, H. Lü, and C. N. Pope, "Killing horizons: Negative temperatures and entropy super-additivity", Phys. Rev. D **98**, 106015 (2018) (Cited on p. 79).

[49] M. Dafermos, "The interior of charged black holes and the problem of uniqueness in general relativity", Communications on Pure and Applied Mathematics **58**, 445 (2005) (Cited on pp. 18, 172).

[50] P. C. W. Davies, S. A. Fulling, and W. G. Unruh, "Energy-momentum tensor near an evaporating black hole", Phys. Rev. D **13**, 2720 (1976) (Cited on p. 228).

[51] P. Davies, S. Fulling, S. Christensen, and T. Bunch, "Energy-momentum tensor of a massless scalar quantum field in a Robertson-Walker universe", Annals of Physics **109**, 108 (1977) (Cited on p. 192).

[52] B. S. DeWitt, "Dynamical theory of groups and fields", Conf. Proc. C **630701**, edited by C. DeWitt and B. DeWitt, 585 (1964) (Cited on p. 71).

[53] B. S. DeWitt, "Quantum field theory in curved spacetime", Phys. Rep. **19**, 295 (1975) (Cited on p. 72).

[54] J. F. Donoghue, "General relativity as an effective field theory: The leading quantum corrections", Phys. Rev. D **50**, 3874 (1994) (Cited on p. 57).

[55] C. Doran, "New form of the Kerr solution", Phys. Rev. D **61**, 067503 (2000) (Cited on p. 45).

[56] M. J. Duff, "Twenty years of the Weyl anomaly", Classical and Quantum Gravity **11**, 1387 (1994) (Cited on p. 200).

[57] A. Erdélyi, "The Fuchsian equation of second order with four singularities", Duke Mathematical Journal **9**, 48 (1942) (Cited on p. 281).

[58] A. Erdélyi, "Certain expansions of solutions of the Heun equation", The Quarterly Journal of Mathematics **os-15**, 62 (1944) (Cited on p. 281).

[59] Event Horizon Telescope Collaboration, The Astrophysical Journal Letters **875**, L1 (2019) (Cited on p. 2).

[60] Event Horizon Telescope Collaboration, "First Sagittarius A* Event Horizon Telescope results. I. The shadow of the supermassive black hole in the center of the Milky Way", The Astrophysical Journal Letters **930**, L12 (2022) (Cited on pp. 2, 231).

[61] A. Fabbri and J. Navarro-Salas, *Modeling black hole evaporation* (Imperial College Press, London, 2005) (Cited on pp. 205, 271).

[62] P. G. S. Fernandes, "Rotating black holes in semiclassical gravity", Phys. Rev. D **108**, L061502 (2023) (Cited on p. 230).

[63] R. P. Feynman, *Feynman lectures on gravitation*, edited by F. B. Morinigo, W. G. Wagner, and B. Hatfield (Addison-Wesley, 1996) (Cited on p. 237).

[64] F. D. Filippo, S. Liberati, and M. Visser, "Fully extremal black holes: a black hole graveyard?", 10.48550/arXiv.2405.08069 (2024) (Cited on p. 217).

[65] E. E. Flanagan, "Quantum mechanical instabilities of Cauchy horizons in two dimensions - a modified form of the blueshift instability mechanism", 10.48550/arXiv.gr-qc/9711066 (1997) (Cited on p. 176).

[66] A. Fletcher, "Spheroidal wave functions. by C. Flammer. pp. ix, 220. 68s. 1957. (Stanford University Press, Stanford, California)", The Mathematical Gazette **43**, 217 (1959) (Cited on p. 280).

[67] E. Franzin, S. Liberati, J. Mazza, and V. Vellucci, "Stable rotating regular black holes", Phys. Rev. D **106**, 104060 (2022) (Cited on pp. 102, 114–116, 202).

[68] A. V. Frolov, K. R. Kristjánsson, and L. Thorlacius, "Semiclassical geometry of charged black holes", Phys. Rev. D **72**, 021501 (2005) (Cited on p. 176).

[69] S. A. Fulling, L. Parker, and B. L. Hu, "Conformal energy-momentum tensor in curved spacetime: Adiabatic regularization and renormalization", Phys. Rev. D **10**, 3905 (1974) (Cited on p. 185).

[70] S. Fulling and L. Parker, "Renormalization in the theory of a quantized scalar field interacting with a Robertson-Walker spacetime", Annals of Physics **87**, 176 (1974) (Cited on p. 185).

[71] S. A. Fulling, M. Sweeny, and R. M. Wald, "Singularity structure of the two-point function in quantum field theory in curved spacetime", Communications in Mathematical Physics **63**, 257 (1978) (Cited on p. 203).

[72] *Gaia all-sky colour map, Early Data Release 3, ESA/Gaia/DPAC*, esa.int, 2020 (Cited on p. 7).

[73] J. García-Bellido, J. F. N. Siles, and E. R. Morales, "Bayesian analysis of the spin distribution of LIGO/Virgo black holes", Physics of the Dark Universe **31**, 100791 (2021) (Cited on p. 197).

[74] R. Genzel, R. Schödel, T. Ott, A. Eckart, T. Alexander, F. Lacombe, D. Rouan, and B. Aschenbach, "Near-infrared flares from accreting gas around the supermassive black hole at the galactic centre", Nature **425**, 934 (2003) (Cited on p. 2).

[75] R. P. Geroch, A. Held, and R. Penrose, "A space-time calculus based on pairs of null directions", J. Math. Phys. **14**, 874 (1973) (Cited on p. 154).

[76] A. M. Ghez, B. L. Klein, M. Morris, and E. E. Becklin, "High proper-motion stars in the vicinity of Sagittarius A*: Evidence for a supermassive black hole at the center of our galaxy", The Astrophysical Journal **509**, 678 (1998) (Cited on p. 2).

[77] L. Gou, J. E. McClintock, M. J. Reid, J. A. Orosz, J. F. Steiner, R. Narayan, J. Xiang, R. A. Remillard, K. A. Arnaud, and S. W. Davis, "The extreme spin of the black hole in Cygnus X-1", The Astrophysical Journal **742**, 85 (2011) (Cited on p. 197).

[78] GRAVITY Collaboration, "Detection of orbital motions near the last stable circular orbit of the massive black hole SgrA*", Astronomy & Astrophysics **618**, L10 (2018) (Cited on pp. 2, 231).

[79] E. Greenwood and D. Stojkovic, "Hawking radiation as seen by an infalling observer", Journal of High Energy Physics **2009**, 058 (2009) (Cited on pp. 68, 76).

[80] J. Hadamard, *Lectures on Cauchy's problem in linear partial differential equations*, Mrs. Hepsa Ely Silliman memorial lectures (Yale University Press, 1923) (Cited on p. 71).

[81] A. J. S. Hamilton, "Black Hole Flight Simulator", in, Vol. 204, American Astronomical Society Meeting Abstracts (2004), p. 78.06 (Cited on p. 6).

[82] A. J. S. Hamilton, "The black hole particle accelerator as a machine to make baby universes", 10.48550/arXiv.1305.4524 (2013) (Cited on p. 5).

[83] A. J. S. Hamilton and T. McMaken, "Unification of the four forces in the Spin(11,1) geometric algebra", Physica Scripta **98**, 085306 (2023) (Cited on p. vi).

[84] A. J. S. Hamilton, "Interior structure of rotating black holes. II. Uncharged black holes", Phys. Rev. D **84**, 124056 (2011) (Cited on pp. 14, 19, 32–34, 37, 179, 217, 231–236, 238, 239).

[85] A. J. S. Hamilton, "Interior structure of rotating black holes. III. Charged black holes", Phys. Rev. D **84**, 124057 (2011) (Cited on pp. 14, 19, 32, 217, 233, 235, 238).

[86] A. J. S. Hamilton, "Mass inflation followed by Belinskii-Khalatnikov-Lifshitz collapse inside accreting, rotating black holes", Phys. Rev. D **96**, 084041 (2017) (Cited on pp. 19, 20, 30, 32, 33, 38, 53, 232, 234, 236, 238).

[87] A. J. S. Hamilton, "Hawking radiation inside a Schwarzschild black hole", General Relativity and Gravitation **50**, 50 (2018) (Cited on pp. 68, 69, 76, 90, 92, 117, 119, 122–125, 131, 137, 142, 172).

[88] A. J. S. Hamilton and J. P. Lisle, "The river model of black holes", American Journal of Physics **76**, 519 (2008) (Cited on pp. 11, 93).

[89] A. J. S. Hamilton and T. McMaken, "Wave equations in conformally separable, accreting, rotating black holes", Phys. Rev. D **106**, 124031 (2022) (Cited on pp. vi, 154, 189, 239).

[90] A. J. S. Hamilton and G. Polhemus, "Interior structure of rotating black holes. I. Concise derivation", Phys. Rev. D **84**, 124055 (2011) (Cited on pp. 14, 19, 32, 217, 233, 235, 238).

[91] A. J. Hamilton and P. P. Avelino, "The physics of the relativistic counter-streaming instability that drives mass inflation inside black holes", Physics Reports **495**, 1 (2010) (Cited on pp. 19, 38).

[92] S. W. Hawking, "Black holes in general relativity", Communications in Mathematical Physics **25**, 152 (1972) (Cited on p. 231).

[93] S. W. Hawking, "Black hole explosions?", Nature **248**, 30 (1974) (Cited on pp. 63, 68, 75, 168, 228).

[94] S. W. Hawking, "Particle creation by black holes", Communications in Mathematical Physics **43**, 199 (1975) (Cited on pp. 63, 68, 78, 166, 241).

[95] W. A. Hiscock, "Quantum-mechanical instability of the Kerr-Newman black-hole interior", Phys. Rev. D **21**, 2057 (1980) (Cited on pp. 98, 177).

[96] S. Hollands, A. Ishibashi, and H. S. Reall, "A stationary black hole must be axisymmetric in effective field theory", Communications in Mathematical Physics **401**, 2757 (2023) (Cited on p. 231).

[97] S. Hollands, R. M. Wald, and J. Zahn, "Quantum instability of the Cauchy horizon in Reissner–Nordström–deSitter spacetime", Class. Quant. Grav. **37**, 115009 (2020) (Cited on pp. 176, 201).

[98] K. Jhurani and T. McMaken, "Existence of time-like geodesics in asymptotically flat spacetimes: A generalized topological criterion", Adv. Stud. Theor. Phys. **17**, 109 (2023) (Cited on p. vi).

[99] E. Kasner, "Geometrical theorems on Einstein's cosmological equations", American Journal of Mathematics **43**, 217 (1921) (Cited on pp. 29, 178).

[100] E. Kasner, *Mathematics and the imagination* (Simon and Schuster, New York, 1940) (Cited on p. 30).

[101] A. Y. Kazakov, "The central two-point connection problem for the reduced confluent Heun equation", Journal of Physics A: Mathematical and General **39**, 2339 (2006) (Cited on p. 263).

[102] R. P. Kerr, "Do black holes have singularities?", 10.48550/arXiv.2312.00841 (2023) (Cited on p. 4).

[103] C. Klein, M. Soltani, M. Casals, and S. Hollands, "Infinite quantum twisting at the Cauchy horizon of rotating black holes", Phys. Rev. Lett. **132**, 121501 (2024) (Cited on pp. 217, 219, 220, 224, 226, 228, 231, 237, 238).

[104] C. Klein and J. Zahn, "Long-range correlations of the stress tensor near the Cauchy horizon", Phys. Rev. D **109**, L061702 (2024) (Cited on p. 237).

[105] C. Klein, J. Zahn, and S. Hollands, "Quantum (dis)charge of black hole interiors", Phys. Rev. Lett. **127**, 231301 (2021) (Cited on p. 176).

[106] C. K. M. Klein, "Construction of the Unruh state for a real scalar field on the Kerr-de Sitter spacetime", Annales Henri Poincaré **24**, 2401 (2023) (Cited on p. 219).

[107] A. Krasi ński and K. Bolejko, "Avoidance of singularities in spherically symmetric charged dust", Phys. Rev. D **73**, 124033 (2006) (Cited on p. 86).

[108] A. Lanir, A. Levi, A. Ori, and O. Sela, "Two-point function of a quantum scalar field in the interior region of a Reissner-Nordstrom black hole", Phys. Rev. D **97**, 024033 (2018) (Cited on pp. 152, 164).

[109] A. Lanir, A. Ori, N. Zilberman, O. Sela, A. Maline, and A. Levi, "Analysis of quantum effects inside spherical charged black holes", Phys. Rev. D **99**, 061502 (2019) (Cited on p. 176).

[110] H. Lass, "Accelerating frames of reference and the clock paradox", American Journal of Physics **31**, 274 (1963) (Cited on p. 182).

[111] A. Levi, "Renormalized stress-energy tensor for stationary black holes", Phys. Rev. D **95**, 025007 (2017) (Cited on p. 208).

[112] A. Levi and A. Ori, "Pragmatic mode-sum regularization method for semiclassical black-hole spacetimes", Phys. Rev. D **91**, 104028 (2015) (Cited on pp. 184, 208).

[113] A. Levi and A. Ori, "Mode-sum regularization of $\langle \phi^2 \rangle$ in the angular-splitting method", Phys. Rev. D **94**, 044054 (2016) (Cited on p. 184).

[114] A. Levi and A. Ori, "Versatile method for renormalized stress-energy computation in black-hole spacetimes", Phys. Rev. Lett. **117**, 231101 (2016) (Cited on p. 208).

[115] E. Lifshitz and I. Khalatnikov, "Investigations in relativistic cosmology", Advances in Physics **12**, 185 (1963) (Cited on p. 17).

[116] H. C. D. Lima Junior, L. C. B. Crispino, and A. Higuchi, "On-axis tidal forces in Kerr spacetime", The European Physical Journal Plus **135**, 334 (2020) (Cited on p. 110).

[117] D. J. Loranz and W. A. Hiscock, "Quantized fields and temperature in charged dilatonic black hole spacetimes", Phys. Rev. D **55**, 3893 (1997) (Cited on p. 97).

[118] S. Mano, H. Suzuki, and E. Takasugi, "Analytic solutions of the Teukolsky equation and their low frequency expansions", Progress of Theoretical Physics **95**, 1079 (1996) (Cited on pp. 219, 279, 282).

[119] S. Mano and E. Takasugi, "Analytic solutions of the Teukolsky equation and their properties", Progress of Theoretical Physics **97**, 213 (1997) (Cited on pp. 219, 279, 282).

[120] J. Matyjasek, "Quantum fields in Bianchi type I spacetimes: The Kasner metric", Phys. Rev. D **98**, 104054 (2018) (Cited on p. 185).

[121] T. McMaken, "Notes on primordial black hole origin for thermal gamma-ray bursts", Monthly Notices of the Royal Astronomical Society **511**, 1218 (2022) (Cited on p. vi).

[122] T. McMaken, "Pancakification and negative Hawking temperatures", International Journal of Modern Physics D **32**, 2342017 (2023) (Cited on pp. vi, 78, 241).

[123] T. McMaken, "Semiclassical instability of inner-extremal regular black holes", Phys. Rev. D **107**, 125023 (2023) (Cited on pp. v, 75, 199).

[124] T. McMaken, "Backreaction from quantum fluxes at the Kerr inner horizon", `10.48550/arXiv.2405.13221` (2024) (Cited on pp. v, 199).

[125] T. McMaken and A. J. S. Hamilton, "Geometry near the inner horizon of a rotating, accreting black hole", Phys. Rev. D **103**, 084014 (2021) (Cited on pp. v, 17, 132, 178, 180, 196, 231).

[126] T. McMaken and A. J. S. Hamilton, "Renormalization of $\langle \phi^2 \rangle$ at the inner horizon of rotating, accreting black holes", Phys. Rev. D **105**, 125020 (2022) (Cited on pp. v, 175).

[127] T. McMaken and A. J. S. Hamilton, "Hawking radiation inside a charged black hole", Phys. Rev. D **107**, 085010 (2023) (Cited on pp. v, 75–77, 105, 119, 137).

[128] T. McMaken and A. J. S. Hamilton, "Hawking radiation inside a rotating black hole", Phys. Rev. D **109**, 065023 (2024) (Cited on pp. v, 75–77, 219).

[129] J. Meixner and F. Schäfke, "Mathieusche Funktionen und Sphäroidfunktionen, mit Anwendungen auf physikalische und technische Probleme", Die Grundlehren der mathematischen Wissenschaften **71**, 98 (1954) (Cited on p. 219).

[130] E. Minguzzi, "The Minkowski metric in non-inertial observer radar coordinates", American Journal of Physics **73**, 1117 (2005) (Cited on p. 30).

[131] Y. Mino, "Perturbative approach to an orbital evolution around a supermassive black hole", Phys. Rev. D **67**, 084027 (2003) (Cited on p. 88).

[132] C. Møller, "The energy-momentum complex in general relativity and related problems", Colloq. Int. CNRS **91**, edited by M. A. Lichnerowicz and M. A. Tonnelat, 15 (1962) (Cited on pp. 59, 173).

[133] O. V. Motygin, "On evaluation of the confluent Heun functions", in 2018 days on diffraction (dd) (2018), pp. 223–229 (Cited on p. 263).

[134] T. Müller and F. Grave, "Catalogue of spacetimes", `10.48550/arXiv.0904.4184` (2009) (Cited on p. 22).

[135] K. K. Ng, C. Zhang, J. Louko, and R. B. Mann, "A little excitement across the horizon", New Journal of Physics **24**, 103018 (2022) (Cited on p. 64).

[136] Y. C. Ong and M. R. R. Good, "Quantum atmosphere of Reissner-Nordström black holes", Phys. Rev. Research **2**, 033322 (2020) (Cited on pp. 78, 96).

[137] J. Oppenheim, "A postquantum theory of classical gravity?", Phys. Rev. X **13**, 041040 (2023) (Cited on p. 237).

[138] A. Ori, "Inner structure of a charged black hole: An exact mass-inflation solution", Phys. Rev. Lett. **67**, 789 (1991) (Cited on p. 18).

[139] A. Ori, "Structure of the singularity inside a realistic rotating black hole", Phys. Rev. Lett. **68**, 2117 (1992) (Cited on p. 18).

[140] A. Ori, "Null weak singularities in plane-symmetric space-times", Phys. Rev. D **57**, 4745 (1998) (Cited on p. 18).

[141] A. Ori, "Oscillatory null singularity inside realistic spinning black holes", Phys. Rev. Lett. **83**, 5423 (1999) (Cited on p. 19).

[142] A. Ori and É. É. Flanagan, "How generic are null spacetime singularities?", Phys. Rev. D **53**, R1754 (1996) (Cited on p. 18).

[143] A. C. Ottewill and E. Winstanley, "Renormalized stress tensor in Kerr space-time: General results", Phys. Rev. D **62**, 084018 (2000) (Cited on p. 177).

[144] D. N. Page, "Particle emission rates from a black hole. II. Massless particles from a rotating hole", Phys. Rev. D **14**, 3260 (1976) (Cited on pp. 154, 167).

[145] G. O. Papadopoulos and K. D. Kokkotas, "Preserving Kerr symmetries in deformed spacetimes", Classical and Quantum Gravity **35**, 185014 (2018) (Cited on p. 230).

[146] M.-I. Park, "Can Hawking temperatures be negative?", Physics Letters B **663**, 259 (2008) (Cited on p. 79).

[147] L. Parker, "Quantized fields and particle creation in expanding universes. I", Phys. Rev. **183**, 1057 (1969) (Cited on pp. 188, 189).

[148] L. Parker and S. A. Fulling, "Adiabatic regularization of the energy-momentum tensor of a quantized field in homogeneous spaces", Phys. Rev. D **9**, 341 (1974) (Cited on pp. 181, 185, 189, 192).

[149] A. Peltola and J. Mäkelä, "Radiation of the inner horizon of the Reissner–Nordström black hole", en, Internat. J. Modern Phys. D **15**, 817 (2006) (Cited on p. 79).

[150] G. Penington, "Entanglement wedge reconstruction and the information paradox", Journal of High Energy Physics **2020**, 2 (2020) (Cited on p. 2).

[151] R. Penrose, "Gravitational collapse and space-time singularities", Phys. Rev. Lett. **14**, 57 (1965) (Cited on pp. 2, 3, 17).

[152] R. Penrose, "Structure of space-time", in Battelle Rencontres: 1967 lectures in mathematics and physics, edited by C. de Witt-Morette and J. A. Wheeler (1968), pp. 121–235 (Cited on pp. 13, 18, 76, 98, 120).

[153] Planck Collaboration, "Planck 2015 results. XIII. Cosmological parameters", Astronomy & Astrophysics **594**, A13 (2016) (Cited on pp. 55, 231).

[154] E. Poisson and W. Israel, "Internal structure of black holes", Phys. Rev. D **41**, 1796 (1990) (Cited on pp. 18, 240).

[155] A. Polyakov, "Quantum geometry of bosonic strings", Physics Letters B **103**, 207 (1981) (Cited on p. 202).

[156] R. H. Price, "Nonspherical perturbations of relativistic gravitational collapse. I. Scalar and gravitational perturbations", Phys. Rev. D **5**, 2419 (1972) (Cited on p. 19).

[157] A. del Río and J. Navarro-Salas, "Equivalence of adiabatic and DeWitt-Schwinger renormalization schemes", Phys. Rev. D **91**, 064031 (2015) (Cited on p. 192).

[158] L. Rosenfeld, "On quantization of fields", Nuclear Physics **40**, 353 (1963) (Cited on pp. 59, 173).

[159] A. Saffer, N. Yunes, and K. Yagi, "The gravitational wave stress–energy (pseudo)-tensor in modified gravity", Classical and Quantum Gravity **35**, 055011 (2018) (Cited on pp. 56, 57).

[160] A. Saini and D. Stojkovic, "Hawking-like radiation and the density matrix for an infalling observer during gravitational collapse", Phys. Rev. D **94**, 064028 (2016) (Cited on pp. 68, 76).

[161] M. Sasaki and H. Tagoshi, "Analytic black hole perturbation approach to gravitational radiation", Living Reviews in Relativity **6**, 6 (2003) (Cited on pp. 281, 283).

[162] M. O. Scully, S. Fulling, D. M. Lee, D. N. Page, W. P. Schleich, and A. A. Svidzinsky, "Quantum optics approach to radiation from atoms falling into a black hole", en, Proc. Natl. Acad. Sci. U. S. A. **115**, 8131 (2018) (Cited on p. 64).

[163] O. Sela, "Quantum effects near the Cauchy horizon of a Reissner-Nordström black hole", Phys. Rev. D **98**, 024025 (2018) (Cited on pp. 201, 210).

[164] O. Semerák, "Stationary frames in the Kerr field", General Relativity and Gravitation **25**, 1041 (1993) (Cited on pp. 111, 114).

[165] M. Simpson and R. Penrose, "Internal instability in a Reissner-Nordström black hole", Int. J. Theor. Phys. **7**, 183 (1973) (Cited on pp. 18, 76, 120).

[166] A. A. Starobinsky, "Amplification of waves reflected from a rotating "black hole".", Sov. Phys. JETP **37**, 28 (1973) (Cited on pp. 150, 161, 163, 166).

[167] K. S. Stelle, "Classical gravity with higher derivatives", General Relativity and Gravitation **9**, 353 (1978) (Cited on p. 55).

[168] N. Svartholm, "Die Lösung der Fuchsschen Differentialgleichung zweiter Ordnung durch hypergeometrische Polynome", Mathematische Annalen **116**, 413 (1939) (Cited on p. 281).

[169] P. Taylor, "Regular quantum states on the Cauchy horizon of a charged black hole", Class. Quant. Grav. **37**, 045004 (2020) (Cited on p. 176).

[170] S. A. Teukolsky, "Rotating black holes: separable wave equations for gravitational and electromagnetic perturbations", Phys. Rev. Lett. **29**, 1114 (1972) (Cited on pp. 154, 155, 218, 279).

[171] K. S. Thorne, "Disk-accretion onto a black hole. II. Evolution of the hole", The Astrophysical Journal **191**, 507 (1974) (Cited on pp. 33, 57, 58, 182).

[172] Y. Tiandho, "Implication of negative temperature in the inner horizon of Reissner-Nordström black hole", J. Math. Fundam. Sci. **49**, 294 (2017) (Cited on p. 79).

[173] W. G. Unruh, "Notes on black-hole evaporation", Phys. Rev. D **14**, 870 (1976) (Cited on pp. 79, 80, 84, 86–88, 188, 206, 219).

[174] H. S. Vieira, V. B. Bezerra, and C. R. Muniz, "Instability of the charged massive scalar field on the Kerr–Newman black hole spacetime", The European Physical Journal C **82**, 932 (2022) (Cited on p. 261).

[175] R. M. Wald, "The back reaction effect in particle creation in curved spacetime", Commun. Math. Phys. **54**, 1 (1977) (Cited on pp. 71, 72, 185).

[176] S. Weinberg, "Photons and gravitons in perturbation theory: Derivation of Maxwell's and Einstein's equations", Phys. Rev. **138**, B988 (1965) (Cited on p. 55).

[177] J. Yang, Z. Zhao, and W. Liu, "Tortoise coordinate and Hawking effect in a dynamical Kerr black hole", Astrophysics and Space Science **331**, 627 (2011) (Cited on p. 230).

[178] N. Zilberman, M. Casals, A. Ori, and A. C. Ottewill, "Quantum fluxes at the inner horizon of a spinning black hole", Phys. Rev. Lett. **129**, 261102 (2022) (Cited on pp. 77, 142, 189, 215–220, 224, 225, 237, 285).

[179] N. Zilberman, M. Casals, A. Ori, and A. C. Ottewill, "Two-point function of a quantum scalar field in the interior region of a Kerr black hole", Phys. Rev. D **106**, 125011 (2022) (Cited on pp. 87, 154, 156, 177, 189, 215, 218–220).

[180] N. Zilberman, A. Levi, and A. Ori, "Quantum fluxes at the inner horizon of a spherical charged black hole", Phys. Rev. Lett. **124**, 171302 (2020) (Cited on pp. 98, 176, 201, 209, 210, 213, 216, 224, 227).

[181] N. Zilberman and A. Ori, "Quantum fluxes at the inner horizon of a near-extremal spherical charged black hole", Phys. Rev. D **104**, 024066 (2021) (Cited on pp. 99, 176).

[182] R. L. Znajek, "Black hole electrodynamics and the Carter tetrad", Monthly Notices of the Royal Astronomical Society **179**, 457 (1977) (Cited on p. 232).

Appendix A

Inflationary Kasner viewing angles

This appendix defines and elaborates on the usage of the observer's viewing angles χ and ψ employed throughout Chapter 2. To determine the path of a null geodesic in a 3+1D spacetime uniquely, one needs to specify at most two constants of motion. For the inflationary Kasner metric, the spatial four-momentum components k_x, k_y, and k_z uniquely label a null geodesic, but there is an extra degree of freedom associated with an arbitrary normalization factor for the four momentum's magnitude. Thus, one can transform to a new set of constants that represents the celestial coordinates for an observer in the inflationary Kasner tetrad frame. In particular, the viewing angle $\chi \in [0, \pi]$ is defined to be the angle between the x^1-axis and $-k_{\mathrm{IK}}$ (negative since the observer is seeing the photon reach the origin of their frame of reference), and $\psi \in [0, 2\pi)$ is the angle between the x^2-axis and the projection of $-k_{\mathrm{IK}}$ onto the x^2-x^3 plane. These viewing angles are shown in Fig. A.1.

The definitions of the observer's viewing angles and their relation to the spatial covariant momenta via Eqs. (2.40) are given by

$$\tan \chi \equiv \frac{\sqrt{\left(-k_{\mathrm{IK}}^2\right)^2 + \left(-k_{\mathrm{IK}}^3\right)^2}}{-k_{\mathrm{IK}}^1} = \frac{\sqrt{k_y^2 + k_z^2}}{-k_x} \frac{a_1^{\mathrm{obs}}}{a_2^{\mathrm{obs}}}, \tag{A.1a}$$

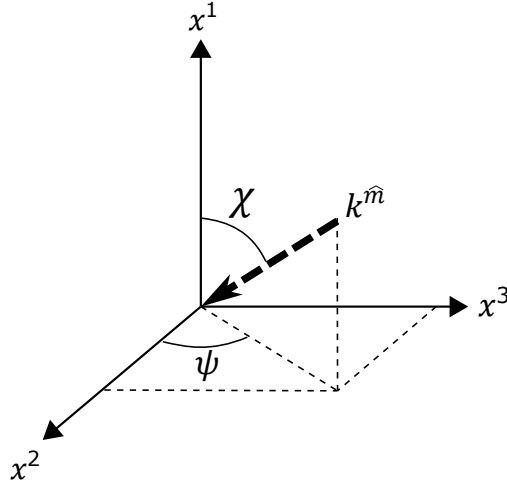$$\tan \psi \equiv \frac{-k_{\mathrm{IK}}^3}{-k_{\mathrm{IK}}^2} = \frac{-k_z}{-k_y}, \tag{A.1b}$$

Figure A.1: Definition of the viewing angles χ and ψ with respect to the tetrad frame axes x^1, x^2, and x^3, for a photon with tetrad-frame four-momentum $k^{\hat{m}}$.

or equivalently,

$$k_x = -\mathcal{E}a_1^{\text{obs}}\cos\chi, \tag{A.2a}$$

$$k_y = -\mathcal{E}a_2^{\text{obs}}\sin\chi\cos\psi, \tag{A.2b}$$

$$k_z = -\mathcal{E}a_2^{\text{obs}}\sin\chi\sin\psi, \tag{A.2c}$$

where a_1^{obs} and a_2^{obs} are the values of the scales factors from Eq. (2.6) at time $T = T_{\text{obs}}$, and $\mathcal{E}$ is some positive normalization factor (the additional degree of freedom mentioned earlier).

Physically, the x^1-axis of the tetrad frame is parallel to the principal null directions of the black hole, and the x^2-axis points in the $\hat{\theta}$ direction. When $\chi = 0°$, the observer is looking along the positive x^1-axis, away from the black hole, at ingoing photons. When $\psi = 0°$ and $\chi = 90°$, the observer is looking straight down along the positive x^2-axis, in the $\hat{\theta}$ direction. Geodesics with constant Boyer-Lindquist latitude are then given by $\psi = 90°$ and $\psi = 270°$.

When matching the tetrad-frame four-momenta of the inflationary Kasner solution with the Kerr solution at a Boyer-Lindquist radius of $r = r_1$, one can find the relation between the observer's viewing angles and the Kerr orbital parameters defined by Eqs. (2.42). Inverting Eqs. (2.46) and

combining with Eqs. (A.1) yields

$$\tan \chi = \frac{\sqrt{K(-\Delta_r)}}{E - \omega_r L} \frac{a_1^{\text{obs}}}{a_2^{\text{obs}}}, \tag{A.3a}$$

$$\sin \psi = \frac{\omega_\theta E - L}{\sqrt{K \Delta_\theta}}. \tag{A.3b}$$

This relation holds for viewing angles defined for an observer in the interior Carter frame, within the event horizon. Outside the event horizon, the exterior Carter observer also possesses a set of viewing angles (χ, ψ), still defined by Fig. A.1. However, those angles' relations to the Kerr orbital parameters will differ from the interior case, since the interior Carter frame differs from the exterior frame of Eqs. (2.35) in the swapping of $e^0{}_\mu \leftrightarrow e^1{}_\mu$ and $\sqrt{-\Delta_r} \leftrightarrow \sqrt{+\Delta_r}$. In the Kerr exterior, the viewing angles are related to the Kerr parameters by

$$\sin \chi = \frac{\sqrt{K \Delta_r}}{E - \omega_r L}, \tag{A.4a}$$

$$\sin \psi = \frac{\omega_\theta E - L}{\sqrt{K \Delta_\theta}}. \tag{A.4b}$$

The interior versus exterior region also differs in how the Mollweide projection of the observer's sky is defined, with reference to Figs. 2.6 and 2.7. In the exterior region outside the event horizon, it is natural to choose the $-x^1$ direction ($\chi = 180°$) for the center of the projection, since it corresponds to the direction toward the center of the black hole. However, in the interior region, it is more natural to choose the $-x^3$ direction ($\chi = 90°$, $\psi = 270°$) for the center of the projection, so that the black hole's shadow occupies the lower half of the field of view and the sky occupies the upper half, so as to coincide with the general notion of "uprightness" as perceived on Earth.

In terms of the Mollweide projection's latitude $\varphi \in [-\frac{\pi}{2}, \frac{\pi}{2}]$ and longitude $\lambda \in [-\pi, \pi)$ for

Figs. 2.6 and 2.7, defined by

$$\varphi = \sin^{-1}\left(\frac{2}{\pi}\left(y\sqrt{1-y^2} + \sin^{-1}y\right)\right), \tag{A.5a}$$

$$\lambda = \frac{\pi}{2}\frac{x}{\sqrt{1-y^2}}, \tag{A.5b}$$

where $x \in [-2, 2]$ and $y \in [-1, 1]$, the viewing angles in the Kerr exterior are given by

$$\tan\chi = \frac{\sqrt{\sin^2\varphi + \cos^2\varphi\sin^2\lambda}}{-\cos\varphi\cos\lambda}, \tag{A.6a}$$

$$\tan\psi = \frac{\tan\varphi}{\sin\lambda}, \tag{A.6b}$$

and the viewing angles in the Kerr interior are given by

$$\chi = \frac{\pi}{2} - \varphi, \tag{A.7a}$$

$$\psi = \left(\frac{3\pi}{2} - \lambda\right)\mathrm{mod}\,2\pi. \tag{A.7b}$$

For reference, Fig. A.2 shows the $\chi - \psi$ coordinate grid for both the interior and exterior Mollweide projection views of Figs. 2.6 and 2.7.

(a)   (b)

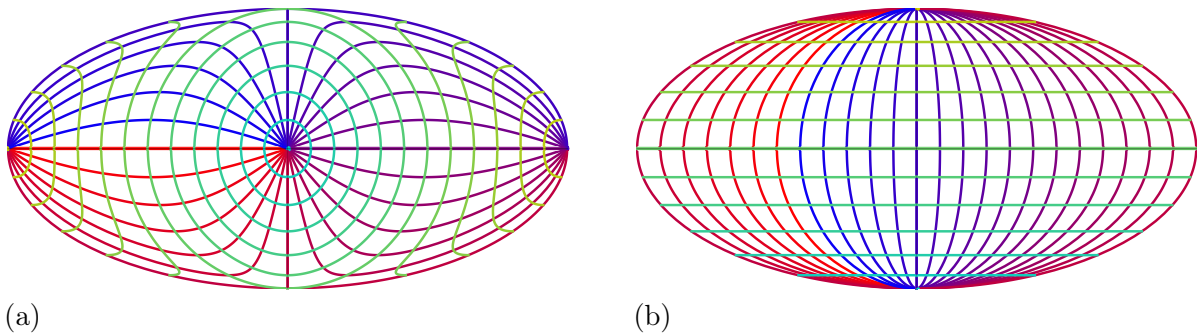Figure A.2: Coordinate grid of the viewing angles χ and ψ on a Mollweide projection of the full field of view of an exterior (a) and interior (b) Carter observer. Lines of constant ψ are equally spaced at $15°$ intervals from $\psi = 0°$ (red) to $\psi = 360°$ (blue), and lines of constant χ are equally spaced at $15°$ intervals from $\chi = 0°$ (yellow) to $\chi = 180°$ (cyan).

Appendix B

Backscattering coefficients via confluent Heun functions

In this Appendix we outline the methodology to compute the backscattering coefficients used in Sec. 4.5.1 to find the graybody factors associated with the Reissner-Nordström Hawking spectrum at infinity, the event horizon, and the inner horizon. Eqs. (4.122)–(4.124) provide the boundary conditions for the observer's backscattered mode functions in terms of the reflection coefficients $\mathcal{R}^{\pm}_{\mathrm{int,ext}}$ and transmission coefficients $\mathcal{T}^{\pm}_{\mathrm{int,ext}}$, where the subscript labels whether the scattering occurs in the black hole's interior ("int") or exterior ("ext"), and the superscript labels whether the modes are outgoing $(+)$ or ingoing $(-)$ prior to backpropagation, at the future null surface in the relevant spacetime sector. Conservation of the Wronskian dictates that these coefficients satisfy the following normalization conditions:

$$\left|\mathcal{T}^{\pm}_{\mathrm{int}}\right|^2 - \left|\mathcal{R}^{\pm}_{\mathrm{int}}\right|^2 = 1, \tag{B.1a}$$

$$\left|\mathcal{T}^{\pm}_{\mathrm{ext}}\right|^2 + \left|\mathcal{R}^{\pm}_{\mathrm{ext}}\right|^2 = 1, \tag{B.1b}$$

which will provide a check to ensure the accuracy of the numerical scheme. The negative sign associated with $\mathcal{R}^{\pm}_{\mathrm{int}}$ in Eq. (B.1a) is due to the fact that the corresponding substates have a negative norm; the scattering potential inside the black hole allows for the existence of both the observer's original modes $\exp(-i\omega r^*)$ (positive frequency with respect to the timelike coordinate r^*) and the anomalous modes $\exp(+i\omega r^*)$.

The backscattering coefficients can be calculated either by implementing an implicit numerical

ODE method to solve the Klein-Gordon wave Eq. (4.114), or by matching analytic solutions to that equation. Here we will explore the latter option.

Instead of the mode separation of Eq. (4.113), the Klein-Gordon scalar field can be separated as

$$\phi_{\omega\ell m} = \frac{R_{\omega\ell}(r) \; \mathrm{e}^{\pm i\omega t} \; Y_{\ell m}(\theta,\varphi)}{\sqrt{4\pi\omega}}, \tag{B.2}$$

with the upper (+) sign in the exponential for the outgoing modes observed at the right leg of the inner horizon (which can be written as $^{\mathrm{int}}R_{\mathrm{ob}}^{+}$) and the lower (−) sign for both the ingoing modes observed at the left leg of the inner horizon ($^{\mathrm{int}}R_{\mathrm{ob}}^{-}$) as well as the outgoing modes observed at future null infinity ($^{\mathrm{ext}}R_{\mathrm{ob}}^{+}$). In terms of the modes of Eq. (4.114), $R_{\omega\ell}$ and $f_{\omega\ell}$ are related by

$$f_{\omega\ell}(t,r) = r R_{\omega\ell}(r) \; \mathrm{e}^{\pm i\omega t}. \tag{B.3}$$

The Klein-Gordon wave equation for the spatial modes $R_{\omega\ell}$, or equivalently, the wave Eq. (4.114) for $f_{\omega\ell}$, contains three singular points throughout the spacetime, which occur whenever $r^{*} \to \pm\infty$. Two of these are the regular singularities located at the inner and outer horizons, and the third is an irregular, rank-1 singularity at spatial infinity. This structure suggests that the wave equation can be cast into confluent Heun form: first, apply a Möbius transformation to define the new coordinate

$$z \equiv \frac{r - r_{-}}{r_{+} - r_{-}} \tag{B.4}$$

so that the singular points are shifted from $r = (r_{-}, r_{+}, \infty)$ to $z = (0, 1, \infty)$. Then, apply a gauge transformation to the field variable that keeps the singular points fixed (such a shift in the Frobenius solution indices is known as an F-homotopic transformation):

$$R(z) = z^{\frac{\gamma-1}{2}} |z - 1|^{\frac{\delta-1}{2}} \; \mathrm{e}^{\frac{\varepsilon}{2}z} \; Z(z), \tag{B.5}$$

so that the Klein-Gordon wave Eq. (3.11) reduces to:

$$\frac{d^2 Z}{dz^2} + \left(\frac{\gamma}{z} + \frac{\delta}{z-1} + \varepsilon \right) \frac{dZ}{dz} + \left(\frac{q}{z} + \frac{\alpha - q}{z-1} \right) Z = 0 \tag{B.6}$$

provided

$$q = \ell(\ell+1) + 2i\omega \frac{r_+ r_-}{r_+ - r_-} - 4\omega^2 r_-^2 + 4\omega^2 \left(\frac{r_+ r_-}{r_+ - r_-} \right)^2, \tag{B.7a}$$

$$\alpha = -2i\omega(r_+ - r_-) - 4\omega^2 r_-^2, \tag{B.7b}$$

$$\gamma = 1 - 2i\omega \frac{r_-^2}{r_+ - r_-}, \tag{B.7c}$$

$$\delta = 1 - 2i\omega \frac{r_+^2}{r_+ - r_-}, \tag{B.7d}$$

$$\varepsilon = -2i\omega(r_+ - r_-). \tag{B.7e}$$

For the more general Kerr-Newman case, the corresponding version of these parameters can be inferred from, e.g. Ref. [174]. Also, note that the signs of the three exponents in Eq. (B.5) can be either positive or negative, corresponding either to outgoing or ingoing waves at each of the singular points. Regardless of this gauge choice, both ingoing and outgoing modes will always be recovered by the choice of linear combinations of modes for $Z(z)$.

Two linearly independent solutions to Eq. (B.6) that are regular at the inner horizon are given via confluent Heun functions for the equation's allowed F-homotopic automorphisms:

$$Z_{(0)}(z) = A_{(0)} Z_{(0)}^A(z) + B_{(0)} Z_{(0)}^B(z), \tag{B.8a}$$

$$Z_{(0)}^A(z) = \text{HeunC} \left(q, \alpha, \gamma, \delta, \varepsilon; z \right), \tag{B.8b}$$

$$Z_{(0)}^B(z) = z^{1-\gamma} \text{HeunC} \left(q', \alpha', 2 - \gamma, \delta, \varepsilon; z \right), \tag{B.8c}$$

with arbitrary complex coefficients $A_{(0)}$ and $B_{(0)}$, with the definitions

$$q' = q - (\delta - \varepsilon)(1 - \gamma), \tag{B.9a}$$

$$\alpha' = \alpha + \varepsilon(1 - \gamma), \tag{B.9b}$$

and with the functions' argument structure following the convention used in `Mathematica`, which has newly implemented Heun functions in version 12.1. These negative- and positive-frequency solutions can be computed with a forwardly stable set of power series that are convergent everywhere except at the singular points $z = 1, \infty$ and are linearly independent except when $\gamma = 1$, in which case the factor $z^{1-\gamma}$ can be replaced with $\ln(z)$.

As a reminder, the goal here is to compute the values of the reflection and transmission coefficients $\mathcal{R}^{\pm}_{\text{int,ext}}$ and $\mathcal{T}^{\pm}_{\text{int,ext}}$, which can be used to calculate the observed spectra of Eq. (4.147). These coefficients are tied to the asymptotic forms of the field modes given in Eqs. (4.122)–(4.124), which in the present notation take the form

$$^{\text{ext}}R^{+}_{\text{ob}}(z) \to \begin{cases} \frac{e^{i\omega r_-}}{r_+ - r_-} e^{i\omega(r_+ - r_-)z} |z|^{2i\omega - 1} + \mathcal{R}^{+}_{\text{ext}} \frac{e^{-i\omega r_-}}{r_+ - r_-} e^{-i\omega(r_+ - r_-)z} |z|^{-2i\omega - 1}, & z \to \infty \\[2mm] \mathcal{T}^{+}_{\text{ext}} \frac{e^{i\omega r_+}}{r_+} |z - 1|^{i\omega \frac{r_+^2}{r_+ - r_-}}, & z \to 1 \\[2mm] 0, & z \to 0 \end{cases}, \tag{B.10a}$$

$$^{\text{int}}R^{+}_{\text{ob}}(z) \to \begin{cases} \mathcal{R}^{+}_{\text{int}} \mathcal{T}^{-}_{\text{ext}} \frac{e^{i\omega r_-}}{r_+ - r_-} e^{i\omega(r_+ - r_-)z} |z|^{2i\omega - 1}, & z \to \infty \\[2mm] \mathcal{R}^{+}_{\text{int}} \frac{e^{i\omega r_+}}{r_+} |z - 1|^{i\omega \frac{r_+^2}{r_+ - r_-}} + (\mathcal{T}^{+}_{\text{int}} + \mathcal{R}^{+}_{\text{int}} \mathcal{R}^{-}_{\text{ext}}) \frac{e^{-i\omega r_+}}{r_+} |z - 1|^{-i\omega \frac{r_+^2}{r_+ - r_-}}, & z \to 1 \\[2mm] \frac{e^{-i\omega r_-}}{r_-} |z|^{i\omega \frac{r_-^2}{r_+ - r_-}}, & z \to 0 \end{cases}, \tag{B.10b}$$

$$^{\text{int}}R^{-}_{\text{ob}}(z) \to \begin{cases} \mathcal{T}^{-}_{\text{int}} \mathcal{T}^{-}_{\text{ext}} \frac{e^{-i\omega r_-}}{r_+ - r_-} e^{-i\omega(r_+ - r_-)z} |z|^{-2i\omega - 1}, & z \to \infty \\[2mm] \mathcal{T}^{-}_{\text{int}} \frac{e^{-i\omega r_+}}{r_+} |z - 1|^{-i\omega \frac{r_+^2}{r_+ - r_-}} + (\mathcal{R}^{-}_{\text{int}} + \mathcal{T}^{-}_{\text{int}} \mathcal{R}^{-}_{\text{ext}}) \frac{e^{i\omega r_+}}{r_+} |z - 1|^{i\omega \frac{r_+^2}{r_+ - r_-}}, & z \to 1 \\[2mm] \frac{e^{-i\omega r_-}}{r_-} |z|^{i\omega \frac{r_-^2}{r_+ - r_-}}, & z \to 0 \end{cases}. \tag{B.10c}$$

Here the integration constant for the tortoise coordinate r^* of Eq. (4.5) is chosen so that

$$r^* = r + \frac{r_+^2}{r_+ - r_-} \ln|z - 1| - \frac{r_-^2}{r_+ - r_-} \ln|z|. \tag{B.11}$$

Asymptotically, the modes of Eq. (B.8) at the inner horizon ($z = 0$) reduce to

$$R(z) \to A_{(0)} z^{-\frac{1-\gamma}{2}} + B_{(0)} z^{\frac{1-\gamma}{2}}, \qquad z \to 0, \tag{B.12}$$

since the confluent Heun functions are normalized to unity when the independent variable equals zero, provided γ is not a nonpositive integer. This asymptotic form can then be matched to the modes of Eq. (B.10) to find expressions for $A_{(0)}$ and $B_{(0)}$. One obtains $A_{(0)} = 0$ for all three sets of modes in Eq. (B.10), since by definition the inner horizon observer only sees positive frequency waves there. For the interior observer modes $^{\text{int}}R_{\text{ob}}^{\pm}(z)$, $B_{(0)} = \exp(-i\omega r_-)/r_-$, while the exterior observer modes $^{\text{ext}}R_{\text{ob}}^{+}(z)$ are only defined for $z \geq 1$ and must be treated separately.

Unfortunately, analytic asymptotic forms for the modes of Eq. (B.8) are not known at the spacetime's two other singular points. An explicit solution to the central two-point connection problem for confluent Heun functions is still outstanding and is directly related to the inverse of Hilbert's 21st problem; currently, analytic forms of the monodromy matrices have only been found for the reduced confluent Heun equation with $\varepsilon = 0$ [101].

Thus, we proceed by defining a new set of local Heun modes at each singular point and numerically matching their coefficients via the algorithm set forth in Ref. [133].

At the event horizon ($z = 1$), a set of regular, linearly independent solutions to Eq. (B.6) that are convergent everywhere except at the singular points $z = 0, \infty$ can be written as:

$$Z_{(1)}(z) = A_{(1)} Z_{(1)}^A(z) + B_{(1)} Z_{(1)}^B(z), \tag{B.13a}$$

$$Z_{(1)}^A(z) = \text{HeunC}\left(q - \alpha, -\alpha, \delta, \gamma, -\varepsilon; 1 - z\right), \tag{B.13b}$$

$$Z_{(1)}^B(z) = (1 - z)^{1-\delta} \text{HeunC}\left(q' - \alpha', -\alpha', 2 - \delta, \gamma, -\varepsilon; 1 - z\right), \tag{B.13c}$$

with arbitrary complex coefficients $A_{(1)}$ and $B_{(1)}$, and with the definitions

$$q' = q - \gamma(1 - \delta), \tag{B.14a}$$

$$\alpha' = \alpha + \varepsilon(1 - \delta). \tag{B.14b}$$

Asymptotically, the modes of Eq. (B.13) at the event horizon ($z = 1$) reduce to

$$R(z) \to e^{\frac{\varepsilon}{2}} |z - 1|^{-\frac{1-\delta}{2}} \left(A_{(1)} + B_{(1)}(1 - z)^{1-\delta} \right), \tag{B.15}$$

which leads to the matching

$$^{\mathrm{ext}}A_{(1)}^+ = 0,$$
$$^{\mathrm{ext}}B_{(1)}^+ = \mathcal{T}_{\mathrm{ext}}^+ \frac{e^{i\omega(2r_+ - r_-)}}{r_+}; \tag{B.16a}$$

$$^{\mathrm{int}}A_{(1)}^+ = \left(\mathcal{T}_{\mathrm{int}}^+ + \mathcal{R}_{\mathrm{int}}^+ \mathcal{R}_{\mathrm{ext}}^- \right) \frac{e^{-i\omega r_-}}{r_+},$$
$$^{\mathrm{int}}B_{(1)}^+ = \mathcal{R}_{\mathrm{int}}^+ \frac{e^{i\omega(2r_+ - r_-)}}{r_+}; \tag{B.16b}$$

$$^{\mathrm{int}}A_{(1)}^- = \mathcal{T}_{\mathrm{int}}^- \frac{e^{-i\omega r_-}}{r_+},$$
$$^{\mathrm{int}}B_{(1)}^- = \left(\mathcal{R}_{\mathrm{int}}^- + \mathcal{T}_{\mathrm{int}}^- \mathcal{R}_{\mathrm{ext}}^- \right) \frac{e^{i\omega(2r_+ - r_-)}}{r_+}; \tag{B.16c}$$

for each respective set of modes; i.e., the coefficients from Eq. (B.13) for $^{\mathrm{ext,int}}R_{\mathrm{ob}}^{\pm}$ are labeled $^{\mathrm{ext,int}}A_{(1)}^{\pm}$ and $^{\mathrm{ext,int}}B_{(1)}^{\pm}$. Eqs. (B.16) are strictly only valid for $z < 1$; for the exterior ($z > 1$), an additional factor of $\exp[2\pi\omega r_+^2/(r_+ - r_-)]$ must be included in the right-hand side of the equations for each of the B coefficients to account for the lack of absolute values in the trailing factor of Eq. (B.15).

At some point z_* in the interior (we take $z_* = 0.5$ for simplicity), both Eqs. (B.8) and (B.13) provide regular solutions to the wave Eq. (B.6). One can convert between them with the respective

linear systems

$$Z_{(1)}^{A,B}(z_*) = C_A^{A,B} Z_{(0)}^A(z_*) + C_B^{A,B} Z_{(0)}^B(z_*), \tag{B.17a}$$

$$(Z_{(1)}^{A,B})'(z)\big|_{z_*} = C_A^{A,B}(Z_{(0)}^A)'(z)\big|_{z_*} + C_B^{A,B}(Z_{(0)}^B)'(z)\big|_{z_*}. \tag{B.17b}$$

The functions $Z_{(0)}^A(z_*)$, $Z_{(0)}^B(z_*)$, $Z_{(1)}^A(z_*)$ and $Z_{(1)}^B(z_*)$ can be computed numerically, and therefore the constants C_A^A, C_A^B, C_B^A, and C_B^B can also be computed. Once these constants are known, the total eigenmodes $Z_{(0)}(z)$ and $Z_{(1)}(z)$ can be matched to solve for each of the backscattering coefficients:

$$A_{(0)} = A_{(1)} C_A^A + B_{(1)} C_A^B, \tag{B.18a}$$

$$B_{(0)} = A_{(1)} C_B^A + B_{(1)} C_B^B. \tag{B.18b}$$

Once the backscattering coefficients connecting $z = 0$ to $z = 1$ are known, a similar process will yield the coefficients connecting $z = 1$ to $z = \infty$. As z approaches infinity, the confluent Heun solutions to Eq. (B.6) asymptotically (in a sector) take the form

$$Z_{(\infty)}(z) = A_{(\infty)} Z_{(\infty)}^A(z) + B_{(\infty)} Z_{(\infty)}^B(z), \tag{B.19a}$$

$$Z_{(\infty)}^A(z) = z^{-\frac{\alpha}{\varepsilon}}, \tag{B.19b}$$

$$Z_{(\infty)}^B(z) = \mathrm{e}^{-\varepsilon z} z^{\frac{\alpha}{\varepsilon} - \gamma - \delta}, \tag{B.19c}$$

with arbitrary complex coefficients $A_{(\infty)}$ and $B_{(\infty)}$. Comparison with the asymptotic forms of Eq. (B.10) reveals the following matched values for these coefficients:

$$^{\text{ext}}A_{(\infty)}^+ = \mathcal{R}_{\text{ext}}^+ \frac{\mathrm{e}^{-i\omega r_-}}{r_+ - r_-},$$

$$^{\text{ext}}B_{(\infty)}^+ = \frac{\mathrm{e}^{i\omega r_-}}{r_+ - r_-}; \tag{B.20a}$$

$$^{\text{int}}A_{(\infty)}^+ = 0,$$

$$^{\text{int}}B_{(\infty)}^+ = \mathcal{R}_{\text{int}}^+ \mathcal{T}_{\text{ext}}^- \frac{\mathrm{e}^{i\omega r_-}}{r_+ - r_-}; \tag{B.20b}$$

$$^{\text{int}}A^-_{(\infty)} = \mathcal{T}^-_{\text{int}}\mathcal{T}^-_{\text{ext}}\frac{\mathrm{e}^{-i\omega r_-}}{r_+ - r_-},$$

$$^{\text{int}}B^-_{(\infty)} = 0, \tag{B.20c}$$

where the coefficient notation is the same as in Eq. (B.16).

For some sufficiently large radial coordinate $z = z^*$ (heuristically found to be $z^* = 18/(\omega\sqrt{1-Q^2})$ is more than sufficient to ensure convergence at machine-level precision), both Eqs. (B.13) and (B.19) satisfy the wave Eq. (B.6), and so the two sets of solutions can be matched. One has the system

$$Z^{A,B}_{(1)}(z^*) = D^{A,B}_A Z^A_{(\infty)}(z^*) + D^{A,B}_B Z^B_{(\infty)}(z^*), \tag{B.21a}$$

$$\left.(Z^{A,B}_{(1)})'(z)\right|_{z^*} = D^{A,B}_A \left.(Z^A_{(\infty)})'(z)\right|_{z^*} + D^{A,B}_B \left.(Z^B_{(\infty)})'(z)\right|_{z^*} \tag{B.21b}$$

to solve for the constants D^A_A, D^B_A, D^A_B, and D^B_B, which can then be used to solve for the backscattering coefficients with the system

$$A_{(\infty)} = A_{(1)}D^A_A + B_{(1)}D^B_A, \tag{B.22a}$$

$$B_{(\infty)} = A_{(1)}D^A_B + B_{(1)}D^B_B. \tag{B.22b}$$

Altogether, the relevant backscattering coefficients can be written as follows (note that multiple variations to the below equations are possible based on implicit relations between and among the C and D coefficients):

$$\mathcal{T}^+_{\text{ext}} = \frac{r_+}{r_+ - r_-}\frac{1}{D^B_B}\,\mathrm{e}^{-2i\omega(r_+-r_-)-\pi\omega/\kappa_+}, \tag{B.23a}$$

$$\mathcal{T}^-_{\text{ext}} = \frac{r_+ - r_-}{r_+}\frac{\widetilde{D}}{D^B_B}, \tag{B.23b}$$

$$\mathcal{R}^+_{\text{ext}} = \frac{D^B_A}{D^B_B}\,\mathrm{e}^{2i\omega r_-}, \tag{B.23c}$$

$$\mathcal{R}^-_{\text{ext}} = -\frac{D^A_B}{D^B_B}\,\mathrm{e}^{-2i\omega r_+ - \pi\omega/\kappa_+}, \tag{B.23d}$$

$$\mathcal{T}_{\text{int}}^+ = -\frac{r_+}{r_-} \frac{C_A^B D_B^B - C_A^A D_B^A \; \mathrm{e}^{-4i\omega r_+ - \pi\omega/\kappa_+}}{\widetilde{C} D_B^B}, \tag{B.23e}$$

$$\mathcal{T}_{\text{int}}^- = -\frac{r_+}{r_-} \frac{C_A^B}{\widetilde{C}}, \tag{B.23f}$$

$$\mathcal{R}_{\text{int}}^+ = \frac{r_+}{r_-} \frac{C_A^A}{\widetilde{C}} \; \mathrm{e}^{-2i\omega r_+}, \tag{B.23g}$$

$$\mathcal{R}_{\text{int}}^- = \frac{r_+}{r_-} \frac{C_A^A D_B^B - C_A^B D_B^A}{\widetilde{C} D_B^B} \; \mathrm{e}^{-2i\omega r_+}, \tag{B.23h}$$

where

$$\widetilde{C} \equiv C_A^A C_B^B - C_A^B C_B^A, \tag{B.24}$$

$$\widetilde{D} \equiv D_A^A D_B^B - D_A^B D_B^A. \tag{B.25}$$

The resulting numerical values of the backscattering coefficients are used to calculate the Hawking spectra of Fig. (4.14).

Appendix C

Evaluation of Bogoliubov coefficient scalar products

In this Appendix, details are given for the calculation of the inner products of Eqs. (4.115) and (3.21) leading to the number operators of Eqs. (4.147). Focus will be placed on the scalar (spin-0) case, though the final result holds true for any integer-spin modes.

For the scalar product along past null infinity ($\mathscr{I}^-$), where the ingoing Eddington-Finkelstein coordinate v runs from $-\infty$ to ∞, one may choose

$$d\Sigma\, n^\mu \sqrt{-g_\Sigma}\, \partial_\mu = dv\, d(\cos\theta) d\varphi R^2 \partial_v, \tag{C.1}$$

while for the scalar product along the past horizon ($\mathcal{H}_{\text{past}} = \mathcal{H}_{\text{past}}^{\text{ext}} \cup \mathcal{H}_{\text{past}}^{\text{int}}$), where the outgoing Kruskal-Szekeres coordinate U runs from $-\infty$ to 0 in the interior and from 0 to ∞ in the exterior, one has

$$d\Sigma\, n^\mu \sqrt{-g_\Sigma}\, \partial_\mu = dU\, d(\cos\theta) d\varphi_+ R_+^2 \partial_U. \tag{C.2}$$

The modes to be evaluated along these null hypersurfaces are those of the emitter:

$$\phi_{\text{em}} \to \begin{cases} \dfrac{e^{i\bar{m}\varphi} S_{\bar{\ell}\bar{m}}^{\bar{\omega}}(\theta)}{\sqrt{4\pi\bar{\omega}}R}\, e^{-i\bar{\omega}v}, & \mathscr{I}^- \\[3mm] \dfrac{e^{i\bar{m}\varphi_+} S_{\bar{\ell}\bar{m}}^{\bar{\omega}}(\theta)}{\sqrt{4\pi\bar{\omega}}R_+}\, e^{-i\bar{\omega}U}, & \mathcal{H}_{\text{past}} \end{cases}, \tag{C.3}$$

and those of one of four classes of observers, initialized either at infinity, at the event horizon, or at

the left or right leg of the inner horizon:

$$
\phi_{\text{ob}} \rightarrow
\begin{cases}
\hat{\mathcal{S}}_v \dfrac{\mathrm{e}^{\pm im\varphi} S_{\ell m}^{\omega}(\theta)}{\sqrt{4\pi\omega}R} \, \mathrm{e}^{\mp i\hat{\omega}v}, & \mathscr{I}^- \\[4mm]
\hat{\mathcal{S}}_{u_{\text{ext}}} \dfrac{\mathrm{e}^{\pm im\varphi_+} S_{\ell m}^{\omega}(\theta)}{\sqrt{4\pi\omega}R_+} \, \mathrm{e}^{\mp i(\hat{\omega}-m\Omega_+)u}, & \mathcal{H}_{\text{past}}^{\text{ext}}, \\[4mm]
\hat{\mathcal{S}}_{u_{\text{int}}} \dfrac{\mathrm{e}^{\pm im\varphi_+} S_{\ell m}^{\omega}(\theta)}{\sqrt{4\pi\omega}R_+} \, \mathrm{e}^{\mp i(\hat{\omega}-m\Omega_+)u}, & \mathcal{H}_{\text{past}}^{\text{int}}
\end{cases}
\tag{C.4}
$$

where the upper sign corresponds to the observer modes ${}^{\text{ext}}\phi_{\text{ob}}^+$, ${}^{\text{ext}}\phi_{\text{ob}}^-$, and ${}^{\text{int}}\phi_{\text{ob}}^-$, the lower sign corresponds to the observer modes ${}^{\text{int}}\phi_{\text{ob}}^+$, and where quantities with hats also take on different forms for each family of observers:

$$
\begin{aligned}
{}^{\text{ext}}\phi_{\text{ob},\omega}^+ : \quad & \hat{\omega} = \omega, & \hat{\mathcal{S}}_v &= \mathcal{R}_{\text{ext},\omega}^+, & \hat{\mathcal{S}}_{u_{\text{ext}}} &= \mathcal{T}_{\text{ext},\omega}^+, & \hat{\mathcal{S}}_{u_{\text{int}}} &= 0, \\[2mm]
{}^{\text{ext}}\phi_{\text{ob},\omega}^- : \quad & \hat{\omega} = \omega + m\Omega_+, & \hat{\mathcal{S}}_v &= \mathcal{T}_{\text{ext},\omega}^-, & \hat{\mathcal{S}}_{u_{\text{ext}}} &= \mathcal{R}_{\text{ext},\omega}^-, & \hat{\mathcal{S}}_{u_{\text{int}}} &= 0, \\[2mm]
{}^{\text{int}}\phi_{\text{ob},\omega}^- : \quad & \hat{\omega} = \omega + m\Omega_-, & \hat{\mathcal{S}}_v &= \mathcal{T}_{\text{int},\omega}^- \mathcal{T}_{\text{ext},\omega}^-, & \hat{\mathcal{S}}_{u_{\text{ext}}} &= \mathcal{T}_{\text{int},\omega}^- \mathcal{R}_{\text{ext},\omega}^-, & \hat{\mathcal{S}}_{u_{\text{int}}} &= \mathcal{R}_{\text{int},\omega}^-, \\[2mm]
{}^{\text{int}}\phi_{\text{ob},\omega}^+ : \quad & \hat{\omega} = \omega + m\Omega_-, & \hat{\mathcal{S}}_v &= \mathcal{R}_{\text{int},\omega}^+ \mathcal{T}_{\text{ext},\omega}^-, & \hat{\mathcal{S}}_{u_{\text{ext}}} &= \mathcal{R}_{\text{int},\omega}^+ \mathcal{R}_{\text{ext},\omega}^-, & \hat{\mathcal{S}}_{u_{\text{int}}} &= \mathcal{T}_{\text{int},\omega}^+.
\end{aligned}
\tag{C.5}
$$

Due to the orthogonality of the spheroidal harmonics, the angular pieces can be integrated out to yield Kronecker δ functions between the observer's and emitter's mode numbers ℓ and m. Then one has (where the $\pm$ sign is once again defined as above)

$$
\begin{aligned}
\langle \phi_{\text{em}} | \hat{\phi}_{\text{ob}}^* \rangle = \frac{\delta_{\bar{\ell}\ell} \delta_{(\pm\bar{m})m}}{4\pi i \sqrt{\omega\bar{\omega}}} \Bigg(& \hat{\mathcal{S}}_v \int_{-\infty}^{\infty} dv \, \mathrm{e}^{-i\bar{\omega}v} \overleftrightarrow{\partial}_v \mathrm{e}^{\mp i\hat{\omega}v} \\
& + \hat{\mathcal{S}}_{u_{\text{ext}}} \int_{-\infty}^{0} dU \, \mathrm{e}^{-i\bar{\omega}U} \overleftrightarrow{\partial}_U \mathrm{e}^{\mp i(\hat{\omega}-m\Omega_+)u} \\
& + \hat{\mathcal{S}}_{u_{\text{int}}} \int_{0}^{\infty} dU \, \mathrm{e}^{-i\bar{\omega}U} \overleftrightarrow{\partial}_U \mathrm{e}^{\mp i(\hat{\omega}-m\Omega_+)u} \Bigg).
\end{aligned}
\tag{C.6}
$$

In evaluating the bidirectional derivative defined by $\psi \overleftrightarrow{\partial}_{\mu} \phi \equiv \psi \partial_{\mu} \phi - \phi \partial_{\mu} \psi$, the terms in the second and third lines of Eq. (C.6) that have the form $\partial_U \mathrm{e}^{\mp i(\hat{\omega}-m\Omega_+)u}$ can be simplified through integration

by parts, yielding a surface term that can be safely discarded:

$$
\begin{aligned}
\langle \phi_{\text{em}} | \hat{\phi}_{\text{ob}}^{*} \rangle = \frac{\delta_{\bar{\ell}\ell}\delta_{(\pm\bar{m})m}}{4\pi\sqrt{\omega\bar{\omega}}} \bigg((\bar{\omega} \mp \hat{\omega})\hat{\mathcal{S}}_{v} \int_{-\infty}^{\infty} dv \ e^{-i(\bar{\omega}\pm\hat{\omega})v} \\
+ 2\bar{\omega}\hat{\mathcal{S}}_{u_{\text{ext}}} \int_{-\infty}^{0} dU \ e^{-i(\bar{\omega}U\pm(\hat{\omega}-m\Omega_{+})u)} \\
+ 2\bar{\omega}\hat{\mathcal{S}}_{u_{\text{int}}} \int_{0}^{\infty} dU \ e^{-i(\bar{\omega}U\pm(\hat{\omega}-m\Omega_{+})u)} \bigg).
\end{aligned}
\tag{C.7}
$$

The observed number operator $\langle \hat{N} \rangle_{\omega\ell m}$ can now be evaluated via Eq. (4.115) by taking the square of the complex conjugate of Eq. (C.7) and summing over all emitter modes. The integral in the first line of Eq. (C.7) reduces to a Dirac δ function that either vanishes (upper sign) or leaves a small additive factor (lower sign)—these values can be ascertained by noting that the emitter's modes ϕ_{em} are normalized along past null infinity as

$$
\begin{aligned}
\langle \phi_{\text{em}}^{\omega\ell m} | \phi_{\text{em}}^{\bar{\omega}\bar{\ell}\bar{m}} \rangle = -\langle \phi_{\text{em}}^{\omega\ell m *} | \phi_{\text{em}}^{\bar{\omega}\bar{\ell}\bar{m} *} \rangle = \delta(\omega - \bar{\omega})\delta_{\ell\bar{\ell}}\delta_{m\bar{m}}, \\
\langle \phi_{\text{em}}^{\omega\ell m} | \phi_{\text{em}}^{\bar{\omega}\bar{\ell}\bar{m} *} \rangle = 0.
\end{aligned}
\tag{C.8}
$$

The integrals in the second and third lines of Eq. (C.7), on the other hand, are the origin of the Planckian distribution. Using the definition of U from Eq. (4.16), these can be evaluated in terms of Γ functions [20]. The resulting number operator can then be found after taking the modulus squared:

$$
\langle \hat{N} \rangle_{\omega\ell\{\pm m\}} = \frac{1}{4\pi^{2}\omega} \int_{0}^{\infty} d\bar{\omega} \ \bar{\omega} \left| \left\{ \begin{matrix} 0 \\ 2\pi\hat{\mathcal{S}}_{v}\delta(\bar{\omega} - \hat{\omega}) \end{matrix} \right\} + \left(\hat{\mathcal{S}}_{u_{\text{ext}}} + (-1)^{-z}\hat{\mathcal{S}}_{u_{\text{int}}} \right) \Gamma(z)(-i\bar{\omega})^{-z}\kappa_{+}^{z-1} \right|^{2},
\tag{C.9}
$$

where we have defined the quantity

$$
z \equiv 1 \pm \frac{i(\hat{\omega} - m\Omega_{+})}{\kappa_{+}}.
\tag{C.10}
$$

The squared modulus of Eq. (C.9) can be simplified by the property

$$|\Gamma(1+bi)|^2 = \frac{\pi b}{\sinh(\pi b)}. \tag{C.11}$$

First, consider the upper sign of Eq. (C.9), corresponding to the observer modes $^{\text{ext}}\phi_{\text{ob}}^+$, $^{\text{ext}}\phi_{\text{ob}}^-$, and $^{\text{int}}\phi_{\text{ob}}^-$ (i.e., all modes except those originating from an outgoing observer at the inner horizon, who has $\exp(i\omega t)$ instead of $\exp(-i\omega t)$). Then, assuming the frequencies $\hat{\omega}$ and $\bar{\omega}$ are strictly positive, the first term in the integrand of Eq. (C.9) will vanish, and the observed number operator will simplify to

$$\langle \hat{N} \rangle_{\omega\ell m} = \frac{\hat{\omega} - m\Omega_+}{\omega} \frac{\left| \hat{\mathcal{S}}_{u_{\text{ext}}} - e^{\frac{\pi}{\kappa_+}(\hat{\omega} - m\Omega_+)} \hat{\mathcal{S}}_{u_{\text{int}}} \right|^2}{e^{\frac{2\pi}{\kappa_+}(\hat{\omega} - m\Omega_+)} - 1} \int_0^\infty \frac{d\bar{\omega}}{2\pi \kappa_+ \bar{\omega}}. \tag{C.12}$$

The integral over the emitter's frequency modes in the second line of Eq. (C.12) diverges, but such behavior is not a problem and is actually to be expected. The divergence originates from the use of continuum-normalized plane waves to initialize the modes detected over an entire Cauchy hypersurface, which inevitably leads to an infinite amount of Hawking radiation reaching an observer throughout the infinite amount of time left in the future. If instead of plane waves, a more physically realistic choice is used to represent the observer's modes, such as a finite wave packet distribution, then the resulting integral will be regularized and the integral in Eq. (C.12) will reduce to unity [61]. In particular, one may model the observer as a particle detector sensitive only to frequencies within a small ϵ of $\omega \sim j\epsilon \sim (j+1)\epsilon$, which is turned on at a time $u = 2\pi n/\epsilon$ for a duration $2\pi/\epsilon$ (for integers j and n). Then the observer's modes will appear as

$$\phi_{\text{ob}}^{\text{reg}} = \frac{1}{\sqrt{\epsilon}} \int_{j\epsilon}^{(j+1)\epsilon} d\omega \, e^{2\pi i \omega n/\epsilon} \phi_{\text{ob}}. \tag{C.13}$$

At late times (large n), the above expression will yield exactly the first line of Eq. (C.12), with the remaining terms on the second line reducing to unity. This expression for the expectation value of the number operator $\langle \hat{N} \rangle_{\omega\ell m}$ reproduces Eqs. (4.147a)–(4.147c) after substituting the respective observer quantities from Eqs. (C.5).

Finally, consider the lower sign of Eq. (C.9), corresponding to the observer modes $^{\text{int}}\phi_{\text{ob}}^{+}$. As in the previous case, it will be helpful to consider a wave-packet version of the observer's modes, since the integral over the complex square modulus of a Dirac delta distribution must be regularized in some meaningful way.

For the portion of the observer's modes along past null infinity, performing the integral of Eq. (C.13) gives

$$\phi_{\text{ob}}^{\text{reg}} \propto \hat{\mathcal{S}}_{v} \frac{\sqrt{\epsilon}}{\frac{v\epsilon}{2} + n\pi} \; e^{i \frac{v\epsilon}{2}(2j-1)} \sin\left(\frac{v\epsilon}{2}\right). \tag{C.14}$$

The Fourier transform of these modes over the emitter's frequency yields the inner product

$$\langle \phi_{\text{em}} | \hat{\phi}_{\text{ob}}^{\text{reg}*} \rangle_{\mathscr{I}^{-}} = \delta_{\bar{\ell}\ell} \delta_{(-\bar{m})m} \hat{\mathcal{S}}_{v} \sqrt{\frac{\bar{\omega}}{\omega}} \frac{e^{2\pi i \bar{\omega} n / \epsilon}}{\sqrt{\epsilon}} \tag{C.15}$$

in the frequency range $(j-1)\epsilon < \bar{\omega} < j\epsilon$, and 0 everywhere else. Once this quantity's complex modulus is squared and summed over the emitter's modes, a constant term will remain of the form

$$\frac{(2j-1)\epsilon}{2\omega} \hat{\mathcal{S}}_{v} \sim \frac{\hat{\omega}}{\omega} \hat{\mathcal{S}}_{v}, \tag{C.16}$$

since for small ϵ the quantity $j\epsilon$ is precisely the observer's frequency $\hat{\omega}$ back-propagated to past null infinity. Thus, the number operator of Eq. (4.115) for an outgoing observer at the inner horizon reduces to

$$\langle \hat{N} \rangle_{\omega\ell(-m)} = -\frac{\hat{\omega} - m\Omega_{+}}{\omega} \frac{\left| \hat{\mathcal{S}}_{u_{\text{ext}}} - e^{-\frac{\pi}{\kappa_{+}}(\hat{\omega} - m\Omega_{+})} \hat{\mathcal{S}}_{u_{\text{int}}} \right|^{2}}{e^{-\frac{2\pi}{\kappa_{+}}(\hat{\omega} - m\Omega_{+})} - 1} + \frac{\hat{\omega}}{\omega} \hat{\mathcal{S}}_{v}. \tag{C.17}$$

Note that in principle Eq. (C.17) will contain an additional cross term when the complex modulus of Eq. (C.9) is squared, which can be expressed in terms of incomplete gamma functions. However, in the late-time limit of large n, this term and its complex conjugate become negligibly small and thus are not included here.

The expression in Eq. (C.17) for the expectation value of the number operator $\langle \hat{N} \rangle_{\omega\ell m}$ reproduces Eq. (4.147d) after substituting the respective observer quantities from Eqs. (C.5).

Appendix D

Deriving the effective temperature as a rate of redshift

The starting point for calculating the effective temperature κ_{eff} (defined in Sec. 3.2) as the rate of redshift in some spacetime is to specify a metric $g_{\mu\nu}$ and a set of coordinates x^μ. If an observer follows along some geodesic parametrized by x^μ, then one can solve the geodesic equations to find the observer's 4-velocity, $u^\mu \equiv dx^\mu/d\tau$, in terms of the coordinates and the set of conserved quantities associated with each geodesic. Similarly, one can find the components of a photon's energy-momentum $k^\mu \equiv dx^\mu/d\lambda$ as it travels along a null geodesic in the spacetime.

The quantities u^μ and k^μ are defined in a coordinate basis, with vectors ∂_μ such that $\partial_\mu \cdot \partial_\nu = g_{\mu\nu}$, but to understand what the observer sees, it will be necessary to define a set of orthonormal vector fields to specify a reference frame. These vectors, known as tetrads and denoted $\gamma_{\hat{m}}$, satisfy the condition $\gamma_{\hat{m}} \cdot \gamma_{\hat{n}} = \eta_{\hat{m}\hat{n}}$ (i.e., the observer's reference frame is locally flat) and are related to the coordinate basis vectors e_μ via a transformation matrix $e^{\hat{m}}_{\ \mu}$ known as a vierbein. One can always construct a vierbein directly from the line element, through the identity

$$ds^2 = g_{\mu\nu}dx^\mu dx^\nu = \eta_{\hat{m}\hat{n}}e^{\hat{m}}_{\ \mu}e^{\hat{n}}_{\ \nu}dx^\mu dx^\nu. \tag{D.1}$$

In the simplest case that the metric is diagonal, the vierbein is simply a diagonal matrix with each element given by the square root of the corresponding metric component.

Here and following, *abstract* indices for quantities in a coordinate basis are given by lowercase Greek letters, while abstract indices for quantities in a tetrad basis are given by Latin letters with

carets. Indices for *specific components* of vectors in the coordinate basis are given using standard notation (e.g., (t, x, y, z) or (t, r, θ, φ)), while indices for specific components of vectors in the tetrad basis are given by numerals $(0, 1, 2, 3)$.

Once a vierbein is specified, the observer's 4-velocity and the photon's energy-momentum can be specified in the tetrad frame, as

$$u^{\hat{m}} = e^{\hat{m}}_{\ \mu} u^{\mu}, \qquad k^{\hat{m}} = e^{\hat{m}}_{\ \mu} k^{\mu}. \tag{D.2}$$

In the observer's own tetrad rest frame (which will be denoted with a subscript "ob"), the observer by definition has 4-velocity $u^{\hat{m}}_{\text{ob}} = (1, 0, 0, 0)$. The relation between this frame and the coordinate frame can be found by performing a series of Lorentz transformations (and note that the following assumes that all spatial components are nonzero—if $u^3 = 0$, for example, the rotation in Eq. (D.4) can be omitted):

First, transform $u^{\hat{m}} \to (u^{\hat{m}})'$ by rotating counterclockwise about the x^2 axis (in the x^1-x^3 plane) by an angle φ into a frame that satisfies the condition $(u^3)' = 0$:

$$(u^0)' = u^0, \quad (u^1)' = \cos(\varphi) u^1 + \sin(\varphi) u^3, \quad (u^2)' = u^2, \quad (u^3)' = -\sin(\varphi) u^1 + \cos(\varphi) u^3. \tag{D.3}$$

Requiring $(u^3)' = 0$ leads to the following expressions for the pitch angle φ and the new x^1-component of the 4-velocity:

$$\tan(\varphi) = \frac{u^3}{u^1}$$

$$\implies (u^0)' = u^0, \quad (u^1)' = u^1 \sqrt{1 + \frac{(u^3)^2}{(u^1)^2}}, \quad (u^2)' = u^2, \quad (u^3)' = 0. \tag{D.4}$$

Next, transform $(u^{\hat{m}})' \to (u^{\hat{m}})''$ by rotating counterclockwise about the x^3 axis (in the x^1-x^2 plane)

by an angle ϑ into a frame that satisfies the condition $(u^2)'' = 0$:

$$(u^0)'' = (u^0)', \qquad (u^1)'' = \cos(\vartheta)(u^1)' - \sin(\varphi)(u^2)',$$

$$(u^2)'' = \sin(\vartheta)(u^1)' + \cos(\vartheta)(u^2)', \qquad (u^3)'' = (u^3)'. \tag{D.5}$$

Requiring $(u^2)'' = 0$ leads to the following expressions for the yaw angle ϑ and the new components of the 4-velocity:

$$\tan(\vartheta) = -\frac{u^2}{u^1 \sqrt{1 + \frac{(u^3)^2}{(u^1)^2}}}$$

$$\implies (u^0)'' = u^0, \qquad (u^1)'' = u^1 \sqrt{1 + \frac{(u^3)^2}{(u^1)^2}} \sqrt{1 + \frac{(u^2)^2}{(u^1)^2 + (u^3)^2}}, \qquad (u^2)'' = 0, \qquad (u^3)'' = 0. \tag{D.6}$$

Finally, transform $(u^{\hat{m}})'' \to u^{\hat{m}}_{\text{ob}}$ by boosting into the observer's rest frame, where $u^1_{\text{ob}} = 0$:

$$u^0_{\text{ob}} = \gamma(u^0)'' - \beta\gamma(u^1)'', \qquad u^1_{\text{ob}} = \gamma(u^1)'' - \beta\gamma(u^0)'', \qquad u^2_{\text{ob}} = (u^2)'', \qquad u^3_{\text{ob}} = (u^3)''. \tag{D.7}$$

Requiring $u^1_{\text{ob}} = 0$ leads to the following expressions for the boost parameter β (which also gives the Lorentz factor $\gamma \equiv (1 - \beta^2)^{-1/2}$) and the new components of the 4-velocity:

$$\beta = \frac{u^1}{u^0} \sqrt{1 + \frac{(u^3)^2}{(u^1)^2}} \sqrt{1 + \frac{(u^2)^2}{(u^1)^2 + (u^3)^2}} = \text{sgn}(u^1) \frac{\sqrt{(u^0)^2 - 1}}{u^0}$$

$$u^0_{\text{ob}} = 1, \qquad u^1_{\text{ob}} = 0, \qquad u^2_{\text{ob}} = 0, \qquad u^3_{\text{ob}} = 0, \tag{D.8}$$

where u^0_{ob} simplifies to 1 when the condition $u_{\hat{m}} u^{\hat{m}} = -1$ is applied, given u^0 is positive.

What does the photon's energy-momentum look like in the observer's rest frame? Perform the same process, beginning with the tetrad-frame energy-momentum $k^{\hat{m}}$, rotating around the x^2-axis by the angle φ defined above, rotating around the x^3-axis by the angle ϑ defined above, and boosting

in the x^1-direction by β defined above. The result can be simplified to the following:

$$k^0_{\text{ob}} = k^0 u^0 - k^1 u^1 - k^2 u^2 - k^3 u^3,$$

$$k^1_{\text{ob}} = \text{sgn}(u^1) \frac{k^0 - k^0_{\text{ob}} u^0}{\sqrt{(u^0)^2 - 1}},$$

$$k^2_{\text{ob}} = \frac{k^2 \left((u^1)^2 + (u^3)^2\right) - u^2 \left(k^1 u^1 + k^3 u^3\right)}{\sqrt{(u^0)^2 - 1}\sqrt{(u^1)^2 + (u^3)^2}}, \tag{D.9}$$

$$k^3_{\text{ob}} = \text{sgn}(u^1) \frac{k^3 u^1 - k^1 u^3}{\sqrt{(u^1)^2 + (u^3)^2}}.$$

From $k^{\hat{m}}_{\text{ob}}$, one can find both the frequency of the photon and the observer's viewing angles of the photon. The frequency ω_{ob} is simply the x^0-component of the photon energy-momentum seen by the observer $(\omega_{\text{ob}} \equiv k^0_{\text{ob}})$, since $E = \hbar\omega$ and $\hbar = 1$:

$$\omega_{\text{ob}} = -k^{\hat{m}} u_{\hat{m}}. \tag{D.10}$$

The viewing angles (χ, ψ) at which the observer detects the photon are defined as follows:

$$\tan(\chi) \equiv \frac{k^3_{\text{ob}}}{k^1_{\text{ob}}}, \qquad \tan(\psi) \equiv \frac{\sqrt{\left(k^1_{\text{ob}}\right)^2 + \left(k^3_{\text{ob}}\right)^2}}{k^2_{\text{ob}}},$$

$$k^1_{\text{ob}} = \omega_{\text{ob}} \sin(\psi) \cos(\chi), \qquad k^2_{\text{ob}} = \omega_{\text{ob}} \cos(\psi), \qquad k^3_{\text{ob}} = \omega_{\text{ob}} \sin(\psi) \sin(\chi) \tag{D.11}$$

(note that these viewing angles, used in Chapter 4 for the Carter observers in the Kerr spacetime, are different than the ones defined in Chapter 2 for Carter observers in the conformally separable spacetime).

Once the frequency detected by the observer and the viewing angle are known, one can calculate the rate of redshift seen by an observer staring at a fixed viewing angle. The redshift rate is given by the effective temperature κ_{eff} defined in Sec. 3.2, which is given by the formula

$$\kappa_{\text{eff}} \equiv -\frac{d\ln(\omega_{\text{ob}}/\omega_{\text{em}})}{d\tau_{\text{ob}}}, \tag{D.12}$$

where the subscripts "ob" and "em" here and following denote a function evaluated at the observer position x_{ob} or emitter position x_{em}, respectively. Practically, the frequency ratio will usually not be known explicitly as a function of τ_{ob}; instead, it will in principle be a function of the observer coordinates x_{ob}, the emitter coordinates x_{em}, and the constants of motion k_μ associated with the photon path (the covariant components of the 4-momentum that are conserved: the photon's energy $-k_t = \mathcal{E}$, angular momentum $k_\theta = \mathcal{L}$, and, in the case of Kerr black holes, the Carter constant $\mathcal{K}$). Assuming the observer stares in a fixed direction given by the viewing angles (χ, ψ), the effective temperature κ_{eff} can be expanded with the help of the chain rule as follows:

$$\kappa_{eff}\big|_\chi = \sum_{i=0}^{3}\left(-\frac{dx_{ob}^i}{d\tau_{ob}}\frac{\partial \ln \omega_{ob}}{\partial x_{ob}^i} + \frac{\omega_{ob}}{\omega_{em}}\frac{dx_{em}^i}{d\tau_{em}}\frac{\partial \ln \omega_{em}}{\partial x_{em}^i} - \frac{dk_i}{d\tau_{ob}}\frac{\partial \ln(\omega_{ob}/\omega_{em})}{\partial k_i}\right), \tag{D.13}$$

where a vertical bar $\big|_x$ signifies quantities evaluated with x held constant. The form of the above expression made use of the equality $d\tau_{em}/d\tau_{ob} = \omega_{ob}/\omega_{em}$. This simplifies in the spherically symmetric case (setting $\mathcal{E} = 1$ without loss of generality) to

$$\kappa_{eff}\big|_\chi = \omega_{ob}\sum_{i=0}^{3}\left(\left[\frac{u^i}{\omega^2}\frac{d\omega}{dx^i}\right]_{x_{ob}}^{x_{em}}\right) - \frac{\omega_{em}}{\omega_{ob}}\frac{d\mathcal{L}}{d\tau_{ob}}\bigg|_\chi \frac{\partial(\omega_{ob}/\omega_{em})}{\partial \mathcal{L}}\bigg|_{r_{ob},r_{em}}. \tag{D.14}$$

In order to find $d\mathcal{L}/d\tau_{ob}$, note that the viewing angle is kept constant, so one can write

$$0 = \frac{d\chi}{d\tau_{ob}} = \frac{dr_{ob}}{d\tau_{ob}}\frac{d\chi}{dr_{ob}}\bigg|_\mathcal{L} + \frac{d\mathcal{L}}{d\tau_{ob}}\bigg|_\chi \frac{d\chi}{d\mathcal{L}}\bigg|_{r_{ob}} \tag{D.15}$$

$$\implies \frac{d\mathcal{L}}{d\tau_{ob}}\bigg|_\chi = -u_{ob}^r \frac{d\chi}{dr_{ob}}\bigg|_\mathcal{L} \bigg/ \frac{d\chi}{d\mathcal{L}}\bigg|_{r_{ob}}. \tag{D.16}$$

One final component necessary for the calculation of the rate of redshift is the restriction that the observer must be watching the same emitted in-mode as the emitter's angular position on the sky is varied (see Sec. 4.2 for details). For an emitter at infinity, this restriction can usually be trivially applied without any changes to the above calculations. However, for an emitter at a horizon, the affine distance between the emitter and the observer may diverge, so it becomes necessary to

calculate the final term in Eq. (D.14) differently. Normalized to a frame at rest at infinity, the affine distance λ between the emitter and the observer for spherically symmetric black holes is obtained by integrating $dr/d\lambda$, giving

$$\lambda = \int_{r_{\text{em}}}^{r_{\text{ob}}} \frac{dr}{k^r}. \tag{D.17}$$

The emitted and observed affine distances λ_{em} and λ_{ob} are then

$$\lambda_{\text{em}} = \omega_{\text{em}}\lambda, \qquad \lambda_{\text{ob}} = \omega_{\text{ob}}\lambda. \tag{D.18}$$

If λ_{em} is held fixed as the emitter's position is varied, then the derivative with respect to $\mathcal{L}$ in Eq. (D.14) can be expressed as

$$\left. \frac{\partial \ln(\omega_{\text{ob}}/\omega_{\text{em}})}{\partial \mathcal{L}} \right|_{r_{\text{ob}},r_{\text{em}}} = \left. \frac{\partial \ln \lambda_{\text{ob}}}{\partial \mathcal{L}} \right|_{r_{\text{ob}},r_{\text{em}}}. \tag{D.19}$$

The effective temperature κ_{eff} is calculated using the above framework in Chapter 4.

Appendix E

Backscattering coefficients via the MST method

The Black Hole Perturbation Toolkit (BHPT) [30] makes use of the Mano-Suzuki-Takasugi (MST) method [118, 119] to calculate the scattering coefficients for a Klein-Gordon field with spin weight s in the Kerr spacetime. In this Appendix, we review the implementation of this method for the scattering of exterior modes between the event horizon and spatial infinity, and we extend the analysis to include the scattering of interior modes between the event horizon and the Cauchy horizon.

The notation used throughout this Appendix is self-consistent but may differ from the notation used in the main body of the paper; instead it is chosen to match that of the BHPT and its relevant references. The most notable change is that R here no longer represents the scale length defined below Eq. (4.13) and instead represents the Teukolsky radial mode function defined via the mode expansion

$$\phi_{\omega\ell m} = \frac{R_{\omega\ell m}(r) \; _sS_{\ell m}^\omega(\theta) \; \mathrm{e}^{im\varphi - i\omega t}}{\sqrt{4\pi\omega}}, \tag{E.1}$$

vis-à-vis Eq. (4.130) (therefore $\psi_{\omega\ell}(r) = R_{\omega\ell m}(r)\sqrt{r^2 + a^2}$). The modes $_sS_{\ell m}^\omega(\theta)$ represent spin-weighted spheroidal wave functions [27], while the radial modes $R_{\omega\ell m}(r)$ satisfy the homogeneous radial Teukolsky equation [170]:

$$\left(\frac{K_{\omega m}^2 - 2is(r - M)K_{\omega m}}{\Delta} + 4is\omega r - \lambda_{\omega\ell m} \right) R_{\omega\ell m}$$
$$+ \Delta^{-s}\frac{d}{dr}\left(\Delta^{s+1}\frac{dR_{\omega\ell m}}{dr} \right) = 0, \tag{E.2}$$

for a black hole of mass M and spin a, vis-à-vis Eq. (4.132). The horizon function Δ is defined in the same way as in the text following Eq. (4.13), the function $K_{\omega m} \equiv (r^2 + a^2)\omega - ma$, and the constant $\lambda_{\omega\ell m} \equiv \mathscr{E}_{\ell m} - 2ma\omega + a^2\omega^2 - s(s+1)$, where $\mathscr{E}_{\ell m}$ is the eigenvalue of the spin-weighted spheroidal wave function $_s S_{\ell m}^\omega(\theta)$ [66] and reduces to $\mathscr{E}_{\ell m} \to \ell(\ell+1)$ in the Schwarzschild limit.

The BHPT allows for the following boundary value problem to be solved: consider two sets of modes $R_{\omega\ell m}^{\text{in}}$ (initialized on past null infinity) and $R_{\omega\ell m}^{\text{up}}$ (initialized on the past horizon), which asymptotically approach the boundary values

$$R_{\omega\ell m}^{\text{in}} \to \begin{cases} B_{\text{ext}}^{\text{ref}} r^{-1-2s}\mathrm{e}^{i\omega r^*} + B_{\text{ext}}^{\text{inc}} r^{-1}\mathrm{e}^{-i\omega r^*}, & r \to \infty \\[2ex] B_{\text{ext}}^{\text{trans}}|\Delta|^{-s}\mathrm{e}^{-i\omega_+ r^*}, & r \to r_+ \\[2ex] B_{\text{int}}^{\text{ref}}\ \mathrm{e}^{i\omega_- r^*} + B_{\text{int}}^{\text{trans}}|\Delta|^{-s}\mathrm{e}^{-i\omega_- r^*}, & r \to r_- \end{cases} \tag{E.3}$$

$$R_{\omega\ell m}^{\text{up}} \to \begin{cases} C_{\text{ext}}^{\text{trans}} r^{-1-2s}\mathrm{e}^{i\omega r^*}, & r \to \infty \\[2ex] C_{\text{ext}}^{\text{up}}\ \mathrm{e}^{i\omega_+ r^*} + C_{\text{ext}}^{\text{ref}}|\Delta|^{-s}\mathrm{e}^{-i\omega_+ r^*}, & r \to r_+ \\[2ex] C_{\text{int}}^{\text{trans}}\ \mathrm{e}^{i\omega_- r^*} + C_{\text{int}}^{\text{ref}}|\Delta|^{-s}\mathrm{e}^{-i\omega_- r^*}, & r \to r_- \end{cases} \tag{E.4}$$

where $\omega_\pm$ is given by Eq. (4.137) and the complex constants B and C are scattering coefficients for either the reflection, incidence, or transmission of the mode waves. The tortoise coordinate r^* is chosen to be

$$r^* \equiv r + \frac{1}{2\kappa_+}\ln\left|\frac{r-r_+}{2M}\right| + \frac{1}{2\kappa_-}\ln\left|\frac{r-r_-}{2M}\right|, \tag{E.5}$$

with the surface gravities $\kappa_\pm$ (which is negative at the inner horizon) given by Eq. (4.17). Note that the forward-propagated modes $R_{\omega\ell m}$ and scattering coefficients B and C defined here are different from the backward-propagated modes ψ_{ob} and scattering coefficients $\mathcal{T}$ and $\mathcal{R}$ used in the main text; the relation between the two will be given at the end of this Appendix.

Conservation of the Wronskian in the scalar case leads to the following relations between the

scattering coefficients:

$$\left|B_{\text{ext}}^{\text{ref}}\right|^2 + \frac{\omega_+(r_+^2 + a^2)}{\omega}\left|B_{\text{ext}}^{\text{trans}}\right|^2 = \left|B_{\text{ext}}^{\text{inc}}\right|^2,$$

$$\left|C_{\text{ext}}^{\text{ref}}\right|^2 + \frac{\omega}{\omega_+(r_+^2 + a^2)}\left|C_{\text{ext}}^{\text{trans}}\right|^2 = \left|C_{\text{ext}}^{\text{up}}\right|^2,$$

$$\frac{C_{\text{ext}}^{\text{trans}}}{C_{\text{ext}}^{\text{up}}} = \frac{\omega_+(r_+^2 + a^2)}{\omega}\frac{B_{\text{ext}}^{\text{trans}}}{B_{\text{ext}}^{\text{inc}}},$$

$$\frac{C_{\text{ext}}^{\text{trans}}}{C_{\text{ext}}^{\text{ref}}} = -\frac{\omega_+(r_+^2 + a^2)}{\omega}\frac{B_{\text{ext}}^{\text{trans}*}}{B_{\text{ext}}^{\text{ref}*}},$$

$$\left|B_{\text{int}}^{\text{ref}}\right|^2 + \frac{\omega_+(r_+^2 + a^2)}{\omega_-(r_-^2 + a^2)}\left|B_{\text{ext}}^{\text{trans}}\right|^2 = \left|B_{\text{int}}^{\text{trans}}\right|^2,$$

$$\left|C_{\text{int}}^{\text{up}}\right|^2 - \frac{\omega_-(r_-^2 + a^2)}{\omega_+(r_+^2 + a^2)}\left(\left|C_{\text{int}}^{\text{trans}}\right|^2 - \left|C_{\text{int}}^{\text{ref}}\right|^2\right) = \left|C_{\text{ext}}^{\text{ref}}\right|^2,$$

$$B_{\text{int}}^{\text{trans}}C_{\text{int}}^{\text{trans}} - B_{\text{int}}^{\text{ref}}C_{\text{int}}^{\text{ref}} = \frac{\omega_+(r_+^2 + a^2)}{\omega_-(r_-^2 + a^2)}B_{\text{ext}}^{\text{trans}}C_{\text{int}}^{\text{up}},$$

$$B_{\text{int}}^{\text{trans}*}C_{\text{int}}^{\text{ref}} - B_{\text{int}}^{\text{ref}*}C_{\text{int}}^{\text{trans}} = \frac{\omega_+(r_+^2 + a^2)}{\omega_-(r_-^2 + a^2)}B_{\text{ext}}^{\text{trans}*}C_{\text{ext}}^{\text{ref}}, \tag{E.6}$$

where a superscript asterisk (*) here and elsewhere denotes complex conjugation, except in the case of the tortoise coordinate r^*. In what follows, we will focus on the *in* modes; the scattering coefficients for the *up* modes can be obtained from the *in* modes through the above Wronskian conditions. The main results for the application of the MST method in the exterior portion of the spacetime will be quoted here; for a more complete review, see Ref. [161].

The solutions to the radial wave Eq. (E.2) belong to a class of functions known as confluent Heun functions. However, the mathematical properties of these functions (especially their asymptotic behavior at each horizon) has been a mathematical enigma, and to this day, the central two-point connection problem for these functions still has no explicit solution. However, Svartholm [168] and Erdélyi [57, 58] early on discovered an integral transform for confluent Heun functions with a hypergeometric kernel, so that they could be expressed in a series representation as the sum of (the more tractable) hypergeometric functions.

Under the MST method, two infinite series expansions of the solutions to Eq. (E.2) are found that are valid in different but overlapping regimes. The first of these expansions, in terms of ordinary

hypergeometric functions $_2F_1$, is valid for all finite values of r but breaks down as $r \to \infty$. Defining the dimensionless parameters[1]

$$x \equiv \frac{\omega}{\epsilon\kappa}(r_+ - r), \qquad \epsilon \equiv 2M\omega, \qquad \kappa \equiv \sqrt{1 - \left(\frac{a}{M}\right)^2}, \qquad \epsilon_\pm \equiv \frac{\epsilon \pm \tau}{2}, \qquad \tau \equiv \frac{\epsilon - m\left(\frac{a}{M}\right)}{\kappa}, \qquad \text{(E.7)}$$

such that the outer $(+)$ and inner $(-)$ horizon radii are given by $r_\pm \equiv (1 \pm \kappa)M$, this first series is:

$$R_\nu^{\text{in}} = e^{i\epsilon\kappa x}|-x|^{-s-i\epsilon_+}|1-x|^{i\epsilon_-} \sum_{n=-\infty}^{\infty} a_n^\nu(s)_2F_1(n+\nu+1-i\tau, -n-\nu-i\tau; 1-s-2i\epsilon_+; x), \qquad \text{(E.8)}$$

where the parameter ν, called the renormalized angular momentum, is a generalization of ℓ to non-integer values that is fixed by requiring that the series solution to the Teukolsky equation converges.

Likewise, the second series expansion can be written in terms of confluent hypergeometric functions and is valid for asymptotically large values of r but fails as $r \to r_+$. By matching these two expansions, the coefficients $a_n^\nu(s)$ in both expansions will satisfy the same three-term recurrence relation that can be solved numerically to find the minimal solution.

As $r \to r_+$ (or equivalently, as $x \to 0$), Eq. (E.8) reduces to

$$R_\nu^{\text{in}} \to |-x|^{-s-i\epsilon_+} \sum_{n=-\infty}^{\infty} a_n^\nu(s), \qquad \text{(E.9)}$$

while Eq. (E.3) can be written in terms of the parameters of Eq. (E.7) as

$$R_{\omega\ell m}^{\text{in}} \to B_{\text{ext}}^{\text{trans}} \left(\frac{\epsilon\kappa}{\omega}\right)^{-2s} |-x|^{-s} \, e^{-i\epsilon_+\left(\ln|-x|+\kappa+\frac{2\kappa\ln\kappa}{1+\kappa}\right)}. \qquad \text{(E.10)}$$

The coefficient $B_{\text{ext}}^{\text{trans}}$ can then be read off by equating the two expressions from Eqs. (E.9) and

---

[1]As a reminder, the parameters defined here and used throughout Appendix E should be treated independently from the notation of the main body of the thesis and instead are chosen to align with the notation used by MST [118, 119]. In particular, κ does not represent the surface gravity or the effective temperature, ϵ does not represent the adiabatic control function, and τ does not represent proper time.

(E.10). A similar matching process leads to expressions for the scattering parameters at infinity. The resulting formulae for $B_{\text{ext}}^{\text{trans}}$, $B_{\text{ext}}^{\text{inc}}$, and $B_{\text{ext}}^{\text{ref}}$ are given respectively by Eqs. (167)–(169) of Ref. [161].

Now, consider how the above formalism may be extended to the black hole's interior. As $r \to r_-$ (or equivalently, as $x \to 1$), based on the asymptotic behavior of the hypergeometric function with argument unity, Eqs. (E.8) and (E.3) respectively reduce to

$$R_\nu^{\text{in}} \to e^{i\epsilon\kappa}\left[|1-x|^{i\epsilon_-} \sum_{n=-\infty}^{\infty} a_n^\nu(s)\frac{\Gamma(1-s-2i\epsilon_+)\Gamma(-s-2i\epsilon_-)}{\Gamma(-n-\nu-s-i\epsilon)\Gamma(n+\nu+1-s-i\epsilon)}H(-s)\right.$$
$$\left. + |1-x|^{-s-i\epsilon_-} \sum_{n=-\infty}^{\infty} a_n^\nu(s)\frac{\Gamma(1-s-2i\epsilon_+)\Gamma(s+2i\epsilon_-)}{\Gamma(-n-\nu-i\tau)\Gamma(n+\nu+1-i\tau)}H(s)\right], \tag{E.11}$$

$$R_{\omega\ell m}^{\text{in}} \to B_{\text{int}}^{\text{ref}} \exp\left[i\epsilon_-\left(\ln|1-x|-\kappa-\frac{2\kappa\ln\kappa}{1-\kappa}\right)\right]$$
$$+ B_{\text{int}}^{\text{trans}}\left(\frac{\epsilon\kappa}{\omega}\right)^{-2s}|1-x|^{-s}\exp\left[-i\epsilon_-\left(\ln|1-x|-\kappa-\frac{2\kappa\ln\kappa}{1-\kappa}\right)\right], \tag{E.12}$$

where $H(s)$ is the Heaviside step function defined by

$$H(s) \equiv \begin{cases} 1, & s \geq 0 \\ 0, & s < 0 \end{cases}. \tag{E.13}$$

Eq. (E.11) breaks down for scalar modes when either $\omega = 0$ or $a = 0$; these cases, whose modes asymptotically scale as $\ln(1-x)$, must be treated separately.

Matching Eqs. (E.11) and (E.12) leads to expressions for the internal scattering parameters:

$$B_{\text{int}}^{\text{ref}} = H(-s)\; e^{i\kappa\left[\epsilon+\epsilon_-\left(1+\frac{2\ln\kappa}{1-\kappa}\right)\right]} \sum_{n=-\infty}^{\infty} a_n^\nu(s)\frac{\Gamma(1-s-2i\epsilon_+)\Gamma(-s-2i\epsilon_-)}{\Gamma(-n-\nu-s-i\epsilon)\Gamma(n+\nu+1-s-i\epsilon)}, \tag{E.14}$$

$$B_{\text{int}}^{\text{trans}} = H(s)\left(\frac{\epsilon\kappa}{\omega}\right)^{2s} e^{i\kappa\left[\epsilon-\epsilon_-\left(1+\frac{2\ln\kappa}{1-\kappa}\right)\right]} \sum_{n=-\infty}^{\infty} a_n^\nu(s)\frac{\Gamma(1-s-2i\epsilon_+)\Gamma(s+2i\epsilon_-)}{\Gamma(-n-\nu-i\tau)\Gamma(n+\nu+1-i\tau)}. \tag{E.15}$$

The step functions in Eqs. (E.14) and (E.15) imply that close to the inner horizon, only the non-negative (non-positive) spin-weighted components of ingoing (outgoing) waves survive, since these are the radiative (i.e., dominant propagating; see Footnote 7) components.

The expressions above for the inner horizon scattering coefficients can then be implemented in `Mathematica` alongside the rest of the BHPT's Teukolsky package to compute the relevant *in* scattering coefficients. In order to connect these results to the calculations in Chapter 4, a transformation must be made between the two sets of scattering coefficients (B and C on the one hand and $\mathcal{T}$ and $\mathcal{R}$ on the other). One of the main problems that gives rise to the need for such a non-trivial matching is that Chapter 4's back-propagated modes $^{\text{ext,int}}\psi_{\text{ob}}^{\pm}$ are initialized on the future null boundaries, while this Appendix's forward-propagated modes $R_{\omega\ell m}^{\text{in,up}}$ are initialized on the past null boundaries.

To find the back-propagated scattering coefficients, first note that through the conservation of the Wronskian, the transmission and reflection coefficients $\mathcal{T}_{\text{ext,int}}^{\pm}$ and $\mathcal{R}_{\text{ext,int}}^{\pm}$ must satisfy the normalization conditions

$$\left|\mathcal{R}_{\text{ext},\omega}^{\pm}\right|^2 + \left|\mathcal{T}_{\text{ext},\omega}^{\pm}\right|^2 \left(\frac{\omega \mp m\Omega_+}{\omega}\right) = 1, \tag{E.16a}$$

$$\left(\left|\mathcal{R}_{\text{int},\omega}^{\pm}\right|^2 - \left|\mathcal{T}_{\text{int},\omega}^{\pm}\right|^2\right)\left(\frac{\omega_+ + m\Omega_-}{\omega}\right) = 1. \tag{E.16b}$$

Consider first the exterior set of modes used to calculate $\langle N_{\text{ext}}^{\pm}\rangle_{\omega\ell m}$, encoded by a family of observers asymptotically close to future null infinity and the event horizon. Through time reversal, these modes $^{\text{ext}}\psi_{\text{ob}}^{\pm}$ map to the modes $R_{\omega\ell m}^{\text{in,up}}$ by the transformation $(\omega, m) \mapsto (-\omega, -m)$, which corresponds to taking the complex conjugate of the scattering coefficients, since

$$R_{(-\omega)\ell(-m)} = R_{\omega\ell m}^*, \qquad B_{(-\omega)\ell(-m)}^{\text{trans,ref}} = B_{\omega\ell m}^{\text{trans,ref}*}. \tag{E.17}$$

By matching the asymptotic relations for the complete set of modes $R_{\omega\ell m}^{\text{in}}$ and $R_{\omega\ell m}^{\text{up}}$ in the spin-0 limit of Eqs. (E.3) and (E.4) with the appropriately rescaled set of exterior modes $^{\text{ext}}\psi_{\text{ob}}^{-*}$ and $^{\text{ext}}\psi_{\text{ob}}^{+*}$ from Eqs. (4.141) and (4.142), respectively, one arrives at the following equalities, after fixing $B_{\text{ext}}^{\text{inc}} = 1$

and $C_{\text{ext}}^{\text{up}} = 1/\sqrt{r_+^2 + a^2}$:

$$\mathcal{T}_{\text{ext},\omega}^+ = B_{\text{ext},\omega}^{\text{trans}*}\sqrt{r_+^2 + a^2}, \tag{E.18a}$$

$$\mathcal{R}_{\text{ext},\omega}^+ = B_{\text{ext},\omega}^{\text{ref}*}, \tag{E.18b}$$

$$\mathcal{T}_{\text{ext},\omega_+}^- = C_{\text{ext},\omega}^{\text{trans}*}, \tag{E.18c}$$

$$\mathcal{R}_{\text{ext},\omega_+}^- = C_{\text{ext},\omega}^{\text{ref}*}\sqrt{r_+^2 + a^2}. \tag{E.18d}$$

Notice the addition of the mode frequency subscripts in the above scattering coefficients that help highlight a key difference between the (B, C) coefficients and the $(\mathcal{T}, \mathcal{R})$ coefficients—the scattering process defined by the former is initialized with the frequency eigenmodes of the wave equation, while the scattering process of the latter is initialized so that the observer always sees a frequency ω.

Now consider the interior modes used to calculate $\langle N_{\text{int}}^{\pm}\rangle_{\omega\ell m}$, encoded by a family of observers reaching the ingoing and outgoing portions of the inner horizon (together with observers asymptotically close to future null infinity, to form a complete Cauchy slice). Since the global scattering process now depends on three singular points and the interior scattering potential is dynamical, the backward-propagated modes will not map trivially onto the forward-propagated modes by time reversal. One may instead consider the transformation $(M, r) \mapsto (-M, -r)$ as in Ref. [178], which leaves the radial wave Eq. (4.132) unchanged aside from a swapping of the asymptotic regimes at the inner and outer horizons. However, since that transformation leaves the irregular singular point at $r \to \infty$ unchanged, the forward- and backward-propagated modes must transform into linear combinations of one another.

In order to solve for the interior scattering coefficients, define coefficients $\alpha_{\text{in,up}}^{\pm}$ that form linear combinations of the modes $R_{\omega\ell m}^{\text{in}}$ and $R_{\omega\ell m}^{\text{up}}$. These linear combinations can be asymptotically equated to the modes $^{\text{int}}\psi_{\text{ob}}^-$ initialized along the ingoing portion of the future Cauchy slice and the

modes $^{\mathrm{int}}\psi_{\mathrm{ob}}^{+^*} + {}^{\mathrm{ext}}\psi_{\mathrm{ob}}^{+}$ initialized along the outgoing portions of the future Cauchy slice:

$$\left(\alpha_{\mathrm{in}}^{-} R_{\omega\ell m}^{\mathrm{in}} + \alpha_{\mathrm{up}}^{-} R_{\omega\ell m}^{\mathrm{up}}\right) \sqrt{r^2 + a^2} = {}^{\mathrm{int}}\psi_{\mathrm{ob}}^{-}, \tag{E.19a}$$

$$\left(\alpha_{\mathrm{in}}^{+} R_{\omega\ell m}^{\mathrm{in}} + \alpha_{\mathrm{up}}^{+} R_{\omega\ell m}^{\mathrm{up}}\right) \sqrt{r^2 + a^2} = {}^{\mathrm{int}}\psi_{\mathrm{ob}}^{+^*} + {}^{\mathrm{ext}}\psi_{\mathrm{ob}}^{+} \tag{E.19b}$$

Matching the asymptotic relations for the above sets of modes along the inner horizon leads to the linear coefficient values

$$\alpha_{\mathrm{in}}^{+} = \frac{C_{\mathrm{int}}^{\mathrm{ref}}}{D}, \qquad\qquad \alpha_{\mathrm{up}}^{+} = -\frac{B_{\mathrm{int}}^{\mathrm{trans}}}{D}, \tag{E.20a}$$

$$\alpha_{\mathrm{in}}^{-} = -\frac{C_{\mathrm{int}}^{\mathrm{trans}}}{D}, \qquad\qquad \alpha_{\mathrm{up}}^{-} = \frac{B_{\mathrm{int}}^{\mathrm{ref}}}{D}, \tag{E.20b}$$

where

$$D \equiv \left(B_{\mathrm{int}}^{\mathrm{ref}} C_{\mathrm{int}}^{\mathrm{ref}} - B_{\mathrm{int}}^{\mathrm{trans}} C_{\mathrm{int}}^{\mathrm{trans}}\right) \sqrt{r_{-}^2 + a^2}. \tag{E.21}$$

The scattering coefficients can then be found by matching the asymptotic relations along the event horizon and at infinity:

$$\mathcal{T}_{\mathrm{int},\omega_{-}}^{-} = \left(\alpha_{\mathrm{in},\omega}^{-} B_{\mathrm{ext},\omega}^{\mathrm{trans}} + \alpha_{\mathrm{up},\omega}^{-} C_{\mathrm{ext},\omega}^{\mathrm{ref}}\right) \sqrt{r_{+}^2 + a^2}, \tag{E.22a}$$

$$\mathcal{R}_{\mathrm{int},\omega_{-}}^{-} = \alpha_{\mathrm{up},\omega}^{-} C_{\mathrm{int},\omega}^{\mathrm{up}} \sqrt{r_{+}^2 + a^2}, \tag{E.22b}$$

$$\mathcal{T}_{\mathrm{int},\omega_{-}}^{+} = \alpha_{\mathrm{up},\omega}^{+^*} C_{\mathrm{int},\omega}^{\mathrm{up}^*} \sqrt{r_{+}^2 + a^2}, \tag{E.22c}$$

$$\mathcal{R}_{\mathrm{int},\omega_{-}}^{+} = \left(\alpha_{\mathrm{in},\omega}^{+^*} B_{\mathrm{ext},\omega}^{\mathrm{trans}^*} + \alpha_{\mathrm{up},\omega}^{+^*} C_{\mathrm{ext},\omega}^{\mathrm{ref}^*}\right) \sqrt{r_{+}^2 + a^2}, \tag{E.22d}$$

$$\mathcal{T}_{\mathrm{ext},\omega_{+}}^{-} = \frac{\alpha_{\mathrm{in},\omega}^{-} B_{\mathrm{ext},\omega}^{\mathrm{inc}}}{\mathcal{T}_{\mathrm{int},\omega_{-}}^{-}}, \tag{E.22e}$$

$$\mathcal{R}_{\mathrm{ext},\omega_{+}}^{-} = \frac{\alpha_{\mathrm{up},\omega}^{-} C_{\mathrm{ext},\omega}^{\mathrm{up}}}{\mathcal{T}_{\mathrm{int},\omega_{-}}^{-}} \sqrt{r_{+}^2 + a^2}, \tag{E.22f}$$

$$\mathcal{T}_{\mathrm{ext},\omega}^{+} = \alpha_{\mathrm{up},\omega}^{+} C_{\mathrm{ext},\omega}^{\mathrm{up}} \sqrt{r_{+}^2 + a^2} - \mathcal{R}_{\mathrm{int},\omega_{-}}^{+^*} \mathcal{R}_{\mathrm{ext},\omega_{+}}^{-^*}, \tag{E.22g}$$

$$\mathcal{R}_{\mathrm{ext},\omega}^{+} = \alpha_{\mathrm{in},\omega}^{+} B_{\mathrm{ext},\omega}^{\mathrm{inc}} - \mathcal{R}_{\mathrm{int},\omega_{-}}^{+^*} \mathcal{T}_{\mathrm{ext},\omega_{+}}^{-^*}. \tag{E.22h}$$

Note that, unlike in the exterior case of Eqs. (E.18), the B^{inc} and C^{up} coefficients from Eqs. (E.22) do not need to be fixed since all the B and C coefficients are written in a normalization-free form. Thus, one may retain the default normalization choice $B^{\mathrm{trans}} = 1$ used by the BHPT.

Once the scattering coefficients B and C are computed with the help of the BHPT, Eqs. (E.18) can be used to calculate the back-scattering coefficients $\mathcal{T}$ and $\mathcal{R}$ used in Eqs. (4.147a)–(4.147b), while Eqs. (E.22) can be used to calculate the back-scattering coefficients used in Eqs. (4.147c)–(4.147d).